# Quantum Simulation of Fermionic Models


Juha Mikael Kreula

Christ Church

University of Oxford

A thesis submitted to the Mathematical, Physical and Life Sciences Division for the degree of Doctor of Philosophy at the University of Oxford.

Hilary Term, 2017

# Abstract

This work is a theoretical study of fermionic models. We focus on problems where highly controllable quantum simulators of these models have an important role, and we utilise both the analogue and the digital paradigm of quantum simulation.

In the part on analogue quantum simulation, we focus on the proposed 'spin-asymmetric' Josephson effect where Cooper-paired spins display frequency synchronized Josephson oscillations with spin-dependent amplitudes. We consider different scenarios where the phenomenon could manifest in ultracold atomic Fermi gases. We study a Fermi gas Josephson junction in the recently realized Josephson plasma oscillation regime with an additional spin-dependent potential and show that the asymmetry in the resulting spin-dependent plasma oscillation amplitudes is on the order of a couple of per cent. We also demonstrate numerically that spin-asymmetric Josephson-like currents occur in a one-dimensional spin-dependent optical superlattice, with amplitude asymmetries up to 39%. Finally, we show that at zero temperature the tunable critical current in ferromagnetic Josephson junctions can be explained by the spin-asymmetric Josephson effect.

In the part where digital quantum simulation is used, we propose a hybrid quantum-classical approach to studying strongly correlated fermion models. In this approach, a digital quantum simulator works in conjunction with a classical feedback loop to solve the infinite-dimensional Hubbard model directly in the thermodynamic limit. The scheme implements the well-established dynamical mean-field theory (DMFT) method, such that the digital quantum simulator solves the classically hard DMFT impurity problem and self-consistency is taken care of in a classical computer. We first present a few-qubit proof-of-principle setup for equilibrium systems that implements the simplified 'two-site' DMFT. This few-qubit setup is used for a qualitative description of the Mott transition in the half-filled infinite-dimensional Hubbard model. We then describe a scalable setup for simulating non-equilibrium many-body quantum dynamics by proposing the implementation of the non-equilibrium extension of DMFT with the hybrid device.

# ACKNOWLEDGEMENTS

This thesis concludes the roughly three and a half years of research I did in the Clarendon Laboratory at the University of Oxford with funding from the Department of Physics, Christ Church, and the Osk. Huttunen Foundation. The results presented in this thesis were not obtained in a vacuum. I am indebted to many people for the progress in my DPhil studies and would like to take the opportunity to thank them.

Firstly, I am truly grateful to Professor Dieter Jaksch for giving me the opportunity pursue research under his supervision in this world-class institution. His physics knowledge and careful scrutiny of my work constantly pushed me to learn, challenge myself, and develop as an independent scientist. He furthermore encouraged me to conceive my own projects, which improved my scientific creativity, and authorized my engagement in several collaborations, which allowed me to create a network of connections with scientists from different fields of expertise around the world. I am grateful for all this. I would also like to thank Stephen Clark for all his help and patience, and for the numerous fruitful conversations during my DPhil. Anna–Maija Uimonen is thanked for useful discussions on Green functions. In addition, all members of the Dieter Jaksch group are acknowledged for creating a nice working environment.

I want to extend my gratitude to my collaborators and the coauthors of my papers [1–4]. I would especially like to acknowledge Professor Päivi Törmä, the fruitful collaboration with whom on the spin-asymmetric Josephson effect forms a significant part of this thesis. It has been a true pleasure and privilege to work with a theoretical physicist of her calibre. I thank Miikka Heikkinen, Francesco Massel, and Giacomo Valtolina for their important contributions. The fun and extremely efficient collaboration with Laura García–Álvarez, Lucas Lamata, and Professor Enrique Solano is also gratefully acknowledged.

Outside academic work, I wish to thank my friends and acquaintances both in

Oxford and in Finland for making this experience in the United Kingdom a truly memorable one. In particular, thank you, Simone, for all your kind, never-ending support, understanding, and companionship even in the darkest hours when it seemed that this work would never be finished. A special thank you also to Franz, Manuel, Giulia, Margherita, Niccolò, FengTing, Josh, Visa, Katri, Kinga, Lise, Alix, Elliot, Jukka, Mikko, Harri, and all the numerous wonderful people I've met in Oxford.

Finally, and most importantly, I want to thank my parents for everything they have so warm-heartedly done for me and for all their unconditional support and love. Thank you for always being there for me, without you I would not have made it this far. Kiitos.

Oxford, March 31, 2017

Juha Kreula

# Contents

# PUBLICATIONS

The results presented in this thesis are based on original research articles in Refs. [1–4]. In chronological order, along with the author's original contribution, they are:

- J. M. Kreula, M. O. J. Heikkinen, F. Massel, and P. Törmä, Tunable critical supercurrent and spin-asymmetric Josephson effect in superlattices, *Phys. Rev. B* **89**, 064502 (2014).

  – This work was done in collaboration with the group of Päivi Törmä. The author carried out the numerical time-evolving block decimation simulations, analysed the results, and studied with Miikka Heikkinen the connection between the tunable critical current in SFIFS junctions and the spin-asymmetric Josephson effect. The author wrote a significant part of the manuscript.

- J. M. Kreula, L. García-Álvarez, L. Lamata, S. R. Clark, E. Solano, and D. Jaksch, Few-qubit quantum-classical simulation of strongly correlated lattice fermions, *EPJ Quantum Technol.* **3**, 11 (2016).

  – This work was done in collaboration with the group of Enrique Solano. The author conceived the project, did the analytical calculations and the numerical simulations on two-site dynamical mean-field theory, analysed the results, and was the main writer of the manuscript.

- J. M. Kreula, S. R. Clark, and D. Jaksch, Non-linear quantum-classical scheme to simulate non-equilibrium strongly correlated fermionic many-body dynamics, *Sci. Rep.* **6**, 32940 (2016).

  – The author contributed to the development of the idea, worked out the quantum algorithm for the time-dependent single-impurity Anderson model, carried out the corresponding numerical non-equilibrium dynamical mean-field theory simulations, contributed to analysing the results, and wrote a significant part of the manuscript.

- J. M. Kreula, G. Valtolina, and P. Törmä, Spin-asymmetric Josephson plasma oscillations, *Phys. Rev. A* **95**, 013634 (2017)

  – This work was done in collaboration with the groups of Päivi Törmä and Giacomo Roati. The author conceived the project together with Päivi Törmä, did the analytical calculations and numerical simulations for the spin-dependent Josephson plasma oscillations, analysed the results, and was the main writer of the paper.

# PART I INTRODUCTION

# Chapter 1

# INTRODUCTION

## 1.1 Quantum simulation

A quantum simulator is a highly controllable quantum device that is used for simulating model Hamiltonians [5–7]. These model Hamiltonians then try and capture the essential physics of real systems such as electrons in metals. The proposal of using a quantum simulator to study other (usually less controllable) quantum systems goes back to Richard Feynman [8], who noted that classical simulations of quantum systems quickly become intractable due to the exponential growth in the required computational resources with the number of simulated particles.

The idea of quantum simulation has been widely adopted and several different types of quantum hardware have been proposed as platforms for quantum simulations. They include, e.g., ultracold atoms in laser-created periodic potentials called optical lattices [9], trapped ions [10], superconducting circuits [11], and photons [12]. Also the problems that quantum simulators aim to solve and their proof-of-principle demonstrations are varied, ranging, e.g., from quantum chemistry [13] and the Mott transition [14–16] to the Dirac equation [17, 18] and the lattice Schwinger model [19–21]. One of the important future applications of quantum simulations is the possibility to study controlled quantum dynamics that cannot be simulated with classical computers. Depending on the features of the

quantum hardware, quantum simulations are usually implemented using either analogue or digital techniques, although analogue–digital combinations are also possible.

An analogue quantum simulator aims to continuously reproduce the dynamics of the simulated system by directly mapping the model Hamiltonian onto the Hamiltonian of the simulator. Ultracold atoms are among the most advanced analogue quantum simulation platforms. For example, ultracold atoms in optical lattices implement the Hubbard Hamiltonian in an analogue manner, with atoms in different hyperfine levels representing the spin-$\frac{1}{2}$ electrons that can tunnel between lattice sites and interact when occupying the same lattice site. Optical-lattice-based quantum simulators have also been proposed, e.g., for relativistic field theories and topological insulators [22–24]. For further examples of applications of ultracold atoms, see Refs. [9, 25–31].

In a digital quantum simulator, the dynamics of the model system is decomposed into a set of quantum gates which are usually easier to implement in the platform of choice than directly mapping the model Hamiltonian in an analogue manner. With a universal set of quantum gates, the device can be programmed to simulate any local quantum system, which makes digital quantum simulators in principle universal [32]. Proof-of-principle demonstrations of digital quantum simulations of spin models [33] and lattice gauge theories [21] have been done in trapped ions, and digital implementations of Hubbard-like fermionic dynamics have been achieved in superconducting circuits [34].

We note that sometimes the term quantum simulation is used in a completely different context. For example, the Oxford Dictionary of Physics [35] defines quantum simulation as 'the mathematical modelling of systems of large numbers of atoms or molecules by computer studies of relatively small clusters.' We would call this definition of quantum simulation as 'classical simulation of a quantum system' instead of the 'quantum simulation of a quantum system' which is the

definition we adopt. However, note that in this work we resort to classical simulations in our numerical calculations.

## 1.2 This thesis

In this thesis, we theoretically propose different scenarios and applications of quantum simulators of fermionic models.[1] We utilize both the analogue and the digital paradigm of quantum simulation in this work. The thesis has four parts.

The first, general introduction part consists of this Chapter and is completed by Chapter 2, in which we present some key concepts of many-body quantum theory needed in the rest of the thesis. We begin with introducing the Hubbard Hamiltonian which is an important toy model to describe strongly correlated electron materials as well as ultracold atoms in optical lattices. We then proceed to the Green function formalism both in the equilibrium and in the non-equilibrium case.

The second part of this thesis considers the analogue quantum simulation of fermions, focusing on ultracold atoms. It has three Chapters. Chapter 3 introduces ultracold atoms and the theoretical and experimental concepts, such as Bardeen–Cooper–Schrieffer theory, Josephson effect, and optical lattices, which are relevant to this work. In Chapter 4, we study the proposed spin-asymmetric Josephson effect [36, 37]. In this phenomenon, Cooper-paired spin-$\frac{1}{2}$ fermions Josephson-oscillate at the same Josephson frequency for both spin components but the critical Josephson current is different for the two spin components in the presence of a spin-dependent 'voltage' across the Josephson junction. We propose different scenarios where the spin-asymmetric currents could manifest in ultracold atom setups. The control over individual degrees of freedom and the high tunability of parameters achievable in ultracold Fermi gas setups are instrumental for the possi-

[1] Fermions are particles with half-integer spin obeying Fermi–Dirac statistics. For example electrons are fermions. They are omnipresent in condensed matter systems, making their modelling and quantum simulation highly relevant.

ble realization of an analogue of a Josephson junction with spin-dependent potentials. Motivated by the observation of Josephson plasma oscillations in ultracold Fermi gases [38], we study the plasma oscillation regime in a spin-dependent double well potential and show that the spin-asymmetric Josephson effect manifests as a spin-dependent plasma oscillation amplitude. We also demonstrate numerically that spin-asymmetric Josephson-like currents are present in the dynamics of a one-dimensional spin-dependent optical superlattice setup. In Chapter 5, we show that the tunable direct critical Josephson current in ferromagnetic Josephson junctions [39] can be explained by the spin-asymmetric Josephson effect at zero temperature.

In the third part, we concentrate on the digital paradigm of quantum simulation and propose a non-linear, hybrid quantum-classical simulation scheme, in which a digital quantum simulator works in conjunction with a classically computed feedback loop to study the infinite-dimensional Hubbard model directly in the thermodynamic limit. The scheme implements the dynamical mean-field theory (DMFT) method [40]. Chapter 6 introduces key concepts of digital quantum simulation and discusses superconducting circuits and trapped ions as physical realizations. Chapter 7 gives an overview of the DMFT method. In Chapter 8, we propose a proof-of-principle demonstration of the hybrid quantum-classical implementation of DMFT, based on a variant of DMFT called 'two-site' DMFT, the realization of which requires only five quantum bits (qubits). In Chapter 9, we present a scalable setup for non-equilibrium dynamics which implements the non-equilibrium extension of DMFT [41] using multiqubit Mølmer–Sørensen gates and analyse its performance in a simple example case.

The fourth part provides the conclusions of the thesis. We summarise the results of this work in Chapter 10. We also present some possible future directions and extensions of this work.

In the Appendices we present further background and calculation details. Regarding the units used in this work, we set the reduced Planck constant $\hbar = 1$ throughout the thesis.

# Chapter 2

## MANY-BODY QUANTUM THEORY

In this Chapter we introduce the central concepts of many-body quantum theory used in the thesis, starting from the Hubbard Hamiltonian. We then introduce Green functions both in the equilibrium and in the non-equilibrium case.

## 2.1 Hubbard model

Real electronic systems such as novel quantum materials [42] are very complex systems to describe [43]. However, in many cases a drastically simplified toy model can capture the essential features of the physical phenomena while neglecting many of the complexities of the material. This is one reason why lattice models are used in condensed matter physics.

An important and much studied strongly correlated lattice model is the Hubbard Hamiltonian [44–46]. Originally, it was introduced to study the ferromagnetism of transition metals. It has since been adopted as the model of choice in other scenarios as well, in particular in ultracold atoms in optical lattices [27, 47]. In its simplest form the Hubbard Hamiltonian is given by

$$\hat{H} = -J \sum_{\langle i,j\rangle,\sigma} \left( \hat{c}^{\dagger}_{i,\sigma} \hat{c}_{j,\sigma} + \text{H.c.} \right) + U \sum_{i} \hat{n}_{i,\uparrow} \hat{n}_{i,\downarrow}. \tag{2.1}$$

Here, spin-$\frac{1}{2}$ fermions, such as electrons, which have spin projections $\sigma = \downarrow, \uparrow$, tunnel between adjacent lattice sites with 'hopping' energy $J$. This process is described in the first term, where $\langle i, j\rangle$ denotes the sum over all nearest-neighbour

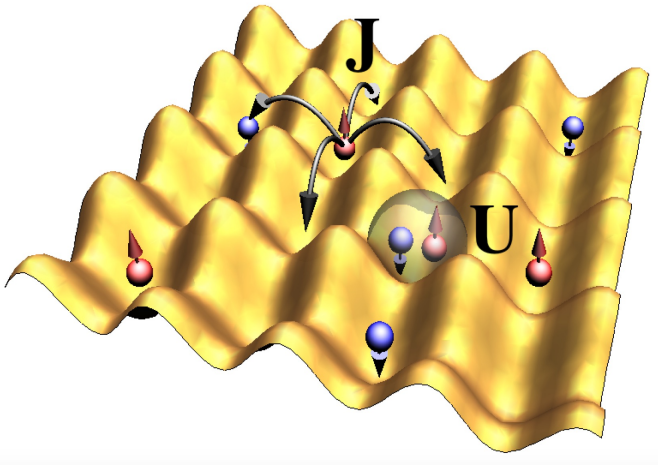


Figure 2.1: Illustration of the Hubbard model. We depict the two terms in the Hamiltonian in Eq. (2.1) in a two-dimensional lattice.

sites $i$ and $j$, and $\hat{c}^\dagger_{i,\sigma}$ and $\hat{c}_{j,\sigma}$ are the fermionic creation and annihilation operators, respectively, which obey the fermionic anticommutation relations

$$\{\hat{c}_{i,\sigma}, \hat{c}_{j,\sigma'}\} = 0, \tag{2.2}$$

$$\{\hat{c}^\dagger_{i,\sigma}, \hat{c}^\dagger_{j,\sigma'}\} = 0, \tag{2.3}$$

$$\{\hat{c}_{i,\sigma}, \hat{c}^\dagger_{j,\sigma'}\} = \delta_{i,j}\delta_{\sigma,\sigma'}, \tag{2.4}$$

where $\{\cdot,\cdot\}$ denotes the anticommutator, and $\delta_{i,j}$ and $\delta_{\sigma,\sigma'}$ are Kronecker deltas. The abbreviation H.c. in Eq. (2.1) stands for Hermitian conjugate. The fermions interact with on-site interaction strength $U$, which is described in the latter term in Eq. (2.1) by the product of the local number operators $\hat{n}_{i,\downarrow} = \hat{c}^\dagger_{i,\downarrow}\hat{c}_{i,\downarrow}$ and $\hat{n}_{i,\uparrow} = \hat{c}^\dagger_{i,\uparrow}\hat{c}_{i,\uparrow}$. In electron systems, the on-site interaction corresponds to a screened Coulomb interaction and is usually repulsive, i.e., $U > 0$. With ultracold fermions in optical lattices it is possible to consider the attractive Hubbard model where $U < 0$, since in these systems the strength and sign of the two-body interaction is charactised by the scattering length of ultracold collisions of atoms and the scattering length can be tuned with a so-called Feshbach resonance [48]. We illustrate the two terms of the Hubbard model in the case of a two-dimensional lattice in Fig. 2.1.

In Appendix A we show how the Hubbard model can be derived from a general many-body Hamiltonian in the context ultracold atoms in deep optical lattices. However, the derivation is conceptually general and be applied in other contexts as well. Note that with ultracold atoms it is also possible to realize the Bose–Hubbard model, in which the particles described by the model are bosons instead of fermions. The Bose–Hubbard model has had a central role in the development of optical lattices and studying the quantum phase transition from the superfluid phase to a Mott insulating phase [14,15]. In this thesis we only consider the fermionic Hubbard model.

In the thermodynamic limit, one often considers the Hubbard model in the grand-canonical ensemble with a chemical potential term that controls the particle filling included in the Hamiltonian. In this case the Hubbard model reads

$$\hat{H} = -J \sum_{\langle i,j \rangle, \sigma} \left( \hat{c}^{\dagger}_{i,\sigma} \hat{c}_{j,\sigma} + \text{H.c.} \right) + U \sum_{i} \hat{n}_{i,\uparrow} \hat{n}_{i,\downarrow} - \sum_{i,\sigma} \mu_{\sigma} \hat{n}_{i,\sigma}, \tag{2.5}$$

where $\mu_\sigma$ the chemical potential for spin $\sigma$. In the paramagnetic phase the chemical potential does not depend on spin, i.e., $\mu_\uparrow = \mu_\downarrow \equiv \mu$. In the case of half-filling, i.e., $\langle \hat{n}_i \rangle = \langle \hat{n}_{i,\uparrow} \rangle + \langle \hat{n}_{i,\downarrow} \rangle = 1$, this grand-canonical Hubbard Hamiltonian is often written as [40]

$$\hat{H} = -J \sum_{\langle i,j \rangle, \sigma} \left( \hat{c}^{\dagger}_{i,\sigma} \hat{c}_{j,\sigma} + \text{H.c.} \right) + U \sum_{i} \left( \hat{n}_{i,\uparrow} - \frac{1}{2} \right) \left( \hat{n}_{i,\downarrow} - \frac{1}{2} \right), \tag{2.6}$$

since now half-filling occurs conveniently at chemical potential $\mu = 0$. One way to see this is to note that the Hamiltonian in Eq. (2.6) remains unaltered under a particle-hole transformation in a bipartite lattice.

In recent years, there has been rapid progress in experiments studying non-equilibrium dynamics in strongly correlated systems, both in real materials [49–55] and in ultracold atom setups (see, e.g., Refs. [56,57] and references therein). In the non-equilibrium case, the parameters of the Hamiltonian become time-dependent

due to an external perturbation, such as an applied laser field, and we can write, e.g., the half-filled Hubbard model as [41]

$$\hat{H}(t) = -J(t) \sum_{\langle i,j \rangle, \sigma} \left( \hat{c}^{\dagger}_{i,\sigma} \hat{c}_{j,\sigma} + \text{H.c.} \right) + U(t) \sum_{i} \left( \hat{n}_{i,\uparrow} - \frac{1}{2} \right) \left( \hat{n}_{i,\downarrow} - \frac{1}{2} \right). \tag{2.7}$$

The Hubbard model has had a central role in theory of magnetism, metal-insulator transitions, and is conjectured to be important in the description of high-temperature superconductors [43, 58]. Many analytical and numerical techniques have been developed to study the Hubbard model. In one spatial dimension, powerful tools include the Bethe ansatz [59] and matrix product state methods such as the density matrix renormalization group (DMRG) [60–62] algorithm and the time-evolving block decimation (TEBD) [63, 64] algorithm (see also Appendix C). For high-dimensional lattices, dynamical mean-field theory [40] and its non-equilibrium extension [41] (see Chapter 7) are successful methods which become exact in the limit of infinite spatial dimensions. One established prediction of the half-filled Hubbard model is the Mott transition [65], where above a critical repulsive interaction strength fermions become localized with one fermion per lattice site. Such a system is called a Mott insulator.

The Hubbard model has a central role also in this thesis. In Chapter 4 we show numerically using TEBD that the spin-asymmetric particle currents characteristic of the spin-asymmetric Josephson effect can be produced in the Hubbard model in a one-dimensional spin-dependent optical superlattice. In Chapters 8 and 9, we propose a hybrid quantum-classical simulation scheme to study the infinite-dimensional Hubbard model with a digital quantum simulator and a classical feedback loop. The hybrid quantum-classical scheme implements the DMFT method.

## 2.2 Green function formalism

Green functions are a powerful and widely used tool in many-body quantum physics. Their name is taken from integral kernels used in the solution of differential equations (see, e.g., Ref. [66] for further details). Here, we follow the standard order of first presenting the single-particle Green function $G$ in the zero and then in the finite-temperature equilibrium formalism before proceeding to the generalisation to non-equilibrium systems. We use Green functions in this work both in Part II in the context of the spin-asymmetric Josephson effect and Part III in the context of DMFT. The purpose of this Section is mostly to list some useful relations. There are many textbooks on Green function theory with more pedagogical and extensive treatments along with applications (see, e.g., Refs. [43, 66–70]).

### 2.2.1 Equilibrium Green functions

#### 2.2.1.1 Zero-temperature Green functions

The zero-temperature single-particle Green function is defined as [67]

$$\begin{aligned} G(\mathbf{r}t,\mathbf{r}'t') &= -\mathrm{i}\langle\mathcal{T}\hat{\Psi}_H(\mathbf{r},t)\hat{\Psi}_H^\dagger(\mathbf{r}',t')\rangle_{GS} \\ &= -\mathrm{i}\theta(t-t')\langle\hat{\Psi}_H(\mathbf{r},t)\hat{\Psi}_H^\dagger(\mathbf{r}',t')\rangle_{GS} + \mathrm{i}\theta(t'-t)\langle\hat{\Psi}_H^\dagger(\mathbf{r}',t')\hat{\Psi}_H(\mathbf{r},t)\rangle_{GS}, \end{aligned} \tag{2.8}$$

where $\mathrm{i}$ is the imaginary unit, $\mathbf{r}$ is position, and $\hat{\Psi}_H(\mathbf{r},t)$ is the fermionic field operator in the Heisenberg picture, i.e., $\hat{\Psi}_H(\mathbf{r},t) = e^{\mathrm{i}\hat{H}t}\hat{\Psi}(\mathbf{r})e^{-\mathrm{i}\hat{H}t}$, where $\hat{H}$ is the time-independent Hamiltonian of the system (recall that we consider equilibrium systems in this subsection). Further, $t$ and $t'$ are real-time variables, $\mathcal{T}$ is the time-ordering operator, the average is calculated in the ground-state $|\Psi_{\mathrm{GS}}\rangle$ of $\hat{H}$, and $\theta(t-t')$ is the Heaviside step function given by

$$\theta(t-t') = \begin{cases} 1, & \text{for } t \geq t' \\ 0, & \text{for } t < t' \end{cases} . \tag{2.9}$$

Note that since the Hamiltonian $\hat{H}$ is time-independent, equilibrium Green functions actually depend only on $t - t'$ instead of $t$ and $t'$ separately.

An intuitive meaning for the single-particle Green function in Eq. (2.8) is the following. It describes the probability amplitude for the event in a 'thought experiment' where one starts at the many-body ground-state at equilibrium and adds a particle at position $\mathbf{r}'$ at time $t'$ to the state and removes a particle at position $\mathbf{r}$ at time $t$ from it. The time-ordering tells us which of these disturbances occurs first. However, we point out that the name 'single-particle' Green function is slightly misleading, since it still involves the full many-body Hamiltonian $\hat{H}$ and is computed with respect to a many-body state. As a result, obtaining single-particle Green functions in the presence of interactions is non-trivial in general. The term 'single-particle' refers to the fact that only a single particle is added or removed.

The full field operators can be expanded in a complete set of single-particle states $|\nu\rangle$, and the Green functions can be written in this representation in terms of fermionic creation and annihilation operators. One can then consider the single-particle Green function

$$\begin{aligned} G_{\nu\nu'}(t-t') &= -\mathrm{i}\langle \mathcal{T}\hat{c}_{\nu,H}(t)\hat{c}^{\dagger}_{\nu',H}(t')\rangle_{GS} \\ &= -\mathrm{i}\theta(t-t')\langle \hat{c}_{\nu,H}(t)\hat{c}^{\dagger}_{\nu',H}(t')\rangle_{GS} + \mathrm{i}\theta(t'-t)\langle \hat{c}^{\dagger}_{\nu',H}(t')\hat{c}_{\nu,H}(t)\rangle_{GS}. \end{aligned} \tag{2.10}$$

Here, $\hat{c}_{\nu,H}(t) = e^{\mathrm{i}\hat{H}t}\hat{c}_{\nu}e^{-\mathrm{i}\hat{H}t}$. In this thesis, we will work with Green functions in different representations, and thus we consider them in terms of the $\hat{c}$-operators. The single-particle state label $\nu$ can refer, e.g., to a lattice site and spin, or to momentum and spin. The corresponding Green functions are respectively given by

$$G_{i\sigma,j\sigma'}(t-t') = -\mathrm{i}\langle \mathcal{T}\hat{c}_{i\sigma,H}(t)\hat{c}^{\dagger}_{j\sigma',H}(t')\rangle_{GS}, \tag{2.11}$$

$$G_{\mathbf{k}\sigma,\mathbf{k}'\sigma'}(t-t') = -\mathrm{i}\langle \mathcal{T}\hat{c}_{\mathbf{k}\sigma,H}(t)\hat{c}^{\dagger}_{\mathbf{k}'\sigma',H}(t')\rangle_{GS}, \tag{2.12}$$

where $i$ and $j$ lattice site indices, $\sigma$ and $\sigma'$ denote the spin-$\frac{1}{2}$ projections ($\uparrow$ and $\downarrow$), and $\mathbf{k}$ and $\mathbf{k}'$ denote momenta.

We now list some useful definitions (for further details, see, e.g., Refs. [43, 67]). The retarded, advanced, greater, and lesser Green functions are defined as [67]

$$G^R_{\nu\nu'}(t-t') = -\mathrm{i}\theta(t-t')\langle\{\hat{c}_{\nu,H}(t), \hat{c}^\dagger_{\nu',H}(t')\}\rangle_{GS}, \tag{2.13}$$

$$G^A_{\nu\nu'}(t-t') = \mathrm{i}\theta(t'-t)\langle\{\hat{c}_{\nu,H}(t), \hat{c}^\dagger_{\nu',H}(t')\}\rangle_{GS}, \tag{2.14}$$

$$G^>_{\nu\nu'}(t-t') = -\mathrm{i}\langle\hat{c}_{\nu,H}(t)\hat{c}^\dagger_{\nu',H}(t')\rangle_{GS}, \tag{2.15}$$

$$G^<_{\nu\nu'}(t-t') = \mathrm{i}\langle\hat{c}^\dagger_{\nu',H}(t')\hat{c}_{\nu,H}(t)\rangle_{GS}, \tag{2.16}$$

respectively. We have following relations between the retarded and advanced and the greater as lesser components:

$$G^R_{\nu\nu'}(t-t') = \theta(t-t')\left[G^>_{\nu\nu'}(t-t') - G^<_{\nu\nu'}(t-t')\right], \tag{2.17}$$

$$G^A_{\nu\nu'}(t-t') = \theta(t'-t)\left[G^<_{\nu\nu'}(t-t') - G^>_{\nu\nu'}(t-t')\right]. \tag{2.18}$$

In this thesis, we shall mostly consider translationally-invariant systems. If in such a system spin is a good quantum number, we have [43]

$$G_{\mathbf{k}\sigma,\mathbf{k}'\sigma'}(t-t') = \delta_{\sigma,\sigma'}\delta_{\mathbf{k},\mathbf{k}'}G_{\mathbf{k},\sigma}(t-t'), \tag{2.19}$$

where the Kronecker delta implies the absence of spin-flipping interactions. Furthermore in translationally-invariant systems, the Green function in Eq. (2.8) depends on $\mathbf{r}-\mathbf{r}'$, and the Fourier transform from momentum to real space is defined as [43]

$$G_\sigma(\mathbf{r}-\mathbf{r}', t) = \int \frac{d\mathbf{k}}{(2\pi)^3} e^{\mathrm{i}\mathbf{k}\cdot(\mathbf{r}-\mathbf{r}')}G_{\mathbf{k},\sigma}(t). \tag{2.20}$$

The Fourier transform from time to frequency is defined as [43]

$$G_{\mathbf{k},\sigma}(\omega) = \int_{-\infty}^{\infty} d\omega\, e^{\mathrm{i}\omega t}G_{\mathbf{k},\sigma}(t). \tag{2.21}$$

**Observables and the spectral function**

If we know the single-particle Green function, we can compute the expectation value of any single-particle operator in the ground-state of the system [68]. For example, the (in general) position-dependent particle density is obtained as [43]

$$\begin{aligned}\langle\hat{n}(\mathbf{r})\rangle &= \sum_{\sigma}\langle\hat{\Psi}^{\dagger}_{\sigma}(\mathbf{r})\hat{\Psi}_{\sigma}(\mathbf{r})\rangle_{GS} \\ &= -\sum_{\sigma}\langle\mathcal{T}\hat{\Psi}_{\sigma}(\mathbf{r},0)\hat{\Psi}^{\dagger}_{\sigma}(\mathbf{r},0^{+})\rangle_{GS} \\ &= -\mathrm{i}2G_{\sigma}(\mathbf{r},0),\end{aligned} \tag{2.22}$$

or equivalently,

$$\langle\hat{n}(\mathbf{r})\rangle_{GS} = -\mathrm{i}2G^{<}_{\sigma}(\mathbf{r},0). \tag{2.23}$$

Here the factor of two comes from the spin-degeneracy and the infinitesimal $0^{+}$ ensures correct time-ordering.

A quantity of great importance is the single-particle spectral function, defined as [67]

$$A_{\mathbf{k},\sigma}(\omega) = -\frac{1}{\pi}\mathrm{Im}[G^{R}_{\mathbf{k},\sigma}(\omega)]. \tag{2.24}$$

This is valid for all temperatures. From the so-called Lehmann representation[1] of $A_{\mathbf{k},\sigma}(\omega)$, one can see that $A_{\mathbf{k},\sigma}(\omega) > 0$ (for details, see Ref. [67]). Furthermore, its integral over all frequencies is unity. The spectral function $A_{\mathbf{k},\sigma}(\omega)$ is often given the physical interpretation of a probability that a spin $\sigma$ fermion has momentum $\mathbf{k}$ and energy $\omega$ (recall that $\hbar = 1$) [67]. The spectral function is also a central quantity in DMFT [40]. We can use the spectral function, e.g., to calculate the occupation number in the state $|\mathbf{k}\sigma\rangle$ at $T = 0$ as [43]

$$\begin{aligned}\langle\hat{n}_{\mathbf{k},\sigma}\rangle &= \int_{-\infty}^{\infty} d\omega\, n_{F}(\omega)A_{\mathbf{k},\sigma}(\omega) \\ &= \int_{-\infty}^{0} d\omega\, A_{\mathbf{k},\sigma}(\omega),\end{aligned} \tag{2.25}$$

[1] In the Lehmann, or spectral, representation, one writes the Green functions in terms of the eigenenergies and eigenstates of the governing Hamiltonian [67].

where in the second line we have used the fact that only the states with $\omega < 0$ (measured with respect to the chemical potential) are filled at $T = 0$. Here, $n_F(\omega) = 1/(e^{\beta\omega} + 1)$ denotes the Fermi distribution function. The first line of Eq. (2.25), which is valid also for non-zero temperatures, tells us that the number of fermions in the state $|\mathbf{k}\sigma\rangle$ is obtained by the summation over all energies $\omega$, weighted by $A_{\mathbf{k},\sigma}(\omega)$ which gives the probability that a spin $\sigma$ fermion with momentum $\mathbf{k}$ has energy $\omega$ and by the thermal occupation factor $n_F(\omega)$ [67].

**Green function for non-interacting fermions**

As an example calculation, we consider the Green function in Eq. (2.10) for a degenerate Fermi gas of non-interacting spinless fermions of mass $m$ at $T = 0$, where $T$ is temperature, described by the Hamiltonian

$$\hat{H} = \sum_{\mathbf{k}} (\epsilon_{\mathbf{k}} - E_F)\hat{c}^\dagger_{\mathbf{k}}\hat{c}_{\mathbf{k}}. \tag{2.26}$$

Here $\epsilon_{\mathbf{k}} = \frac{|\mathbf{k}|^2}{2m}$, and $E_F = \frac{|\mathbf{k}_F|^2}{2m} = \mu(T = 0)$ is the Fermi energy, with $\mathbf{k}_F$ being the Fermi momentum. The ground-state of the system is given by the Fermi sea

$$|\Psi_{\mathrm{GS}}\rangle = \prod_{|\mathbf{k}|<|\mathbf{k}_F|} \hat{c}^\dagger_{\mathbf{k}}|\emptyset\rangle, \tag{2.27}$$

where $|\emptyset\rangle$ is the empty state. The Heisenberg equations of motion for the creation and annihilation operators,

$$\frac{d}{dt}\hat{c}^\dagger_{\mathbf{k},H}(t) = \mathrm{i}[\hat{H}, \hat{c}^\dagger_{\mathbf{k},H}(t)], \tag{2.28}$$

$$\frac{d}{dt}\hat{c}_{\mathbf{k},H}(t) = \mathrm{i}[\hat{H}, \hat{c}_{\mathbf{k},H}(t)], \tag{2.29}$$

yield the time-dependence

$$\hat{c}^\dagger_{\mathbf{k},H}(t) = e^{\mathrm{i}(\epsilon_{\mathbf{k}} - E_F)t}\hat{c}^\dagger_{\mathbf{k}}, \tag{2.30}$$

$$\hat{c}_{\mathbf{k},H}(t) = e^{-\mathrm{i}(\epsilon_{\mathbf{k}} - E_F)t}\hat{c}_{\mathbf{k}}. \tag{2.31}$$

Substituting these into Eq. (2.10) gives the non-interacting Green function as (setting $t' = 0$)

$$\begin{aligned} G^{(0)}_{\mathbf{k}}(t) &= -\mathrm{i}\left\{[1 - n_F(\epsilon_{\mathbf{k}} - E_F)]\theta(t) - n_F(\epsilon_{\mathbf{k}} - E_F)\theta(-t)\right\} e^{-\mathrm{i}(\epsilon_{\mathbf{k}} - E_F)t} \\ &= -\mathrm{i}\left[\theta(t) - n_F(\epsilon_{\mathbf{k}} - E_F)\right] e^{-\mathrm{i}(\epsilon_{\mathbf{k}} - E_F)t}, \end{aligned} \tag{2.32}$$

where $n_F(\epsilon_{\mathbf{k}} - E_F) = \theta(|\mathbf{k}_F| - |\mathbf{k}|)$ is the Fermi distribution function at $T = 0$. The temporal Fourier transform is given by

$$G^{(0)}_{\mathbf{k}}(\omega) = \int_{-\infty}^{\infty} dt\, e^{\mathrm{i}\omega t} G^{(0)}_{\mathbf{k}}(t) \tag{2.33}$$

$$= \frac{1}{\omega - (\epsilon_{\mathbf{k}} - E_F) + \mathrm{i}0^{+}\mathrm{sgn}(|\mathbf{k}| - |\mathbf{k}_F|)}, \tag{2.34}$$

where $0^+$ is a positive infinitesimal to make the integral convergent at large times, and $\mathrm{sgn}$ is the sign function.

Using the formula [67]

$$\frac{1}{x \pm \mathrm{i}0^{+}} = \mathcal{P}\frac{1}{x} \mp \mathrm{i}\pi\delta(x), \tag{2.35}$$

where $\mathcal{P}$ denotes the principal value and $\delta(x)$ is the Dirac delta function, we find that the spectral function for the non-interacting Green function is a mere delta function

$$A_{\mathbf{k}}(\omega) = \delta(\omega - \epsilon_{\mathbf{k}} + E_F). \tag{2.36}$$

**Dyson equation**

The non-interacting Green function of a system is often straightforward to determine [see Eqs. (2.32) and (2.34)]. The Green function for an *interacting* system is usually far from trivial to obtain. However, there is an important and useful relation between the interacting and non-interacting single-particle Green functions. This relation is the Dyson equation which reads [67]

$$G_{\mathbf{k},\sigma}(\omega) = G^{(0)}_{\mathbf{k},\sigma}(\omega) + G^{(0)}_{\mathbf{k},\sigma}(\omega)\Sigma_{\mathbf{k},\sigma}(\omega)G_{\mathbf{k},\sigma}(\omega), \tag{2.37}$$

where $\Sigma_{\mathbf{k},\sigma}(\omega)$ is the self-energy. The self-energy describes the effect of interactions on the fermion without referring to many-particle Green functions for the addition or removal of several particles[2] [69]. The Dyson equation is a formal way to write the perturbation expansion of $G_{\mathbf{k},\sigma}(\omega)$, where the self-energy is described by the sum of one-particle irreducible Feynman diagrams[3] which cannot be separated into two parts by cutting single $G^{(0)}$ lines [69]. The Dyson equation generalises to the finite-temperature and non-equilibrium cases and is widely used in the context of DMFT and its non-equilibrium extension, where the self-energy is approximated to be momentum-independent [40, 41].

#### 2.2.1.2 Finite-temperature Matsubara Green functions

The definition of the Green function in Eq. (2.10) can be extended to finite temperatures by defining [70]

$$G_{\nu\nu'}(t-t') = -\mathrm{i}\langle \mathcal{T}\hat{c}_{\nu,H}(t)\hat{c}_{\nu',H}(t')\rangle = -\mathrm{i}\frac{\mathrm{Tr}\left[e^{-\beta\hat{H}}\mathcal{T}\hat{c}_{\nu,H}(t)\hat{c}^{\dagger}_{\nu',H}(t')\right]}{\mathrm{Tr}\left[e^{-\beta\hat{H}}\right]}. \tag{2.38}$$

Here, $\beta = \frac{1}{k_B T}$, where $k_B$ is the Boltzmann constant, and $\mathrm{Tr}$ denotes the trace. In many cases, the Hamiltonian is of the form $\hat{H} = \hat{H}_0 + \hat{H}'$, where $\hat{H}_0$ can be solved exactly and $\hat{H}'$ is treated as a perturbation. However, since $\hat{H}'$ appears in the exponentials $e^{\pm\mathrm{i}\hat{H}t}$ and $e^{-\beta\hat{H}}$, it makes the use of perturbation theory cumbersome [67]. This can be remedied by the use of the Matsubara formalism which is often the method of choice at finite temperatures [67].

In the finite-temperature Matsubara formalism, time is considered to be imaginary, and we make the replacement $\mathrm{i}t \to \tau$, where $\tau$ is a real quantity with the

[2] Formally the equations of motion for $N$-particle Green functions $G_N$ lead to a set of coupled differential equations where $G_N$ depends on $G_{N-1}$ and $G_{N+1}$. This is called the Martin–Schwinger hierarchy [71]. Thus, the single-particle Green function $G$ depends on the two-particle Green function $G_2$ as $G = G^{(0)} + G^{(0)}UG_2$, where $U$ is the two-particle interaction. The two-particle Green function then depends on the three-particle Green function $G_3$, and so on. The idea of the self-energy is to truncate the Martin–Schwinger hierarchy to include only $G$ and $G^{(0)}$ by defining $\Sigma$ implicitly via the functional equation $\Sigma G = UG_2$, which leads to the Dyson equation. For further details, we refer to Chapters 5 and 9 in Ref. [69].

[3] For an introduction to Feynman diagrams, see, e.g., Refs. [43, 69, 70, 72].

domain $-\beta \leq \tau \leq \beta$. Then the temporal exponentials become $e^{\pm\tau\hat{H}}$ and have the same form as $e^{-\beta\hat{H}}$. As a result, the imaginary-time formalism allows the easier use of standard perturbation expansion techniques at finite temperature than working directly in the real-time domain [67, 70]. However, an additional step of analytic continuation from imaginary to real time is required before observables can the extracted from the Green function.

The Matsubara Green function is defined as [67]

$$G^M_{\nu\nu'}(\tau,\tau') = -\frac{\mathrm{Tr}\left[e^{-\beta\hat{H}}\mathcal{T}_\tau \hat{c}_{\nu,M}(\tau)\hat{c}^\dagger_{\nu',M}(\tau')\right]}{\mathrm{Tr}\left[e^{-\beta\hat{H}}\right]} = -\langle \mathcal{T}_\tau \hat{c}_{\nu,M}(\tau)\hat{c}^\dagger_{\nu',M}(\tau')\rangle, \tag{2.39}$$

where $\mathcal{T}_\tau$ is the $\tau$-ordering operator, and the $\tau$-dependent Matsubara operators are given by [67]

$$\hat{c}_{\nu,M}(\tau) = e^{\hat{H}\tau}\hat{c}_\nu e^{-\hat{H}\tau}, \tag{2.40}$$

$$\hat{c}^\dagger_{\nu,M}(\tau) = e^{\hat{H}\tau}\hat{c}^\dagger_\nu e^{-\hat{H}\tau}. \tag{2.41}$$

Note that $\hat{c}^\dagger_{\nu,M}(\tau)$ is not the adjoint of $\hat{c}_{\nu,M}(\tau)$ since $\tau$ is real. Using the cyclic property of the trace, one can show that $G_{\nu\nu'}(\tau,\tau')$ depends only on $\tau-\tau'$, i.e., we can define

$$G^M_{\nu\nu'}(\tau) = -\langle \mathcal{T}_\tau \hat{c}_{\nu,M}(\tau)\hat{c}^\dagger_{\nu',M}(0)\rangle. \tag{2.42}$$

Furthermore, for $0 < \tau < \beta$, we find again using the cyclic property of the trace that [67]

$$G^M_{\nu\nu'}(\tau) = -G^M_{\nu\nu'}(\tau-\beta), \tag{2.43}$$

i.e., the Matsubara Green function is antiperiodic in the variable $\tau$ with period $\beta$. We can write $G^M_{\nu\nu'}(\tau)$ as a Fourier series as [67]

$$G^M_{\nu\nu'}(\tau) = \frac{1}{\beta}\sum_n G^M_{\nu\nu'}(\mathrm{i}\omega_n)e^{-\mathrm{i}\omega_n\tau}. \tag{2.44}$$

Applying Eq. (2.43), we have

$$e^{-\mathrm{i}\omega_n\tau} = -e^{-\mathrm{i}\omega_n(\tau-\beta)} \implies e^{\mathrm{i}\omega_n\beta} = -1, \tag{2.45}$$

which defines the fermionic Matsubara frequency as [67]

$$\omega_n = \frac{(2n+1)\pi}{\beta}, \qquad n \in \mathbb{Z}. \tag{2.46}$$

Using Matsubara frequencies, one can write, e.g., the Fermi distribution function $n_F(E)$, as a series given by [67]

$$n_F(E) = \frac{1}{e^{\beta E}+1} = \frac{1}{2} + \frac{1}{\beta}\sum_n \frac{1}{\mathrm{i}\omega_n - E}. \tag{2.47}$$

This result follows from a theorem stating that a meromorphic function can be expanded as a sum over its poles and residues at the poles [73]. It is also sometimes used as an alternative motivation for the Matsubara formalism [67].

Physical quantities are defined in the real-time or real-frequency domain. For example, conductivities or susceptibilities are retarded correlation functions and thus related to the retarded Green function in Eq. (2.13) which can be defined for finite temperatures by replacing the ground-state expectation value by the thermodynamic average [67]. In practice, however, the Matsubara Green function $G^M_{\nu\nu'}(\mathrm{i}\omega_n)$ is often easiest to calculate [67]. The retarded Green function in the real-frequency domain is then (uniquely [74]) obtained via the analytic continuation [67]

$$G^R_{\nu\nu'}(\omega) = G^M_{\nu\nu'}(\mathrm{i}\omega_n)|_{\mathrm{i}\omega_n\to\omega+\mathrm{i}0^+}, \tag{2.48}$$

i.e., by replacing the discrete Matsubara frequencies by the continuous variable $\omega + \mathrm{i}0^+$ (see also Section 8.4 in Ref. [70]). We point out that, e.g., in computing the Matsubara Green function numerically in DMFT using quantum Monte Carlo impurity solvers (see Section 7.4), executing the analytic continuation is a non-trivial task due to numerical noise caused by Monte Carlo errors. As a result of the noise,

the mapping in Eq. (2.48) is not necessarily unique and one has to resort to optimization procedures to find a 'best' solution. For details and further clarifications, we refer to Chapter 12 in Ref. [75].

Finally, we state that in Matsubara space, the Dyson equation in Eq. (2.37) becomes

$$G^{M}_{\mathbf{k},\sigma}(\mathrm{i}\omega_n) = G^{M(0)}_{\mathbf{k},\sigma}(\mathrm{i}\omega_n) + G^{M(0)}_{\mathbf{k},\sigma}(\mathrm{i}\omega_n)\Sigma_{\mathbf{k},\sigma}(\mathrm{i}\omega_n)G^{M}_{\mathbf{k},\sigma}(\mathrm{i}\omega_n). \tag{2.49}$$

### 2.2.2 Non-equilibrium Green functions

We now proceed to the Green function formalism in the non-equilibrium case where the Hamiltonian of the system is time-dependent. We begin with describing the time contour on which the Green functions are formally defined before introducing the contour Green functions.

#### 2.2.2.1 Time contour

To introduce the time contour, we consider the time-evolution of a many-body quantum system which is at time $t = t_0$ in thermal equilibrium and is described by the density operator

$$\hat{\rho}(t_0) = \frac{e^{-\beta\hat{H}(t_0)}}{Z}, \tag{2.50}$$

where $\hat{H}(t_0)$ is the initial grand-canonical Hamiltonian, and the equilibrium partition function is given by $Z = \mathrm{Tr}\left(e^{-\beta\hat{H}(t_0)}\right)$. At $t = t_0^+$, the Hamiltonian of the system changes, either via a sudden quantum quench of its parameters or via a continuous driving field [76]. The resulting non-equilibrium dynamics of the density operator in the Schrödinger picture is given by the von Neumann equation [77]

$$\mathrm{i}\frac{d\hat{\rho}(t)}{dt} = [\hat{H}(t), \hat{\rho}(t)], \tag{2.51}$$

the formal solution of which can be written as

$$\hat{\rho}(t) = \hat{U}(t, t_0)\hat{\rho}(t_0)\hat{U}(t_0, t), \tag{2.52}$$

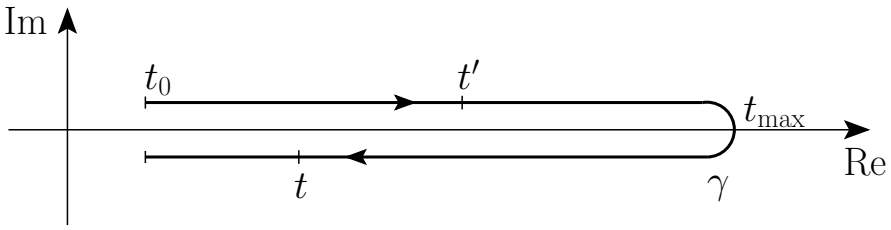


Figure 2.2: The time contour $\gamma$. The forward and backward branches are on top of each other on the real time axis, but we have shifted them only to clarify their orientation.

where the time-evolution operator reads [69]

$$\hat{U}(t,t') = \begin{cases} \mathcal{T} e^{-\mathrm{i}\int_{t'}^{t} d\bar{t}\,\hat{H}(\bar{t})}, & \text{for } t > t' \\ \overline{\mathcal{T}} e^{+\mathrm{i}\int_{t}^{t'} d\bar{t}\,\hat{H}(\bar{t})}, & \text{for } t < t' \end{cases} . \tag{2.53}$$

Here, $\overline{\mathcal{T}}$ denotes the anti-time-ordering operator.

We then consider the time-dependent ensemble average of a Schrödinger operator $\hat{O}$, given by

$$\begin{aligned} \langle \hat{O} \rangle(t) &= \mathrm{Tr}\left( \hat{\rho}(t)\hat{O}(t) \right) \\ &= \mathrm{Tr}\left( \hat{\rho}(t_0)\hat{U}(t_0,t)\hat{O}(t)\hat{U}(t,t_0) \right) \\ &= \mathrm{Tr}\left( \hat{\rho}(t_0)\mathcal{T}_\gamma \left\{ e^{-\mathrm{i}\int_\gamma d\bar{t}\,\hat{H}(\bar{t})}\hat{O}(t) \right\} \right) . \end{aligned} \tag{2.54}$$

We point out explicitly that here the operator $\hat{O}(t)$ is *not* in the Heisenberg picture but in the Schrödinger picture[4], and the time-argument refers to the explicit time-dependence of the operator, or, if the operator does not depend on time, to the time instant when the operator acts. The formal time-argument is important in order to have the correct time-ordering of the operators [69]. In the second line of Eq. (2.54), we have used Eq. (2.52) and the cyclic property of the trace. In the third line, we have compiled the time-evolution to a single contour $\gamma$ illustrated in Fig. 2.2, where the system evolves from time $t_0$ to $t$ (this is called the forward branch of $\gamma$), then

[4]However, the same contour idea can be derived using operators in the Heisenberg picture, but then the time-evolution operators are absorbed in the time-dependence of the operator $\hat{O}$.

the operator $\hat{O}$ is applied, followed by an evolution back from $t$ to $t_0$ (this is called the backward branch of $\gamma$). We have also introduced the corresponding contour-ordering operator $\mathcal{T}_\gamma$ that arranges operators on $\gamma$ according to the direction of the arrows in Fig. 2.2. Note also that we can write

$$\hat{U}(t_0,t)\hat{O}(t)\hat{U}(t,t_0) = \hat{U}(t_0,t_{\max})\hat{U}(t_{\max},t)\hat{O}(t)\hat{U}(t,t_0), \tag{2.55}$$

or

$$\hat{U}(t_0,t)\hat{O}(t)\hat{U}(t,t_0) = \hat{U}(t_0,t)\hat{O}(t)\hat{U}(t,t_{\max})\hat{U}(t_{\max},t_0), \tag{2.56}$$

i.e., we can extend the contour $\gamma$ to chosen maximal time $t_{\max}$ (formally we can also set $t_{\max}=\infty$), and the operator $\hat{O}$ can act either on the forward or the backward branch.

We now proceed to include the description of the initial thermal state into the time contour and write Eq. (2.54) explicitly as

$$\langle\hat{O}\rangle(t) = \frac{\mathrm{Tr}\left(e^{-\beta\hat{H}(t_0)}\mathcal{T}_\gamma\left\{e^{-\mathrm{i}\int_\gamma d\bar{t}\,\hat{H}(\bar{t})}\hat{O}(t)\right\}\right)}{\mathrm{Tr}\left(e^{-\beta\hat{H}(t_0)}\right)}. \tag{2.57}$$

Since $\mathcal{T}_\gamma\left\{e^{-\mathrm{i}\int_\gamma d\bar{t}\,\hat{H}(\bar{t})}\right\} = \hat{U}(t_0,t_{\max})\hat{U}(t_{\max},t_0) = \hat{I}$, where $\hat{I}$ is the identity operator, it can be included inside the trace in the denominator in Eq. (2.57). Moreover, we can write $e^{-\beta\hat{H}(t_0)} = e^{-\mathrm{i}\int_{\gamma_\iota} d\bar{z}\hat{H}(t_0)}$, where $\gamma_\iota$ is any contour in the complex plane with an arbitrary starting point $\bar{z}_0$ and an ending point $\bar{z}_f$ such that $\bar{z}_f - \bar{z}_0 = -\mathrm{i}\beta$ [69]. A common strategy is to choose a vertical track and attach $\gamma_\iota$ at the end of the contour $\gamma$ by setting $\bar{z}_0 = t_0$ and $\bar{z}_f = t_0 - \mathrm{i}\beta$ [69]. We denote the resulting L-shaped contour depicted in Fig. 2.3 by $\mathcal{C}$, and write

$$\langle\hat{O}\rangle(t) = \frac{\mathrm{Tr}\left(\mathcal{T}_\mathcal{C}\left\{e^{-\mathrm{i}\int_\mathcal{C} d\bar{z}\,\hat{H}(\bar{z})}\hat{O}(t)\right\}\right)}{\mathrm{Tr}\left(\mathcal{T}_\mathcal{C}\left\{e^{-\mathrm{i}\int_\mathcal{C} d\bar{z}\,\hat{H}(\bar{z})}\right\}\right)}, \tag{2.58}$$

where $\mathcal{T}_\mathcal{C}$ is the contour-ordering operator on $\mathcal{C}$ and $\hat{H}(\bar{z}\in\gamma_\iota) = \hat{H}(t_0)$. In the literature, the time contour $\mathcal{C}$ is sometimes called the Keldysh, Schwinger–Keldysh,

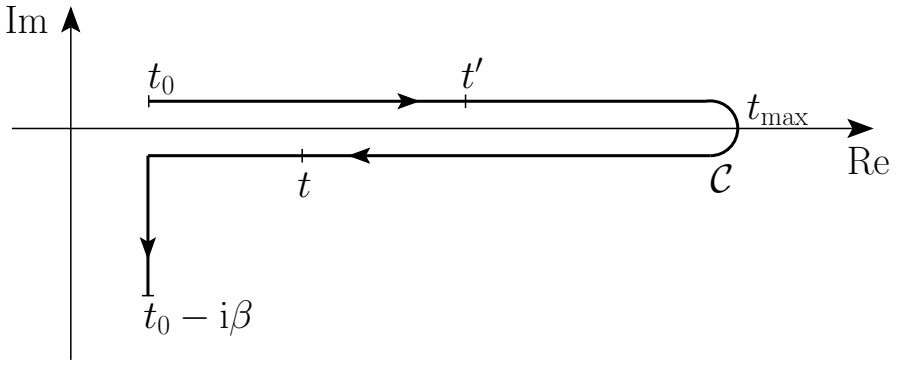


Figure 2.3: The time contour $\mathcal{C}$. It consists of the real-time contour in Fig 2.2 and an imaginary-time branch which accounts for the initial thermal state.

or the Kadanoff–Baym contour, or a different combination of these names [69, 70, 76].

The contour $\mathcal{C}$ is the time contour on which all Green functions are formally defined. However, in the special case of zero temperature, the imaginary part of $\mathcal{C}$ is not required since the initial density operator reduces to a projector onto the ground state of the system, $\hat{\rho}(t_0) = |\Psi_{GS}(t_0)\rangle\langle\Psi_{GS}(t_0)|$, and the real-time contour $\gamma$ suffices. As per the usual convention, we denote the real time argument on $\mathcal{C}$ by $t$ and the imaginary time argument $it$ by $\tau$ [69,70].

#### 2.2.2.2 Contour Green functions

We define the action for the Hamiltonian $\hat{H}$ as

$$\hat{S} = -\mathrm{i}\int_{\mathcal{C}} d\bar{z}\, \hat{H}(\bar{z}). \tag{2.59}$$

The single-particle contour Green function is then given by [41, 69]

$$G_{\nu\nu'}(z, z') = -\mathrm{i}\langle \mathcal{T}_{\mathcal{C}} \hat{c}_\nu(z)\hat{c}^\dagger_{\nu'}(z')\rangle_S = -\mathrm{i}\frac{\mathrm{Tr}\left[\mathcal{T}_{\mathcal{C}} \exp(\hat{S})\hat{c}_\nu(z)\hat{c}^\dagger_{\nu'}(z')\right]}{\mathrm{Tr}\left[\mathcal{T}_{\mathcal{C}} \exp(\hat{S})\right]}, \tag{2.60}$$

where $z$ and $z'$ are arguments on the Keldysh contour $\mathcal{C}$ that give the time instants in which the operators $\hat{c}_\nu$ and $\hat{c}^\dagger_{\nu'}$ are applied. There is no other time-dependence

in these operators. However, it is equivalently possible to use creation and annihilation operators in the Heisenberg or Matsubara picture. We give an example of this with non-interacting fermions below.

The location of $z$ and $z'$ on $\mathcal{C}$ defines nine entries for $G_{\nu\nu'}(z,z')$, which we label as $G^{ab}_{\nu\nu'}(z,z')$. Here, $a$ and $b$ indicate the placing of $z$ and $z'$ on $\mathcal{C}$, respectively. We use the convention $a,b=1,2,3$, where 1 denotes the forward branch, 2 denotes the backward branch, and 3 denotes the imaginary branch of $\mathcal{C}$. We have the following relations [41]

$$G^{11}_{\nu\nu'}(t,t') = G^{12}_{\nu\nu'}(t,t'), \quad \text{for } t \leq t', \tag{2.61}$$

$$G^{11}_{\nu\nu'}(t,t') = G^{21}_{\nu\nu'}(t,t'), \quad \text{for } t > t', \tag{2.62}$$

$$G^{22}_{\nu\nu'}(t,t') = G^{21}_{\nu\nu'}(t,t'), \quad \text{for } t < t' \quad (t >_{\mathcal{C}} t'), \tag{2.63}$$

$$G^{22}_{\nu\nu'}(t,t') = G^{12}_{\nu\nu'}(t,t'), \quad \text{for } t \geq t' \quad (t \leq_{\mathcal{C}} t'), \tag{2.64}$$

$$G^{13}_{\nu\nu'}(t,\tau') = G^{23}_{\nu\nu'}(t,\tau'), \tag{2.65}$$

$$G^{31}_{\nu\nu'}(\tau,t') = G^{32}_{\nu\nu'}(\tau,t'). \tag{2.66}$$

Here, $>_{\mathcal{C}}$ and $\leq_{\mathcal{C}}$ refer to the order of the time-arguments according to the orientation of the contour $\mathcal{C}$. For example, in Fig. 2.3 we have $t' > t$, but instead $t >_{\mathcal{C}} t'$, since $t$, being on the backward branch, is later on the contour. Note that the location of the largest real-time argument (largest according to the standard ordering of real numbers, not contour ordering) can be chosen to be either on the forward or on the backward branch. We define the lesser, greater, left-mixing, right-mixing, and Matsubara Green functions as [41]

$$G^{<}_{\nu\nu'}(t,t') = G^{12}_{\nu\nu'}(t,t') = \mathrm{i}\langle \hat{c}^{\dagger}_{\nu'}(t')\hat{c}_{\nu}(t)\rangle_S, \tag{2.67}$$

$$G^{>}_{\nu\nu'}(t,t') = G^{21}_{\nu\nu'}(t,t') = -\mathrm{i}\langle \hat{c}_{\nu}(t)\hat{c}^{\dagger}_{\nu'}(t')\rangle_S, \tag{2.68}$$

$$G^{\rceil}_{\nu\nu'}(t,\tau') = \frac{1}{2}\left[G^{13}_{\nu\nu'}(t,\tau') + G^{23}_{\nu\nu'}(t,\tau')\right] = \mathrm{i}\langle \hat{c}^{\dagger}_{\nu'}(\tau')\hat{c}_{\nu}(t)\rangle_S, \tag{2.69}$$

$$G^{\lceil}_{\nu\nu'}(\tau,t') = \frac{1}{2}\left[G^{31}_{\nu\nu'}(\tau,t') + G^{32}_{\nu\nu'}(\tau,t')\right] = -\mathrm{i}\langle \hat{c}_{\nu}(\tau)\hat{c}^{\dagger}_{\nu'}(t')\rangle_S, \tag{2.70}$$

$$G^{M}_{\nu\nu'}(\tau,\tau') = -\mathrm{i}G^{33}_{\nu\nu'}(\tau,\tau') = -\langle \mathcal{T}_{\tau}\hat{c}_{\nu}(\tau)\hat{c}^{\dagger}_{\nu'}(\tau')\rangle_S, \tag{2.71}$$

respectively. We have the following conjugate symmetry relations

$$\left[G^{</>}_{\nu\nu'}(t,t')\right]^* = -G^{</>}_{\nu'\nu}(t',t), \tag{2.72}$$

$$\left[G^{\urcorner}_{\nu\nu'}(t,\tau')\right]^* = G^{\ulcorner}_{\nu'\nu}(\beta-\tau',t), \tag{2.73}$$

where the superscript $^*$ denotes complex conjugation.

We prove the relation in Eq. (2.73) since it might not be obvious by inspection. We set the initial time $t_0 = 0$ for simplicity. The left-mixing Green function is explicitly given by

$$G^{\urcorner}_{\nu\nu'}(t,\tau') = \mathrm{i}\frac{\mathrm{Tr}\left[\mathcal{T}_{\mathcal{C}}\exp(\hat{S})\hat{c}^\dagger_{\nu'}(\tau')\hat{c}_\nu(t)\right]}{\mathrm{Tr}\left[\mathcal{T}_{\mathcal{C}}\exp(\hat{S})\right]}. \tag{2.74}$$

We consider the numerator, which is written out as

$$\mathrm{iTr}\left[\mathcal{T}_{\mathcal{C}}\exp(\hat{S})\hat{c}^\dagger_{\nu'}(\tau')\hat{c}_\nu(t)\right] = \mathrm{iTr}\left[\hat{U}^M(\beta,\tau')\hat{c}^\dagger_{\nu'}\hat{U}^M(\tau',0)\hat{U}(0,t)\hat{c}_\nu\hat{U}(t,0)\right], \tag{2.75}$$

where $\hat{U}(t,t')$ is the time-evolution operator in Eq. (2.53), and the Matsubara propagator reads

$$\hat{U}^M(\tau,\tau') = e^{-\hat{H}(0)(\tau-\tau')}. \tag{2.76}$$

We conjugate both sides of Eq. (2.75) to obtain

$$\begin{aligned}
\left\{\mathrm{iTr}\left[\mathcal{T}_{\mathcal{C}}e^{\hat{S}}\hat{c}^\dagger_{\nu'}(\tau')\hat{c}_\nu(t)\right]\right\}^* &= \left\{\mathrm{iTr}\left[\hat{U}^M(\beta,\tau')\hat{c}^\dagger_{\nu'}\hat{U}^M(\tau',0)\hat{U}(0,t)\hat{c}_\nu\hat{U}(t,0)\right]\right\}^* \\
&= -\mathrm{iTr}\left[\hat{U}(0,t)\hat{c}^\dagger_\nu\hat{U}(t,0)\underbrace{\hat{U}^M(\tau',0)}_{=\hat{U}^M(\beta,\beta-\tau')}\hat{c}_{\nu'}\underbrace{\hat{U}^M(\beta,\tau')}_{=\hat{U}^M(\beta-\tau',0)}\right] \\
&= -\mathrm{iTr}\left[\hat{U}^M(\beta,\beta-\tau')\hat{c}_{\nu'}\hat{U}^M(\beta-\tau',0)\hat{U}(0,t)\hat{c}^\dagger_\nu\hat{U}(t,0)\right] \\
&= -\mathrm{iTr}\left[\mathcal{T}_{\mathcal{C}}\exp(\hat{S})\hat{c}_{\nu'}(\beta-\tau')\hat{c}^\dagger_\nu(t)\right],
\end{aligned} \tag{2.77}$$

where in going from the second to the third line we have repeatedly used the cyclic property of the trace. Dividing both sides of Eq. (2.77) by $\mathrm{Tr}\left[\mathcal{T}_{\mathcal{C}}\exp(\hat{S})\right]$, which is real, directly yields Eq. (2.73).

Similarly using the cyclic property of the trace one can show that the following Kubo–Martin–Schwinger boundary conditions hold [41,69]

$$G_{\nu\nu'}(z_0, z') = -G_{\nu\nu'}(z_f, z'), \tag{2.78}$$

$$G_{\nu\nu'}(z, z_0) = -G_{\nu\nu'}(z, z_f), \tag{2.79}$$

where $z_0 = t_0$ is the starting point and $z_f = t_0 - \mathrm{i}\beta$ is the end point of the contour $\mathcal{C}$.

**Non-interacting fermions**

Again as an example calculation, we consider a simple case of non-interacting spinless fermions, this time at finite temperature, governed by the time-dependent Hamiltonian

$$\hat{H}(t) = \sum_{\mathbf{k}} \left[\epsilon_{\mathbf{k}}(t) - \mu\right] \hat{c}^\dagger_{\mathbf{k}} \hat{c}_{\mathbf{k}}, \tag{2.80}$$

where $\epsilon_{\mathbf{k}}(t)$ is a time-dependent energy. The Heisenberg equation of motion yields the time-dependence for the creation and annihilation operators as

$$\hat{c}^\dagger_{\mathbf{k},H}(t) = e^{\mathrm{i}\int_0^t d\bar{t}[\epsilon_{\mathbf{k}}(\bar{t})-\mu]} \hat{c}^\dagger_{\mathbf{k}}(0), \tag{2.81}$$

$$\hat{c}_{\mathbf{k},H}(t) = e^{-\mathrm{i}\int_0^t d\bar{t}[\epsilon_{\mathbf{k}}(\bar{t})-\mu]} \hat{c}_{\mathbf{k}}(0). \tag{2.82}$$

The contour Green function is given by

$$\begin{aligned} G_{\mathbf{k}}(t, t') &= -\mathrm{i}\langle \mathcal{T}_{\mathcal{C}} \hat{c}_{\mathbf{k},H}(t) \hat{c}^\dagger_{\mathbf{k},H}(t')\rangle \\ &= -\mathrm{i}\theta_{\mathcal{C}}(t, t')\langle \hat{c}_{\mathbf{k},H}(t) \hat{c}^\dagger_{\mathbf{k},H}(t')\rangle + \mathrm{i}\theta_{\mathcal{C}}(t', t)\langle \hat{c}^\dagger_{\mathbf{k},H}(t') \hat{c}_{\mathbf{k},H}(t)\rangle, \end{aligned} \tag{2.83}$$

where $\theta_{\mathcal{C}}(t, t')$ is the contour step function, and the thermodynamic average is calculated with respect to the initial Hamiltonian $\hat{H}(0)$. Equation (2.83) is an equivalent definition of the contour Green function in Eq. (2.60). Here, we have explicitly taken the contour arguments to be on the real-time axis. Plugging the creation

and annihilation operators in Eqs. (2.81) and (2.82) into Eq. (2.83) yields the non-interacting contour Green function as

$$G^{(0)}_{\mathbf{k}}(t,t') = -\mathrm{i}\left\{\theta_{\mathcal{C}}(t,t') - n_F\left[\epsilon_{\mathbf{k}}(0)-\mu\right]\right\} e^{-\mathrm{i}\int_{t'}^{t} d\bar{t}\left[\epsilon_{\mathbf{k}}(\bar{t})-\mu\right]}. \tag{2.84}$$

Note that this reduces to Eq. (2.32) for a time-independent Hamiltonian at zero temperature.

**Contour Dyson equation**

The Dyson equation can be written for contour Green functions as well, using the contour convolution defined as [69]

$$f * g = \int_{\mathcal{C}} d\bar{z} f(z,\bar{z}) g(\bar{z},z'). \tag{2.85}$$

The contour Dyson equation reads (omitting arguments) [41,69]

$$G_{\nu\nu'} = G^{(0)}_{\nu\nu'} + G^{(0)}_{\nu\nu'} * \Sigma_{\nu\nu'} * G_{\nu\nu'} \tag{2.86}$$

$$= G^{(0)}_{\nu\nu'} + G_{\nu\nu'} * \Sigma_{\nu\nu'} * G^{(0)}_{\nu\nu'}. \tag{2.87}$$

By convoluting with the operator $\delta_{\mathcal{C}}(z,z')\left[\mathrm{i}\partial_z - h(z)\right]$ from the left and with the operator $\left[-\mathrm{i}\overleftarrow{\partial_{z'}} - h(z')\right]\delta_{\mathcal{C}}(z,z')$ from the right, where $\delta_{\mathcal{C}}(z,z')$ is contour Dirac delta function and $h(z)$ is the single-particle Hamitonian, these integral equations can be converted into integro-differential equations for each time argument, given by [41,69]

$$\left[\mathrm{i}\partial_z - h(z)\right] G_{\nu\nu'}(z,z') - \int_{\mathcal{C}} d\bar{z}\Sigma_{\nu\nu'}(z,\bar{z}) G_{\nu\nu'}(\bar{z},z') = \delta_{\mathcal{C}}(z,z'), \tag{2.88}$$

$$G_{\nu\nu'}(z,z')\left[-\mathrm{i}\overleftarrow{\partial_{z'}} - h(z')\right] - \int_{\mathcal{C}} d\bar{z} G_{\nu\nu'}(z,\bar{z})\Sigma_{\nu\nu'}(\bar{z},z') = \delta_{\mathcal{C}}(z,z'), \tag{2.89}$$

which can be solved numerically (for details, see, e.g., Refs. [41,78]). Here, the left derivative is defined as $G_{\nu\nu'}(z,z')\overleftarrow{\partial_{z'}} = \partial_{z'} G_{\nu\nu'}(z,z')$. The physical interpretation of the contour Dyson equation is the same as in the equilibrium case, i.e., it is a formal way to write the perturbation expansion of $G_{\nu\nu'}(z,z')$ [69].

# PART II ANALOGUE QUANTUM SIMULATION OF FERMIONS

# Chapter 3

## ANALOGUE QUANTUM SIMULATION: ULTRACOLD ATOMIC GASES

In this Chapter, we introduce some relevant concepts in ultracold atomic gases that are one of the most widely used platforms for analogue quantum simulations of condensed matter systems. The concepts presented in this Chapter provide the necessary background for Chapter 4.

## 3.1 Introduction

In analogue quantum simulation, one, controllable quantum system mimics or emulates another, usually less controllable quantum system by mapping the model Hamiltonian of the simulated system directly onto the Hamiltonian of the simulator [7]. Ultracold atoms, both trapped in continuum and loaded in optical lattices, have proven to offer good realizations of toy models of condensed matter systems. A case in point is the Hubbard model in Eq. (2.1), which has been realized both with bosonic [15] and with fermionic [16, 79, 80] atoms. Another example is the experimental realization of analogues of Josephson junctions [38, 81–83].

In this Chapter, we give an introduction to ultracold atomic gases, with a focus on Fermi gases since we are interested in the quantum simulation of fermionic systems. We begin with some general properties of quantum gases before explaining how quantum degeneracy is achieved in these systems and how the interac-

tions between atoms can be tuned with a Feshbach resonance. We then describe the Bardeen–Cooper–Schrieffer (BCS) theory of superfluidity, Josephson effect, and optical lattices that are required in Chapter 4 where we study the 'spin-asymmetric' Josephson effect in ultracold Fermi gases. There are several theoretical and experimental review articles and books on ultracold atoms. For more extensive treatments and applications of ultracold atoms in quantum simulation, we refer, e.g., to Refs. [9, 25–31, 48, 84, 85].

## 3.2 Ultracold neutral atoms

### 3.2.1 General properties

Ultracold atomic gases, or quantum gases, are physical systems which consist of a large number of usually either fermionic or bosonic isotopes of neutral atoms[1] cooled down to the regime of quantum degeneracy where the average spacing between the particles is comparable to or less than their thermal de Broglie wavelength [86]. Alkali metal isotopes are usually favoured because of their simpler atomic structure compared to most elements, although also non-alkali atoms are used [87]. Alkali metals only have one valence electron in an $s$ orbital, implying the ground-state $\bar{n}\,^2\mathrm{S}_{1/2}$. Here, the Russell–Saunders notation is used, i.e., the level $\bar{n}\,^2\mathrm{S}_{1/2}\,(=\bar{n}\,^{2S+1}L_J)$ corresponds to principal quantum number $\bar{n}$ whose value depends on the element, spin quantum number $S=\frac{1}{2}$, orbital angular momentum quantum number $L=0$ (denoted by the letter $\mathrm{S}$), and total electronic angular momentum quantum number $J=\frac{1}{2}$. It turns out that this kind of atomic structure is also favourable to magnetically tunable interactions between the atoms [48].

[1] However, Bose–Fermi mixtures of atoms are also studied. We point out that with a neutral atom, since it has an equal number of protons and electrons, the quantum statistics obeyed by the atom is determined solely by the number of neutrons. If the atom has an odd number of neutrons, it is a fermion, and if it has an even number, it is a boson. With alkali metals, which are the most commonly used quantum gas elements, this is equivalent to having an integer or a half-integer nuclear spin quantum number $I$, respectively, since alkali metals have an odd atomic number. For example, $^6$Li ($I=1$) and $^{40}$K ($I=4$) are fermions, and $^7$Li ($I=\frac{3}{2}$) and $^{41}$K ($I=\frac{3}{2}$) are bosons [84].

To suppress three-body recombination processes and solidification, atomic gases are extremely dilute with a particle density $n \sim 10^{12} - 10^{14}\ \mathrm{cm}^{-3}$ [86]. To compare, the density of molecules in air at room temperature and atmospheric pressure is roughly $10^{19}\ \mathrm{cm}^{-3}$, and liquids and solids have an atom density of approximately $10^{22}\ \mathrm{cm}^{-3}$ [84], meaning that ultracold atomic gases are several orders of magnitude more dilute than these systems. The particle number in quantum gases is on the order of $10^5 - 10^6$. To be precise, quantum gases are actually a metastable phase of matter with a lifetime on the order of seconds [86].

To reach the regime of quantum degeneracy in atomic gases, temperatures on the order of 1 $\mu$K are required, e.g., in Ref. [88] the Fermi temperature for a cloud of $^6$Li was measured to be 810 nK, hence the name *ultracold* gases [86]. The experimental study of these quantum degenerate gases requires a combination of techniques in trapping, cooling, manipulation, and detection of atoms that took decades to develop. These experimental techniques have been described extensively in the literature (see, e.g., Refs. [84, 86, 87, 89, 90]). In the following we focus only on some selected key concepts in ultracold Fermi gases.

### 3.2.2 Evaporative and sympathetic cooling

Evaporative cooling is the standard experimental technique allowing to reach the temperatures required for quantum degeneracy, starting from atomic cloud temperatures that have been obtained first with laser cooling[2] [86, 87]. In evaporative cooling, the atoms with kinetic energies above some cut-off value are controllably let to escape from the trap, and the remaining atoms are let to thermalize via elastic atom-atom collisions. The procedure is repeated several times to lower the temperature of the system. We point out that since evaporative cooling relies on repeated thermalizations of the sample via collision processes, there is a difference in the implementation of the scheme for Fermi gases of spin-polarized identical

[2] With $^6$Li, laser cooling achieves temperatures on the order of 300 $\mu$K [91].

fermions as compared to bosonic gases. This is due to the Pauli exclusion principle which forbids $s$-wave scattering of spin-polarized identical fermions (i.e., the $s$-wave scattering cross section is zero [87]). Note that at low temperatures for dilute gases, collisions between atoms are primarily $s$-wave.[3] As a result of the Pauli blocking, evaporative cooling of spin-polarized identical fermions works inefficiently because of the lack of rethermalization. Thus, other strategies, such as cooling fermions in different internal states or sympathetic cooling with other atomic species, are required for Fermi degeneracy [87]. In sympathetic cooling, the temperature of the atomic species of interest is lowered by thermal contact with the other species which can be evaporatively cooled. For example, cooling of fermionic $^6$Li can be achieved via collisions with the evaporatively cooled bosonic $^7$Li [87]. In this case, $^7$Li cools $^6$Li 'by sympathy', hence the name of the scheme.

With these tools, the first quantum degenerate Fermi gas of atoms was realized in 1999 using $^{40}$K [93]. The evaporative cooling was perfomed by preparing the $^{40}$K atoms in the Zeeman sublevels $\left|F=\frac{9}{2}, m_F=\frac{9}{2}\right\rangle$ and $\left|F=\frac{9}{2}, m_F=\frac{7}{2}\right\rangle$ of the $F=\frac{9}{2}$ hyperfine level of the ground-state $4\,^2\mathrm{S}_{1/2}$. Here $F$ denotes the total angular momentum (i.e, the sum of electronic angular momentum and nuclear spin) quantum number and and $m_F$ is the corresponding secondary quantum number (i.e., the quantized projection of total angular momentum along the field axis). The other stable fermionic isotope in alkali metals, $^6$Li, was cooled to quantum degeneracy

[3] To see this, recall the three-dimensional elastic scattering of two identical atoms which interact with each other via a spherically symmetric potential $U(r)$, where $r$ is the relative distance of the atoms. The radial part $u_l(r)$ (here, $l$ is the angular momentum quantum number) of the wave function of the 'relative particle' then obeys the time-independent Schrödinger equation [92]

$$-\frac{1}{2m_r}\frac{\partial^2 u_l(r)}{\partial r^2}+\left[U(r)+\frac{l(l+1)}{2m_r r^2}\right]u_l(r)=Eu_l(r),$$

where $m_r$ is the reduced mass of the two atoms and $E$ is the collision energy. The term $l(l+1)/2m_r r^2$ is a centrifugal barrier which limits the number of relevant partial waves for low energy scattering. For ultracold atoms (e.g., Li at temperatures below a few millikelvin), scattering processes involving partial waves with $l>0$ (i.e., $p$, $d$, $f$, ... waves) are energetically suppressed, and thus only $s$-wave (i.e., $l=0$, in which case the centrifugal barrier vanishes) scattering needs to be considered [87].

in 2001 by sympathetic cooling with $^{7}$Li [88, 94]. Examples of non-alkali Fermi gases cooled to quantum degeneracy include $^{173}$Yb [95], $^{171}$Yb [96], $^{87}$Sr [97, 98], and $^{161}$Dy [99].

### 3.2.3 Feshbach resonance

Following the realization of Fermi degeneracy, great experimental effort was put into obtaining proof of superfluid behaviour in two-component atomic Fermi gases. After some pioneering experiments in fermion pairing [100–108], superfluidity in two-component Fermi gases was unequivocally demonstrated in 2005 by the observation of quantized vortices in $^{6}$Li [109]. These superfluid atomic Fermi gases can be used, e.g., for the analogue quantum simulation of solid-state superconductors [9].

In two-component ultracold Fermi gases, atoms are prepared in different Zeeman sublevels (often loosely called just hyperfine levels, or spin states) that represent effective spin-$\frac{1}{2}$ projections in the presence of a magnetic bias field. In quantum simulation, these Zeeman states thus correspond to the $\uparrow$ and $\downarrow$ spin projections of electrons in a metal. For example, with $^{6}$Li one usually chooses the two lowest-lying Zeeman states, $|1\rangle = \left|F = \frac{1}{2}, m_F = \frac{1}{2}\right\rangle$ and $|2\rangle = \left|F = \frac{1}{2}, m_F = -\frac{1}{2}\right\rangle$, from the Zeeman-split $F = \frac{1}{2}$ hyperfine manifold of the ground-state level $2\,^{2}\mathrm{S}_{1/2}$ such that $|1\rangle = |\downarrow\rangle$ and $|2\rangle = |\uparrow\rangle$ (see for example Ref. [38]).[4]

The interaction between these effective spin-$\frac{1}{2}$ particles is characterized by the dimensionless parameter $k_F a_s$ [9, 87]. Here $k_F$ is the Fermi wave number and $a_s$ is the $s$-wave scattering length in three dimensions (3D). The absolute value of the scattering length quantifies the strength of the interactions, and its sign determines

[4] We point out that strictly speaking $F$ is not a good quantum number for the magnetic field strengths usually used in ultracold Fermi gas experiments (the so-called Paschen–Back regime), but in practice it is still used for labelling the states for simplicity. The label then indicates the value of $F$ at zero field which the sublevel in a strong field adiabatically correlates with [48]. A more precise notation for the $|1\rangle$ and $|2\rangle$ states in $^{6}$Li is $|1\rangle = \left|S = \frac{1}{2}, I = 1, m_S = -\frac{1}{2}, m_I = 1\right\rangle$ and $|2\rangle = \left|S = \frac{1}{2}, I = 1, m_S = -\frac{1}{2}, m_I = 0\right\rangle$. Here, $m_S$ ($m_I$) is the secondary spin (nuclear spin) quantum number.

the character of the interactions [87]. For $a_s > 0$, the interaction is repulsive. For $a_s < 0$, it is attractive.

What makes interactions between ultracold atoms particularly interesting is the phenomenon of Feshbach resonance [48,110] which enables the tuning of the absolute value *and* the sign of the scattering length with an external magnetic field $B$.[5] This ability to control the interactions between particles to a great extent is a useful feature for quantum simulations as it allows the study of physical phenomena over a variety of parameter regimes.

To explain Feshbach resonances one considers the *multi*channel scattering of two ultracold atoms, i.e., a minimum of two scattering channels is required for the phenomenon [48, 110]. The atoms 1 and 2 are prepared in a particular choice of Zeeman states, $|F_1, m_{F_1}\rangle$ and $|F_2, m_{F_2}\rangle$, respectively. They scatter in an open channel characterized by the quantum numbers $\{F_1 m_{F_1}, F_2 m_{F_2}, l = 0\}$ [110]. Open channel means that the total scattering energy $E$ of the atoms is greater than the asymptotic value of the interaction potential which is given by the sum of the internal energies of the atoms, i.e., $E > E_{F_1 m_{F_1}} + E_{F_2 m_{F_2}}$. For the same pair of atoms in some other Zeeman states, $|F_1', m_{F_1'}\rangle$ and $|F_2', m_{F_2'}\rangle$, the interaction potential is in general different from that of the open channel [110]. The potential corresponding to these other Zeeman states represents an energetically closed scattering channel if its asymptotic energy is above $E$, i.e., $E_{F_1' m_{F_1'}} + E_{F_2' m_{F_2'}} > E$. We assume that this other channel is closed in the following.

Two features are crucial for the existence of Feshbach resonances. First, due to interatomic interactions at short distances, dynamical changes in the couplings among the angular momenta of the two atoms are induced, and thus the (suitable) closed channel becomes coupled to the atoms in the open channel when the atoms are close to each other [110]. For alkali metal atoms, this occurs typically in the

[5] We consider only magnetic Feshbach resonances in this work. There are also optical Feshbach resonances (see Ref. [48]).

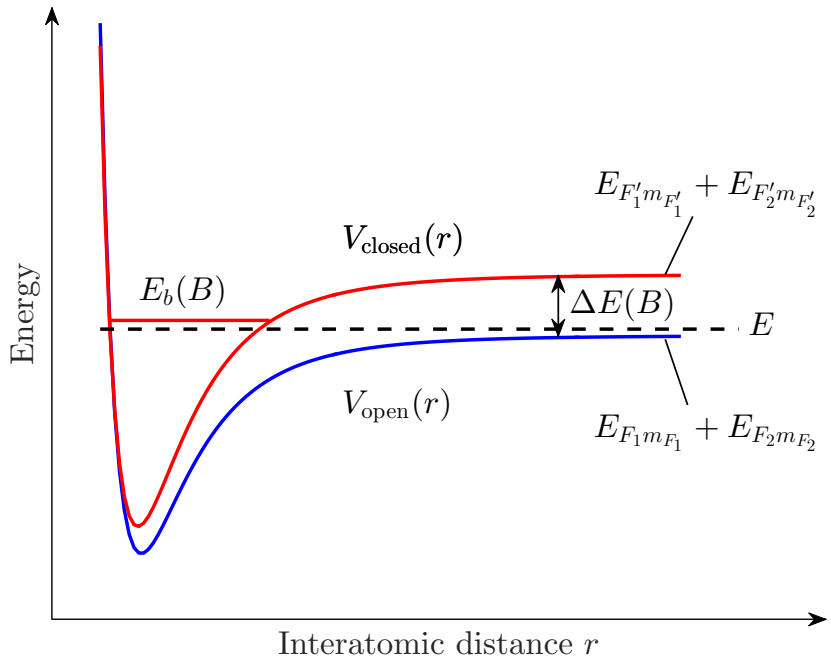


Figure 3.1: Feshbach resonance. Two atoms, 1 and 2, in Zeeman states $|F_1, m_{F_1}\rangle$ and $|F_2, m_{F_2}\rangle$, respectively, scatter in an open channel potential $V_{\text{open}}(r)$ (blue curve), where $r$ is the interatomic distance. The open channel has asymptotic energy $E_{F_1m_{F_1}} + E_{F_2m_{F_2}} < E$, where $E$ is the total energy of the atoms (black dashed curve). Another pair of Zeeman states of the atoms, $|F_1', m_{F_1'}\rangle$ and $|F_2', m_{F_2'}\rangle$, corresponds to a closed channel potential $V_{\text{closed}}(r)$ (red curve) with asymptotic energy $E_{F_1'm_{F_1'}} + E_{F_2'm_{F_2'}} > E$. For small $r$, interatomic interactions induce a coupling between the two channels. If the open and closed channels have different magnetic moments, the energies of the channels can be tuned with respect to each other with an external magnetic field $B$ as $\Delta E(B) = \Delta\mu_m B$, where $\Delta\mu_m$ is the difference in the magnetic moments. For ultracold atoms, $E - (E_{F_1m_{F_1}} + E_{F_2m_{F_2}}) \simeq k_B T \ll \Delta\mu_m B$. Changing the magnetic field also affects the energies $E_b(B)$ of the bound states of the closed channel. If at a magnetic field value $B = B_0$, the energy of a bound state in the closed channel becomes degenerate with the total energy of the atoms in the open channel, i.e., $E_b(B_0) = E$, resonant scattering occurs and is characterised by a diverging scattering length. The atoms in the open channel are then said to have a Feshbach resonance at $B = B_0$.

interatomic distance range of 20 to 25$a_0$, where $a_0$ is the Bohr radius [110]. Since the two colliding atoms cannot belong to the continuum of the closed channel, the interchannel coupling is a second-order process [84]. In other words, the atoms can virtually populate an intermediate state in the closed channel and then return to the open channel. Second, if the closed channel has a magnetic moment which

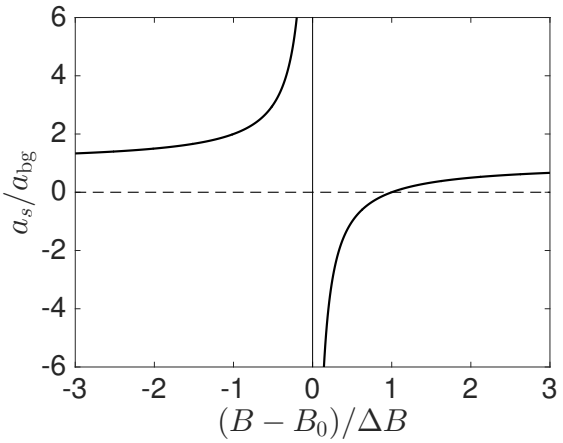


Figure 3.2: The $s$-wave scattering length $a_s(B)$ in Eq. (3.1) diverges at $B = B_0$, changes sign when $B$ goes through $B_0$, and vanishes when $B = B_0 + \Delta B$.

is different from that of the open channel by $\Delta\mu_m$, the shift of the asymptotic energies of the two potentials, $\Delta E(B) = \Delta\mu_m B$, can be changed with the external magnetic field $B$. If one then tunes the energy of a molecular bound state in the closed channel to degeneracy with the total energy of the atoms, the mixing of the two channels due to the interchannel coupling is maximal and resonant scattering occurs [48]. This Feshbach resonance is characterized by a diverging scattering length and cross section, and it allows strong interactions for ultracold atoms that have very low collision energies. We illustrate the idea of a Feshbach resonance in Fig. 3.1.

Using for example the $T$-matrix formalism (see Ref. [84] for details), one can show that the $s$-wave scattering length as a function of $B$ is given by [48]

$$a_s(B) = a_{\rm bg}\left(1 - \frac{\Delta B}{B - B_0}\right). \tag{3.1}$$

Here, $a_{\rm bg}$ is the background scattering length which characterizes the scattering in the open channel without coupling to the closed channel, $B_0$ is the magnetic field at resonance, and $\Delta B$ is the resonance width corresponding to the difference between $B_0$ and the magnetic field value at which the scattering length vanishes. The scattering length therefore diverges at $B = B_0$, changes sign when $B$ goes

through $B_0$, and vanishes when $B = B_0 + \Delta B$. We illustrate this behaviour of the scattering length in Eq. (3.1) in Fig. 3.2.

To make the description a bit more concrete and to give a sense of experimental parameters, we consider the Feshbach resonances of $^6$Li as an example. The two lowest-lying Zeeman states $|1\rangle$ and $|2\rangle$ have a background scattering length $a_{\mathrm{bg},12} = -1582a_0$, and a Feshbach resonance at $B_{0,12} = 832$ G with $\Delta B_{12} = -262$ G [111].[6] The Zeeman states $|1\rangle$ and $|3\rangle$, and $|2\rangle$ and $|3\rangle$ have background scattering lengths $a_{\mathrm{bg},13} = -1770a_0$ and $a_{\mathrm{bg},23} = -1642a_0$, respectively, and Feshbach resonances at $B_{0,13} = 690$ G with $\Delta B_{13} = -167$ G, and at $B_{0,23} = 810$ G with $\Delta B_{23} = -200$ G, respectively [111]. Here, $|3\rangle = \left|F = \frac{3}{2}, m_F = -\frac{3}{2}\right\rangle$ is the third lowest-lying Zeeman state of $^6$Li.[7]

The physics of these $^6$Li Feshbach resonances is the following. For magnetic fields above 500 G, the spin of the valence electron of $^6$Li is fully polarized by the field, and $m_S = -\frac{1}{2}$ for each of the states $|1\rangle$, $|2\rangle$, and $|3\rangle$ [113]. This means that the open channel of two colliding $^6$Li atoms in these states belongs to the spin-triplet (i.e., $S_{\mathrm{tot}} = 1$, where $S_{\mathrm{tot}}$ is the total spin quantum number of the two valence electrons) molecular potential of $^6$Li [114]. The closed channel consists of states belonging to the spin-singlet (i.e., $S_{\mathrm{tot}} = 0$) molecular potential of $^6$Li [114]. Since the spin-singlet wave function of the valence electrons is antisymmetric, the corresponding spatial wave function has to be symmetric. This means that the Pauli principle does not exclude the valence electrons from the region between the nuclei, and the Coulomb attraction between the electrons and the nuclei leads to a deep singlet potential well which can support suitable bound states for a Feshbach resonance. When the distance of the colliding $^6$Li atoms is on the order of the atomic scale, the hyperfine interaction $V_{\mathrm{hf}} = \alpha_{\mathrm{hf}} \left(\hat{\mathbf{S}}_1 \cdot \hat{\mathbf{I}}_1 + \hat{\mathbf{S}}_2 \cdot \hat{\mathbf{I}}_2\right) = \frac{\alpha_{\mathrm{hf}}}{2}(\hat{\mathbf{S}}_1 + \hat{\mathbf{S}}_2) \cdot (\hat{\mathbf{I}}_1 + \hat{\mathbf{I}}_2) + \frac{\alpha_{\mathrm{hf}}}{2}(\hat{\mathbf{S}}_1 - \hat{\mathbf{S}}_2) \cdot (\hat{\mathbf{I}}_1 - \hat{\mathbf{I}}_2)$, where $\alpha_{\mathrm{hf}}$ is the hyperfine constant and $\hat{\mathbf{S}}_{1,2}$ and

[6] The states $|1\rangle$ and $|2\rangle$ also have a very narrow Feshbach resonance at $B_0 = 543$ G with $\Delta B = 0.1$ G [112].

[7] More precisely, $|3\rangle = \left|S = \frac{1}{2}, I = 1, m_S = -\frac{1}{2}, m_I = -1\right\rangle$.

$\hat{\mathbf{I}}_{1,2}$ are the electron spin and nuclear spin operators for the atoms, respectively, induces a coupling between the triplet and the singlet potentials (intuitively, the hyperfine interaction allows the trade of electron spin for nuclear spin) [114]. Since the singlet and triplet potentials correspond to different magnetic moments, their relative energies can be tuned with a magnetic field. A Feshbach resonance then emerges when a bound state in the singlet potential is tuned to degeneracy with the total energy of the $^6$Li atoms in one of the three combinations of the states $|1\rangle$, $|2\rangle$, and $|3\rangle$ discussed above in the open channel. See Ref. [48] and references therein for further details on $^6$Li Feshbach resonances. In this work, we propose to use the different locations of these three Feshbach resonances of $^6$Li to create an effective spin-dependent potential for the spin-asymmetric Josephson effect in Chapter 4.

We conclude this introduction to Feshbach resonances by mentioning for completeness that the ability to tune the scattering length and thus the interaction enables the study and quantum simulation of the so-called BCS–BEC crossover [114] with superfluid Fermi gases.[8] Here, BEC stands for Bose–Einstein condensate. The BCS limit ($1/k_F a_s \to -\infty$) of the crossover corresponds to a weak attractive interaction between the atoms. The emergence of superfluidity can be explained in terms of BCS theory (see Section 3.2.4): the weak attraction between atoms leads to the formation of Cooper pairs of atoms of opposite spin and momentum. In the opposite BEC limit ($1/k_F a_s \to \infty$), atoms form effectively bosonic dimers (with binding energy $E_b = -1/ma_s^2$) that undergo Bose–Einstein condensation. Feshbach resonances allow the study of the transition from one limit to the other. There is much theoretical and experimental interest in the intermediate *unitarity* regime where $1/k_F|a_s| \lesssim 1$. This is because a unitary Fermi gas, for which $1/k_F|a_s| = 0$, can be considered universal and scale invariant in the sense that its properties are

[8] The idea of such a crossover was originally studied in the contexts of exciton condensation, superconductivity in doped semiconductors, and $^3$He [114].

independent of the details of the two-body interaction and are determined by its density and temperature similarly to an ideal Fermi gas even though a unitary gas is strongly interacting. For further details on the BCS–BEC crossover and the unitary Fermi gas, see, e.g., Ref. [114] and references therein.

### 3.2.4 BCS theory

Here, we introduce the basic concepts of a simple theory of superfluidity in Fermi gases that is based on the BCS theory for conventional superconductors [115], as considered, e.g., in Refs. [116–118]. Therefore, at least for weak attractive interactions, ultracold Fermi gases act as analogue quantum simulators of BCS superconductors. There are also approaches that are more accurate than BCS theory [114]. For instance, if one includes the effect of the other particles on the two-particle interaction[9], the BCS critical temperature is suppressed by a factor of roughly two. However, the simplicity of BCS theory makes it a good starting point before advancing to more accurate schemes. We use BCS theory in Chapters 4 and 5 to study the spin-asymmetric Josephson effect. For a further description of alternative theoretical approaches, such as Monte Carlo calculations and corrections to BCS theory, we refer to Ref. [114].

The starting point of BCS theory is the theoretical observation by Cooper [120] that two fermions near the Fermi surface in a degenerate Fermi gas form a bound state called a Cooper pair if there is even an arbitrarily weak attractive interaction between them. In conventional superconductors this attractive interaction arises from a lattice distortion that creates an effective attraction between electrons [121], whereas in ultracold Fermi gases the attractive interaction between two atoms in different hyperfine levels comes from the two-body scattering process characterised by the $s$-wave scattering length $a_s$ [87]. Bardeen, Cooper, and Schrieffer [115] showed that superfluidity arises from the condensation of Cooper

[9] This is also known as the Gor'kov–Melik–Barkhudarov correction [119].

pairs below a critical temperature $T_c$, taking the ground-state of the system to be of the form

$$|\Psi_{\mathrm{BCS}}\rangle = \prod_{\mathbf{k}} \left( u_{\mathbf{k}} + v_{\mathbf{k}} \hat{c}^{\dagger}_{\mathbf{k},\uparrow} \hat{c}^{\dagger}_{-\mathbf{k},\downarrow} \right) |\emptyset\rangle, \tag{3.2}$$

where the Bogoliubov coefficients for the momentum state $\mathbf{k}$ satisfy $|u_{\mathbf{k}}|^2 + |v_{\mathbf{k}}|^2 = 1$. The expressions for $u_{\mathbf{k}}$ and $v_{\mathbf{k}}$ are obtained variationally by minimizing over $|\Psi_{\mathrm{BCS}}\rangle$ the expectation value of the BCS Hamiltonian [119]

$$\hat{H}_{\mathrm{BCS}} = \sum_{\mathbf{k},\sigma} (\epsilon_{\mathbf{k}} - \mu)\, \hat{c}^{\dagger}_{\mathbf{k},\sigma} \hat{c}_{\mathbf{k},\sigma} + \frac{g}{V_s} \sum_{\mathbf{k},\mathbf{k}'} \hat{c}^{\dagger}_{\mathbf{k}',\uparrow} \hat{c}^{\dagger}_{-\mathbf{k}',\downarrow} \hat{c}_{-\mathbf{k},\downarrow} \hat{c}_{\mathbf{k},\uparrow}, \tag{3.3}$$

where $\epsilon_{\mathbf{k}} = \frac{|\mathbf{k}|^2}{2m}$, $\mu$ is the chemical potential, $V_s$ is the system volume, and $g$ is the coupling constant which in the case of ultracold Fermi gases and a contact pseudo-potential[10] of the form $U(\mathbf{r}) = g\delta(\mathbf{r})$ is given by $g = \frac{4\pi}{m} a_s < 0$.[11] The resulting expressions for the Bogoliubov coefficients are given by [119]

$$u_{\mathbf{k}} = \sqrt{\frac{1}{2}\left(1 + \frac{\xi_{\mathbf{k}}}{E_{\mathbf{k}}}\right)}, \tag{3.4}$$

and

$$v_{\mathbf{k}} = \sqrt{\frac{1}{2}\left(1 - \frac{\xi_{\mathbf{k}}}{E_{\mathbf{k}}}\right)}, \tag{3.5}$$

where $\xi_{\mathbf{k}} = \epsilon_{\mathbf{k}} - \mu$, $E_{\mathbf{k}} = \sqrt{\xi^2_{\mathbf{k}} + \Delta^2}$ is the quasiparticle energy, and $\Delta$ is the BCS energy gap which characterises the superfluid phase. In ultracold Fermi gases, the gap can be measured for example with radio-frequency spectroscopy (see, e.g., Refs. [107, 122–124]).

In theory calculations for a homogeneous Fermi gas, $\Delta$ is obtained numerically

[10] A contact potential is a good approximation in ultracold gases due to the diluteness and low temperature of the atomic clouds [27].

[11] Alternatively, the expressions for the Bogoliubov coefficients can be derived using the Bogoliubov–Valatin transformation [121].

by solving the BCS gap equation [119, 125]

$$\frac{m}{4\pi|a_s|} = \frac{1}{2V_s}\sum_{\mathbf{k}}\left(\frac{1-2\,n_F(E_{\mathbf{k}})}{E_{\mathbf{k}}} - \frac{1}{\epsilon_{\mathbf{k}}}\right)$$
$$= \frac{1}{2V_s}\sum_{\mathbf{k}}\left(\frac{1-2\,n_F\left(\sqrt{(\epsilon_{\mathbf{k}}-\mu)^2+\Delta^2}\right)}{\sqrt{(\epsilon_{\mathbf{k}}-\mu)^2+\Delta^2}} - \frac{1}{\epsilon_{\mathbf{k}}}\right), \tag{3.6}$$

in which the Fermi distribution function reads $n_F(E_{\mathbf{k}}) = 1/\left[\exp(\beta E_{\mathbf{k}})+1\right]$. Equation (3.6) is solved along with the number equation [119, 125]

$$n = \frac{1}{V_s}\sum_{\mathbf{k}}\left\{1 - \frac{\xi_{\mathbf{k}}}{E_{\mathbf{k}}}\left[1-2\,n_F(E_{\mathbf{k}})\right]\right\}$$
$$= \frac{1}{V_s}\sum_{\mathbf{k}}\left\{1 - \frac{\xi_{\mathbf{k}}}{\sqrt{(\epsilon_{\mathbf{k}}-\mu)^2+\Delta^2}}\left[1-2\,n_F\left(\sqrt{(\epsilon_{\mathbf{k}}-\mu)^2+\Delta^2}\right)\right]\right\}, \tag{3.7}$$

where $n$ is the total number density. Together Eqs. (3.6) and (3.7) fix the values for $\Delta$ and $\mu$ for a given temperature and interaction strength. Note that the gap equation (3.6) contains an extra term compared to the standard gap equation (see, e.g., Ref. [121]) which takes care of the unphysical ultraviolet divergence caused by the contact pseudo-potential. See, e.g., Refs. [119, 125] for further details.

We now introduce the Nambu–Gor'kov Green function which complements the Green functions discussed in Section 2.2 and enables the study of superfluidity with the Green function approach. The Nambu–Gor'kov Green function is actually a matrix Green function which allows describing the propagation of single particles as well as Cooper pairing correlations within the same Green function. It is defined in momentum space and imaginary time as [43]

$$\mathcal{G}_{NG}(\mathbf{k},\tau) = -\langle \mathcal{T}_\tau \hat{\psi}_{\mathbf{k},M}(\tau)\hat{\psi}^\dagger_{\mathbf{k},M}(0)\rangle, \tag{3.8}$$

where the Nambu spinor reads [43]

$$\hat{\psi}_{\mathbf{k}}(\tau) = \begin{pmatrix} \hat{c}_{\mathbf{k}\uparrow,M}(\tau) \\ \hat{c}^\dagger_{-\mathbf{k}\downarrow,M}(\tau)\end{pmatrix}. \tag{3.9}$$

Inserting the Nambu spinor in Eq. (3.9) into Eq. (3.8), the Nambu–Gor'kov Green function becomes

$$\mathcal{G}_{NG}(\mathbf{k},\tau) = -\begin{pmatrix} \langle \mathcal{T}_\tau \hat{c}_{\mathbf{k}\uparrow,M}(\tau)\hat{c}^\dagger_{\mathbf{k}\uparrow,M}(0)\rangle & \langle \mathcal{T}_\tau \hat{c}_{\mathbf{k}\uparrow,M}(\tau)\hat{c}_{-\mathbf{k}\downarrow,M}(0)\rangle \\ \langle \mathcal{T}_\tau \hat{c}^\dagger_{-\mathbf{k}\downarrow,M}(\tau)\hat{c}^\dagger_{\mathbf{k}\uparrow,M}(0)\rangle & \langle \mathcal{T}_\tau \hat{c}^\dagger_{-\mathbf{k}\downarrow,M}(\tau)\hat{c}_{-\mathbf{k}\downarrow,M}(0)\rangle \end{pmatrix}. \tag{3.10}$$

Here, the diagonal elements are the standard Matsubara Green functions introduced in Section 2.2.1.2, but with a different expression in the superfluid state (see Ref. [43]). The component relevant for superfluidity is the off-diagonal element,

$$\mathcal{F}(\mathbf{k},\tau) = -\langle \mathcal{T}_\tau \hat{c}_{\mathbf{k}\uparrow,M}(\tau)\hat{c}_{-\mathbf{k}\downarrow,M}(0)\rangle, \tag{3.11}$$

along with its conjugate, $\mathcal{F}^\dagger(\mathbf{k},\tau)$. This off-diagonal element is called the anomalous Green function since it is non-zero only in the superfluid phase [43, 67]. By, e.g., deriving and solving the equations of motion for the elements of the matrix Nambu–Gor'kov Green function in Eq. (3.10), one finds the expression for the anomalous Green function in Matsubara space as [67]

$$\begin{aligned} \mathcal{F}(\mathbf{k}, \mathrm{i}\omega_n) &= \frac{-\Delta}{(\mathrm{i}\omega_n)^2 - E_\mathbf{k}^2} \\ &= -u_\mathbf{k} v_\mathbf{k} \left( \frac{1}{\mathrm{i}\omega_n - E_\mathbf{k}} - \frac{1}{\mathrm{i}\omega_n + E_\mathbf{k}} \right). \end{aligned} \tag{3.12}$$

We use the anomalous Green functions in Chapters 4 and 5 in describing the critical Josephson currents in the spin-asymmetric Josephson effect.

### 3.2.5 Josephson effect

As we will discuss the spin-asymmetric Josephson effect in Chapters 4 and 5, we now introduce as background the standard Josephson effect [126], which is an important implication of BCS theory. The Josephson effect refers to the dynamics of macroscopic variables such as the relative phase and particle number in a bipartite quantum many-body system known as a Josephson junction. The classic example of a Josephson junction has two superconductors or superfluids spatially separated by a tunnelling barrier, such as a thin insulator in solid-state systems [121].

The Josephson effect is usually divided into two parts depending on whether or not a bias voltage (i.e., a chemical potential difference) is applied across the junction. If there is a non-vanishing overlap between the macroscopic wave functions of the two superfluids in the junction, even without a bias voltage a supercurrent can flow through the barrier with a sinusoidal dependence on the relative phase between the wave functions. This is the direct-current (DC) Josephson effect. In the presence of an additional bias voltage, the supercurrent oscillates with a Josephson frequency that directly depends on the voltage. This is the alternating-current (AC) Josephson effect. The dynamics of the Josephson junction is obtained from the Josephson relations [85, 126]

$$I^J(t) = I^C \sin \Phi^J(t), \tag{3.13}$$

and

$$\frac{d\Phi^J(t)}{dt} = \Delta V, \tag{3.14}$$

where $I^C$ is the critical Josephson current, $\Phi^J(t)$ is the Josephson phase, and $\Delta V$ is the potential difference across the junction. For a simple derivation of these relations, see, e.g., Ref. [127].

The Josephson effect was observed in superconducting tunnel junctions [128] shortly after the theoretical prediction. An analogous effect has also been demonstrated for example in superfluid $^3$He [129] and $^4$He [130], exciton polaritons [131], and ultracold atoms with both bosonic [81–83] and fermionic [38] species. There has also been theoretical work on the Josephson effect in ultracold Fermi gases, see, e.g., Refs. [132–135].

In atomic systems, the analogue of the solid-state Josephson junction can be obtained by bisecting a trapped superfluid into two reservoirs or wells, $L$ and $R$, with a laser-created optical barrier (see, e.g., Ref. [38]). The 'voltage' $\Delta V$ is then

given by the chemical potential difference between the reservoirs that is induced by a small population difference across the junction.

We point out that in Ref. [38] the observation of the Josephson effect refers to Josephson plasma oscillations instead of the full AC effect. To see the difference, we consider dynamics of the number difference parameter $k_J = \frac{1}{2}(N_L^J - N_R^J)$, where $N_L^J$ ($N_R^J$) is the number of Cooper pairs (i.e., effectively bosonic particles, akin to Ref. [85]) in the left (right) hand side of the double well which can contribute to the Josephson current. The parameter $k_J$ obeys the Josephson relations

$$\frac{dk_J}{dt} = I^C \sin \Phi^J(t), \tag{3.15}$$

and

$$\frac{d\Phi^J(t)}{dt} = \mu_R - \mu_L, \tag{3.16}$$

where $\mu_L$ ($\mu_R$) is the chemical potential for Cooper pairs on the left (right) hand reservoir. For small $\Phi^J$ but long enough times to observe small number oscillations, we have $\sin \Phi^J(t) \approx \Phi^J(t)$, and we obtain the relations

$$\frac{dk_J}{dt} = I^C \Phi^J(t), \tag{3.17}$$

and

$$\frac{d\Phi^J(t)}{dt} = -E_{\mathrm{ch}} k_J, \tag{3.18}$$

where we have introduced the charging energy $E_{\mathrm{ch}} = 2\frac{d\mu_L}{dN_L^J}$, which is calculated at $N_L^J = N_R^J = N^J/2$ [85]. Here, $N^J = N_L^J + N_R^J$. The name charging energy comes from the analogous concept in solid-state Josephson junctions [121]. The relations (3.17) and (3.18) yield a differential equation for $k_J$ as

$$\frac{d^2 k_J}{dt^2} + E_{\mathrm{ch}} E_J k_J = 0, \tag{3.19}$$

where the Josephson energy reads $E_J = I^C$ (recall that $\hbar = 1$) [85]. Equation (3.19) is the equation of motion of a simple harmonic oscillator. We therefore find that the system undergoes small-amplitude harmonic motion with the plasma frequency

$$\omega_p = \sqrt{E_{\rm ch} E_J}. \tag{3.20}$$

Equation (3.20) is sometimes said to give the frequency of the *classical* oscillation of the superfluid between the two reservoirs, since it emerges from the equation of motion of a classical pendulum [85]. Note that the Josephson phase oscillates out of phase from $k_J$ by phase $\frac{\pi}{2}$.

The following pendulum analogy is often used to intuitively explain the difference between full AC Josephson oscillations and Josephson plasma oscillations (see also Refs. [83,136]). Consider the Josephson phase to be a rigid pendulum that experiences an impulsive force. If the impulse is small, the pendulum undergoes small-amplitude harmonic motion around the equilibrium position. This is analogous to the Josephson plasma mode. If the impulse is very large, the pendulum rotates continuously in complete circles with a circular frequency proportional to the impulse. This is analogous to the full AC Josephson oscillations. For an illustration, see Fig. 1a of Ref. [83]. In the context of Fermi gases, we point out that for the plasma oscillation approximation to be valid, the initial relative number difference, $z_0 = \frac{N_L^J - N_R^J}{N_L^J + N_R^J}$, that creates a small difference in chemical potentials across the junction (the 'impulse'), has to be on the order of a few per cent [38,135].

In Chapter 4, we consider an extension of the double well atomic Josephson junction realized with ultracold Fermi gases [38] in that we introduce an additional spin-dependent potential across the junction. The presence of a spin-dependent potential creates an asymmetry between the Cooper-paired spin components as they tunnel through the junction and leads to the so-called spin-asymmetric Josephson effect [1,2,36,37] which we study in Chapters 4 and 5.

In addition to a single Josephson junction, the Josephson effect can be realized in an array of small Josephson junctions. For example, a Josephson-type effect was observed in a one-dimensional (1D) optical lattice in the case of Bose–Einstein condensates [81]. In Section 4.3, we consider the spin-asymmetric Josephson effect in a 1D spin-dependent optical superlattice which can considered an array of spin-dependent double wells, or Josephson junctions.

Finally, we point out that in atomic systems it is possible to study the Josephson effect between the hyperfine, or internal, levels of the atoms. In this case, the phenomenon is often called the 'internal' Josephson effect [137].[12] This is also the case where the spin-asymmetric Josephson effect was first studied [36,37].

### 3.2.6 Optical lattices

An optical lattice is a periodic optical potential for ultracold atoms created by the interference of two or more laser beams. It is analogous to the periodic potential of a metallic lattice and thus allows the analogue quantum simulation of lattice models such as the Hubbard Hamiltonian in Eq. (2.1) with quantum gases. The system sizes of optical lattice setups are varied, ranging from small 1D arrangements of less than 100 lattice sites that can be compared to classical simulations [139] to large 3D systems of over $10^4$ sites (see, e.g., Refs. [16, 140]) that are beyond the reach of exact simulations with current numerical methods. In the recently realized Fermi gas microscopes, a few hundred atoms can currently be imaged with single-site resolution in a 2D arrangement (see, e.g., Refs. [141, 142]). Due to their controllability ultracold atoms in optical lattices have been used for studying a plethora of physical phenomena. For reviews, see, e.g., Refs. [9, 27, 29]. In this thesis, we

[12] Note that the internal Josephson effect discussed here is different from the 'intrinsic' Josephson effect which can occur in a bulk superconductor due to internal variations in the material which create a stack of intrinsic Josephson junctions. This is for example the case in some layered high-temperature superconductors where the Josephson effect occurs between adjacent $CuO_2$ planes [138].

study spin-asymmetric particle currents in a spin-dependent optical superlattice in Chapter 4.

The purpose of this Section is to give only a brief introduction to optical lattices. For more extensive and pedagogical treatments, we refer, e.g., to Refs. [84, 119]. We begin with the generation of optical lattice potentials. We then discuss spin-dependent optical lattices. Finally, optical superlattices are introduced. In Appendix A we show for completeness a simple derivation of the Hubbard model in deep optical lattices.

#### 3.2.6.1 Generation of optical lattices

Optical lattices are created with laser fields and rely on the dispersive interaction between the atom and the electric field of a non-resonant laser. The key physical phenomenon behind optical lattices is the AC Stark shift (also called light shift). In this phenomenon a neutral atom couples to an external laser field of frequency $\omega_L$ via an induced electric dipole moment which causes a shift in the energy levels of the atom [84]. Here, we consider the case of an atom with two selected energy levels that we call the ground-state $|g\rangle$ and excited state $|e\rangle$. This two-level approximation can be done since atomic energy levels are not equally spaced, and $\omega_L$ can be tuned close to the resonant frequency between the levels $|g\rangle$ and $|e\rangle$.

The electric dipole interaction between the atom and the laser field creates a potential called the optical dipole potential. It is given by the energy change of the level $|g\rangle$ which can be calculated using second-order perturbation theory (for details, see, e.g., Refs. [84,119,143]). The expression for the optical dipole potential reads [143]

$$V_{\text{dipole}}(\mathbf{r}) = \frac{3\pi c^2}{2\omega_0^3}\frac{\gamma_e}{\delta} I(\mathbf{r}), \tag{3.21}$$

where $c$ is the speed of light, $\omega_0$ is the resonant transition frequency of the atom, $\delta = \omega_L - \omega_0$ is the laser detuning, and $I(\mathbf{r})$ is the intensity of the laser field. The

parameter $\gamma_e$ in Eq. (3.21) corresponds to the spontaneous decay rate of the excited state $|e\rangle$ and is given by the matrix element of the dipole operator $\hat{\mathbf{d}}$ between the states $|g\rangle$ and $|e\rangle$. Its expression is [143]

$$\gamma_e = \frac{\omega_0^3}{3\pi\epsilon_0 c^3}|\langle e|\hat{\mathbf{d}}\cdot\boldsymbol{\epsilon}|g\rangle|^2, \tag{3.22}$$

where $\epsilon_0$ is the vacuum permittivity and $\boldsymbol{\epsilon}$ is the polarization vector of the laser.

We point out that with real atoms such as alkali metals one often does the calculation of the dipole potential more accurately by taking the fine structure into account [143]. For example, in $^6$Li the ground-state $|g\rangle$ corresponds to the level $2\,^2\mathrm{S}_{1/2}$, and the (first) excited state $|e\rangle$ is split into the levels $2\,^2\mathrm{P}_{1/2}$ and $2\,^2\mathrm{P}_{3/2}$ [86]. With all alkali metals, the transition $\bar{n}\,^2\mathrm{S}_{1/2} \rightarrow \bar{n}\,^2\mathrm{P}_{1/2}$ is referred to as the $D_1$ line and $\bar{n}\,^2\mathrm{S}_{1/2} \rightarrow \bar{n}\,^2\mathrm{P}_{3/2}$ as the $D_2$ line[13], and the laser detuning is calculated with respect to both transitions. However, if the laser detuning is large compared to the fine-structure splitting and the polarization of the laser is linear, the resulting dipole potential reduces to the two-level result with a detuning given relative to the centre of the $D_1$ and $D_2$ lines. For further details, see, e.g., Ref. [143].

The sign of the optical dipole potential depends on the detuning of the laser frequency from the resonant transition frequency. The potential is attractive for a red-detuned ($\delta < 0$, i.e., $\omega_L < \omega_0$) laser field, while for blue detuning ($\delta > 0$, i.e., $\omega_L > \omega_0$) it is repulsive. See Fig. 3.3 for an illustration of the laser frequencies relative to the resonant frequency and the light shifts for a red-detuned laser. We also point out that the scattering rate of photons that is related to the absorptive interaction between the atom and the laser field scales as $I/\delta^2$ as opposed to the $I/\delta$ scaling of the dipole potential (see Ref. [143] for details). As a result, for a fixed intensity $I$ the spontaneous scattering of photons can be suppressed by increasing

[13]Note that the designation of these lines is historical and originates from the sodium doublet in the Fraunhofer spectral lines. They should not be confused with the higher D (i.e., $L = 2$) states of the atom.

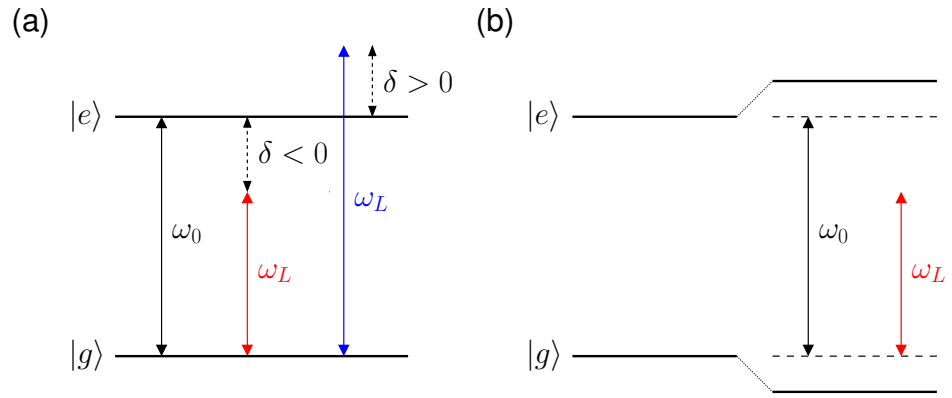


Figure 3.3: (a) Schematic representation of a two-level atom with resonant frequency $\omega_0$ illuminated with laser light of frequency $\omega_L$. If the laser is red-detuned (with detuning $\delta = \omega_L - \omega_0 < 0$, i.e., laser frequency $\omega_L < \omega_0$), the resulting optical dipole potential is attractive. If the laser is blue-detuned (with detuning $\delta = \omega_L - \omega_0 > 0$, i.e., laser frequency $\omega_L > \omega_0$), the optical dipole potential is repulsive. (b) Light shifts for a two-level atom with a red-detuned laser.

$\delta$, and the contribution from the dispersive interaction dominates over dissipative processes [87].

In order to create an optical lattice potential with laser light, $I(\mathbf{r})$ in Eq. (3.21) must be spatially periodic. The usual way to achieve this in 1D is by superimposing two counter-propagating laser beams of wave number $k_L = \frac{2\pi}{\lambda_L}$, where $\lambda_L$ is the wavelength of the beams [47]. This creates a standing wave with intensity $I(x) = I_0 \sin^2(k_L x)$, where $I_0$ is the maximum intensity, and yields a periodic potential of the form

$$V(x) = V_0 \sin^2(k_L x), \tag{3.23}$$

where $V_0$ is the maximum depth of the lattice potential. Usually $V_0$ is given in units of the recoil energy of the atom given by $E_R = k_L^2/2m$, where $m$ is the mass of the atom. Then $V_0 = \tilde{s} E_R$, where the dimensionless parameter $\tilde{s}$ has the expression

$$\tilde{s} = \frac{V_0}{E_R} = \frac{2m}{k_L^2} \cdot \frac{3\pi c^2}{2\omega_0^3} \frac{\gamma_e}{\delta} I_0. \tag{3.24}$$

In ultracold atom experiments, the values for the lattice depth $\tilde{s}$ are usually between 1 and 20 [28], although higher values are also possible. Note that in Eq. (3.23)

we have neglected the Gaussian shape of the laser beam creating the trapping potential, which can be done in the center of the trap for distances much smaller than the beam waist [27].

Higher-dimensional optical lattices are obtained by superimposing more than two laser beams with linearly independent wave vectors [47]. For example, using three pairs of laser beams along orthogonal axes creates the three-dimensional lattice potential

$$V_{3D}(x,y,z) = V_{0,x}\sin^2(k_L x) + V_{0,y}\sin^2(k_L y) + V_{0,z}\sin^2(k_L z), \tag{3.25}$$

where the lattice depths $V_{0,\alpha}$ ($\alpha = x, y, z$) can be varied independently by tuning the intensities of the corresponding pair of laser beams. In addition to dimension, different lattice geometries, such triangular [144], hexagonal [145], and kagome [146] lattices, can also be created by changing the number and orientation of the laser beams [9, 147].

#### 3.2.6.2 Spin-dependent optical lattices for bosons

With ultracold atoms it is possible to create spin- or state-dependent lattices. We first consider the case of bosonic alkali metal atoms, with which pioneering experiments have been done [148, 149]. A state-dependent optical lattice can be created by counter-propagating two linearly polarized laser beams with an angle $\theta$ between their polarization axes[14] [148–151], as we explain in the following. The beams have the same wavelength and intensity. This method is also in principle applicable to the fermionic alkali metals [152], but with them the heating of the system renders this approach impractical as we will discuss in Section 3.2.6.3.

We take the propagation of the electric fields of the laser beams to be along the $z$-axis (see Fig. 3.4 for an illustration). The position-dependent parts of the fields are assumed to have the forms $\mathbf{E}_1 \propto e^{\mathrm{i}k_L z}\left[\cos(\theta/2)\boldsymbol{\epsilon}_x - \sin(\theta/2)\boldsymbol{\epsilon}_y\right]$ and $\mathbf{E}_2 \propto$

[14] This is called a lin-$\theta$-lin or lin$\angle$lin configuration.

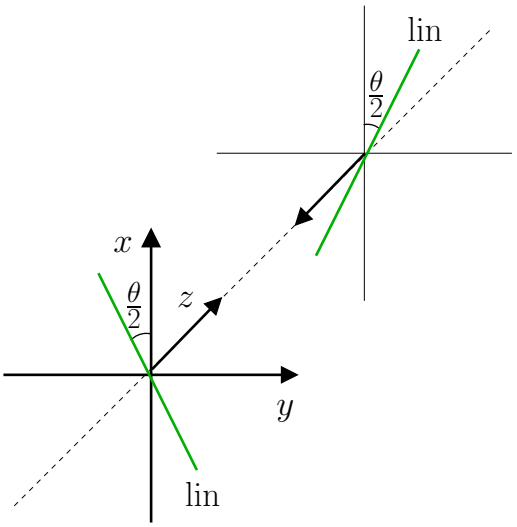


Figure 3.4: Two counter-propagating linearly polarized laser beams of the same wavelength and intensity, and with an angle $\theta$ between their polarization axes (green lines) can be used for creating spin-dependent optical lattices.

$e^{-\mathrm{i}k_L z}\,[\cos(\theta/2)\boldsymbol{\epsilon}_x + \sin(\theta/2)\boldsymbol{\epsilon}_y]$ (here, $\boldsymbol{\epsilon}_x$ and $\boldsymbol{\epsilon}_y$ are unit vectors along the $x$- and $y$-axis, respectively), such that $\mathbf{E}_1 + \mathbf{E}_2 \propto -\cos(k_L z + \theta/2)\boldsymbol{\sigma}^+ + \cos(k_L z - \theta/2)\boldsymbol{\sigma}^-$, where $\boldsymbol{\sigma}^\pm = \mp(\boldsymbol{\epsilon}_x \pm \mathrm{i}\boldsymbol{\epsilon}_y)/\sqrt{2}$. This gives rise to the $\boldsymbol{\sigma}^\pm$ polarized optical lattice potentials [148, 151]

$$V_\pm(z,\theta) = V_{0,\pm}\cos^2(k_L z \pm \theta/2). \tag{3.26}$$

Note that the separation between the minima of the resulting potentials is given by $\Delta z = \theta\lambda_L/2\pi$, which can be controlled with the angle $\theta$.

We consider for concreteness the case of $^{87}$Rb atoms which have nuclear spin $I = \frac{3}{2}$. The standing wave corresponding to the $\boldsymbol{\sigma}^+$ polarized light couples the $m_J = -\frac{1}{2}$ state of the ground-state level $5\,^2\mathrm{S}_{1/2}$ to the $m_J = +\frac{1}{2}$ state in the excited state levels $5\,^2\mathrm{P}_{1/2}$ and $5\,^2\mathrm{P}_{3/2}$.[15] This standing wave also couples the $m_J = +\frac{1}{2}$ state of the level $5\,^2\mathrm{S}_{1/2}$ to the state $m_J = +\frac{3}{2}$ of the level $5\,^2\mathrm{P}_{3/2}$. Similarly, the standing wave corresponding to the $\boldsymbol{\sigma}^-$ polarized light couples the $m_J = +\frac{1}{2}$ state of the ground-state level $5\,^2\mathrm{S}_{1/2}$ to the $m_J = -\frac{1}{2}$ state in the excited state levels $5\,^2\mathrm{P}_{1/2}$

[15] Recall that the electric dipole transition selection rules with $\boldsymbol{\sigma}^\pm$ polarized light have $\Delta m_J = \pm 1$ [153].

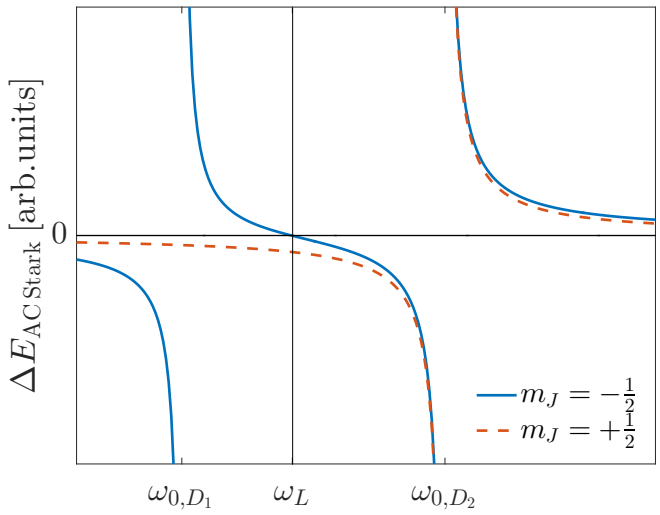


Figure 3.5: Schematic representation of the AC Stark shifts for the $m_J = -\frac{1}{2}$ (blue solid line) and $m_J = +\frac{1}{2}$ (red dashed line) states of $5\,^2\mathrm{S}_{1/2}$ in the case of $\boldsymbol{\sigma}^+$ polarized light. By choosing the laser frequency $\omega_L$ conveniently between the resonant frequencies of the $D_1$ and $D_2$ transitions, $\omega_{0,D_1}$ and $\omega_{0,D_2}$, respectively, it is possible to make the AC Stark shift for the $m_J = -\frac{1}{2}$ state vanish. The AC Stark shift for the $m_J = +\frac{1}{2}$ state remains non-zero. At the same laser frequency $\omega_L$, also the AC Stark shift for the $m_J = +\frac{1}{2}$ state of $5\,^2\mathrm{S}_{1/2}$ with $\boldsymbol{\sigma}^-$ polarized light vanishes, while the AC Stark shift for the $m_J = -\frac{1}{2}$ state remains non-zero.

and $5\,^2\mathrm{P}_{3/2}$. This standing wave also couples the $m_J = -\frac{1}{2}$ state of the level $5\,^2\mathrm{S}_{1/2}$ to the state $m_J = -\frac{3}{2}$ of the level $5\,^2\mathrm{P}_{3/2}$.

By choosing the laser frequency conveniently between the resonant frequencies of the $D_1$ and $D_2$ transitions, it is possible to make the AC Stark shifts[16] for the $m_J = -\frac{1}{2}$ state of $5\,^2\mathrm{S}_{1/2}$ with $\boldsymbol{\sigma}^+$ polarized light and the $m_J = +\frac{1}{2}$ state of $5\,^2\mathrm{S}_{1/2}$ with $\boldsymbol{\sigma}^-$ polarized light equal to zero. This is because in this case the laser detunings with respect to the $D_1$ and $D_2$ lines have opposite signs and the light shifts cancel out [151] (see Fig. 3.5 for an illustration). In the case of $^{87}$Rb, for which $\lambda_{D_1} = 795$ nm and $\lambda_{D_2} = 780$ nm, this occurs at $\lambda_L = 785$ nm [148]. As a result, one is left with the situation where the $m_J = -\frac{1}{2}$ state of $5\,^2\mathrm{S}_{1/2}$ only sees the potential $V_-(z,\theta)$,

[16]The AC Stark shift of the ground-state level $i$ of a multilevel atom has the form $\Delta E_i = \frac{3\pi c^2 \gamma_e}{2\omega_0^3} I \sum_j \frac{b_{ij}^2}{\delta_{ij}}$, where $b_{ij}$ is the transition coefficient and $\delta_{ij}$ is the detuning between the level $i$ and an excited state level $j$ [143].

and the $m_J = +\frac{1}{2}$ state of $5\,^2\mathrm{S}_{1/2}$ only sees the potential $V_+(z,\theta)$.

The trapped Zeeman sublevels of $5\,^2\mathrm{S}_{1/2}$,[17]

$$|JIFm_F\rangle = \sum_{m_J,m_I} c_{J,I,F,m_J,m_I,m_F}|JIm_Jm_I\rangle, \tag{3.27}$$

where $m_I$ is the secondary nuclear spin quantum number, feel potentials that depend on the Clebsch–Gordan coefficients $c_{J,I,F,m_J,m_I,m_F} = \langle JIFm_F|JIm_Jm_I\rangle$ [151].[18] For example, the Zeeman state $|1\rangle = |F=2, m_F=-2\rangle$[19] has the Clebsch-Gordan coefficient $\left\langle F=2, m_F=-2\middle|m_J=-\frac{1}{2}, m_I=-\frac{3}{2}\right\rangle = 1$, i.e., $|1\rangle = \left|m_J=-\frac{1}{2}, m_I=-\frac{3}{2}\right\rangle$. As another example, the Zeeman state $|0\rangle = |F=1, m_F=-1\rangle$ has two non-zero the Clebsch-Gordan coefficients given by $\left\langle F=1, m_F=-1\middle|m_J=\frac{1}{2}, m_I=-\frac{3}{2}\right\rangle = \sqrt{\frac{3}{4}}$ and $\left\langle F=1, m_F=-1\middle|m_J=-\frac{1}{2}, m_I=-\frac{1}{2}\right\rangle = -\frac{1}{2}$, meaning that we have the expansion $|0\rangle = \sqrt{\frac{3}{4}}\left|m_J=\frac{1}{2}, m_I=-\frac{3}{2}\right\rangle - \frac{1}{2}\left|m_J=-\frac{1}{2}, m_I=-\frac{1}{2}\right\rangle$. The AC Stark shift of a Zeeman sublevel is given by the weighted sum of the light shifts of the $|m_J, m_I\rangle$ states with weights given by $|c_{J,I,F,m_J,m_I,m_F}|^2$ [152]. The spin-dependent potentials for the states $|1\rangle$ and $|0\rangle$ are thus given by $V_1(z,\theta) = V_-(z,\theta)$ and $V_0(z,\theta) = \frac{3}{4}V_+(z,\theta) + \frac{1}{4}V_-(z,\theta)$, respectively [148, 151].

These kinds of state-dependent potentials have applications in quantum information science as they allow, e.g., the creation of entangling two-qubit gates and multiqubit cluster states with neutral atoms via controlled atom-atom collisions [149–151]. Shifting the two lattices with respect to each other by varying $\theta$ also allows tuning the on-site interaction strength between the atoms by changing the spatial overlap of the wave functions of the atoms. This is an alternative to using Feshbach resonances to tune the $s$-wave scattering length [147]. In the context

[17] We point out that the spin-dependent optical lattices in Refs. [148, 149] were manipulated in a weak magnetic field of 1 G, in which case $F$ and $m_F$ are good quantum numbers.

[18] The Clebsch–Gordan coefficients can be obtained from the formula [153]

$$c_{J,I,F,m_J,m_I,m_F} = \langle JIFm_F|JIm_Jm_I\rangle = (-1)^{J-I+m_F}\sqrt{2F+1}\begin{pmatrix} J & I & F \\ m_J & m_I & -m_F \end{pmatrix},$$

where the matrix term on the right is the Wigner 3-$j$ symbol.

[19] We leave the fixed quantum numbers $J = \frac{1}{2}$ and $I = \frac{3}{2}$ of the level $5\,^2\mathrm{S}_{1/2}$ out of the notation.

of quantum simulation, spin-dependent optical lattices have been used for example for investigating the coexistence of Mott-insulating and superfluid phases [154] and studying many-body spin Hamiltonians with ultracold atoms [155]. See, e.g., Refs. [147–151] for further details on state-dependent optical lattices for bosonic atoms.

#### 3.2.6.3 Spin-dependent optical lattices for fermions

Spin-dependent optical lattices for fermionic alkali metal atoms can in principle be created using the same lin-$\theta$-lin configuration and the same couplings between the ground-state level $\bar{n}\,^2\mathrm{S}_{1/2}$ and the excited state levels $\bar{n}\,^2\mathrm{P}_{1/2}$ and $\bar{n}\,^2\mathrm{P}_{3/2}$ as in the case of bosonic atoms in Section 3.2.6.2 [152]. By again choosing the laser frequency conveniently between the resonant frequencies of the $D_1$ and $D_2$ transitions, it is possible to make the AC Stark shifts for the $m_J = -\frac{1}{2}$ state of $\bar{n}\,^2\mathrm{S}_{1/2}$ with $\boldsymbol{\sigma}^+$ polarized light and the $m_J = +\frac{1}{2}$ state of $\bar{n}\,^2\mathrm{S}_{1/2}$ with $\boldsymbol{\sigma}^-$ polarized light equal to zero. At this frequency, the $m_J = -\frac{1}{2}$ state of $\bar{n}\,^2\mathrm{S}_{1/2}$ only sees the potential $V_-(z,\theta)$, and the $m_J = +\frac{1}{2}$ state of $\bar{n}\,^2\mathrm{S}_{1/2}$ only sees the potential $V_+(z,\theta)$. The potentials felt by the Zeeman sublevels $|F, m_F\rangle$, e.g., $\left|F = \frac{9}{2}, m_F = \frac{9}{2}\right\rangle$ and $\left|F = \frac{9}{2}, m_F = \frac{7}{2}\right\rangle$ of the $F = \frac{9}{2}$ hyperfine level of the ground-state $4\,^2\mathrm{S}_{1/2}$ in the case of $^{40}$K, are again obtained by calculating the Clebsch–Gordan coefficients [152].

However, there is an important *practical* limitation with this method when it comes to $^6$Li and $^{40}$K. The intrinsic problem is the heating of the system by spontaneous emission. It is caused by the very small fine-structure splitting $\delta_{\mathrm{FS}}$ in $^6$Li and $^{40}$K ($\delta_{\mathrm{FS,Li}} = 0.01$ THz and $\delta_{\mathrm{FS,K}} = 1.73$ THz ) [86]. For standard optical lattices the heating issue can be remedied by detuning the laser further away from the resonances, since the rate of spontaneous emission scales as $1/\delta^2$ as compared to the $1/\delta$ scaling of the conservative dipole potential [143]. This trick is not possible for the spin-dependent potential since the laser frequency needs to be tuned between the $D_1$ and $D_2$ lines. Due to the small $\delta_{\mathrm{FS}}$ in $^6$Li and $^{40}$K, the detuning

is not far off resonance and the rate of spontaneous emission remains significant. This heating by spontaneous emission due to a small fine-structure splitting is the reason why spin-dependent optical lattices have not been realized experimentally with $^6$Li and $^{40}$K using the standard method [156]. In comparison, for example with $^{87}$Rb the heating appears to be less of a problem due to a larger fine-structure splitting ($\delta_{\mathrm{FS,Rb}} = 7.12$ THz) [86, 152].

Spin-dependent lattices have, however, been created with $^{40}$K by using a different strategy [156]. By applying a magnetic field gradient which is sinusoidally modulated in time, one can create an oscillating spin-dependent force acting on the atoms in the lattice. Using Floquet theory, one can show that this then leads to an effective spin-dependent hopping parameter [156].

Other proposed means to obtain spin-dependent lattices for fermionic atoms include relying on, e.g., alkaline-earth and alkaline-earth-like atoms [157–159]. Another possibility could be mixtures of atoms with different masses [160].

#### 3.2.6.4 Optical superlattices

Optical superlattices[20] can be created by superimposing two standing wave laser fields of different wavelengths. For instance, superimposing two standing waves created with lasers of wavelengths $\lambda_L$ and $\lambda_L/2$ realises a superlattice potential of the form $V_{\mathrm{super}}(x) = V_{0,\lambda_L} \sin^2(2\pi x/\lambda_L) + V_{0,\lambda_L/2} \sin^2(4\pi x/\lambda_L)$ (in 1D) that mimics an array of asymmetrical double wells [161, 162], as depicted in Fig. 3.6. Optical superlattices have been used experimentally in quantum simulation, e.g., in studying quantum magnetism with both bosonic [162, 163] and fermionic [164] atoms, and as well as in studying the time-evolution of fermionic systems after different parameter quenches [165].

[20] The terminology for these kinds of optical lattices originates from solid-state physics where a superlattice refers to a periodic structure of material layers consisting of two or more materials. The different materials break the usual period of a lattice of a single material, and thus more complex lattice potentials can be created this way.

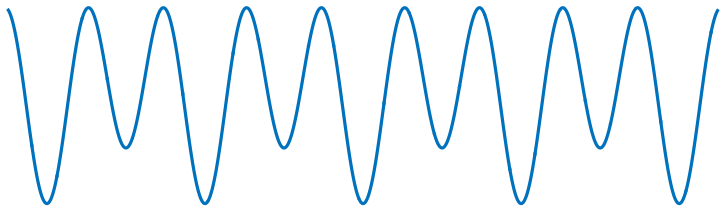

Figure 3.6: Schematic representation of a superlattice mimicking an array of asymmetrical double wells.

In this thesis, we study the spin-asymmetric Josephson effect in a spin-dependent optical superlattice of fermionic atoms that mimics an array of spin-dependent double wells. In 1D, this kind of potential has the form $V^{\sigma}_{\mathrm{super}}(x) = V^{\sigma}_{0,\lambda_L} \sin^2\left(\frac{2\pi x}{\lambda_L}\right) + V^{\sigma}_{0,\lambda_L/2} \sin^2\left(\frac{4\pi x}{\lambda_L}\right)$ (see Fig. 4.8 for an illustration). Spin-dependent superlattices have been realized with bosons (see, e.g., Ref. [166]), but not yet with fermions.

# Chapter 4

## Spin-asymmetric Josephson effect in ultracold Fermi gases

In this Chapter, we describe the so-called spin-asymmetric Josephson effect, and present two ultracold Fermi gas setups, possibly realizable with present-day or near-future technology, where the phenomenon could manifest.

## 4.1 Introduction

In Section 3.2.5, we introduced the Josephson effect which has been observed in various contexts, including in ultracold atom systems which act as analogue quantum simulators of solid-state Josephson junctions. The unprecedented control and tunability of parameters and individual degrees of freedom that are achievable in ultracold atomic gas setups offer also the possibility to consider going beyond the standard Josephson phenomenon.

In this Chapter, we study the proposed 'spin-asymmetric' Josephson effect [36, 37] in the context of ultracold Fermi gases. In this effect, the Cooper-paired spin-$\frac{1}{2}$ particles undergo frequency-synchronized AC Josephson oscillations with spin-dependent critical currents in the presence of spin-dependent 'voltages' across the Josephson junction. The fact that the spin components contribute asymmetrically to the Josephson current shows that the standard description of the Josephson effect in terms of bosonic pair tunnelling is insufficient. We emphasize that the spin-

asymmetric Josephson effect is conceptually general and as such not only restricted to ultracold atoms. In Chapter 5, we discuss possible solid-state setups, the analogue quantum simulators of which these ultracold Fermi gas systems could be.

The structure of this Chapter is the following. In Section 4.2, we first describe the original four-component Fermi gas setup for the phenomenon for completeness and give the expressions for the spin-asymmetric Josephson currents. We then describe the conceptually analogous spin-dependent double well setup. We also explain the physical origin of the asymmetry. We then study the Josephson plasma oscillation regime [38] in the double well setup as a possible means to realize the effect with present-day tools and techniques. In Section 4.3, we show using TEBD that the spin-asymmetric Josephson-like currents are present in the dynamics of an ultracold two-component Fermi gas in a one-dimensional spin-dependent optical superlattice. A summary of the results of this Chapter is given in Section 4.4. In Appendix B, we show how the explanation of the physical origin of the asymmetric Josephson currents generalises to a non-momentum conserving coupling. We present a brief description of the TEBD numerical method in Appendix C and some further calculation details in Appendix D.

The spin-dependent double well setup and the plasma oscillation results have been published in Ref. [1]. The spin-dependent superlattice arrangement and the TEBD results have been published in Ref. [2].

## 4.2 Josephson effect in the presence of spin-dependent potentials

### 4.2.1 Internal Josephson effect in a four-component Fermi gas

#### 4.2.1.1 Setup

In Refs. [36, 37], the setup for the spin-asymmetric Josephson effect was given in terms of a four-component[1] Fermi gas where the first two components ($|1\rangle$ and $|2\rangle$)

[1] Here component refers to a hyperfine level of an atom.

form a spatially coexisting superfluid with the superfluid of the other two components ($|3\rangle$ and $|4\rangle$). Transitions between the internal levels of the superfluids are induced by a radio-frequency (RF) field, and the detuning of the RF field with respect to the atomic transitions acts as an effective spin-dependent potential. The studied phenomenon is then the internal Josephson effect. Here, we give an outline of the four-level setup and the linear response calculations for completeness. Further details can be found in Ref. [167] and in the Supplemental Material of Ref. [37].

In the absence of tunnelling couplings and additional potentials, the system is described by the Hamiltonian [37]

$$\begin{aligned}\hat{H}_0 = &\int d\mathbf{r} \sum_{j=1}^{4} \left[\hat{\psi}_j^\dagger(\mathbf{r}) \left(-\frac{\nabla^2}{2m} - \mu_j\right) \hat{\psi}_j(\mathbf{r})\right] \\ &+ \frac{1}{2} \int d\mathbf{r_1} \int d\mathbf{r_2} \sum_{i \neq j} U_{ij}(\mathbf{r_1}, \mathbf{r_2}) \hat{\psi}_i^\dagger(\mathbf{r_1}) \hat{\psi}_j^\dagger(\mathbf{r_2}) \hat{\psi}_j(\mathbf{r_2}) \hat{\psi}_i(\mathbf{r_1}),\end{aligned} \tag{4.1}$$

where $\hat{\psi}_j^\dagger(\mathbf{r})$ ($\hat{\psi}_j(\mathbf{r})$) is a field operator that creates (annihilates) a fermion in the state $|j\rangle$ at position $\mathbf{r}$ with chemical potential $\mu_j$. Consistent with dilute superfluid atomic Fermi gases, we assume an attractive contact interaction, $U_{ij}(\mathbf{r_1}, \mathbf{r_2}) = g_{ij}\delta(\mathbf{r_1} - \mathbf{r_2})$, between particles in the states $|1\rangle$ and $|2\rangle$, and between particles in the states $|3\rangle$ and $|4\rangle$. Here, $\delta(\mathbf{r})$ is the Dirac delta function in 3D and $g_{ij} = \frac{4\pi}{m} a_{ij} < 0$, where $m$ is the mass of the particles and $a_{ij}$ is the 3D $s$-wave scattering length for collisions between atoms in the states $|i\rangle$ and $|j\rangle$. As is customary with ultracold fermions, we give the interaction in terms of the dimensionless parameter $k_F a_{ij}$ as $g_{ij} = \frac{8}{3\pi} k_F a_{ij} \frac{E_F}{n}$. Here, $E_F = (3\pi^2 n)^{2/3}/2m$ denotes the Fermi energy[2] and $n$ the total particle number density.

[2]We point out that in the context of ultracold Fermi gases, the Fermi energy is defined via $E_F = (3\pi^2 n)^{2/3}/2m$ (for a homogeneous gas) also in the case of finite temperatures and interacting systems. Note that in the presence of interactions, this definition of $E_F$ does not coincide with the chemical potential at $T = 0$ [28].

To induce Josephson currents in the system, we assume that at time $t = 0^+$ we switch on a weak RF coupling described by the Hamiltonian [37]

$$\hat{H}_\Omega = \Omega_{13} \int d\mathbf{r}\, \hat{\psi}_1^\dagger(\mathbf{r})\hat{\psi}_3(\mathbf{r}) + \text{H.c.} \\ + \Omega_{24} \int d\mathbf{r}\, \hat{\psi}_2^\dagger(\mathbf{r})\hat{\psi}_4(\mathbf{r}) + \text{H.c.}, \tag{4.2}$$

where $\Omega_{ij}$ is the coupling strength. Note that the states $|1\rangle$ and $|3\rangle$, and $|2\rangle$ and $|4\rangle$ need to be states of the same atom to allow the RF coupling, but $|1\rangle$ and $|2\rangle$ can correspond to hyperfine levels of different atomic species, e.g., $^6$Li and $^{40}$K.

Furthermore, an additional spin-dependent potential $\delta_{ij}$, corresponding to the detunings of the RF fields, is applied across the junction at time $t = 0^+$. In the rotating-wave approximation, this is described by the Hamiltonian [37]

$$\hat{H}_\delta = \int d\mathbf{r}\, \left[ \left( \mu_1 - \frac{\delta_{13}}{2} \right) \hat{\psi}_1^\dagger(\mathbf{r})\hat{\psi}_1(\mathbf{r}) + \left( \mu_3 + \frac{\delta_{13}}{2} \right) \hat{\psi}_3^\dagger(\mathbf{r})\hat{\psi}_3(\mathbf{r}) \right] \\ + \int d\mathbf{r}\, \left[ \left( \mu_2 - \frac{\delta_{24}}{2} \right) \hat{\psi}_2^\dagger(\mathbf{r})\hat{\psi}_2(\mathbf{r}) + \left( \mu_4 + \frac{\delta_{24}}{2} \right) \hat{\psi}_4^\dagger(\mathbf{r})\hat{\psi}_4(\mathbf{r}) \right]. \tag{4.3}$$

For the reason why the chemical potentials are included also in this Hamiltonian, see Section 10.4.1 in Ref. [168] and Section 8.6 in Ref. [67].[3] For our purposes, we can just regard it as a mathematical 'trick' to aid the calculations [37]. We take $\delta_{ij}$ to be smaller than the excitation gap $2\Delta$, so that the potentials do not induce pair breakings.

The total Hamiltonian of the system thus reads

$$\hat{H} = \hat{H}_0 + \hat{H}_\Omega + \hat{H}_\delta. \tag{4.4}$$

The reason for splitting the Hamiltonian in Eq. (4.4) into three parts is that the Josephson current is calculated treating $\hat{H}_\Omega$ as the first order perturbation in linear response theory while separating $\hat{H}_\delta$ from $\hat{H}_0$ allows taking two simple BCS superfluids as the unperturbed initial state [37].

[3] Briefly, since the chemical potentials can in general be different across the junction (i.e., for a BCS state we require $\mu_1 = \mu_2$ and $\mu_3 = \mu_4$, but we can have $\mu_1 \neq \mu_3$), the total Hamiltonian for the Josephson effect needs to measure energies on an absolute scale rather than relative to the chemical potentials. The chemical potentials needed for BCS theory are then introduced by adding and substracting terms of the form $\mu_j N_j$ (which then sum up to zero) in the total Hamiltonian [67,168]. Note that the chemical potentials in Eqs. (4.1) and (4.3) have opposite signs.

#### 4.2.1.2 Josephson currents

We are interested in the Josephson currents in the presence of the spin-dependent potentials. We present a linear response theory calculation of the currents which follows closely Refs. [37, 168] and the Ambegaokar–Baratoff treatment [67, 169] of the Josephson effect. The starting point of the calculation is the Heisenberg equation of motion for the total particle number in, e.g., state $|1\rangle$ given by

$$\dot{\hat{N}}_{1,H}(t) = \mathrm{i} \int d\mathbf{r} \, \left[ \hat{H}, \hat{\psi}^{\dagger}_{1,H}(\mathbf{r},t) \hat{\psi}_{1,H}(\mathbf{r},t) \right] . \tag{4.5}$$

Here, the dot on the left hand side denotes time derivative, and the sub-index $H$ implies that the operator is in the Heisenberg picture. Only the Hamiltonian $\hat{H}_{\Omega,H}$ fails to commute with the number operator, yielding

$$\begin{aligned} \dot{\hat{N}}_{1,H}(t) &= \mathrm{i} \int d\mathbf{r} \, \left[ \hat{H}_{\Omega,H}, \hat{\psi}^{\dagger}_{1,H}(\mathbf{r},t) \hat{\psi}_{1,H}(\mathbf{r},t) \right] \\ &= \mathrm{i} \int d\mathbf{r} \, \left( \Omega^{*}_{13} \hat{\psi}^{\dagger}_{3,H}(\mathbf{r},t) \hat{\psi}_{1,H}(\mathbf{r},t) - \Omega_{13} \hat{\psi}^{\dagger}_{1,H}(\mathbf{r},t) \hat{\psi}_{3,H}(\mathbf{r},t) \right) . \end{aligned} \tag{4.6}$$

We transform Eq. (4.6) into the interaction picture and insert it into the Kubo formula [67]

$$I_1(t) = \langle \dot{\hat{N}}_{1,I}(t) \rangle \approx -\mathrm{i} \int_0^t dt' \, \left\langle \left[ \dot{\hat{N}}_{1,I}(t), \hat{H}_{\Omega,I}(t) \right] \right\rangle_0 , \tag{4.7}$$

where the sub-index $I$ implies that the operator is in the interaction picture, and $\langle \rangle_0$ denotes the thermodynamic average with respect to the unperturbed Hamiltonian. As a result, we obtain the Josephson-contribution to the particle current as [37]

$$I_1^J(t) = \mathrm{i} \int_{-\infty}^{\infty} dt' \int d\mathbf{r} \int d\mathbf{r}' \, \left( e^{-\mathrm{i}\tilde{\delta}_{13} t} e^{-\mathrm{i}\tilde{\delta}_{24} t'} \Omega^{*}_{13} \Omega^{*}_{24} L_{1234}(\mathbf{r}t, \mathbf{r}t, \mathbf{r}'t', \mathbf{r}'t') - \mathrm{H.c.} \right) , \tag{4.8}$$

where $\tilde{\delta}_{ij} = \mu_i - \mu_j - \delta_{ij}$, and the retarded linear response function $L_{1234}$ is defined as [37]

$$L_{1234}(\mathbf{r}t, \mathbf{r}t, \mathbf{r}'t', \mathbf{r}'t') = -\mathrm{i}\theta(t-t') \left\langle \left[ \hat{\psi}^{\dagger}_3(\mathbf{r},t) \hat{\psi}_1(\mathbf{r},t), \hat{\psi}^{\dagger}_4(\mathbf{r}',t') \hat{\psi}_2(\mathbf{r}',t') \right] \right\rangle_0 . \tag{4.9}$$

Here, $\hat{\psi}_j^\dagger(\mathbf{r},t) = e^{\mathrm{i}\hat{H}_0 t}\hat{\psi}_j^\dagger(\mathbf{r})e^{-\mathrm{i}\hat{H}_0 t}$. Note that in Eq. (4.8) we have changed the temporal integration limits in the Kubo formula in Eq. (4.7) as $\int_{t_0}^{t} dt' \hookrightarrow \int_{-\infty}^{\infty} dt'$, which is justified since the perturbation $\hat{H}_\Omega$ vanishes for times $t' < 0$ and the linear response function in Eq. (4.9) is zero for times $t' > t$. The exponentials factors, $e^{-\mathrm{i}\tilde{\delta}_{13}t}$ and $e^{-\mathrm{i}\tilde{\delta}_{24}t'}$, in Eq. (4.8) arise from the transformations (for $t > 0$) [67,168]

$$\begin{aligned}
e^{\mathrm{i}(\hat{H}_0+\hat{H}_\delta)t}\hat{\psi}_1(\mathbf{r})e^{-\mathrm{i}(\hat{H}_0+\hat{H}_\delta)t} &= e^{-\mathrm{i}(\mu_1-\frac{\delta_{13}}{2})t}e^{\mathrm{i}\hat{H}_0 t}\hat{\psi}_1(\mathbf{r})e^{-\mathrm{i}\hat{H}_0 t},\\
e^{\mathrm{i}(\hat{H}_0+\hat{H}_\delta)t}\hat{\psi}_2(\mathbf{r})e^{-\mathrm{i}(\hat{H}_0+\hat{H}_\delta)t} &= e^{-\mathrm{i}(\mu_2-\frac{\delta_{24}}{2})t}e^{\mathrm{i}\hat{H}_0 t}\hat{\psi}_2(\mathbf{r})e^{-\mathrm{i}\hat{H}_0 t},\\
e^{\mathrm{i}(\hat{H}_0+\hat{H}_\delta)t}\hat{\psi}_3^\dagger(\mathbf{r})e^{-\mathrm{i}(\hat{H}_0+\hat{H}_\delta)t} &= e^{\mathrm{i}(\mu_3+\frac{\delta_{13}}{2})t}e^{\mathrm{i}\hat{H}_0 t}\hat{\psi}_3^\dagger(\mathbf{r})e^{-\mathrm{i}\hat{H}_0 t},\\
e^{\mathrm{i}(\hat{H}_0+\hat{H}_\delta)t}\hat{\psi}_4^\dagger(\mathbf{r})e^{-\mathrm{i}(\hat{H}_0+\hat{H}_\delta)t} &= e^{\mathrm{i}(\mu_4+\frac{\delta_{24}}{2})t}e^{\mathrm{i}\hat{H}_0 t}\hat{\psi}_4^\dagger(\mathbf{r})e^{-\mathrm{i}\hat{H}_0 t}.
\end{aligned} \tag{4.10}$$

Since the $\hat{H}_0$ does not depend on time, the linear response function $L_{1234}$ depends only on $\bar{t} = t - t'$, instead of $t$ and $t'$ separately [37,70,167]. Moreover, in a homogeneous system $L$ is a function of $\mathbf{r} - \mathbf{r}'$ [37,70,167]. Thus, we can write Eq. (4.8) as

$$I_1^J(t) = \mathrm{i}\left(\int_{-\infty}^{\infty} d\bar{t}\int d\mathbf{r}\int d\mathbf{r}'\, e^{-\mathrm{i}(\tilde{\delta}_{13}+\tilde{\delta}_{24})t}e^{\mathrm{i}\tilde{\delta}_{24}\bar{t}}\Omega_{13}^*\Omega_{24}^* L_{1234}(\mathbf{r}-\mathbf{r}',\bar{t}) - \mathrm{H.c.}\right). \tag{4.11}$$

We can identify the spatial integrations as a Fourier transform at zero momentum $\mathbf{p} = \mathbf{0}$ [37,167], and the integral over $\bar{t}$ as a temporal Fourier transform at frequency $\omega = \tilde{\delta}_{24} + \mathrm{i}0^+$ [37,167], where the infinitesimal imaginary part ensures convergence of the integral [67,70]. We therefore obtain the expression for the Josephson current as [37]

$$I_1^J(t) = -2\,\mathrm{Im}\Big[e^{-\mathrm{i}\left(\tilde{\delta}_{13}+\tilde{\delta}_{24}\right)t}\Omega_{13}^*\Omega_{24}^* L_{1234}\big(\mathbf{p}=\mathbf{0},\tilde{\delta}_{24}+\mathrm{i}0^+\big)\Big]. \tag{4.12}$$

Here, we have used the relation $\mathrm{i}(a + \mathrm{i}b - \mathrm{H.c.}) = -2b$, where $a + \mathrm{i}b$ is a complex number.

The linear response function in Eq. (4.12) can be calculated analytically in momentum and Matsubara space for example by utilising the so-called Kadanoff–Baym formalism [170,171], where the linear response function is obtained as a variational derivative of the single-particle Green function (here, the Nambu–Gor'kov

Green function) with respect to the coupling $\Omega_\sigma$. The details of the calculation of $L_{1234}$ with the Kadanoff–Baym method can be found in Refs. [37,167]. For the purposes of this Section, we give only the result. The expression for $L_{1234}$ is given by [37,167]

$$L_{1234}(\mathbf{p}, \mathrm{i}\omega_n) = -\Pi_{\mathcal{F}}(\mathbf{p}, \mathrm{i}\omega_n), \tag{4.13}$$

where [67]

$$\Pi_{\mathcal{F}}(\mathbf{p}, \mathrm{i}\omega_n) = \frac{1}{\beta} \sum_{\mathbf{q}, \mathrm{i}\omega_m} \mathcal{F}_{12}(\mathbf{q}, \mathrm{i}\omega_m) \mathcal{F}^{\dagger}_{34}(\mathbf{q}-\mathbf{p}, \mathrm{i}\omega_m - \mathrm{i}\omega_n). \tag{4.14}$$

In this expression, $\omega_n$ and $\omega_m$ denote fermionic Matsubara frequencies, and $\beta = \frac{1}{k_B T}$. Furthermore, $\mathcal{F}_{12}$ and $\mathcal{F}_{34}$ are anomalous Nambu–Gor'kov Green functions given by Eq. (3.12). We thus obtain an expression for the Josephson current in Eq. (4.12) as

$$I^J_{13}(t) = -I^C_{13}(\tilde{\delta}_{24}) \sin\left[\left(\tilde{\delta}_{13} + \tilde{\delta}_{24}\right) t - \varphi\right], \tag{4.15}$$

in which $\varphi$ is the initial phase difference, and the critical current reads

$$I^C_{13}(\tilde{\delta}_{24}) = 2\left|\Omega_{13}\Omega_{24}\Pi_{\mathcal{F}}(\mathbf{p}=\mathbf{0}, \tilde{\delta}_{24} + \mathrm{i}0^+)\right|. \tag{4.16}$$

Similarly, the Josephson current for component 2 is given by

$$I^J_{24}(t) = -I^C_{24}(\tilde{\delta}_{13}) \sin\left[\left(\tilde{\delta}_{13} + \tilde{\delta}_{24}\right) t - \varphi\right], \tag{4.17}$$

with

$$I^C_{24}(\tilde{\delta}_{13}) = 2\left|\Omega_{13}\Omega_{24}\Pi_{\mathcal{F}}(\mathbf{p}=\mathbf{0}, \tilde{\delta}_{13} + \mathrm{i}0^+)\right|. \tag{4.18}$$

These Josephson currents with a generic spin label are interpreted as the internal Josephson effect between the hyperfine levels of an atom [37]. We discuss these results further in the context of the spin-dependent double well in the next Section.

### 4.2.2 Josephson effect in a spin-dependent double well

#### 4.2.2.1 Setup

The four-component setup in Refs. [36, 37] requires finding a suitable combination of atomic hyperfine levels with which the creation of the two spatially coexisting BCS states with the appropriate RF couplings is possible. This is likely to be very challenging in practice. We therefore seek an alternative setup, possibly feasible with existing or near-future experimental techniques, to realize the spin-asymmetric Josephson effect.

Here, and in Ref. [1], we study the spin-asymmetric Josephson effect in terms of a two-component superfluid atomic Fermi gas (e.g., $^6$Li) which is spatially divided into two weakly connected reservoirs, $L$ and $R$, with chemical potentials $\mu_L$ and $\mu_R$, respectively. It forms an effective Josephson junction and is similar to the ones used in the observation of Josephson dynamics in $^6$Li [38] and in quantum transport experiments with $^6$Li [172–177]. This double well setup is conceptually analogous to the four-component one [37], with the following correspondences between the states

$$1 = \uparrow, L, \tag{4.19}$$

$$2 = \downarrow, L, \tag{4.20}$$

$$3 = \uparrow, R, \tag{4.21}$$

$$4 = \downarrow, R. \tag{4.22}$$

We write the Hamiltonian of the spin-dependent double well in momentum space in order to make the connection of the spin-asymmetric Josephson effect to the solid-state phenomena clearer in Chapter 5. In the absence of couplings and spin-dependent potentials, each well is described by the Hamiltonian

$$\hat{H}_{L/R} = \sum_{\mathbf{k},\sigma} \xi_{\mathbf{k},L/R} \hat{n}_{L/R,\mathbf{k},\sigma} + \frac{g}{V_s} \sum_{\mathbf{k},\mathbf{k}'} \hat{c}^\dagger_{L/R,\mathbf{k},\uparrow} \hat{c}^\dagger_{L/R,-\mathbf{k},\downarrow} \hat{c}_{L/R,-\mathbf{k}',\downarrow} \hat{c}_{L/R,\mathbf{k}',\uparrow}, \tag{4.23}$$

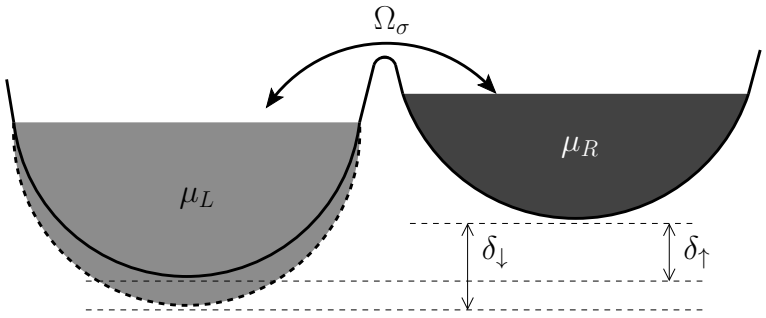


Figure 4.1: Schematic of a spin-dependent Josephson junction. A superfluid Fermi gas, e.g., $^6$Li, is divided into two reservoirs denoted by $L$ and $R$. The reservoirs are connected via the weak tunnelling coupling $\Omega_\sigma$ (we drop the momentum labels for simplicity), which induces Josephson oscillations across the junction. Additionally, a spin-dependent potential $\delta_\sigma$ is applied across the junction, which creates a spin-asymmetry in the Josephson current. Figure from Ref. [1].

where $\xi_{\mathbf{k},L/R} = \frac{|\mathbf{k}|^2}{2m} - \mu_{L/R}$, and $g = \frac{8}{3\pi} k_F a_s \frac{E_F}{n}$. We define $\hat{H}_0 = \hat{H}_L + \hat{H}_R$. The tunnelling Hamiltonian, which is switched on at $t = 0^+$, is given by

$$\hat{H}_\Omega = \sum_{\mathbf{k},\mathbf{p},\sigma} \Omega^\sigma_{\mathbf{k},\mathbf{p}} \left( \hat{c}^\dagger_{L,\mathbf{k},\sigma} \hat{c}_{R,\mathbf{p},\sigma} + \text{H.c.} \right). \tag{4.24}$$

Here, $\Omega^\sigma_{\mathbf{k},\mathbf{p}}$ is the tunnelling matrix element for spin $\sigma$ which couples the momentum states $\mathbf{k}$ and $\mathbf{p}$ on the left and right hand sides of the junction, respectively. The Hamiltonian for the spin-dependent potentials $\delta_\sigma$, also switched on at $t = 0^+$, reads

$$\hat{H}_\delta = \sum_{\mathbf{k},\sigma} \left[ \left( \mu_L - \frac{\delta_\sigma}{2} \right) \hat{n}_{L,\mathbf{k},\sigma} + \left( \mu_R + \frac{\delta_\sigma}{2} \right) \hat{n}_{R,\mathbf{k},\sigma} \right]. \tag{4.25}$$

The total Hamiltonian is again given by Eq. (4.4). See Fig. 4.1 for a schematic illustration of the double well system.

We now describe how the required spin-dependent potential $\delta_\sigma$ could potentially be achieved experimentally in the double well setup in two different ways by utilizing spin-dependent interactions. In an ultracold Fermi gas setup, the spin $\sigma = \uparrow, \downarrow$ corresponds to, e.g., the lowest two hyperfine levels of $^6$Li, $|\tilde{1}\rangle$ and $|\tilde{2}\rangle$ [these are not to be confused with the notation in Eqs. (4.19)–(4.22), hence the tilde], with,

e.g., $|\downarrow\rangle = |\tilde{1}\rangle$ and $|\uparrow\rangle = |\tilde{2}\rangle$, which features a Feshbach resonance at a magnetic field strength of 832 G [111].

Our first suggested implementation exploits a third spin component, e.g., atoms transferred via an RF pulse to the third lowest hyperfine level of $^6$Li, denoted by $|\tilde{3}\rangle$, introduced on one side of the junction. On the BCS side of the Feshbach resonance for the states $|\tilde{1}\rangle$ and $|\tilde{2}\rangle$, i.e., for magnetic fields above 832 G, the atoms in the state $|\tilde{3}\rangle$ interact differently with the atoms in $|\tilde{1}\rangle$ and $|\tilde{2}\rangle$ due to the different positions (at 690 G and 810 G) of the respective pairwise Feshbach resonances [111]. This allows utilizing the density and scattering-length dependent Hartree mean-field shift (see, e.g., Refs. [178,179]) to create a potential difference between the atoms in the states $|\tilde{1}\rangle$ and $|\tilde{2}\rangle$. The mean-field shift is given by $\Delta\delta_{\tilde{1}\tilde{2}} = \frac{4\pi}{m} n_{\tilde{3}}(a_{\tilde{1}\tilde{3}} - a_{\tilde{2}\tilde{3}})$, where $n_{\tilde{3}}$ is the number density of atoms in state $|\tilde{3}\rangle$, and $a_{\tilde{1}\tilde{3}}$ ($a_{\tilde{2}\tilde{3}}$) is the scattering length for collisions between atoms in states $|\tilde{1}\rangle$ ($|\tilde{2}\rangle$) and $|\tilde{3}\rangle$. In order to allow a lifetime on the order of a few hundred milliseconds against three-body recombinations in three-component Fermi gases, a low density $n_{\tilde{3}}$ on the order of $10^{10} - 10^{11}$ cm$^{-3}$ is required for the third spin component [180–182].

Our second proposal is based on the recent experimental realizations of Bose–Fermi superfluid mixtures [183–185]. In particular, we suggest to create a Bose–Fermi superfluid mixture where the bosonic atoms are either $^{87}$Rb or $^{133}$Cs, both of which feature broad Feshbach resonances with the $^6$Li spin components on the BCS side of the $|\tilde{1}\rangle - |\tilde{2}\rangle$ $^6$Li superfluid [186, 187]. This again allows utilizing different Hartree mean-field shifts to create a potential difference between the atoms in the states $|\tilde{1}\rangle$ and $|\tilde{2}\rangle$.

In both of the proposed schemes, as the two spin components $|\tilde{1}\rangle$ and $|\tilde{2}\rangle$ tunnel through the Josephson junction, the difference in the mean-field shifts, $\Delta\delta_{\tilde{1}\tilde{2}}$, creates the required spin-dependent potential difference $\delta_\sigma$ across the junction. Since the scattering lengths can be tuned and the number density can be controlled, this spin-dependent potential difference can be varied as well.

The required experimental tools for the double well with a spin-dependent potential have already been demonstrated with ultracold atoms. Thus, the arrangement that we propose can in principle be realized with existing techniques in ultracold atom systems, but more detailed descriptions of the possible experimental setup are not the focus of this work.

#### 4.2.2.2 Josephson currents

In the double-well system, the calculation of the Josephson currents follows the standard linear response treatment of the Josephson effect [67, 126, 169] with the difference that transformations similar to Eqs. (4.10)–(4.10) yield the Fourier transform (from time to frequency) of the linear response function to be evaluated at the spin-dependent potential. The Josephson current for spin ↑ can then be written as [67]

$$I_{\uparrow}^{J}(t) = -I_{\uparrow}^{C}(\tilde{\delta}_{\downarrow}) \sin\left[\left(\tilde{\delta}_{\uparrow} + \tilde{\delta}_{\downarrow}\right) t - \varphi\right], \tag{4.26}$$

with

$$I_{\uparrow}^{C}(\tilde{\delta}_{\downarrow}) = 2\left|\sum_{\mathbf{k},\mathbf{p}} \Omega_{\mathbf{k},\mathbf{p}}^{\uparrow} \Omega_{-\mathbf{k},-\mathbf{p}}^{\downarrow} \Pi_{\mathcal{F}}(\mathbf{k},\mathbf{p},\tilde{\delta}_{\downarrow} + \mathrm{i}0^{+})\right|. \tag{4.27}$$

Here, $\tilde{\delta}_{\sigma} = \mu_L - \mu_R - \delta_{\sigma}$, and $\Pi_{\mathcal{F}}$ is given by [67]

$$\Pi_{\mathcal{F}}(\mathbf{k},\mathbf{p},\mathrm{i}\omega_n) = \frac{1}{\beta}\sum_{\mathrm{i}\omega_m} \mathcal{F}_L(\mathbf{k},\mathrm{i}\omega_m)\mathcal{F}_R^{\dagger}(\mathbf{p},\mathrm{i}\omega_m - \mathrm{i}\omega_n). \tag{4.28}$$

Similarly the Josephson current for spin ↓ reads

$$I_{\downarrow}^{J}(t) = -I_{\downarrow}^{C}(\tilde{\delta}_{\uparrow}) \sin\left[\left(\tilde{\delta}_{\uparrow} + \tilde{\delta}_{\downarrow}\right) t - \varphi\right], \tag{4.29}$$

where

$$I_{\downarrow}^{C}(\tilde{\delta}_{\uparrow}) = 2\left|\sum_{\mathbf{k},\mathbf{p}} \Omega_{\mathbf{k},\mathbf{p}}^{\uparrow} \Omega_{-\mathbf{k},-\mathbf{p}}^{\downarrow} \Pi_{\mathcal{F}}(\mathbf{k},\mathbf{p},\tilde{\delta}_{\uparrow} + \mathrm{i}0^{+})\right|. \tag{4.30}$$

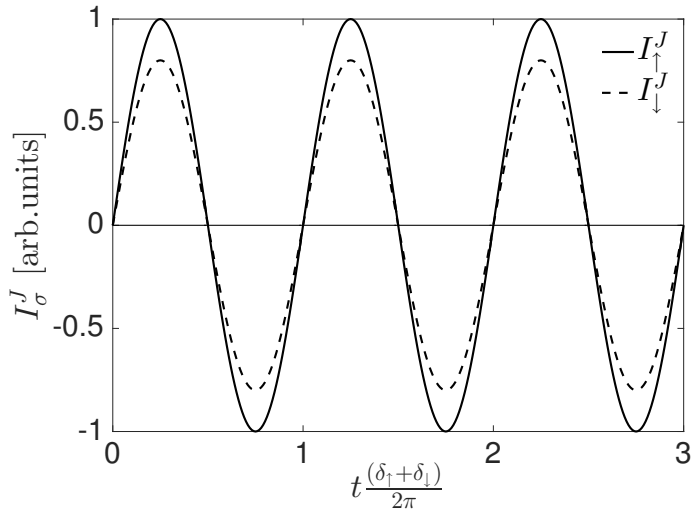


Figure 4.2: Schematic representation of the spin-asymmetric Josephson effect. The two spin components Josephson-oscillate with the same Josephson frequency, $\omega_J = \delta_\uparrow + \delta_\downarrow$, but the amplitude of the oscillations is different for the two spins.

We are now ready for a discussion. Note that in Eqs. (4.26)–(4.30) [and in Eqs. (4.15)–(4.18)] the critical current for the spin $\sigma$ component depends only on the potential $\tilde{\delta}_{\bar{\sigma}}$ of the opposite spin, while the Josephson frequency, $\omega_J = \tilde{\delta}_\uparrow + \tilde{\delta}_\downarrow$, is the same for both spin components. Therefore, when $\tilde{\delta}_\uparrow \neq \tilde{\delta}_\downarrow$, the Cooper-paired spin components undergo AC Josephson oscillations with the same Josephson frequency but with *spin-dependent amplitudes*, as schematically shown in Fig. 4.2. This is the spin-asymmetric Josephson effect. For typical parameter values, the asymmetry $I_\uparrow^C/I_\downarrow^C$ can be over ten per cent [37]. Moreover, the amplitudes and their asymmetry can be tuned with the spin-dependent potentials. Note also that even though these fully coherent Josephson oscillations are spin-dependent, there is no total equilibrium spin-imbalance in our system and the 'instantaneous spin-polarizations' induced by the spin-dependent currents are small (less than 0.01 and can furthermore be made arbitrarily small by changing the potentials). In addition, the linear response description of the phenomenon breaks down if the couplings $\Omega_\sigma$, and thus the currents, are too big. Thus, the currents and the spin-asymmetry can always be made small enough to justify the use of BCS theory. For these

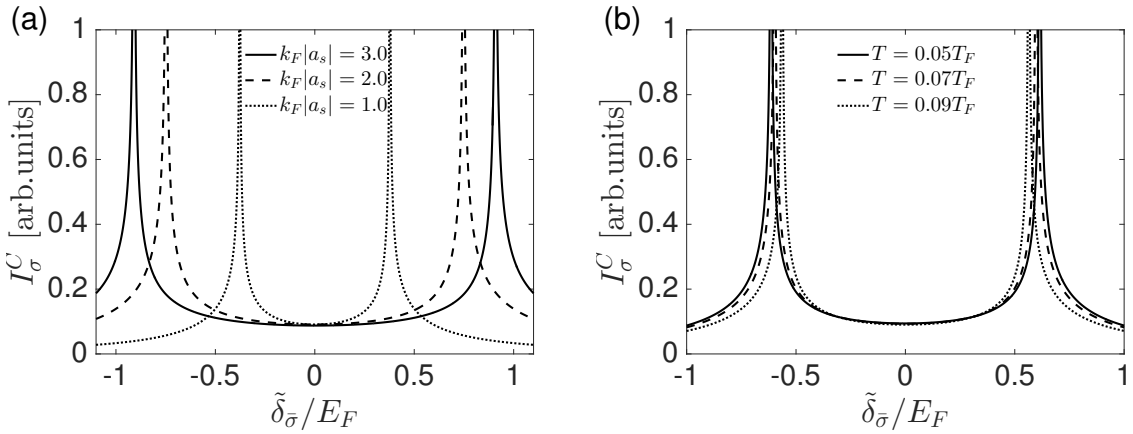


Figure 4.3: Critical Josephson current $I_\sigma^C$. We show $I_\sigma^C$ as a function of $\tilde{\delta}_{\bar{\sigma}}$ for (a) interaction $k_F a_s = -3.0$ (solid curve), $k_F a_s = -2.0$ (dashed curve), and $k_F a_s = -1.0$ (dotted curve) at temperature $T = 0.07T_F$, and (b) temperature $T = 0.05T_F$ (solid curve), $T = 0.07T_F$ (dashed curve), and $T = 0.09T_F$ (dotted curve) for interaction $k_F a_s = -1.5$. Here, $T_F$ denotes the Fermi temperature. The divergence of $I_\sigma^C$ at $\tilde{\delta}_{\bar{\sigma}} = 2\Delta$ is called the Riedel peak. Figure from Ref. [1].

reasons also the possibility, e.g., for equilibrium phase separation and for exotic Fulde–Ferrell–Larkin–Ovchinnikov (FFLO) [188, 189] type pairing is suppressed.[4] FFLO is furthermore unlikely to occur in the 3D case considered here [191–193]. Finally, we point out that in the DC case (i.e., $\omega_J = 0$) there is no spin-asymmetry in the critical currents.

We plot the critical current $I_\sigma^C$ as a function of $\tilde{\delta}_{\bar{\sigma}}$ for different interaction strengths $k_F a_s$ and various temperatures in Fig. 4.3. We clearly see that the critical current can be tuned by varying $\tilde{\delta}_{\bar{\sigma}}$. The critical current diverges at the Riedel peak [194] at the potential $\tilde{\delta}_{\bar{\sigma}} = 2\Delta$, where pair breakings occur. The Riedel peak is located at a potential equal to the minimum energy required for creating a quasiparticle excitation, i.e., $2\min_{\mathbf{k}} E_{\mathbf{k}} = 2\Delta$. The BCS quasiparticle density of states (DOS), $D(E_{\mathbf{k}}) = \frac{E_{\mathbf{k}}}{\sqrt{E_{\mathbf{k}}^2 - \Delta^2}}\theta(E_{\mathbf{k}} - \Delta)$ (given in proportion to the quasiparticle DOS in the normal state) [43], then has a singularity at the corresponding quasiparticle energy

[4] FFLO occurs in an equilibrium spin-imbalanced superfluid when the formation of Cooper pairs of non-zero centre-of-mass momentum $\mathbf{q}$ (due to the mismatch of Fermi surfaces of the two spin components) becomes energetically favorable. This leads to a spatially oscillating superfluid gap $\Delta(\mathbf{r}) \sim \cos(\mathbf{q} \cdot \mathbf{r})$. FFLO has yet to be observed. See, e.g., Ref. [190] for more details.

$E_{\mathbf{k}} = \Delta$, i.e., at the gap edge. This singular behaviour of $D(E_{\mathbf{k}})$ is the physical reason behind the Riedel peak [195].

### 4.2.3 Physical origin of the spin-asymmetric currents

The spin-asymmetric Josephson currents contradict the standard effective bosonic picture of the Josephson effect where Cooper pairs tunnel coherently without any difference in the currents for the two spin components. The explanation for the spin-asymmetry was provided in Ref. [37], where the physical origin of the asymmetric Josephson currents was identified by considering the dynamics of a single Cooper pair across the junction. We use the language of the spin-dependent double well for concreteness. The initial state of the system consists of two BCS states and is given by

$$|\Psi_0\rangle = \prod_{\mathbf{k}} \left(u_{\mathbf{k}} + v_{\mathbf{k}} \hat{c}^{\dagger}_{\mathbf{k},\uparrow} \hat{c}^{\dagger}_{-\mathbf{k},\downarrow}\right) |\emptyset\rangle_L \prod_{\mathbf{k}'} \left(u_{\mathbf{k}'} + v_{\mathbf{k}'} \hat{c}^{\dagger}_{\mathbf{k}',\uparrow} \hat{c}^{\dagger}_{-\mathbf{k}',\downarrow}\right) |\emptyset\rangle_R. \tag{4.31}$$

We now consider for simplicity a momentum-conserving coupling between the two wells. However, in Appendix B we show that the momentum conservation can be relaxed and the conclusions still hold. We thus single out one Cooper pair in each well for momentum $\mathbf{k}$, which yields

$$\begin{aligned} &(u_{\mathbf{k}}|\emptyset\rangle_{\mathbf{k},L} + v_{\mathbf{k}}|\uparrow\downarrow\rangle_{\mathbf{k},L}) (u_{\mathbf{k}}|\emptyset\rangle_{\mathbf{k},R} + v_{\mathbf{k}}|\uparrow\downarrow\rangle_{\mathbf{k},R}) \\ &= u^2_{\mathbf{k}}|\emptyset\rangle_{\mathbf{k},L}|\emptyset\rangle_{\mathbf{k},R} + v_{\mathbf{k}}u_{\mathbf{k}}|\uparrow\downarrow\rangle_{\mathbf{k},L}|\emptyset\rangle_{\mathbf{k},R} + u_{\mathbf{k}}v_{\mathbf{k}}|\emptyset\rangle_{\mathbf{k},L}|\uparrow\downarrow\rangle_{\mathbf{k},R} + v^2_{\mathbf{k}}|\uparrow\downarrow\rangle_{\mathbf{k},L}|\uparrow\downarrow\rangle_{\mathbf{k},L}. \end{aligned} \tag{4.32}$$

The Josephson effect must emerge from the superposition

$$v_{\mathbf{k}}u_{\mathbf{k}}|\uparrow\downarrow\rangle_{\mathbf{k},L}|\emptyset\rangle_{\mathbf{k},R} + u_{\mathbf{k}}v_{\mathbf{k}}|\emptyset\rangle_{\mathbf{k},L}|\uparrow\downarrow\rangle_{\mathbf{k},R},$$

since the empty state $|\emptyset\rangle_{\mathbf{k},L}|\emptyset\rangle_{\mathbf{k},R}$ cannot contribute, nor can the fully occupied state $|\uparrow\downarrow\rangle_{\mathbf{k},L}|\uparrow\downarrow\rangle_{\mathbf{k},L}$ due to Pauli blocking. Motivated by this observation, we take the relevant initial state for the dynamics to be a general superposition of the form

$$|\Psi_0\rangle = \alpha_0|\uparrow\downarrow\rangle_L|\emptyset\rangle_R + \beta_0|\emptyset\rangle_L|\uparrow\downarrow\rangle_R, \tag{4.33}$$

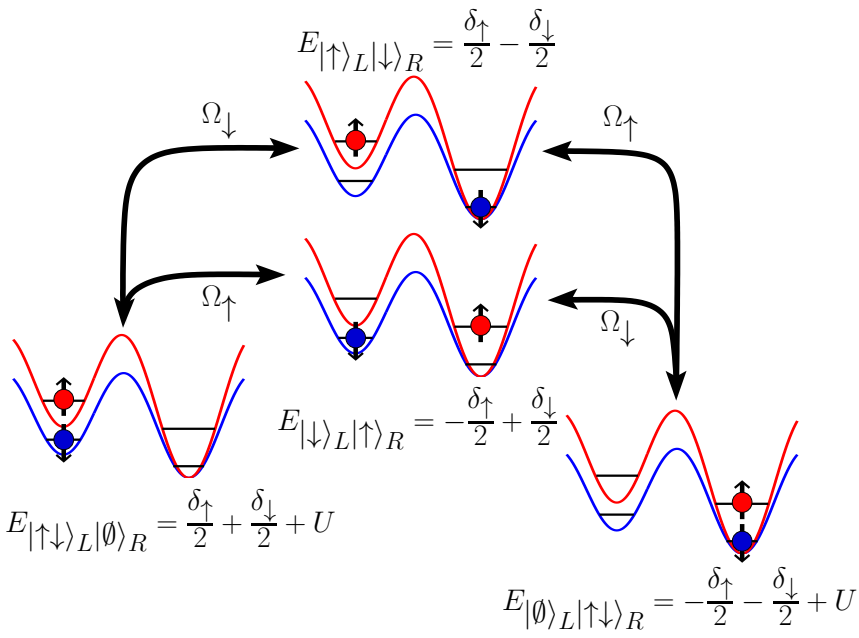


Figure 4.4: Energy levels and couplings of the four-state system described by the Hamiltonian in Eq. (4.34). Figure adapted from Ref. [2].

where $\alpha_0$ and $\beta_0$ are complex numbers with $|\alpha_0|^2 + |\beta_0|^2 = 1$. We consider the simplified system Hamiltonian

$$\begin{aligned}\hat{H} = U(\hat{n}_{\uparrow,L}\hat{n}_{\downarrow,L} + \hat{n}_{\uparrow,R}\hat{n}_{\downarrow,R}) + \frac{\delta_\uparrow}{2}(\hat{n}_{\uparrow,L} - \hat{n}_{\uparrow,R}) + \frac{\delta_\downarrow}{2}(\hat{n}_{\downarrow,L} - \hat{n}_{\downarrow,R}) \\ + \Omega_\uparrow(\hat{c}^\dagger_{\uparrow,R}\hat{c}_{\uparrow,L} + \hat{c}^\dagger_{\uparrow,L}\hat{c}_{\uparrow,R}) + \Omega_\downarrow(\hat{c}^\dagger_{R,\downarrow}\hat{c}_{\downarrow,L} + \hat{c}^\dagger_{\downarrow,L}\hat{c}_{\downarrow,R}),\end{aligned} \tag{4.34}$$

where $U$ is the interaction strength. The Hamiltonian in Eq. (4.34) has a close resemblance to the two-site Hubbard model with an additional spin-dependent potential $\delta_\sigma$.

As demonstrated in Ref. [37], the essential features of the spin-asymmetric Josephson effect can be captured by this simple toy model. The broken-pair 'intermediate' states, $|\uparrow\rangle_L|\downarrow\rangle_R$ and $|\downarrow\rangle_L|\uparrow\rangle_R$, are required to describe the tunnelling processes induced by the Hamiltonian in Eq. (4.34). If no spin-dependent potentials and couplings are present, these intermediate states have the same eigenenergy. However, the degeneracy is lifted by the spin-dependent potentials, as shown

in Fig. 4.4. It turns out that this is the key to understanding the origin of the spin-asymmetric phenomenon.

Time-dependent perturbation theory to second order in $\Omega_\sigma$ yields the Josephson current for spin $\sigma$ as [37]

$$\begin{aligned} I_\sigma^J(t) &= 2\Omega_\uparrow\Omega_\downarrow|\alpha_0\beta_0|\left(M_{\text{pair}} + M_{\text{single}}^\sigma\right)\sin\left[\left(\delta_\uparrow+\delta_\downarrow\right)t+\varphi\right] \\ &= 2\Omega_\uparrow\Omega_\downarrow|\alpha_0\beta_0|\left(\frac{1}{U+\delta_{\bar\sigma}}+\frac{1}{U-\delta_{\bar\sigma}}\right)\sin\left[\left(\delta_\uparrow+\delta_\downarrow\right)t+\varphi\right]. \end{aligned} \tag{4.35}$$

For the details of the calculation, see the Supplemental Material of Ref. [37]. Here,

$$M_{\text{pair}} = \frac{1}{U+\delta_\uparrow}+\frac{1}{U+\delta_\downarrow}. \tag{4.36}$$

This term results from second-order tunnelling processes starting from the state $|\emptyset\rangle_L|\uparrow\downarrow\rangle_R$ and ending in the state $|\uparrow\downarrow\rangle_L|\emptyset\rangle_R$ via either the state $|\uparrow\rangle_L|\downarrow\rangle_R$ or the state $|\downarrow\rangle_L|\uparrow\rangle_R$. Thus, $M_{\text{pair}}$ describes the usual pair interference process that is symmetric with respect to $\delta_\uparrow$ and $\delta_\downarrow$.

It turns out that there is also a contribution from two first-order processes that break the spin-symmetry. These processes yield the terms

$$M_{\text{single}}^\uparrow = \frac{1}{U-\delta_\downarrow}-\frac{1}{U+\delta_\uparrow}, \tag{4.37}$$

and

$$M_{\text{single}}^\downarrow = \frac{1}{U-\delta_\uparrow}-\frac{1}{U+\delta_\downarrow}, \tag{4.38}$$

which are different for the two spin components. The term $M_{\text{single}}^\uparrow$ is the result of the interference of the virtual broken-pair tunnelling processes $|\uparrow\downarrow\rangle_L|\emptyset\rangle_R \to |\uparrow\rangle_L|\downarrow\rangle_R$ and $|\emptyset\rangle_L|\uparrow\downarrow\rangle_R \to |\uparrow\rangle_L|\downarrow\rangle_R$, while $M_{\text{single}}^\downarrow$ emerges from the interference of the processes $|\uparrow\downarrow\rangle_L|\emptyset\rangle_R \to |\downarrow\rangle_L|\uparrow\rangle_R$ and $|\emptyset\rangle_L|\uparrow\downarrow\rangle_R \to |\downarrow\rangle_L|\uparrow\rangle_R$. Since the energy degeneracy of the intermediate states is lifted by the presence of the spin-dependent potentials, the virtual broken-pair tunnelling processes contribute asymmetrically to the Josephson current, and thus produce the spin-asymmetric Josephson effect.

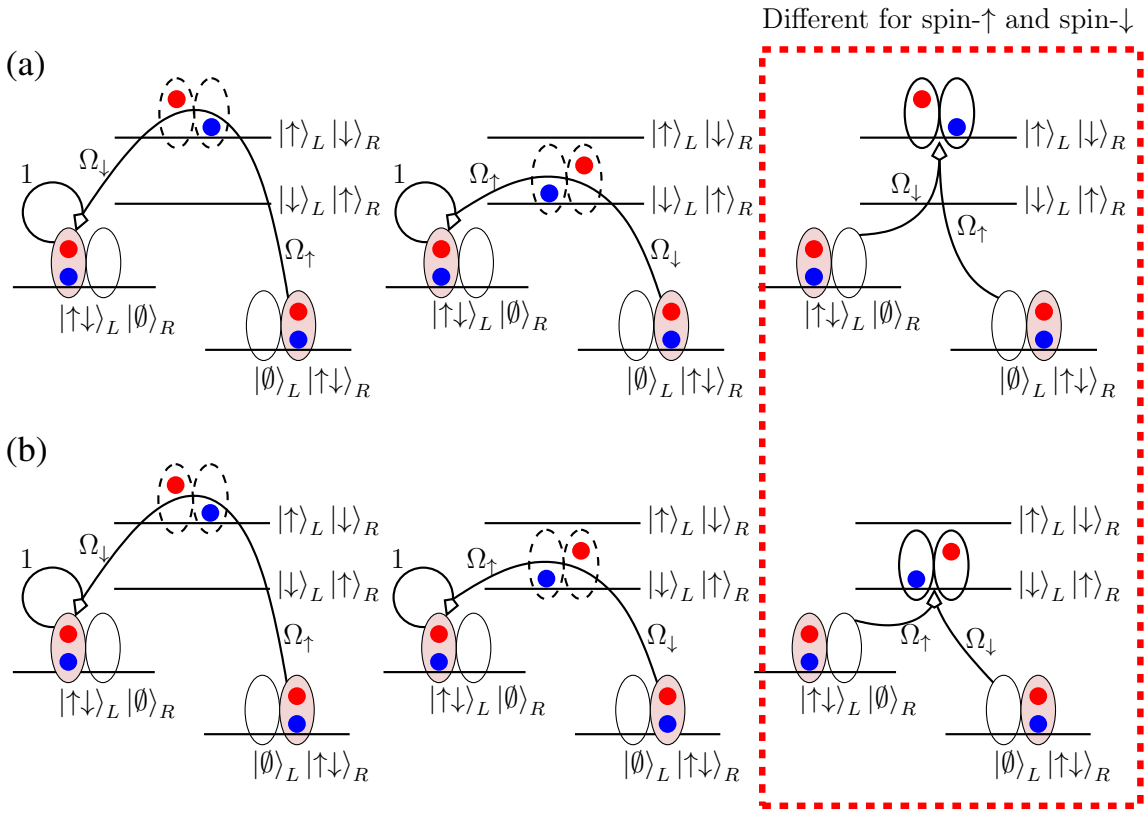


Figure 4.5: Physical origin of the spin-asymmetric critical currents. Considering the dynamics of a single Cooper pair across a Josephson junction with spin-dependent potentials, the Josephson current results from a superposition of the paired states, $|\uparrow\downarrow\rangle_L|\emptyset\rangle_R$ and $|\emptyset\rangle_L|\uparrow\downarrow\rangle_R$. Here, we show the tunnelling processes that contribute to (a) $I^J_\uparrow$ and to (b) $I^J_\downarrow$. The three processes are the following. First, there is a pair-tunnelling contribution via the intermediate state $|\uparrow\rangle_L|\downarrow\rangle_R$ (left panel). Second, there is another pair-tunnelling contribution via the other intermediate state $|\downarrow\rangle_L|\uparrow\rangle_R$ (middle panel). We have included the loop with label 1 to remind that these usual Josephson processes describe the interference between the tunnelled pair and the initial population (indicated by the label 1) of the state $|\uparrow\downarrow\rangle_L|\emptyset\rangle_R$. The pair-tunnelling processes are the same for both spin components. Finally, we find that there is also a virtual *single-particle interference* contribution (right panel). The single-particle interference term is different for the spin-↑ and spin-↓ components, as highlighted by the red rectangle, due to the presence of the spin-dependent potential which lifts the energy degeneracy of the intermediate states. This causes the spin-asymmetric Josephson effect. Figure adapted from Ref. [1].

However, note that the single-particle processes are present also in the standard symmetric case, $\delta_\uparrow = \delta_\downarrow$. We also emphasize that these virtual broken-pair tunnelling processes do not refer to the cosine-term (the 'quasiparticle interference

term') of the Josephson effect (see, e.g., Ref. [121]) which involves actual single-particle transitions and vanishes at zero temperature for potentials smaller than the excitation gap $2\Delta$. The different interference processes contributing to the Josephson current are depicted in Fig. 4.5.

### 4.2.4 Spin-asymmetric Josephson plasma oscillations

The observation of Josephson plasma oscillations throughout the BCS–BEC crossover has been reported in ultracold Fermi gases [38]. Here, and in Ref. [1], motivated by these experimental advances in Josephson dynamics, we consider the possibility to observe the spin-asymmetric Josephson effect via *spin-dependent plasma oscillations* in the setup in Section 4.2.2.

To begin the analysis, we introduce a spin-dependent number difference parameter $\Delta N_\sigma^J = \frac{1}{2}(\langle \hat{N}_{\sigma,L}^J \rangle - \langle \hat{N}_{\sigma,R}^J \rangle) = \frac{1}{2}(N_{\sigma,L}^J - N_{\sigma,R}^J)$, akin to the bosonic case [85] (see also Section 3.2.5). Here, $\hat{N}_{\sigma,L}^J$ ($\hat{N}_{\sigma,R}^J$) denotes the number operator for spin $\sigma$ particles on the left (right) reservoir that belong to the Fermi condensate and can thus contribute to the Josephson current. Using Eqs. (4.26) and (4.29) and the fact that $\partial_t N_{\sigma,L}^J = -\partial_t N_{\sigma,R}^J$, we find that the dynamics of $\Delta N_\sigma^J$ is obtained from

$$\frac{\partial \left(\Delta N_\sigma^J\right)}{\partial t} = -I_\sigma^C(\tilde{\delta}_{\bar{\sigma}}) \sin \Phi^J(t). \tag{4.39}$$

The Josephson phase $\Phi^J(t)$ obeys the equation of motion

$$\frac{\partial \Phi^J(t)}{\partial t} = \tilde{\delta}_\uparrow + \tilde{\delta}_\downarrow = 2(\mu_L - \mu_R) - \delta_\uparrow - \delta_\downarrow. \tag{4.40}$$

The spin-dependent critical Josephson current implies spin-dependent number oscillations also in the plasma oscillation regime. Following Ref. [85], we write Eq. (4.40) as

$$\frac{\partial \Phi^J(t)}{\partial t} = E_{\rm ch}^\uparrow \Delta N_\uparrow^J + E_{\rm ch}^\downarrow \Delta N_\downarrow^J - \delta_\uparrow - \delta_\downarrow, \tag{4.41}$$

where we have introduced the spin-dependent charging energy $E_{\rm ch}^\sigma = 2\frac{d\mu_{\sigma,L}}{dN_{\sigma,L}^J}$ which is evaluated at $N_{\sigma,L}^J = N_{\sigma,R}^J = N_\sigma^J/2$ [85].

For short times (but long enough to observe plasma oscillations), we can approximate $\sin\Phi^J(t) \approx \Phi^J(t)$ to obtain the coupled differential equations

$$\frac{\partial^2(\Delta N_\uparrow^J)}{\partial t^2} = -I_\uparrow^C(\tilde{\delta}_\downarrow)\left(E_{\rm ch}^\uparrow \Delta N_\uparrow^J + E_{\rm ch}^\downarrow \Delta N_\downarrow^J - \delta_\uparrow - \delta_\downarrow\right), \tag{4.42}$$

and

$$\frac{\partial^2(\Delta N_\downarrow^J)}{\partial t^2} = -I_\downarrow^C(\tilde{\delta}_\uparrow)\left(E_{\rm ch}^\uparrow \Delta N_\uparrow^J + E_{\rm ch}^\downarrow \Delta N_\downarrow^J - \delta_\uparrow - \delta_\downarrow\right). \tag{4.43}$$

The solution for spin $\sigma$ has the form

$$\Delta N_\sigma^J(t) = A_p^\sigma \sin(\omega_p t) + \Delta N_\sigma^J(0), \tag{4.44}$$

where the Josephson plasma frequency is given by $\omega_p = \sqrt{E_{\rm ch}^\uparrow I_\uparrow^C + E_{\rm ch}^\downarrow I_\downarrow^C}$. Note that in the spin-symmetric case, we have the standard formula $\omega_p = \sqrt{E_{\rm ch} E_J}$, where $E_J = I_\uparrow^C + I_\downarrow^C = I^C$ is the Josephson energy [38,85] (recall that $\hbar = 1$). As the plasma frequency is the same for both spin components, we leave its quantitative analysis for future work.

Similar to the full AC spin-asymmetric Josephson effect, we therefore find that the system undergoes frequency-synchronized Josephson plasma oscillations with *a spin-dependent amplitude*. The asymmetry in the amplitudes follows the relation

$$\frac{A_p^\uparrow}{A_p^\downarrow} = \frac{I_\uparrow^C(\tilde{\delta}_\downarrow)}{I_\downarrow^C(\tilde{\delta}_\uparrow)}. \tag{4.45}$$

Here we focus on the amplitude asymmetry.

The asymmetry given by Eq. (4.45) is limited by the requirement that the oscillations in the number density between the two reservoirs must be small. For the plasma oscillation approximation to be valid, the relative number difference, $z = \frac{N_L^J - N_R^J}{N_L^J + N_R^J}$, has to be on the order of a few per cent [38,135]. This gives an upper bound to the Josephson frequency, $\omega_J = \tilde{\delta}_\downarrow + \tilde{\delta}_\uparrow$, in the plasma oscillation regime. The maximal Josephson frequency then determines how much the asymmetry in

the plasma oscillation amplitudes can be tuned and how large asymmetries can be obtained.

To give an estimate of the upper bound for $\omega_J$, we assume for simplicity that there are no spin-dependent potentials across the junction. The Josephson dynamics is then induced only by the difference in the chemical potentials, with $\omega_J = 2(\mu_L - \mu_R)$. We want to express $\omega_J$ in terms of the relative number difference $z$, whose values corresponding to the plasma oscillation regime are known [38, 135]. Using the chemical potential for a non-interacting or a unitary[5] trapped Fermi gas, $\mu \propto N^{1/3}$ [38, 125], we find that the relative difference in the chemical potentials and in the particle numbers obey the relation $\zeta = (\mu_L - \mu_R)/(\mu_L + \mu_R) = z/3$, which yields the Josephson frequency as $\omega_J = 4\zeta\mu = \frac{4}{3}z\mu$, where we have denoted $\mu = \mu_L \approx \mu_R$. With the equation $\zeta = z/3$, we note that the relative chemical potential difference $\zeta$ across the junction can only be 1% for $z = 3\%$ and a barrier height of $1.2 \pm 0.1E_F$ between the reservoirs [38]. In [135], the critical value for $z$ was found to be on the order of 9% for a barrier height of $5E_F$, and thus $\zeta \approx 3\%$ in this case. In what follows, we use $\zeta = 3\%$ as the maximum relative difference in the chemical potentials to estimate the maximal Josephson frequency.

To get $\omega_J$, we need a value for the chemical potential $\mu$. In our simple case of a homogeneous Fermi gas, BCS mean-field theory (see Section 3.2.4) with the attractive interaction strength $k_F|a_s|$ between $1.0$ and $3.0$ and the temperature $T$ between $0.05T_F$ and $0.09T_F$, where $T_F$ is the Fermi temperature, yields a chemical potential between approximately $0.81E_F$ and $0.96E_F$. This implies that the maximal Josephson frequency corresponding to the plasma oscillation regime is around $\omega_J^{\max} \approx 0.11E_F$. Since the Josephson frequency is given only by the potential difference across the junction regardless of the type of the potential, as a first approach we take that this is the typical value for the maximal Josephson frequency also in the presence of spin-dependent potentials, which we now consider.

[5] For a unitary Fermi gas, $\mu = \xi_B E_F$, where $\xi_B$ is the so-called Bertsch parameter [114].

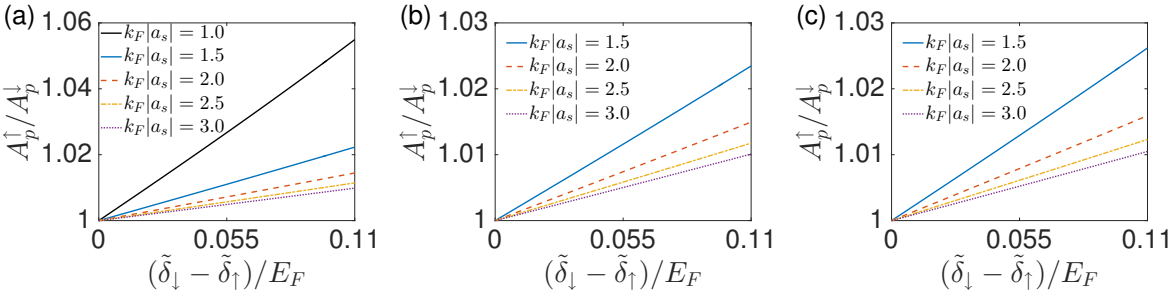


Figure 4.6: Asymmetry in the spin-dependent plasma oscillation amplitudes. The asymmetry is shown as a function of the difference in the spin-dependent potentials for Josephson frequency $\omega_J = 0.11E_F$ and interaction strength $k_F a_s = -1.0$ [black solid curve, only in (a)], $k_F a_s = -1.5$ (blue solid curve), $k_F a_s = -2.0$ (red dashed curve), $k_F a_s = -2.5$ (yellow dash dotted curve), and $k_F a_s = -3.0$ (purple dotted curve). The temperature is (a) $T = 0.05T_F$, (b) $T = 0.07T_F$, and (c) $T = 0.09T_F$. The temperature regime is the same as in the experiment in [38]. In (a), the $k_F a_s = -1.0$ curve is included as the reference line to the unitary Fermi gas regime. Figure from Ref. [1].

Using the estimated $\omega_J^{\max} = 0.11E_F$, we show in Fig. 4.6 the numerically obtained asymmetry in the plasma oscillation amplitudes given by Eq. (4.45) as a function of $\tilde{\delta}_{\downarrow} - \tilde{\delta}_{\uparrow}$ for different temperatures and various strengths of the attractive interaction in the typical regimes for an ultracold atom experiment. Note that we have used basic BCS equations in our calculations for simplicity, since we are interested only in the order of magnitude of the asymmetry. For the interaction strengths in Fig. 4.6, BCS theory roughly estimates the critical temperature to be between $0.13T_F$ and $0.36T_F$. In more accurate schemes [114] there would be some corrections to the BCS parameter values. For example, the critical temperature is suppressed by a factor of roughly two [119, 125]. For a unitary Fermi gas, the critical temperature has been measured to be about $0.17T_F$ [196]. We see in Fig. 4.6 that the asymmetry grows for weaker interactions and can reach over 2%. The asymmetry grows also with increasing temperature.

The behaviour of the asymmetry in the plasma oscillation amplitudes as a function of interaction strength and temperature is explained by the divergence of the critical Josephson current in Eqs. (4.27) and (4.30) at the Riedel peak [194] at

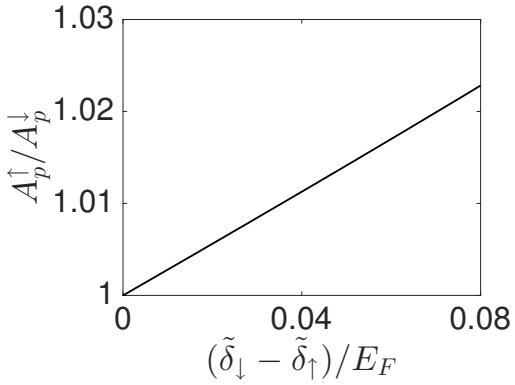


Figure 4.7: Asymmetry in the spin-dependent plasma oscillation amplitudes for experimental parameter values. The asymmetry is shown as a function of the difference in the spin-dependent potentials for parameter values obtained in the experiment in Ref. [124]. The Josephson frequency is $\omega_J = 0.08E_F$, the interaction strength is $k_F a_s = -4.0$, the temperature is $T = 0.06T_F$, and the gap is $\Delta = 0.22E_F$. Figure from Ref. [1].

$\tilde{\delta}_{\bar{\sigma}} = 2\Delta$. Since the gap $\Delta$ becomes smaller for weaker interactions and higher temperatures, the position of the Riedel peak moves closer to small frequencies, as shown in Fig. 4.3. Therefore, for decreasing interaction strength and increasing temperature it becomes easier to obtain greater asymmetries in the critical currents in the plasma oscillation regime and thus in the plasma oscillation amplitudes via Eq. (4.45).

We point out that since BCS theory overestimates the value of the superfluid gap in this interaction regime [114], the Riedel peak is actually closer to small frequencies than Fig. 4.3 suggests. Therefore, in reality we can expect even greater asymmetries than those shown in Fig. 4.6. To demonstrate this, we plot in Fig. 4.7 the asymmetry in the plasma oscillation amplitudes using the experimental value for the gap, $\Delta = 0.22E_F$, obtained for interaction strength $k_F a_s = -4.0$ and temperature $T = 0.06T_F$, as reported in Ref. [124]. This experimentally determined gap is roughly half of the gap given by simple BCS theory. We see in Fig. 4.7 that even with this strong attractive interaction, asymmetries of over 2% are feasible to obtain. Larger asymmetries can be expected for weaker interactions.

We note that the amplitude asymmetry is always a fraction of an already small Josephson plasma mode signal ($z = 3\%$ in Ref. [38]). This makes the detection of the asymmetry challenging for example with *in situ* absorption imaging. However, the evolution of the population imbalance can be mapped onto the center-of-mass (COM) displacement of the atom cloud [38] and its amplitude can be detected in a time-of-flight (TOF) expansion, as was already done in Ref. [38]. If the two spin components have different COM displacements, the asymmetric plasma oscillation amplitudes could be observed with the TOF method. For the parameter values in Ref. [38], a COM displacement of several tens of micrometers can be achieved and observed with a short TOF of duration less than 10 ms. This significantly increases the signal-to-noise ratio for detecting the asymmetry compared to *in situ* imaging.

## 4.3 Spin-asymmetric currents in a spin-dependent superlattice

### 4.3.1 Setup

Here, and in Ref. [2], we consider an alternative approach to realize spin-asymmetric Josephson-type currents, motivated partly by the observation of bosonic Josephson dynamics in 1D optical lattices [81] and superexhange interactions in an array of asymmetrical double wells [162]. With the TEBD numerical method (see, e.g., Refs. [63, 64, 197] and Appendix C), we computationally predict that spin-asymmetric Josephson-type oscillations take place within a single ultracold two-component Fermi gas between the odd and even sites of a 1D spin-dependent optical superlattice, where each pair of adjacent lattice sites mimics the spin-dependent double well in Fig. 4.1. See Fig. 4.8 for an illustration of the superlattice arrangement.

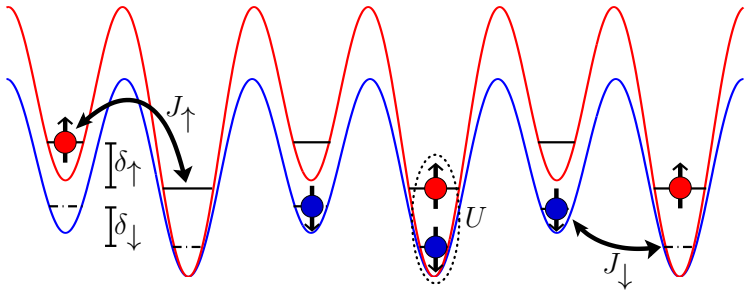


Figure 4.8: Spin-dependent superlattice setup to realize a spin-asymmetric Josephson-type effect. The ↑ spin (red ball) and ↓ spin (blue ball) tunnel between adjacent lattice sites with couplings $J_\uparrow$ and $J_\downarrow$, respectively. The spin-dependent potential difference between neighbouring sites is given by $\delta_\sigma$ and the on-site interaction strength by $U$. The observation of spin-asymmetric Josephson-type oscillations between adjacent lattice sites requires $\delta_\uparrow \neq \delta_\downarrow$. Figure from Ref. [2].

The system of Fig. 4.8 is described by the superlattice Hubbard Hamiltonian

$$\hat{H} = -\sum_{i,\sigma} J_\sigma(\hat{c}^\dagger_{i+1,\sigma}\hat{c}_{i,\sigma} + \text{H.c.}) + U\sum_i \hat{n}_{i,\uparrow}\hat{n}_{i,\downarrow} + \sum_{i,\sigma}\frac{\delta_\sigma}{2}(\hat{n}_{2i-1,\sigma} - \hat{n}_{2i,\sigma}). \tag{4.46}$$

The initial state of the system is the ground-state of the Hamiltonian at half-filling (i.e., $\langle\hat{n}_{i,\uparrow}\rangle = \langle\hat{n}_{i,\downarrow}\rangle = 0.5$) without a superlattice, i.e., $\delta_\uparrow = \delta_\downarrow = 0$.[6] Note that we keep the hopping non-zero. At time $t = 0^+$, the spin-dependent superlattice potential is switched on, resulting in $\delta_\uparrow \neq \delta_\downarrow$, and dynamics is induced. Here we focus on the dynamics of the system.

The spin-dependent potential $\delta_\sigma$ is the crucial control parameter in the superlattice setup. In the relevant region for the spin-asymmetric Josephson effect, $\delta_\sigma$

[6]The ground-state is obtained with TEBD using imaginary-time evolution. To see why imaginary-time evolution results in the ground-state $|\Psi_{\text{GS}}\rangle$ of the governing Hamiltonian $\hat{H}$, consider an initial state $|\Psi_{\text{init}}\rangle$ which has a non-zero overlap with $|\Psi_{\text{GS}}\rangle$, i.e., $\langle\Psi_{\text{GS}}|\Psi_{\text{init}}\rangle \neq 0$. The state $|\Psi_{\text{init}}\rangle$ can be expanded in the eigenbasis $\{|\Psi_j\rangle\}$ of $\hat{H}$ as $|\Psi_{\text{init}}\rangle = \sum_{j\geq 1}\alpha_j|\Psi_j\rangle$, where $\alpha_j = \langle\Psi_j|\Psi_{\text{init}}\rangle$. We choose $|\Psi_1\rangle = |\Psi_{\text{GS}}\rangle$. Then

$$\lim_{\tau\to\infty}\frac{e^{-\tau\hat{H}}|\Psi_{\text{init}}\rangle}{||e^{-\tau\hat{H}}|\Psi_{\text{init}}\rangle||} = \lim_{\tau\to\infty}\frac{\frac{\alpha_1}{|\alpha_1|}|\Psi_1\rangle + \sum_{j\geq 2}e^{-\tau(E_j-E_1)}\frac{\alpha_j}{|\alpha_1|}|\Psi_j\rangle}{\sqrt{1+\sum_{j\geq 2}e^{-2\tau(E_j-E_1)}\left|\frac{\alpha_j}{\alpha_1}\right|^2}} = \frac{\alpha_1}{|\alpha_1|}|\Psi_1\rangle = |\Psi_{\text{GS}}\rangle,$$

where $E_j$ is the eigenenergy of state $|\Psi_j\rangle$. Note that $\alpha_1/|\alpha_1| = e^{i\phi_1}$ is just a global phase factor for the ground-state.

ranges from zero to roughly $10J_\sigma$. In quantum gas experiments with deep optical lattices, the depth of the lattice potential is typically about $10E_R$ [28]. For such lattices the value of $J_\sigma$ estimated from Eq. (A.12) is on the order of $0.01E_R$, whereas the band gap between the two lowest energy bands is on the order of several recoil energies. Thus, the required values of $\delta_\sigma$ are more than an order of magnitude below the band gap and the depth of the lattice potential. As a result, the system is well described by the lowest-band Hubbard model of Eq. (4.46) also in the presence of the spin-asymmetric potential.

TEBD is well-suited for simulating the non-equilibrium real-time dynamics of the 1D superlattice as the Hamiltonian consists of only nearest-neighbour terms. We study a system with $L_s = 50$ lattice sites and matrix product state bond dimension $\chi = 150$. For simplicity, we consider here the case $J_\uparrow = J_\downarrow = J$, but we keep the spin index $\sigma$ present in equations for clarity. We give all energies and frequencies in the units of $J$ and focus on the attractive interaction $U = -10J$ (interactions in the range $-15J < U < -5J$ would give similar results). With $J$ and $U$ fixed, we study the Josephson-like currents as a function of the spin-dependent potentials $\delta_\sigma$.

With ultracold atoms, the superlattice can be constructed by superimposing two optical lattices generated with lasers of wavelengths $\lambda$ and $\lambda/2$, as described in Section 3.2.6.4. There are several possibilities to obtain the required spin-dependence. First, theoretical proposals suggest that it is possible to create state-dependent lattice potentials for alkaline-earth and alkaline-earth-like atoms (e.g., Yb [95], Sr [97, 98], Dy [99]) in two different internal states [157–159]. State-dependent optical lattices have also recently been experimentally realized with $^{40}$K [156]. Second, one could consider a mixture of fermionic atoms with different masses [198–201]. For instance, in the case of a $^6$Li-$^{40}$K mixture an experimentally suitable combination of states could be $|\uparrow\rangle = |F = 1/2, m_F = 1/2\rangle_{\mathrm{Li}}$ and $|\downarrow\rangle = |F = 9/2, m_F = 9/2\rangle_{\mathrm{K}}$ due

to the availability of a reasonably broad Feshbach resonance to tune the interactions [200]. The spin-dependent Hubbard model parametrization arises from the different masses and the different optical properties of these elements. In this work we consider for simplicity the case of equal hoppings (i.e., equal masses) for the spin components in our numerics. We also emphasize that the purpose of this study is not to provide detailed descriptions of the possible experimental setup but to demonstrate with TEBD the presence of spin-asymmetric Josephson-type currents when spin-dependent potentials are switched on.

### 4.3.2 Results

Our observable is the average particle number on odd lattice sites

$$N_{\sigma,\mathrm{odd}}(t) = \frac{1}{L_{s,\mathrm{odd}}} \sum_{i=1}^{L_{s,\mathrm{odd}}} N_{\sigma,2i-1}(t), \tag{4.47}$$

where $L_{s,\mathrm{odd}} = L_s/2$, since the particle number is the directly measurable quantity in an ultracold gas setup, as opposed to the current. We identify the Josephson-type oscillations[7] between odd and even lattice sites from the Fourier transformation $N_{\sigma,\mathrm{odd}}(\omega)$. The Josephson frequency is the same for both spin components even in the presence of spin-asymmetric potentials (compare with the 3D linear response result in Sections 4.2.1 and 4.2.2). There are also single-particle processes present, but the Josephson oscillations dominate the physics. We point out that the spin-asymmetric Josephson-type currents would be identified identically even if considered the time-derivative of Eq. (4.47).

In Fig. 4.9 we show how the amplitudes of the Josephson-type oscillations for each spin component, $A^J_\uparrow$ and $A^J_\downarrow$, become unequal when spin-dependent potentials, $\delta_\downarrow \neq \delta_\uparrow$, are applied. This is a characteristic feature of the spin-asymmetric Josephson effect. Moreover, we show in Fig. 4.10 that for a fixed value of $\delta_\downarrow - \delta_\uparrow$ the

[7] This terminology is justified in the sense that the two spin components oscillate at the same frequency $\delta_\uparrow + \delta_\downarrow$, and the amplitudes of the oscillation become unequal for $\delta_\uparrow \neq \delta_\downarrow$, in a similar fashion as predicted by the linear response result of the spin-asymmetric Josephson effect.

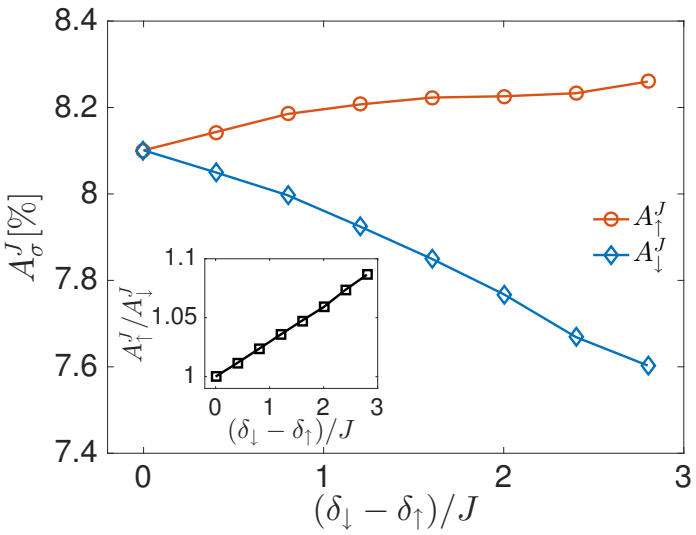


Figure 4.9: The amplitudes of the Josephson-type oscillations as a function of $\delta_\downarrow - \delta_\uparrow$. The amplitudes $A_\uparrow^J$ (red circles) and $A_\downarrow^J$ (blue diamonds) are given in proportion to the initial filling fraction of 0.5 for $\delta_\downarrow + \delta_\uparrow = 3.0J$. For $\delta_\uparrow = \delta_\downarrow$, there is no difference in the amplitudes. For increasing $\delta_\downarrow - \delta_\uparrow$, the amplitudes deviate from the balanced value with $A_\uparrow^J$ increasing and $A_\downarrow^J$ decreasing, and thus spin-asymmetric Josephson oscillations are observed. Inset: The relative asymmetry $A_\uparrow^J/A_\downarrow^J$. For greater values of $\delta_\downarrow - \delta_\uparrow$, an asymmetry of 9% is obtained. Figure adapted from Ref. [2].

Josephson amplitudes $A_\sigma^J$ grow with decreasing $\delta_\downarrow + \delta_\uparrow$. In practice, the quantity $\delta_\uparrow + \delta_\downarrow$ is limited from below (to a value on the order of $0.1J$ or larger, with the inverse hopping being on a timescale of milliseconds) by the requirement of having a sufficient number of oscillations within the duration of the experiment which is typically on the order of $100$ ms. On the other hand, in Fig. 4.10 the difference in the oscillation amplitudes grows towards higher values of $\delta_\downarrow + \delta_\uparrow$.

Based on Figs. 4.9 and 4.10, we suggest that the Josephson amplitudes are large enough to be imaged with existing [141, 142, 202–204] or near-future experimental techniques if one can realize the spin-dependent optical superlattice. The amplitudes can be tuned substantially by varying the values of $\delta_\uparrow$ and $\delta_\downarrow$. Furthermore, the amplitudes exhibit significant spin-asymmetry. In Fig. 4.10 $A_\uparrow^J/A_\downarrow^J$ rises to a remarkable $39$ per cent. We notice in Fig. 4.10 that at the Josephson frequency $\delta_\downarrow + \delta_\uparrow = 8J$ the values of the Josephson amplitudes differ from the trend of the curve and the slope of the asymmetry curve in the inset changes. We interpret

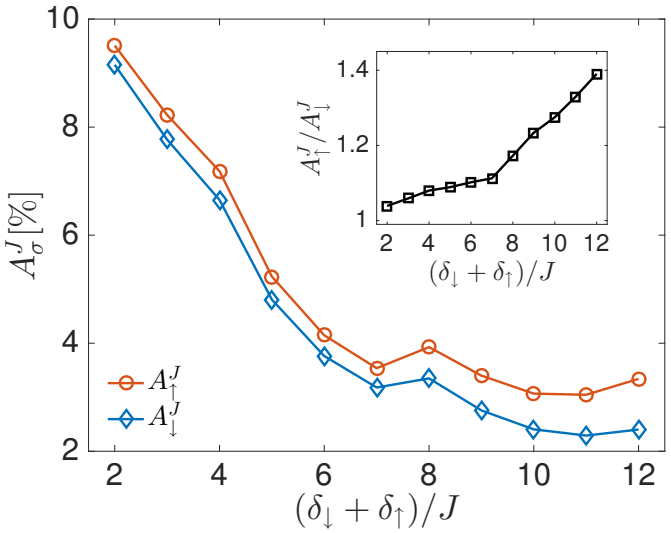


Figure 4.10: The amplitudes of the Josephson-type oscillations as a function of $\delta_\downarrow + \delta_\uparrow$. The amplitudes $A_\uparrow^J$ (red circles) and $A_\downarrow^J$ (blue diamonds) are given in proportion to the initial filling fraction of 0.5 for $\delta_\downarrow - \delta_\uparrow = 2.0J$. The greatest, more easily detectable values of the amplitudes are obtained for small $\delta_\downarrow + \delta_\uparrow$. Inset: The relative asymmetry $A_\uparrow^J/A_\downarrow^J$. Here, significant values of asymmetry up to 39% are obtained. Figure adapted from Ref. [2].

this feature to be due to a single-particle or higher-order process located close to the Josephson frequency, which leads to an effective gain in the spectral weight around the Josephson peaks. Importantly, this feature does not affect any of our main conclusions and is thus not considered meaningful.

We also find that for the used parameter values (in order to have particle number oscillations large enough to be experimentally observable), modifications to the Josephson frequency emerge as demonstrated in Fig. 4.11. The Josephson peak is split into sub-peaks. To elucidate the possible origin of this splitting, we study for simplicity smaller systems as a first approach (see Appendix D). In a system of four lattice sites, we can reproduce the splitting of the Josephson peak using perturbation theory to second order in $J_\sigma$. This suggests that the Josephson sub-peaks in Fig. 4.11 could originate from the different kinetic energy contributions of the states involved in Josephson-type tunnelling processes. In the four-site system, the frequency difference between adjacent sub-peaks can be estimated from

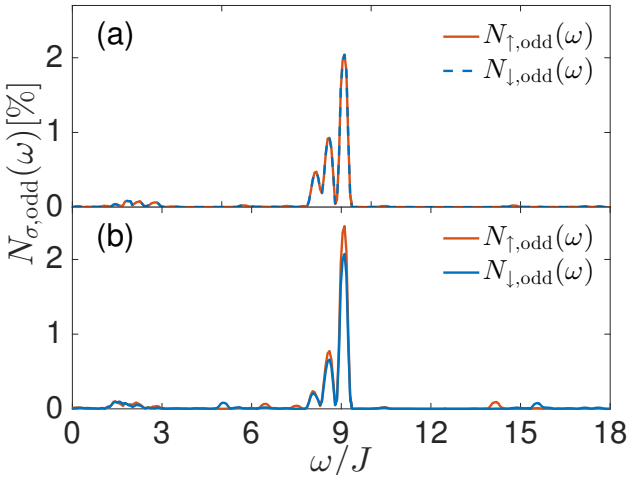


Figure 4.11: Frequency spectrum of the particle number dynamics. The Fourier transformation of the average particle number on odd lattice sites, $N_{\sigma,\mathrm{odd}}(\omega)$, is given relative to the initial filling fraction of $0.5$. Here, $\delta_\downarrow + \delta_\uparrow = 9.0J$, with (a) $\delta_\downarrow - \delta_\uparrow = 0.0$ and (b) $\delta_\downarrow - \delta_\uparrow = 1.6J$. The peak structure about $\omega = \delta_\downarrow + \delta_\uparrow = 9.0J$ is the Josephson contribution. The Josephson signal is split into sub-peaks due to higher-order modifications to the Josephson frequency. Note that the asymmetric potential leads to a clear difference in the Josephson amplitudes of the spin components, while the Josephson frequency remains the same for both spins. In addition to Josephson oscillations, there are minor contributions from single-particle and higher order processes at other frequencies. Figure adapted from Ref. [2].

the expression

$$\Delta\omega_J^{(2)} = 2|U|\left(\frac{J_\uparrow^2}{U^2-\delta_\uparrow^2} + \frac{J_\downarrow^2}{U^2-\delta_\downarrow^2}\right). \tag{4.48}$$

In addition to the splitting of the Josephson signal, the centre of the Josephson peak structure is shifted away from the typical Josephson frequency, $\omega_J = \delta_\downarrow + \delta_\uparrow$. The shift can be roughly estimated as (see Appendix D)

$$\omega_{J,\mathrm{shift}} = \frac{2J_\uparrow^2\delta_\uparrow}{\delta_\uparrow^2 - U^2} + \frac{2J_\downarrow^2\delta_\downarrow}{\delta_\downarrow^2 - U^2}. \tag{4.49}$$

An analogous shift can be found in the two-state problem, where the Rabi frequency $\Omega_{\mathrm{Rabi}}$ is shifted from the detuning $\delta$ because of the finite coupling $J$ [205]. To second order in $J$, the Rabi frequency is given by

$$\Omega_{\mathrm{Rabi}} = \sqrt{\delta^2 + J^2} \approx \delta + \frac{J^2}{2\delta}. \tag{4.50}$$

The effect is also similar to the superexchange shift $\propto \frac{J^2}{U}$ in Bose gases [162]. However, we emphasize that in spite of these higher order effects, the Josephson frequency remains the same for both spin components also in the spin-asymmetric case.

## 4.4 Conclusion

In this Chapter, we have studied the spin-asymmetric Josephson effect which generalises the standard Josephson phenomenon to the case of spin-dependent potentials. As a result of the presence of these potentials, the Cooper paired spin components Josephson-oscillate at the same frequency, but the amplitude, or the critical Josephson current, is different for the two components. We have proposed two schemes where the spin-asymmetric currents could manifest.

First, motivated by the observation of Josephson plasma oscillations in ultracold Fermi gases [38], we have studied the plasma oscillation regime in a spin-dependent Josephson junction that could potentially be realized with an ultracold superfluid Fermi gas. We have proposed methods to experimentally create the required spin-dependent potential across the junction. We have predicted that in this setup the Josephson plasma oscillation amplitude becomes spin-dependent but the plasma frequency is the same for both spin components similarly to the full AC spin-asymmetric Josephson effect. The spin-asymmetry in the plasma oscillation amplitudes is given by the asymmetry in the spin-dependent critical Josephson currents which are characteristic of the spin-asymmetric Josephson effect. Furthermore, we have shown that the asymmetry in the amplitudes can be tuned by varying the spin-dependent potentials. In the parameter regime typical of ultracold atom experiments, we have demonstrated that asymmetries on the order of a couple of per cent could be feasible. The possible observation of these spin-dependent plasma oscillations would establish the so far undetected spin-asymmetric Josephson effect.

Second, we have numerically demonstrated the presence of spin-asymmetric Josephson-type currents in the dynamics of an ultracold two-component Fermi gas in a one-dimensional spin-dependent superlattice that mimics an array of spin-dependent double wells. In this case, the Josephson-type effect occurs between the odd and even sites of the superlattice. This kind of setup could potentially be realized with ultracold atoms in the near future, although it is likely to be challenging. We have shown that significant amplitude asymmetries up to 39% are achievable in this arrangement. We have also shown that there are indications of higher-order modifications affecting the Josephson frequency due to the superlattice potential. However, the Josephson frequency is always the same for the two spin components.

# Chapter 5

# TUNABLE CRITICAL SUPERCURRENT IN SFIFS JUNCTIONS AND THE SPIN-ASYMMETRIC JOSEPHSON EFFECT

In this Chapter, we show that the tunable critical Josephson current in ferromagnetic Josephson junctions [39] can be explained at zero temperature in terms of the DC limit of the spin-asymmetric Josephson effect. The results presented in this Chapter have been published in Ref. [2].

## 5.1 Introduction

The Josephson junction with spin-dependent potentials presented in Chapter 4 has similarities to ferromagnetic Josephson junctions [39, 206–209] (see also Ref. [210]). However, we emphasize that the spin-asymmetric Josephson effect is fundamentally different, e.g., from superconductor-ferromagnet-superconductor (SFS) $\pi$ junctions [206] and from the spin-triplet supercurrent discovered in multilayered ferromagnetic Josephson junctions [208]. In these phenomena, the barrier between the superconductors plays the key role [210–212]. In contrast, in the spin-asymmetric Josephson effect the spin-dependent potentials create the asymmetry and the barrier separating the superfluids is conceptually a mere insulator without a spin-active coupling. In fact, the spin-asymmetric Josephson effect could possibly be

realized in a thin solid-state SIS (I stands for insulator) junction with two superconductors that have different Zeeman splittings for the two spin states in the presence of an in-plane magnetic field that is not strong enough to destroy (singlet) superconductivity [213]. The ultracold atomic Fermi gas double well setup in Chapter 4 would then be a conceptually analogous quantum simulator of such a junction.

There is also no immediate connection between the single-particle interference terms of the spin-asymmetric Josephson effect and Andreev reflections [214] in superconductor-normal metal-superconductor weak links. In an Andreev reflection, an incident electron in the normal metal with sub-gap energy forms a Cooper pair in the superconductor together with an annihilated hole which is expelled into the normal metal and moves back as a reflected object. These Andreev reflections can take place even without Josephson effects [121], whereas the virtual single-particle interferences are always inherent to the coherent Josephson current regardless of the type of the junction. Moreover, the single-particle interference term vanishes in the DC Josephson effect [see Eqs. (4.37) and (4.38)], while Andreev reflections and bound states can be relevant also in the DC limit [211]. Finally, we point out that the spin-asymmetric Josephson effect occurs when the pairing is of the standard singlet-type, and no triplet-pairing (i.e., Cooper pairs with total spin 1) is required for the phenomenon.

In this Chapter, we demonstrate that the spin-asymmetric Josephson effect is more closely related to a phenomenon which can occur in an SFIFS Josephson junction illustrated in Fig. 5.1. It has been predicted that for antiparallel magnetizations in the F layers the critical DC Josephson current can be tuned by varying the strength of the exchange fields [39, 215]. This occurs when the SF bilayer is very thin and can be considered an effective uniform magnetic superconductor. The uniform magnetization plays a role similar to the spin-asymmetric potential but an essential difference is that the exchange field of the ferromagnet affects

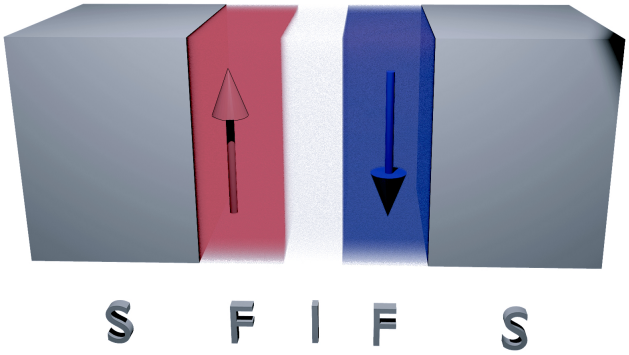


Figure 5.1: Schematic of an SFIFS Josephson junction. Figure adapted from Ref. [2].

also the initial state of the system, unlike in the spin-asymmetric Josephson effect. However, we show that at zero temperature there is a one-to-one correspondence between the magnetically tunable DC critical current in SFIFS junctions and the tunable critical current in the DC limit of the spin-asymmetric Josephson effect. Thus, the DC limit of the spin-asymmetric Josephson effect can be regarded as an analogue quantum simulation of the magnetically tunable DC Josephson effect in SFIFS junctions. Note that in the DC Josephson effect the critical currents for the two spin components are always equal.

Experimental findings that support the magnetically tunable DC critical current in SFNFS junctions (N stands for normal metal) have been reported in Ref. [216], with S being niobium (which is a type-II superconductor), F being iron, and N being chromium, the thickness of which determined the parallel or antiparallel magnetizations of the iron layers. The largest relative critical current difference between antiparallel and parallel configurations was measured to be $(500 \pm 150)\%$ and $(100 \pm 50\%)$ for two sample series with iron layer thicknesses of 1.35 nm and 1.60 nm, respectively. The experimental potential of the spin-asymmetric Josephson effect, however, remains an open question.

The rest of this Chapter proceeds as follows. In Section 5.2 we describe the setup for the tunable critical current and the spin-asymmetric Josephson effect. In

Section 5.3, we show the equivalence of the phenomena at $T = 0$. To do this, we consider both scenarios within the same linear response formalism. Section 5.4 summarises the results.

## 5.2 Setup

The most important difference between the setups for the magnetically tunable critical current and the spin-asymmetric Josephson effect is in the time-dependence of the magnetization and spin-dependent potentials, respectively. As explained in Chapter 4, the spin-asymmetric Josephson effect involves two superfluids or superconductors connected by a tunnelling coupling in the presence of spin-dependent potentials (see Fig 4.1). Initially, the system is in equilibrium without any spin-dependent potentials. At $t = 0^+$, such potentials and the tunnelling couplings are switched on, which results in the spin-asymmetric Josephson effect. However, in the context of the tunable critical current in thin SFIFS junctions [39], the magnetization of the ferromagnetic layers is present already in the initial state of the system as opposed to being switch on at $t = 0^+$.

We now state the assumptions for the SFIFS junction in Fig. 5.1 as per Ref. [39]. Each SF bilayer of the junction is assumed to be an effective uniformly magnetized superconductor with an effective exchange field $h_{\rm eff}$ and an effective superconducting gap $\Delta_{\rm eff}$ which is constant in space (as opposed to, e.g., the FFLO phase). This assumption is valid if the junction is very thin, i.e., if the thickness of the S layer is below the superconducting coherence length and the thickness of the F layer is below the condensate penetration length to the ferromagnet. For further details, see Refs. [39, 210].

In what follows, we drop the subindex $\rm eff$ from the exchange field and gap for simplicity. We take $h$ to be parallel to the interface (i.e., in-plane) which suppresses orbital effects[1] destroying superconductivity in the case of thin films considered

[1] By orbital effects, we refer to effect of the magnetic field on the orbital motions of the electrons.

here [213, 217]. In other words, screening currents are greatly reduced and the magnetic field is spread uniformly in the film [213]. Since the orbital effects are suppressed, it is the paramagnetic (Zeeman) effect that dominates the interaction between the magnetic field and the electrons [213]. Thus, we take the effect of the exchange field $h$ into account by including the term

$$\hat{H}_{\mathrm{Zeeman}} = -h \sum_{\mathbf{k}} \hat{n}_{\mathbf{k},\uparrow} + h \sum_{\mathbf{k}} \hat{n}_{\mathbf{k},\downarrow}, \tag{5.1}$$

into the BCS Hamiltonian. This causes a Zeeman splitting between the quasiparticle energies for the two spin states [see Eq. (5.12) below]. However, we emphasize that we assume $h$ to be below the Clogston–Chandrasekhar limit [218, 219] which is the critical value for $h$, where singlet superconductivity is destroyed.

To highlight the similarities between the effective exchange fields of the SFIFS junction and the spin-asymmetric potentials $\delta_\sigma$ of the spin-asymmetric Josephson effect, we consider both scenarios within the same linear response formalism in the DC limit where the Josephson frequency $\omega_J = 0$. We point out that the DC limit of the spin-asymmetric Josephson effect corresponds to the condition $\delta_\downarrow = -\delta_\uparrow$, and not only to the case where both of the potentials are zero.

The Hamiltonian for the initial state of the system is $\hat{H}_0 = \hat{H}_L + \hat{H}_R$, where $\hat{H}_L$ and $\hat{H}_R$ are the Hamiltonians of the left and right superconductors in the presence of an effective exchange field $h_{L/R}$. The Hamiltonian $\hat{H}_{L/R}$ with conventional BCS-type pairing is given by

$$\begin{aligned}\hat{H}_{L/R} = &\sum_{\mathbf{k},\sigma} \xi_{\mathbf{k}} \hat{n}_{L/R,\mathbf{k},\sigma} + \frac{g}{V_s} \sum_{\mathbf{k},\mathbf{k}'} \hat{c}^\dagger_{L/R,\mathbf{k},\uparrow} \hat{c}^\dagger_{L/R,-\mathbf{k},\downarrow} \hat{c}_{L/R,-\mathbf{k}',\downarrow} \hat{c}_{L/R,\mathbf{k}',\uparrow} \\ &- h_{L/R} \sum_{\mathbf{k}} (\hat{n}_{L/R,\mathbf{k},\uparrow} - \hat{n}_{L/R,\mathbf{k},\downarrow}),\end{aligned} \tag{5.2}$$

where the interaction strength $g$ does not (necessarily) refer to the strength of the pseudo-potential, $g = \frac{4\pi}{m} a_s$, although we use the same notation for simplicity. We

assume that the left and right superconductors are identical when $h_{L/R} = 0$. The tunnelling Hamiltonian, which is switched on at $t = 0^+$, is given by

$$\hat{H}_\Omega = \sum_{\mathbf{k},\mathbf{p},\sigma} \Omega_{\mathbf{k},\mathbf{p}} (\hat{c}^\dagger_{L,\mathbf{k},\sigma} \hat{c}_{R,\mathbf{p},\sigma} + \text{H.c.}). \tag{5.3}$$

Here, $\Omega_{\mathbf{k},\mathbf{p}}$ is the (in general non-momentum conserving) tunnelling matrix element which couples the momentum states $\mathbf{k}$ and $\mathbf{p}$ on the left and right hand sides of the junction, respectively.[2] The Hamiltonian for the spin-dependent potentials $\delta_\sigma$, also switched on at $t = 0^+$, reads

$$\hat{H}_\delta = \sum_{\mathbf{k},\sigma} \left[ \left( \mu - \frac{\delta_\sigma}{2} \right) \hat{n}_{L,\mathbf{k},\sigma} + \left( \mu + \frac{\delta_\sigma}{2} \right) \hat{n}_{R,\mathbf{k},\sigma} \right]. \tag{5.4}$$

Note that in the DC limit, the chemical potentials on the left and right hand sides of the junction are taken to be equal.

The resulting total Hamiltonian $\hat{H} = \hat{H}_0 + \hat{H}_\delta + \hat{H}_\Omega$ resembles the Hamiltonian of the spin-dependent double well in Section 4.2.2. For notational brevity, we formally include both the exchange field of the ferromagnet and the spin-asymmetric potential in the same total Hamiltonian, although we consider separately the cases

(i) $h_{L/R} \neq 0$ and $\delta_\sigma = 0$,

(ii) $h_{L/R} = 0$ and $\delta_\sigma \neq 0$ such that $\delta_\uparrow + \delta_\downarrow = 0$.

In case (i), the zero-temperature BCS energy gap $\Delta$ depends on the effective exchange field $h_{L/R}$ as [39]

$$\Delta(h_{L/R}) = \begin{cases} \Delta_0, & \text{for } h_{L/R} < \Delta_0 \\ 0, & \text{for } h_{L/R} > \Delta_0 \end{cases}, \tag{5.5}$$

where $\Delta_0$ is the gap for $h_{L/R} = 0$. As stated above, we take $h_{L/R} < \Delta_0$, i.e., that the exchange field is not strong enough to destroy the BCS state, and denote $\Delta_0$ by $\Delta$ for simplicity. In case (ii), we also assume the potentials $\delta_\sigma$ to be below the gap.

[2] The generalisation of the four-state model of the spin-asymmetric Josephson effect to a non-momentum conserving coupling is presented in Appendix B.

## 5.3 Results

We derive the critical DC Josephson current in each of the cases (i) and (ii) at zero temperature. We show that in these cases the critical currents have the same mathematical form and that the difference in the magnetizations between the right and left sides of the junction, $h_R - h_L$, and the spin-dependent potential $\delta_\sigma$ have an interchangeable role.

The Ambegaokar–Baratoff-type linear response theory calculation of the (spin-asymmetric) Josephson effect [37, 67, 169] can be followed also in case (i) up to the following expression for the critical Josephson current,

$$I_\sigma^C(\mathrm{i}\omega_n) = 2\left|\sum_{\mathbf{k},\mathbf{p}} \Omega_{\mathbf{k},\mathbf{p}}\Omega_{-\mathbf{k},-\mathbf{p}}\Pi_{\mathcal{F}}(\mathbf{k},\mathbf{p},\mathrm{i}\omega_n)\right|, \tag{5.6}$$

where [67]

$$\Pi_{\mathcal{F}}(\mathbf{k},\mathbf{p},\mathrm{i}\omega_n) = \frac{1}{\beta}\sum_{\mathrm{i}\omega_m} \mathcal{F}_L(\mathbf{k},\mathrm{i}\omega_m)\mathcal{F}_R^\dagger(\mathbf{p},\mathrm{i}\omega_m - \mathrm{i}\omega_n). \tag{5.7}$$

The expressions for the Fourier transforms of the anomalous Green functions on the left and right hand sides of the junction,

$$\mathcal{F}_L(\mathbf{k},\tau) = -\langle \mathcal{T}_\tau \hat{c}_{L,\mathbf{k},\uparrow}(\tau)\hat{c}_{L,-\mathbf{k},\downarrow}(0)\rangle, \tag{5.8}$$

and

$$\mathcal{F}_R^\dagger(\mathbf{k},\tau) = -\left\langle \mathcal{T}_\tau c_{L,-\mathbf{k},\downarrow}^\dagger(\tau)c_{L,\mathbf{k},\uparrow}^\dagger(0)\right\rangle, \tag{5.9}$$

respectively[3], are different for the cases (i) and (ii), as we will see below. However, in both cases we have

$$\mathcal{F}_R^\dagger(\mathbf{k},\mathrm{i}\omega_n) = [\mathcal{F}_R(\mathbf{k},-\mathrm{i}\omega_n)]^* = \mathcal{F}_R(\mathbf{k},\mathrm{i}\omega_n). \tag{5.10}$$

[3]We drop the Matsubara index $M$ from the $\hat{c}$-operators to avoid an overly cumbersome notation.

To show the former equality in Eq. (5.10), we use the following relations

$$\begin{aligned}
\mathcal{F}_R(\mathbf{k},\tau) &= \mathcal{M}^{-1}\left(\mathcal{F}_R(\mathbf{k},\mathrm{i}\omega_n)\right) = \frac{1}{\beta}\sum_n e^{-\mathrm{i}\omega_n\tau}\mathcal{F}_R(\mathbf{k},\mathrm{i}\omega_n) \\
\implies \mathcal{F}_R^\dagger(\mathbf{k},\tau) &= \frac{1}{\beta}\sum_n \left[e^{-\mathrm{i}\omega_n\tau}\mathcal{F}_R(\mathbf{k},\mathrm{i}\omega_n)\right]^* \\
&= \frac{1}{\beta}\sum_n e^{\mathrm{i}\omega_n\tau}\left[\mathcal{F}_R(\mathbf{k},\mathrm{i}\omega_n)\right]^* \\
&= \frac{1}{\beta}\sum_n e^{-\mathrm{i}\omega_n\tau}\left[\mathcal{F}_R(\mathbf{k},-\mathrm{i}\omega_n)\right]^* \\
&= \mathcal{M}^{-1}\left(\left[\mathcal{F}_R(\mathbf{k},-\mathrm{i}\omega_n)\right]^*\right) \\
\implies \mathcal{F}_R^\dagger(\mathbf{k},\mathrm{i}\omega_n) &= \mathcal{M}\left(\mathcal{F}_R^\dagger(\mathbf{k},\tau)\right) \\
&= \int_0^\beta d\tau\, e^{\mathrm{i}\omega_n\tau}\mathcal{F}_R^\dagger(\mathbf{k},\tau) \\
&= \left[\mathcal{F}_R(\mathbf{k},-\mathrm{i}\omega_n)\right]^*.
\end{aligned}$$

Here we have denoted the Matsubara Fourier-transform by $\mathcal{M}$ and its inverse by $\mathcal{M}^{-1}$. In the latter equality in Eq. (5.10), we have assumed that the gap is real [see Eq. (3.12)]. Alternatively, we can take $\Delta$ in Eq. (3.12) to be $|\Delta|$ as per Eq. (5.6).

### 5.3.1 Critical Josephson current in the presence of magnetization

We first consider the case (i), i.e., $h_{L/R} \neq 0$ and $\delta_\sigma = 0$. In the presence of the effective exchange field, the expression for the anomalous Green function in Matsubara space can be written as

$$\mathcal{F}_{L/R}(\mathbf{k},\mathrm{i}\omega_n) = -u_{\mathbf{k}}v_{\mathbf{k}}\left(\frac{1}{\mathrm{i}\omega_n - E^+_{L/R,\mathbf{k}}} - \frac{1}{\mathrm{i}\omega_n + E^-_{L/R,\mathbf{k}}}\right), \tag{5.11}$$

where the quasiparticle energies, modified by the exchange field, are given by[4]

$$E^\pm_{L/R,\mathbf{k}} = \mp h_{L/R} + \sqrt{\xi^2_{\mathbf{k}} + \Delta^2}, \tag{5.12}$$

and the Bogoliubov coefficients $u_{\mathbf{k}}$ and $v_{\mathbf{k}}$ are given by Eqs. (3.4) and (3.5), respectively. Note that $E^\pm_{L/R,\mathbf{k}} > 0$, since $h_{L/R} < \Delta$. A schematic illustration of the quasiparticle energies in the presence of the exchange field is shown in Fig. 5.2.

[4]These expressions can be obtained for example from the Nambu–Gor'kov equations, i.e., the equations of motion for the Nambu–Gor'kov Green function [70].

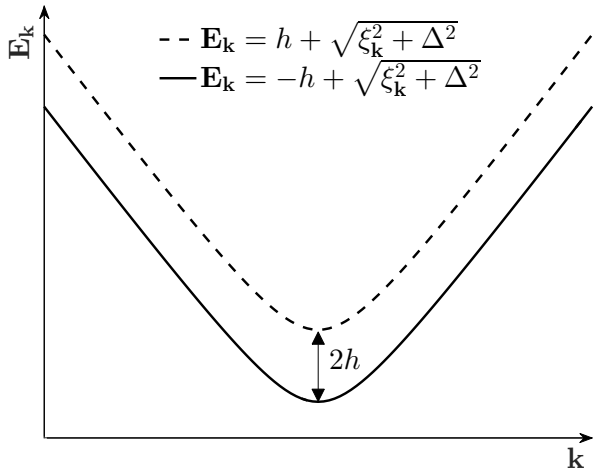


Figure 5.2: Schematic representation of the BCS quasiparticle energies in the presence of a small exhange field $h$. The Zeeman splitting is given by $2h$.

We substitute the anomalous Green function in Eq. (5.11) into Eq. (5.7), which yields

$$
\begin{aligned}
&\Pi_{\mathcal{F}}(\mathbf{k}, \mathbf{p}, \mathrm{i}\omega_n) \\
&= \frac{1}{\beta} \sum_{\mathrm{i}\omega_m} u_\mathbf{k} v_\mathbf{k} u_\mathbf{p} v_\mathbf{p} \left( \frac{1}{\mathrm{i}\omega_m - E^+_{L,\mathbf{k}}} - \frac{1}{\mathrm{i}\omega_m + E^-_{L,\mathbf{k}}} \right) \\
&\quad \times \left( \frac{1}{\mathrm{i}\omega_m - \mathrm{i}\omega_n - E^+_{R,\mathbf{p}}} - \frac{1}{\mathrm{i}\omega_m - \mathrm{i}\omega_n + E^-_{R,\mathbf{p}}} \right) \\
&= \frac{1}{\beta} \sum_{\mathrm{i}\omega_m} u_\mathbf{k} v_\mathbf{k} u_\mathbf{p} v_\mathbf{p} \left( \frac{1}{\mathrm{i}\omega_m - E^+_{L,\mathbf{k}}} \cdot \frac{1}{\mathrm{i}\omega_m - \mathrm{i}\omega_n - E^+_{R,\mathbf{p}}} - \frac{1}{\mathrm{i}\omega_m - E^+_{L,\mathbf{k}}} \cdot \frac{1}{\mathrm{i}\omega_m - \mathrm{i}\omega_n + E^-_{R,\mathbf{p}}} \right. \\
&\quad \left. - \frac{1}{\mathrm{i}\omega_m + E^-_{L,\mathbf{k}}} \cdot \frac{1}{\mathrm{i}\omega_m - \mathrm{i}\omega_n - E^+_{R,\mathbf{p}}} + \frac{1}{\mathrm{i}\omega_m + E^-_{L,\mathbf{k}}} \cdot \frac{1}{\mathrm{i}\omega_m - \mathrm{i}\omega_n + E^-_{R,\mathbf{p}}} \right). \qquad (5.13)
\end{aligned}
$$

We then apply the Matsubara summation formula

$$
\begin{aligned}
&\frac{1}{\beta} \sum_{\mathrm{i}\omega_m} \frac{1}{\mathrm{i}\omega_m - E_1} \cdot \frac{1}{\mathrm{i}\omega_m - \mathrm{i}\omega_n - E_2} \\
&= \frac{1}{E_1 - E_2 - \mathrm{i}\omega_n} \frac{1}{\beta} \sum_{\mathrm{i}\omega_m} \left( \frac{1}{\mathrm{i}\omega_m - E_1} - \frac{1}{\mathrm{i}\omega_m - \mathrm{i}\omega_n - E_2} \right) \\
&= \frac{1}{E_1 - E_2 - \mathrm{i}\omega_n} \left[ \frac{1}{2} + \frac{1}{\beta} \sum_{\mathrm{i}\omega_m} \frac{1}{\mathrm{i}\omega_m - E_1} - \left( \frac{1}{2} + \frac{1}{\beta} \sum_{\mathrm{i}\omega_m} \frac{1}{\mathrm{i}\omega_m - \mathrm{i}\omega_n - E_2} \right) \right] \\
&= \frac{n_F(E_1) - n_F(E_2)}{E_1 - E_2 - \mathrm{i}\omega_n}, \qquad (5.14)
\end{aligned}
$$

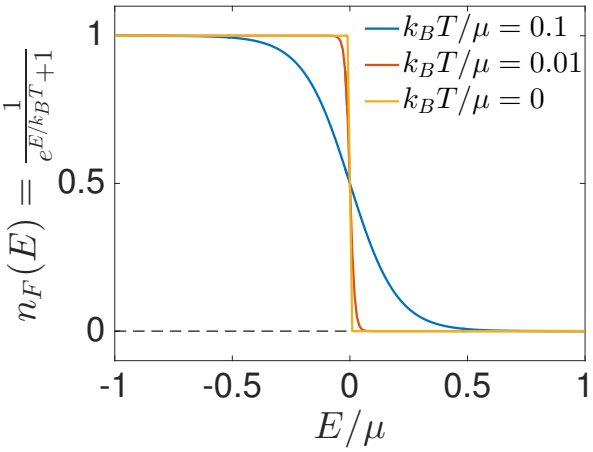


Figure 5.3: Fermi distribution function for different temperatures. At zero temperature, $n_F(E)$ becomes a step function.

where the Fermi distribution function is given by Eq. (2.47). As a result, we obtain

$$\begin{aligned}
&\Pi_{\mathcal{F}}(\mathbf{k},\mathbf{p},\mathrm{i}\omega_n) \\
&= u_{\mathbf{k}}v_{\mathbf{k}}u_{\mathbf{p}}v_{\mathbf{p}}\left(\frac{n_F(E^+_{L,\mathbf{k}})-n_F(E^+_{R,\mathbf{p}})}{E^+_{L,\mathbf{k}}-E^+_{R,\mathbf{p}}-\mathrm{i}\omega_n}-\frac{n_F(E^+_{L,\mathbf{k}})-n_F(-E^-_{R,\mathbf{p}})}{E^+_{L,\mathbf{k}}+E^-_{R,\mathbf{p}}-\mathrm{i}\omega_n}\right. \\
&\qquad\left.-\frac{n_F(-E^+_{L,\mathbf{k}})-n_F(E^-_{R,\mathbf{p}})}{-E^-_{L,\mathbf{k}}-E^+_{R,\mathbf{p}}-\mathrm{i}\omega_n}+\frac{n_F(-E^+_{L,\mathbf{k}})-n_F(-E^-_{R,\mathbf{p}})}{-E^-_{L,\mathbf{k}}+E^-_{R,\mathbf{p}}-\mathrm{i}\omega_n}\right). \qquad (5.15)
\end{aligned}$$

Taking the limit $T \to 0$, the Fermi distribution becomes the step function

$$n_F(E) = \begin{cases} 1, & \text{for } E < 0 \\ 0, & \text{for } E > 0 \end{cases},$$

as shown in Fig. 5.3. This significantly simplifies the expression in Eq. (5.15) and yields

$$\begin{aligned}
&\Pi_{\mathcal{F}}(\mathbf{k},\mathbf{p},\mathrm{i}\omega_n) \\
&= u_{\mathbf{k}}v_{\mathbf{k}}u_{\mathbf{p}}v_{\mathbf{p}}\left(\frac{1}{E^+_{L,\mathbf{k}}+E^-_{R,\mathbf{p}}-\mathrm{i}\omega_n}+\frac{1}{E^-_{L,\mathbf{k}}+E^+_{R,\mathbf{p}}+\mathrm{i}\omega_n}\right) \\
&= u_{\mathbf{k}}v_{\mathbf{k}}u_{\mathbf{p}}v_{\mathbf{p}}\left(\frac{1}{E_{\mathbf{k}}+E_{\mathbf{p}}+h_R-h_L-\mathrm{i}\omega_n}+\frac{1}{E_{\mathbf{k}}+E_{\mathbf{p}}-(h_R-h_L)+\mathrm{i}\omega_n}\right), \qquad (5.16)
\end{aligned}$$

where $E_{\mathbf{k}} = \sqrt{\xi^2_{\mathbf{k}}+\Delta^2}$.

We then apply the analytical continuation from Matsubara to real frequencies (here to $\omega = 0$, since $\delta_\sigma = 0$) by setting $\mathrm{i}\omega_n \to \mathrm{i}0^+$. We find the expression

$$\begin{aligned}
&\Pi_{\mathcal{F}}(\mathbf{k}, \mathbf{p}, 0) \\
&= u_{\mathbf{k}} v_{\mathbf{k}} u_{\mathbf{p}} v_{\mathbf{p}} \left( \frac{1}{E_{\mathbf{k}} + E_{\mathbf{p}} + h_R - h_L - \mathrm{i}0^+} + \frac{1}{E_{\mathbf{k}} + E_{\mathbf{p}} - (h_R - h_L) + \mathrm{i}0^+} \right) \\
&= u_{\mathbf{k}} v_{\mathbf{k}} u_{\mathbf{p}} v_{\mathbf{p}} \left\{ \mathcal{P} \frac{1}{E_{\mathbf{k}} + E_{\mathbf{p}} + h_R - h_L} + \mathrm{i}\pi\delta \left[ E_{\mathbf{k}} + E_{\mathbf{p}} + h_R - h_L \right] \right. \\
&\qquad \left. + \mathcal{P} \frac{1}{E_{\mathbf{k}} + E_{\mathbf{p}} - (h_R - h_L)} - \mathrm{i}\pi\delta \left[ E_{\mathbf{k}} + E_{\mathbf{p}} - (h_R - h_L) \right] \right\},
\end{aligned} \tag{5.17}$$

where in the latter equality we have used Eq. (2.35).

The expression in Eq. (5.17) needs to be inserted into Eq. (5.6) to obtain the critical current. The summation over momenta allows us to simplify the final expression. Since we assume $h_{L/R} < \Delta$ and $E_{\mathbf{k}} \geq \Delta$, we have $E_{\mathbf{k}} + E_{\mathbf{p}} \pm (h_R - h_L) > 0$. This means that the delta function does not contribute and the principal value integral becomes a normal one, since there are no poles. Thus, we finally obtain the critical current in the presence of magnetization as

$$\begin{aligned}
&I_\sigma^C(h_R - h_L) \\
&= 2 \sum_{\mathbf{k},\mathbf{p}} \Omega_{\mathbf{k},\mathbf{p}} \Omega_{-\mathbf{k},-\mathbf{p}} u_{\mathbf{k}} v_{\mathbf{k}} u_{\mathbf{p}} v_{\mathbf{p}} \left[ \frac{1}{E_{\mathbf{k}} + E_{\mathbf{p}} + h_R - h_L} + \frac{1}{E_{\mathbf{k}} + E_{\mathbf{p}} - (h_R - h_L)} \right].
\end{aligned} \tag{5.18}$$

Note that $I_\sigma^C(h_R - h_L)$ can be tuned by changing $h_R - h_L$. Note also that for parallel magnetizations, i.e., $h_R = h_L$, the critical current does not depend on the magnetization, as per Ref. [39].

### 5.3.2 Critical Josephson current in the presence of spin-dependent potentials

We now consider the critical Josephson effect in case (ii), i.e., with $h_{L/R} = 0$, and having $\delta_\sigma = -\delta_{\bar{\sigma}} \neq 0$ in the time-evolution. The calculation steps follow those of case (i) with only two differences. First, we now have $E^{\pm}_{L/R,\mathbf{k}} = E_{\mathbf{k}}$. Second, the

analytical continuation is $\mathrm{i}\omega_n \to -\delta_{\bar{\sigma}} + \mathrm{i}0^+$. With these changes, the expression for the critical current becomes

$$I_\sigma^C(-\delta_{\bar{\sigma}}) = 2\sum_{\mathbf{k},\mathbf{p}} \Omega_{\mathbf{k},\mathbf{p}}\Omega_{-\mathbf{k},-\mathbf{p}} u_{\mathbf{k}} v_{\mathbf{k}} u_{\mathbf{p}} v_{\mathbf{p}} \left[\frac{1}{E_{\mathbf{k}} + E_{\mathbf{p}} + \delta_{\bar{\sigma}}} + \frac{1}{E_{\mathbf{k}} + E_{\mathbf{p}} - \delta_{\bar{\sigma}}}\right]. \tag{5.19}$$

This has exactly the same mathematical form as Eq. (5.18), with $\delta_{\bar{\sigma}} \leftrightarrow h_R - h_L$.

## 5.4 Conclusion

We conclude that at zero temperature, the DC critical current takes the same form both in the case of the magnetically tuned SFIFS junction as well as in the spin-asymmetric Josephson effect. In the former case, the critical current is tuned by the difference of the effective exchange fields, while in the latter case the spin-dependent potentials $\delta_\sigma$ (in the DC limit with the constraint $\delta_\downarrow = -\delta_\uparrow$) act as the control parameters. In other words, the exchange field difference and the spin-asymmetric potentials are interchangeable at $T = 0$.

This result shows that the tunability of the DC Josephson current in SFIFS junctions can be explained in terms of the spin-asymmetric Josephson effect. The origin of the tunable critical current can be elucidated with Fig. 4.4. The energies of the paired states depend only on the interaction strength, but the energies of the intermediater states depend on $|\delta_\uparrow| = |\delta_\downarrow| \equiv \delta$. This allows the tuning of the energies of the intermediate states relative to the paired states and thus the amplitude $I_\uparrow^C(\delta) = I_\downarrow^C(\delta)$ of the supercurrent by varying $\delta$ without changing the Josephson frequency from zero.

# PART III HYBRID QUANTUM-CLASSICAL SIMULATION OF FERMIONS

# Chapter 6

## DIGITAL QUANTUM SIMULATION

In this Chapter, we describe the idea of digital quantum simulation and present as examples two physical platforms, superconducting circuits and trapped ions, where small-scale, proof-of-principle digital quantum simulations have already been demonstrated experimentally.

## 6.1 Introduction

In addition to analogue quantum simulation considered in Part II, there is another paradigm to quantum simulation which is based on digitized quantum evolution via quantum gates that act on the qubits (i.e., controllable two-level quantum systems) of the simulator [7]. This second approach is called digital quantum simulation. There is significant interest in digital quantum simulation platforms and quantum gates due to their central role towards the ultimate goal of a universal quantum computer [32, 220].

In this work, we are interested in how digital quantum simulators can help us solve and understand fermionic models. However, in Chapters 8 and 9 we adopt a slightly unconventional approach, in which the digital quantum simulator works in conjunction with a classically computed feedback loop, according to which we iteratively update the quantum gates of the quantum simulator. We call the resulting device a *hybrid quantum-classical simulator*. The reason for the

hybrid quantum-classical approach is that we engineer our hybrid device to implement the DMFT method (see Chapter 7) to study strongly correlated fermions described, e.g., by the Hubbard model, *directly in the thermodynamic limit*. The digital quantum simulator then solves the classically hard DMFT impurity problem and the DMFT self-consistency condition is taken care of in a classical computer. This hybrid quantum-classical method allows one to obtain non-trivial results with a relatively small near-future quantum device, which also motivates the scheme. Similar ideas have been reported in Ref. [221], where the hybrid quantum-classical DMFT approach was proposed to study correlated materials. Related work on solving strongly correlated electron models on a quantum computer can be found, e.g., in Refs. [222–224].

In this Section, we describe how the digital quantum simulation of the Hamiltonian dynamics of fermionic models described by the unitary time-evolution operator $\hat{U}(t)$ is achieved in general. There are two main steps in this which we now present.

First, since the relevant degrees of freedom in the digital quantum simulator are the qubit states instead of fermionic Fock states, the fermionic creation and annihilation operators of the simulated Hamiltonian need to be mapped via the Jordan–Wigner transformation [225, 226] onto tensor products of Pauli operators acting on the qubits. This mapping is not unique. For example, one possibility of a correspondence between the fermionic operators of a lattice site $j$ (we take the index $j$ to be a positive integer starting from 1) and a tensor product of Pauli operators acting on the qubits of the simulator is given by [226, 227]

$$\hat{c}^{\dagger}_{j\downarrow} = \left(\prod_{p=1}^{2j-2} \hat{\sigma}^{z}_{p}\right) \hat{\sigma}^{-}_{2j-1}, \tag{6.1}$$

$$\hat{c}^{\dagger}_{j\uparrow} = \left(\prod_{p=1}^{2j-1} \hat{\sigma}^{z}_{p}\right) \hat{\sigma}^{-}_{2j}, \tag{6.2}$$

$$\hat{c}_{j\sigma} = \left(\hat{c}^{\dagger}_{j\sigma}\right)^{\dagger}, \tag{6.3}$$

where $\hat{\sigma}_p^z$ is the Pauli-Z operator acting on qubit $p$, and $\hat{\sigma}_p^- = \frac{1}{2}\left(\hat{\sigma}_p^x - \mathrm{i}\hat{\sigma}_p^y\right)$, where $\hat{\sigma}_p^x$ and $\hat{\sigma}_p^y$ are the Pauli-X and Pauli-Y operators, respectively, acting on qubit $p$. For $j = 1$, the product $\prod_{p<2j-1} \hat{\sigma}_p^z$ in Eq. (6.1) is understood to be the identity operator. It can be shown that Eqs. (6.1)–(6.3) define a valid mapping by demonstrating that the right hand sides of Eqs. (6.1)–(6.3) satisfy the fermionic anticommutation relations in Eqs. (2.2)–(2.4). We prove the relation in Eq. (2.3) for $\sigma =\downarrow$, $\sigma' =\uparrow$, and $i < j$ as an example. We find that

$$\begin{aligned}
\left\{\hat{c}_{i,\downarrow}^\dagger, \hat{c}_{j,\uparrow}^\dagger\right\} &= \left\{\left(\prod_{p<2i-1} \hat{\sigma}_p^z\right)\hat{\sigma}_{2i-1}^-, \left(\prod_{p<2j} \hat{\sigma}_p^z\right)\hat{\sigma}_{2j}^-\right\} \\
&= \frac{1}{2}\left\{\hat{\sigma}_{2i-1}^x - \mathrm{i}\hat{\sigma}_{2i-1}^y, \hat{\sigma}_{2i-1}^z\right\}\left(\prod_{p=2i}^{2j-1} \hat{\sigma}_p^z\right)\hat{\sigma}_{2j}^- \\
&= 0, \qquad (6.4)
\end{aligned}$$

where in the second line we have applied the relation $(\hat{\sigma}_p^z)^2 = \hat{I}_p$, where is $\hat{I}_p$ is the identity operator in the local Hilbert space of qubit $p$. However, we have not explicitly included the identity operators in the expression for simplicity. In the third line we have used the fact that different Pauli operators anticommute.

The second step in the digital quantum simulation of fermionic models is obtaining the quantum gates for the time-evolution as follows. The evolution time $t$ is digitised to $N_T$ parts. A Suzuki–Trotter decomposition of the resulting time evolution operator for each time slice of length $t/N_T$ is applied to obtain a product of evolution operators corresponding to each summand $\hat{H}_j$ in the Jordan–Wigner transformed Hamiltonian $\hat{H} = \sum_{j\geq 1} \hat{H}_j$ [for an example of such a Hamiltonian, see, e.g., Eq. (8.21)]. Finally, each term in this product is written in terms of relevant quantum gates. To be explicit, the full time-evolution operator is written as

$$\hat{U}(t) = \left(e^{-\mathrm{i}\hat{H}\frac{t}{N_T}}\right)^{N_T}. \qquad (6.5)$$

The first-order Suzuki–Trotter decomposition for each time-slice gives [32]

$$e^{-\mathrm{i}\sum_j \hat{H}_j \frac{t}{N_T}} = \prod_j e^{-\mathrm{i}\hat{H}_j \frac{t}{N_T}} + \mathcal{O}\left[\left(\frac{t}{N_T}\right)^2\right]. \tag{6.6}$$

Thus, for small $\frac{t}{N_T}$, the full evolution is approximated as

$$\hat{U}(t) \approx \left(\prod_j e^{-\mathrm{i}\hat{H}_j \frac{t}{N_T}}\right)^{N_T}. \tag{6.7}$$

Each term of the form $\exp\left(-\mathrm{i}\hat{H}_j \frac{t}{N_T}\right)$ is written in terms of quantum gates. In principle any set of (universal) quantum gates suffices. In practice, however, the choice of these gates depends on the form of the Jordan–Wigner transformed Hamiltonian and the physical platform that implements the qubits and gates.

## 6.2 Physical realizations

In the rest of this Chapter, we briefly describe two digital quantum simulation platforms where great experimental progress has been made in recent years, namely superconducting circuits and trapped ions. For more extensive treatments of superconducting circuits, we refer to Refs. [11,228,229]. For reviews on trapped ions, see, e.g., Refs. [10,220,230].

### 6.2.1 Superconducting circuits

#### 6.2.1.1 Introduction

Superconducting circuits are a platform for quantum simulation and quantum computing where conventional microchip fabrication techniques can be used to design the experimental setups [11,229]. These circuits are usually manufactured using optical or electron-beam lithography applied, e.g., on an aluminium film on a sapphire substrate and cooled in dilution refrigerators to low temperatures on the order of 10-30 $\mathrm{mK}$ to minimize thermal excitations and reach superconductivity, hence their name [228,229]. Noteworthily superconducting circuit elements are macroscopic in size, on the order of 10–100 $\mu$m [228].

In superconducting circuits, as opposed to, e.g., in neutral atoms or trapped ions, the quantum information is stored in excitations of nonlinear circuit elements based on Josephson junctions.[1] These circuit elements have an anharmonic energy spectrum [11,228,229]. Anharmonicity is needed to enable operations on only two selected qubit states that form artificial two-level atoms [11,231]. The qubit states can then be controlled with currents, voltages, and microwave pulses [231].

#### 6.2.1.2 Qubits

There are several types of superconducting qubits. They are traditionally classified as charge [232, 233], flux [234], or phase [235] qubits, where the quantum information is encoded in the number of Cooper pairs on a small island, in the direction of a current around a loop, or in quantized oscillatory states of the circuit, respectively [7]. However, hybrid qubits are also possible. For a review article on superconducting qubits, see, e.g., Ref. [228]. In the context of quantum simulation, the types of superconducting qubits called transmon qubits [236, 237] and their variants, dubbed as 'Xmon' qubits [238], have received great interest [34,239–241], since they are engineered to be less sensitive to charge noise than normal charge qubits. The name 'Xmon' comes from the shape of the circuit element which resembles a cross [238].

Superconducting qubits can be coupled to neighbouring qubits by many means. For example, nearest-neighbour couplings can be achieved, e.g., capacitively or inductively, where the qubits share a mutual capacitor or inductor, respectively [11]. Long-distance couplings beyond nearest-neighbours can be achieved with a photonic bus mode realised with a transmission-line microwave resonator [242,243]. A qubit coupled to such a transmission-line resonator, which is essentially a Fabry–Perot-type cavity [11], leads to a scenario analogous to cavity quantum electrodynamics (QED), namely circuit QED [244, 245] (for a review, see, e.g, Ref. [246]).

[1] Here, nonlinearity refers to the nonlinear inductance $L_J(I)$ of a Josephson junction which can be deduced from Faraday's law $\Delta V = L_J(I)\dot{I}$ and the Josephson relations [228].

#### 6.2.1.3 Quantum gates

Since we are interested in the digital approach to quantum simulation, we now present two two-qubit quantum gates customarily used in superconducting circuits with transmon or Xmon qubits in addition to single-qubit gates. We use these gates in Chapter 8.

The first one is the $XY$ exchange gate which emerges when coupling two qubits with a transmission-line resonator bus mode [239, 243, 244, 247]. The unitary operator for the $XY$ gate between qubits $l$ and $m$ is given by

$$XY = \exp\left[-\mathrm{i}\frac{g^2}{\delta}\left(\hat{\sigma}_l^x\hat{\sigma}_m^x + \hat{\sigma}_l^y\hat{\sigma}_m^y\right)\right], \tag{6.8}$$

where $g$ is the strength of the (e.g., capacitive) coupling between the qubits and the resonator, and $\delta$ is the detuning between the qubit and resonator frequencies. By controlling the qubit frequencies, e.g, in transmon qubits by varying a magnetic flux *in situ*[2] [243], the coupling between any pair of qubits can be dynamically turned on and off. The entanglement of 10 superconducting transmon qubits with $XY$ gates has been reported in Ref. [249]. The derivation of the unitary operator in Eq. (6.8) from the Jaynes–Cummings Hamiltonian describing the interaction between the qubits and the photons in the transmission-line resonator can be found, e.g., in Ref. [250].

The second gate is the tunable Controlled-$\mathrm{Z}_\phi$ ($\mathrm{CZ}_\phi$) gate which is realized between two nearest-neighbour transmon qubits via capacitive couplings. To perform the $\mathrm{CZ}_\phi$ gate, one qubit is kept at a fixed frequency while the other carries out a 'fast adiabatic' trajectory which takes the two-qubit $|11\rangle$ state close to the avoided level crossing with the $|02\rangle$ state (here, $|2\rangle$ is a third, non-computational state in the anharmonic spectrum) [251]. This creates a relative phase shift $|11\rangle \xrightarrow{\mathrm{CZ}_\phi} e^{\mathrm{i}\phi}|11\rangle$.

[2] This can be done because the transmon qubit frequencies $\omega_q$ depend on the magnetic flux $\Phi$ as $\omega_q \sim \sqrt{8E_CE_J|\cos(\Phi/\Phi_0)|} - E_C$, where $E_C$ is the charging energy, $E_J$ is the Josephson energy, and $\Phi_0$ is the flux quantum [248].

The other computational states $|00\rangle$, $|10\rangle$, and $|01\rangle$ are left unaltered by the operation. By varying the amplitude of the trajectory, one can tune the conditional phase $\phi$. For further details, see Refs. [248, 251–253]. For Xmon qubits, fidelities of over 99% have been achieved with a 43 ns gate operation time [251]. The time to apply the gate is three orders of magnitude faster than the coherence time (the so-called $T_2$ dephasing time) for Xmon qubits which is on the order of 20 $\mu$s [238]. These $\mathrm{CZ}_\phi$ gates were used in the proof-of-principle digital quantum simulation of fermionic models [34]. The unitary operator for the $\mathrm{CZ}_\phi$ gate is represented in the computational basis by the matrix

$$\mathrm{CZ}_\phi = \begin{pmatrix} 1 & 0 & 0 & 0 \\ 0 & 1 & 0 & 0 \\ 0 & 0 & 1 & 0 \\ 0 & 0 & 0 & e^{\mathrm{i}\phi} \end{pmatrix}. \tag{6.9}$$

#### 6.2.1.4 Quantum simulations

The versatility and tunability of superconducting circuits make them a promising platform for quantum simulation. In addition to the experimentally realized analogue quantum simulation of cavity QED and the related Jaynes–Cummings model [254], several other analogue quantum simulation schemes have been proposed and in some cases realized with superconducting circuits. Examples include the quantum simulations of impurity models [255,256], lattice boson models [257], dynamical gauge fields [258], and ultrastrong coupling dynamics [259].

Recently, proposals for digital quantum simulation schemes have also emerged (see, e.g., Refs. [239, 240, 260, 261]) along with proof-of-principle experiments [34, 241]. For us, Refs. [34, 260] are particularly interesting since they describe a proposal and an experimental realization of digital quantum simulation of fermionic models. For review articles on quantum simulations with superconducting circuits, see, e.g., Refs. [11, 262, 263].

### 6.2.2 Trapped ions

#### 6.2.2.1 Introduction

Trapped ions were one of the earliest proposed experimental systems for quantum information processing [220,264]. These setups involve atomic ions, obtained, e.g., via photoionization of atoms, trapped often in linear radio-frequency Paul traps, although also other types of ion traps are used [230]. Different laser cooling schemes, such as Doppler and sideband cooling, are applied on the ions to cool their motional degrees of freedom to the quantum regime [230]. The quantized motional degrees of freedom can then be used as a quantum bus for distributing quantum information between the ions [220,264]. Note that since ions have an electric charge, the Coulomb interaction between them couples the ions together [220].

#### 6.2.2.2 Qubits

There are two main approaches to encode the qubit states in trapped ions [220, 230]. The first one is an optical qubit where the qubit states are encoded on an electronic ground-state and a metastable excited state which are separated by an optical frequency. An example of a commonly used isotope for an optical qubit is $^{40}Ca^{+}$ [220]. The qubit states can be encoded on the ground-state level $4\,^2\mathrm{S}_{1/2}$ and the metastable excited state level $3\,^2\mathrm{D}_{5/2}$ (which has a life-time on the order of 1 s) of $^{40}Ca^{+}$ [265]. The level separation is 729 nm.

The second approach is a hyperfine qubit, in which the qubit states are chosen from the hyperfine levels of the electronic ground-state in the presence of a magnetic field. The transition frequencies of hyperfine qubits are in the microwave regime. Examples of isotopes for hyperfine qubits include $^{9}Be^{+}$, $^{43}Ca^{+}$, $^{111}Cd^{+}$, and $^{171}Yb^{+}$ [266]. In $^{43}Ca^{+}$ (which has nuclear spin $I = \frac{7}{2}$), the qubit states can be encoded on the $F = 4$ and $F = 3$ hyperfine levels (separated by 3.2 GHz) of the ground-state $4\,^2\mathrm{S}_{1/2}$ [265]. The transition between the Zeeman sublevels

$|F = 4, m_F = 0\rangle$ and $|F = 3, m_F = 1\rangle$ (a so-called 'clock transition') allows particularly long coherence times ($T_2 = 50$ s) since it becomes independent of the magnetic field (to first order, that is) at field strength of 146 G and is effectively immune to small magnetic field noise [267]. To compare, with optical qubits laser and magnetic field fluctuations limit the $T_2$ coherence time to a range of about 10 to 100 ms [268].

#### 6.2.2.3 Quantum gates

An important feature of trapped ion systems is the ability to perform entangling quantum gates in addition to high-fidelity single-qubit gates. A trapped-ion implementation of the Controlled-NOT (CNOT) gate was proposed by Cirac and Zoller in 1995 [264]. This protocol requires single-ion addressing and cooling of the ions to their motional ground state, which made its experimental realization challenging. Already in the same year, a proof-of-principle demonstration of CNOT gate (but not the Cirac–Zoller gate) type dynamics was reported at NIST in Boulder using a single $^9\mathrm{Be}^+$ ion [269]. The Cirac–Zoller protocol for a CNOT gate was experimentally realized in Innsbruck in 2003 using two $^{40}\mathrm{Ca}^+$ ions [270].

Another scheme for an entangling gate is the multiqubit Mølmer–Sørensen (MS) gate [271–273] (see also related work in Refs. [274, 275]) which does not require single-ion addressing nor cooling to the motional ground state. Instead, the MS gate involves the use of a bichromatic light field (e.g., two co-propagating lasers of different frequency, addressed on the set of ions of interest) tuned close to the blue and red sidebands of the bus mode.[3]

To elucidate the workings of the MS gate, we consider the case of two qubits. For concreteness, we consider an optical qubit, e.g., $^{40}\mathrm{Ca}^+$ with qubit levels $4\,^2\mathrm{S}_{1/2}$ and $3\,^2\mathrm{D}_{5/2}$. We denote the correponding qubit states by $|\mathrm{S}\rangle$ and $|\mathrm{D}\rangle$ to distinguish

[3] MS-type gates have also been proposed in superconducting circuits, where the multiparticle interaction is mediated by the transmission line resonator bus mode [240, 260].

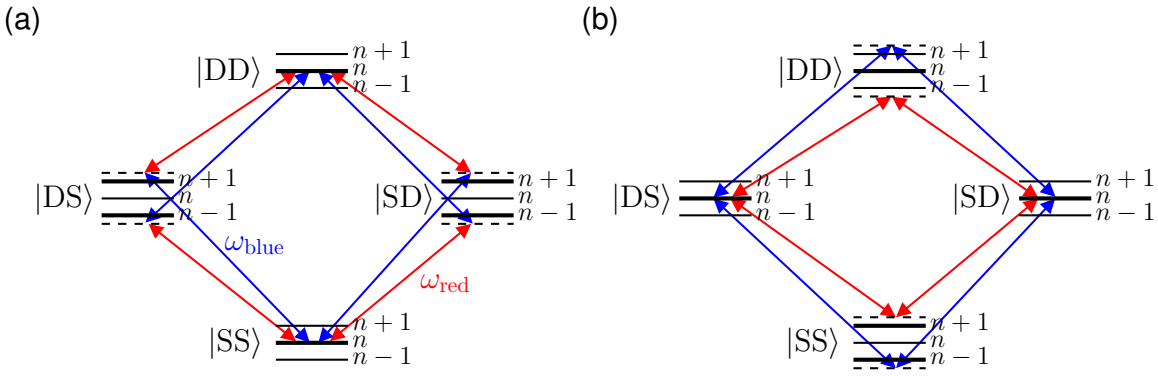


Figure 6.1: Mølmer–Sørensen scheme. (a) The $|\mathrm{SS}\rangle$ and $|\mathrm{DD}\rangle$ states sharing a common vibrational mode are coupled via the four depicted interfering virtual transitions. The red and blue lasers have frequencies $\omega_{\mathrm{red}} = \omega_0 - \nu - \delta$ and $\omega_{\mathrm{blue}} = \omega_0 + \nu + \delta$, respectively. Note that $\omega_{\mathrm{red}} + \omega_{\mathrm{blue}} = 2\omega_0$. Since the detunings of the red and blue lasers are opposite, it can be shown with second-order perturbation theory that the two-qubit transition rate does not depend on the vibrational quantum number $n$ [271]. This means that the MS gate does not require cooling the ions to the motional ground state. (b) Similar processes induce a coupling between the states $|\mathrm{DS}\rangle$ and $|\mathrm{SD}\rangle$ in a common vibrational mode.

them from the quantized centre-of-mass motional degrees of freedom $|n\rangle$. The idea of the MS gate is that the two qubits are made to change their internal state only collectively. In the MS protocol, a bichromatic laser field composed of frequencies $\omega_{\mathrm{red}} = \omega_0 - \nu - \delta$ and $\omega_{\mathrm{blue}} = \omega_0 + \nu + \delta$, where $\omega_0$ is the $|\mathrm{S}\rangle \leftrightarrow |\mathrm{D}\rangle$ transition frequency, $\nu$ is the level spacing of the quantized motional states, and $\delta$ is the detuning from the sideband frequencies, is applied on the two qubits [272]. Note that $\omega_{\mathrm{red}} + \omega_{\mathrm{blue}} = 2\omega_0$, i.e., the two-photon process can excite the pair of qubits. However, the laser frequencies are not resonant with any single-qubit transition. Therefore the qubits can change their internal state only collectively. The ions are assumed to be in the Lamb-Dicke regime (i.e., transitions can change the motional quantum number only by one) and the lasers drive both ions with the same intensity. The couplings induced by the field are shown in Fig. 6.1 (see also Ref. [272]). The Hamiltonian describing the interaction between the qubits and the laser field has the form of an off-resonantly driven harmonic oscillator (see, e.g., Ref. [276] for

details). By choosing the laser intensity (i.e., Rabi frequency) and the interaction time appropriately, one can induce for example the following entangling dynamics [277]

$$|\mathrm{SS}\rangle \rightarrow \frac{1}{\sqrt{2}}\left(|\mathrm{SS}\rangle + \mathrm{i}|\mathrm{DD}\rangle\right), \tag{6.10}$$

$$|\mathrm{DS}\rangle \rightarrow \frac{1}{\sqrt{2}}\left(|\mathrm{DS}\rangle - \mathrm{i}|\mathrm{SD}\rangle\right), \tag{6.11}$$

$$|\mathrm{SD}\rangle \rightarrow \frac{1}{\sqrt{2}}\left(|\mathrm{SD}\rangle - \mathrm{i}|\mathrm{DS}\rangle\right), \tag{6.12}$$

$$|\mathrm{DD}\rangle \rightarrow \frac{1}{\sqrt{2}}\left(|\mathrm{DD}\rangle + \mathrm{i}|\mathrm{SS}\rangle\right). \tag{6.13}$$

The MS scheme to create an entangling gate with a bichromatic laser field generalises to the case of many qubits via pairwise two-qubit interaction terms following the above protocol [272, 278]. The multiqubit MS gate allows, e.g., the creation of Greenberger–Horne–Zeilinger states of the form $\left(|\mathrm{SS}\ldots\mathrm{S}\rangle + |\mathrm{DD}\ldots\mathrm{D}\rangle\right)/\sqrt{2}$ [268, 272]. Note that only one bichromatic field addressed globally on the set of ions is required [279]. Experimental studies of MS gates for up to 14 qubits have been reported in Ref. [268]. It should be noted, however, that in practice the fidelity of MS gates falls rapidly with the number of qubits involved. For example, two-qubit MS gates for optical qubits have been performed with 99.3% fidelity [277], whereas the reported fidelities for 5-qubit, 10-qubit, and 14-qubit MS gates were 94.4%, 62.6%, and 50.8%, respectively [268].

The MS gate can be described by an effective unitary operator parametrized by two angles, $\theta$ and $\phi$, where $\theta$ depends on the Lamb–Dicke parameter[4], Rabi frequency, and the detuning $\delta$ of the light field from the sideband transitions, and $\phi$ is defined by the phase of the light field [279]. The effective unitary operator acting on many qubits $l, l+1, \ldots, m$ is given by [278–280]

$$\hat{U}_{\mathrm{MS}}^{l,m}(\theta,\phi) = \exp\left[-\mathrm{i}\frac{\theta}{4}\left(\cos\phi\,\hat{S}_x + \sin\phi\hat{S}_y\right)^2\right], \tag{6.14}$$

[4]The Lamb–Dicke parameter is defined as the product of the laser wave number and the ion trap oscillator length along a chosen axis [220].

where $\hat{S}_{x,y} = \sum_{j=l}^{m} \hat{\sigma}_j^{x,y}$, and $\hat{\sigma}_j^x$ and $\hat{\sigma}_j^y$ are Pauli operators acting on qubit $j$. In the two-qubit case, the mappings in Eqs. (6.10)–(6.13) are obtained with $\theta = \pi/2$ and $\phi = \pi/2$. We use the MS gates given by Eq. (6.14) in Chapter 9, where we present a scalable hybrid quantum-classical scheme to simulate the infinite-dimensional time-dependent Hubbard model in the thermodynamic limit.

The achievable fidelities of trapped ion single- and two-qubit quantum gates are very high. For example, fidelities of 99.9999% for single-qubit gates [267] and 99.9% for two-qubit gates [281] have been reported. For two-qubit MS gates, fidelities of 99.3% [277] using an optical $^{40}Ca^+$ qubit with gate operation time $t_{\mathrm{gate}} = 50$ $\mu$s, and 99.7% [282] with a hyperfine $^{43}Ca^+$ qubit and $t_{\mathrm{gate}} \approx 3$ ms have been achieved. This high precision of the fundamental operations makes trapped ions a viable candidate platform for quantum error correction schemes and for a scalable quantum computer in the future.

#### 6.2.2.4 Quantum simulations

Like superconducting circuits, trapped ions are a promising platform for quantum simulations. Trapped ions have already been used in proof-of-principle demonstrations of digital quantum simulations. For example, digital quantum simulation of spin models with a six-qubit processor was reported in Ref. [33], and the dynamics of the lattice Schwinger model was simulated with a four-qubit processor using MS gates in Ref. [21]. Digital quantum simulation schemes for fermionic models in trapped ions have been proposed, e.g., in Refs. [227, 280].

However, we point out for completeness that despite their suitability for digital simulation schemes, trapped ions have been useful as analogue quantum simulators as well. Examples of analogue quantum simulations with trapped ions include spin models [283–285], *Zitterbewegung* [17, 18], Klein tunnelling [17, 286, 287], Majorana equation [288], quantum field theories [289, 290], and quantum chemistry [291]. For reviews on quantum simulations with trapped ions, see Refs. [10, 230].

# Chapter 7

## DYNAMICAL MEAN-FIELD THEORY

In this Chapter, we introduce the central concepts of dynamical mean-field theory. We discuss both the equilibrium case and the extension to non-equilibrium problems. We restrict ourselves to single-site DMFT. For cluster extensions of DMFT, see, e.g., Ref. [292]. For applications of DMFT, see, e.g., Refs. [40, 41, 293]. We use DMFT in the context of quantum simulation in Chapters 8 and 9.

## 7.1 Introduction

Dynamical mean-field theory [40] is a widely-used and well-established method to study high-dimensional strongly correlated fermion systems. It can be considered an extension of static single-site mean-field approaches, such as the Weiss mean-field theory of the Ising model [40]. It has been especially helpful in studying the Hubbard model and the Mott transition due to its ability to capture the physics of strong electronic correlations by including the description of local quantum fluctuations [40, 41].

There were two essential stages in the development of DMFT. The first step was the demonstration that strongly correlated lattice fermions have a non-trivial behaviour in the limit $d \to \infty$ ($d$ is the spatial dimension), where local correlations survive, but non-local contributions to the self-energy vanish [294–296]. To show this, we take as an example the Hubbard model in Eq. (2.1) in the thermodynamic

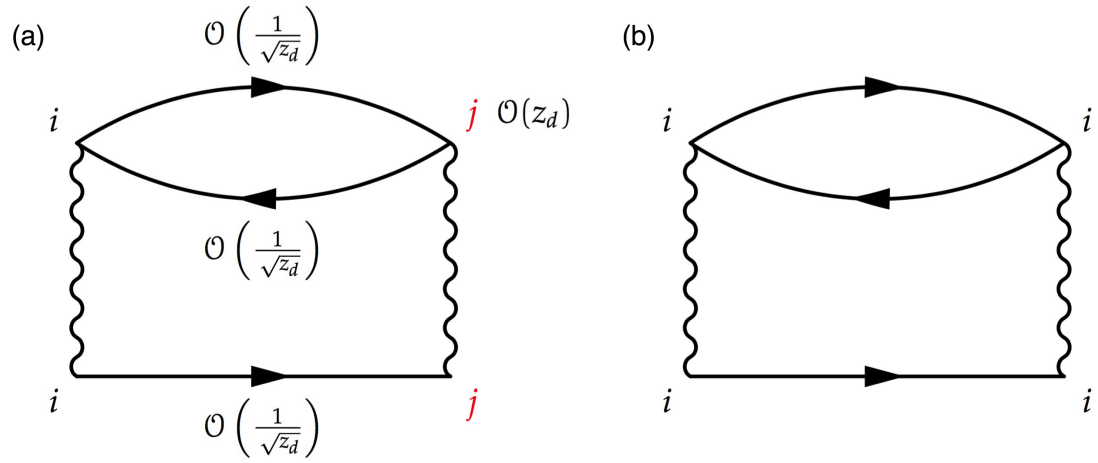


Figure 7.1: Vanishing self-energy Feynman diagrams in infinite dimensions. (a) An example of a self-energy Feynman diagram between lattice sites $i$ and $j$. The summation over $j$ is indicated by the red color and has $z_d$ terms in the sum. The arrowed lines denote the non-interacting Green function $G_{ij}^{(0)} \sim \frac{1}{\sqrt{z_d}}$ and the wiggly line is the local interaction $U$. (b) In the limit $z_d \to \infty$, only the local diagram with $i = j$ survives. We point out that sometimes the Green function arrows are written from right to left [69]. This difference is not crucial here.

limit in a lattice with $z_d$ nearest-neighbours per lattice site. We consider the limit $z_d \to \infty$ (or equivalently $d \to \infty$). Due to the summation over nearest-neighbour sites in the first term of Eq. (2.1), the hopping $J$ needs to be scaled as [297]

$$J \sim \frac{J_\infty}{\sqrt{z_d}}, \tag{7.1}$$

where the hopping $J_\infty$ is $z_d$-independent. This is done in order to avoid a diverging kinetic energy per lattice site. Also the single-particle Green function $G_{ij}$ needs to be scaled as $1/\sqrt{z_d}$, unless $i = j$, in which case no scaling is required [297]. Since the interaction term of the Hubbard model involves only local terms, the interaction strength $U$ does not need to be scaled. Consider now the self-energy Feynman diagram in Fig. 7.1a. The labels $i$ and $j$ denote lattice sites connected by three Green function lines. In the summation over $j$, the contribution from non-local terms with $i \neq j$ scales as $z_d \times \left(\frac{1}{\sqrt{z_d}}\right)^3 = \frac{1}{\sqrt{z_d}}$ and vanishes in the limit $z_d \to \infty$. Only the local diagram with $i = j$ in Fig. 7.1b survives this limit. Thus, all self-

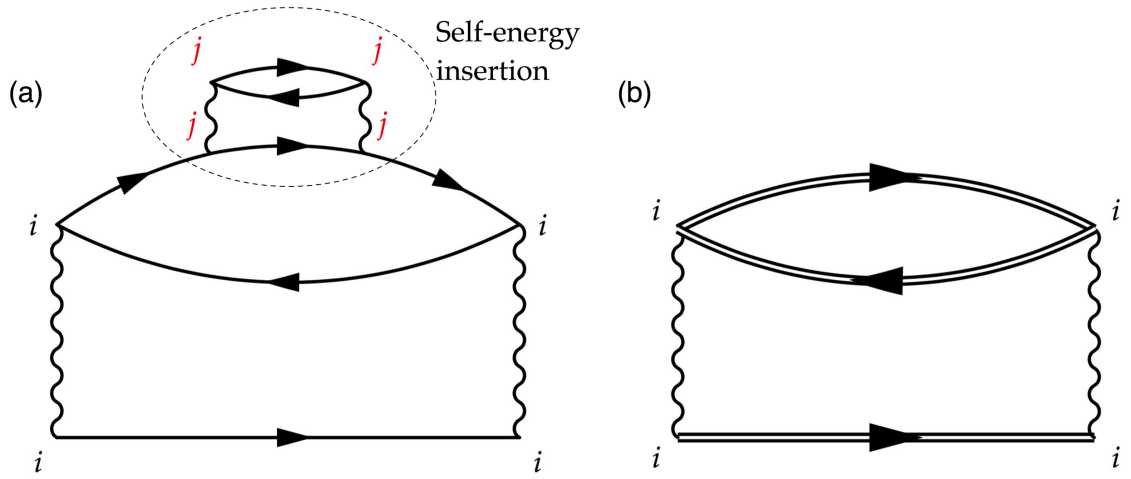


Figure 7.2: Surviving self-energy Feynman diagrams in infinite dimensions. (a) An example of a self-energy Feynman diagram between lattice sites $i \neq j$ which survives the limit $z_d \to \infty$. The summation over $j$ is indicated by the red color. (b) The diagram in (a) is included in the local skeleton diagram, where all self-energy insertions have been removed and the non-interacting Green function lines have been replaced by the bold interacting Green function lines.

energy diagrams connecting two lattice sites with more than two Green function lines vanish as $z_d \to \infty$.

There are also Feynman diagrams connecting lattice sites $i \neq j$ with two Green function lines as shown in Fig. 7.2a. These kind of diagrams have a non-vanishing contribution in the limit $z_d \to \infty$. However, these diagrams are included in local *skeleton* Feynman diagrams, such as that depicted in Fig. 7.2b, where all self-energy insertions[1] have been removed and the non-interacting Green function lines have been replaced by the bold interacting Green function lines. Thus, in the limit $z_d \to \infty$, the self-energy of correlated lattice models consisting only of skeleton diagrams is strictly local in space. Note, however, that this does not mean that there cannot be any dynamics in the system. A fermion can leave a site $i$, interact on other sites, and return to the site $i$ retardedly. These processes are described by the local skeleton diagrams due to the interacting Green function lines [297].

[1] A self-energy insertion is a piece that can be severed from the Feynman diagram by cutting two Green function lines [69]. An example is illustrated in Fig. 7.2a.

In the second step in the development of DMFT, it was shown that a lattice fermion system which has a strictly local self-energy can be mapped exactly onto a quantum impurity problem [298,299]. This was an important discovery for practical calculations, since it enabled the use of the numerical methods developed for tackling impurity problems for solving the high-dimensional Hubbard model in the thermodynamic limit [40]. This step reduces the complexity of the Hubbard model by mapping it onto a simpler impurity problem that is subject to a self-consistency condition. This condition relates the properties of the impurity problem to those of the original model.

The 'impurity' consists of a single lattice site taken from the original problem, and so inherits on-site interactions from the Hubbard model. This impurity site is then immersed into a time-dependent, self-consistent mean-field $\Lambda(\tau - \tau')$ (see Fig. 7.3a for an illustration) with which it can dynamically exchange fermions at time instants $\tau$ and $\tau'$, leading to the local temporal dynamics in Fig. 7.3b. The mean-field thus attempts to model the rest of the lattice and by being dynamical it can describe retardation phenomena. Thus, many features of strong correlations, such as the Mott transition, are captured correctly [40]. However, although DMFT maps a Hubbard model onto an impurity model, we still have a non-trivial quantum many-body problem to solve because of the interactions at the impurity site. Many numerical methods have been developed for this task.

In the last ten years, DMFT has been successfully extended to the study of non-equilibrium dynamics [41], aided by the increase in classical computing power. Conceptually, non-equilbrium DMFT is similar to the equilibrium formulation. In the limit of infinite dimensions, the scaling in Eq. (7.1) is required also for the time-dependent Hubbard model in Eq. (2.7). The Feynman diagrams for out-of-equilibrium scenarios follow the same rules as in equilibrium systems [69], and thus the locality of the self-energy applies also in non-equilibrium DMFT. The main difference between the equilibrium and non-equilibrium formulations of DMFT is

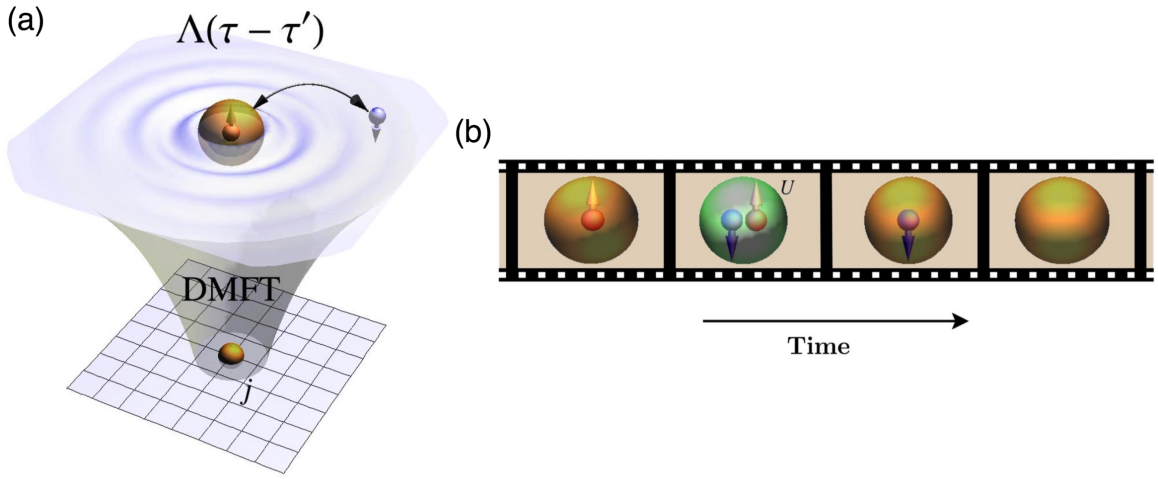


Figure 7.3: Dynamical mean-field theory. (a) DMFT focuses on the quantum dynamics of an arbitrarily chosen lattice site $j$ and replaces the rest of the lattice with an effective mean-field $\Lambda(\tau - \tau')$ with which the isolated site dynamically exchanges fermions subject to a self-consistency condition. In finite dimensions, the single-site DMFT approximation corresponds to neglecting spatial fluctuations. (b) Since the mean-field is dynamical, the isolated site undergoes temporal quantum fluctuations between the four states of the local Hilbert space.

that non-equilibrium DMFT works directly in the real-time domain and uses the non-equilibrium contour Green function formalism introduced in Section 2.2.2.

We mention that while in the limit of infinite spatial dimensions the mapping onto an impurity problem is exact with a local self-energy, for finite dimensions it is an approximation since the self-energy is then not strictly local in space[2]. Since an impurity problem is spatially local, in finite dimensions the mapping corresponds to neglecting spatial fluctuations. Despite this, for lattice geometries with a large coordination number (for example the 3D face-centered cubic lattice has $z_d = 12$), self-consistently solving the impurity problem can yield an accurate approximate solution to the original Hubbard problem [40].

In the rest of this Chapter, we proceed as follows. In Section 7.2, we introduce the basic concepts of DMFT for equilibrium systems, such as the DMFT action, Anderson model, and the self-consistency loop. In Section 7.3 we do the same for non-equilibrium systems, and describe in detail the Hamiltonian-based approach [300]

[2]However, DMFT is always exact in the atomic limit and in the non-interacting limit [40].

to non-equilibrium DMFT, which we apply in Chapter 9 in the context of quantum simulation. Finally, in Section 7.4 we present some commonly used classical impurity solvers and their limitations which partly motivate the use of a quantum simulator to solve the DMFT impurity problem.

## 7.2 Dynamical mean-field theory for equilibrium systems

In equilibrium DMFT, one is usually interested in local observables, such as the local spectral function of the Hubbard model in Eq. (2.5). These observables are in the frequency domain. To get these observables, one must repeatedly solve the auxiliary DMFT impurity problem subject to a DMFT self-consistency condition. The solution of the impurity problem is the retarded single-particle impurity Green function $G^R_{\mathrm{imp}}(\omega)$. At finite temperature, one often first computes the Matsubara impurity Green function $G^M_{\mathrm{imp}}(\mathrm{i}\omega_n)$ and then applies the analytic continuation in Eq. (2.48) to obtain $G^R_{\mathrm{imp}}(\omega)$. The impurity problem can be expressed using an action-based formalism or a Hamiltonian-based approach. We present the main equations for both cases below for completeness. We take the original Hubbard model to be in the paramagnetic phase for simplicity. In this case the Green functions and the mean-field $\Lambda$ are spin symmetric and we only need to consider one spin configuration. We suppress the spin-index from the Green functions and $\Lambda$ for simplicity.

### 7.2.1 DMFT action formalism

The DMFT impurity problem can be given in terms of an effective action that has the form [41]

$$\hat{S} = \hat{S}_{\mathrm{loc}} + \hat{S}_{\mathrm{hyb}}, \tag{7.2}$$

where

$$\hat{S}_{\mathrm{loc}} = -\int_0^\beta d\tau\, \hat{H}_{\mathrm{loc}}(\tau), \tag{7.3}$$

and

$$\hat{S}_{\mathrm{hyb}} = -\int_0^\beta d\tau \int_0^\beta d\tau' \sum_\sigma \hat{c}_\sigma^\dagger(\tau)\Lambda(\tau-\tau')\hat{c}_\sigma(\tau'). \tag{7.4}$$

Here, $\hat{S}_{\mathrm{loc}}$ includes the local part of the Hubbard model given by

$$\hat{H}_{\mathrm{loc}} = U\hat{n}_\uparrow\hat{n}_\downarrow - \mu\sum_\sigma \hat{n}_\sigma. \tag{7.5}$$

This is the local Hamiltonian of an arbitrarily chosen site (assuming translational invariance) which is directly adopted in the impurity model. For studying the special case of the half-filled Hubbard model, $\hat{H}_{\mathrm{loc}}$ is usually equivalently written as [compare with Eq. (2.6)]

$$\hat{H}_{\mathrm{loc}} = U\left(\hat{n}_\uparrow - \frac{1}{2}\right)\left(\hat{n}_\downarrow - \frac{1}{2}\right) - \mu\sum_\sigma \hat{n}_\sigma, \tag{7.6}$$

since here half-filling is again obtained when $\mu = 0$. However, the chemical potential term is often retained in equations for generality even if one is interested in the half-filled case. In computations, the chemical potential is then set equal to zero.

The other part of the action, $\hat{S}_{\mathrm{hyb}}$, describes the impurity embedded in a time-dependent (i.e, dynamical) mean-field that is described by a hybridization function $\Lambda(\tau-\tau')$. In many-body physics outside the context of DMFT, $\Lambda(\tau-\tau')$ is also called the embedding self-energy [69]. The impurity can exchange fermions with the dynamical mean-field at imaginary time instants $\tau'$ and $\tau$, which give the argument of the hybridization function.

The hybridization function defines an important auxiliary quantity, the so-called Weiss function denoted by $\mathcal{G}_0$[3]. It is given in Matsubara space by [41]

$$\mathcal{G}_0^{-1}(\mathrm{i}\omega_n) = \mathrm{i}\omega_n + \mu - \Lambda(\mathrm{i}\omega_n), \tag{7.7}$$

[3]Other names for the Weiss function include the bath Green function and the non-interacting impurity Green function which justifies the subindex 0.

where $\Lambda(\mathrm{i}\omega_n) = \int_0^\beta d\tau\, \Lambda(\tau) e^{\mathrm{i}\omega_n \tau}$. We point out that in equilibrium DMFT the action in Eq. (7.4) is also often written in terms of the Weiss function in Eq. (7.7), whereas in non-equilibrium DMFT the hybridization function $\Lambda$ is used [see Eq. (7.19)]. For our purposes this distinction is not crucial, and we choose write the action using the hybridization function to highlight the similarities between equilibrium and non-equilibrium DMFT as per Ref. [41].

The main quantity to be computed in DMFT is the impurity Green function defined in the imaginary time domain as

$$G^M_{\mathrm{imp}}(\tau - \tau') = -\langle \mathcal{T}_\tau \hat{c}_\sigma(\tau) \hat{c}^\dagger_\sigma(\tau') \rangle_S, \tag{7.8}$$

where we have used the notation of Eq. (2.60). The impurity Green function can be computed using for example perturbation theory or quantum Monte Carlo. These are numerical methods (impurity solvers) that compute $G^M_{\mathrm{imp}}$ using Feynman diagram techniques [41]. The impurity Green function is related to the Weiss function in Eq. (7.7) and the impurity self-energy $\Sigma_{\mathrm{imp}}$ via the Dyson equation

$$\begin{aligned} G^M_{\mathrm{imp}}(\mathrm{i}\omega_n) &= \int_0^\beta d\tau\, G^M_{\mathrm{imp}}(\tau) e^{\mathrm{i}\omega_n \tau} \\ &= \frac{1}{\mathcal{G}_0^{-1}(\mathrm{i}\omega_n) - \Sigma_{\mathrm{imp}}(\mathrm{i}\omega_n)} \\ &= \frac{1}{\mathrm{i}\omega_n + \mu - \Lambda(\mathrm{i}\omega_n) - \Sigma_{\mathrm{imp}}(\mathrm{i}\omega_n)}. \end{aligned} \tag{7.9}$$

In order to have a self-consistent solution, the impurity Green function must equal the local part of the Green function for the original lattice model, i.e., the Hubbard model. The DMFT self-consistency condition thus reads [40]

$$G^M_{\mathrm{imp}}(\mathrm{i}\omega_n) = G^M_{\mathrm{latt},jj}(\mathrm{i}\omega_n), \tag{7.10}$$

where $j$ is the (arbitrarily chosen) lattice site from which the removal or addition of a particle occurs in the translationally invariant lattice model. Here, $G^M_{\mathrm{latt},jj}(\mathrm{i}\omega_n)$

is given by [40]

$$G^M_{\mathrm{latt},jj}(\mathrm{i}\omega_n) = \sum_{\mathbf{k}} G_{\mathbf{k}}(\mathrm{i}\omega_n) \\ = \int d\epsilon \, \frac{D(\epsilon)}{\mathrm{i}\omega_n + \mu - \epsilon - \Sigma_{\mathrm{latt}}(\mathrm{i}\omega_n)}, \tag{7.11}$$

where $D(\epsilon)$ is the density of states of the lattice. In the second line of Eq. (7.11), we have taken the lattice self-energy to be momentum-independent, i.e., local in space, $\Sigma_{\mathrm{latt},ij} = \delta_{ij}\Sigma_{\mathrm{latt},jj} \equiv \Sigma_{\mathrm{latt}}$. This is the only approximation in DMFT apart from those needed for solving the impurity model. The approximation becomes exact in the limit of infinite spatial dimensions as explained in Section 7.1. It also allows for equating the local lattice self-energy with the impurity self-energy, i.e.,

$$\Sigma_{\mathrm{imp}}(\mathrm{i}\omega_n) = \Sigma_{\mathrm{latt}}(\mathrm{i}\omega_n). \tag{7.12}$$

### 7.2.2 Single-impurity Anderson model

One can also give a Hamiltonian presentation to the DMFT impurity problem, which basically corresponds to discretizing the continuous mean-field described by the hybridization function $\Lambda$ into a set of non-interacting 'bath' sites. This allows for using Hamiltonian-based impurity solvers such as exact diagonalization or matrix product states to compute the impurity Green function in Eq. (7.8).

There is some freedom in the choice of the impurity Hamiltonian [40]. The standard representation is given by the single-impurity Anderson model (SIAM) [40]

$$\hat{H}_{\mathrm{SIAM}} = U\hat{n}_{1\uparrow}\hat{n}_{1\downarrow} - \mu\left(\hat{n}_{1\uparrow} + \hat{n}_{1\downarrow}\right) + \sum_{p>1,\sigma} \epsilon_p \hat{n}_{p\sigma} + \sum_{p,\sigma} \left(V_p \hat{c}^\dagger_{1\sigma}\hat{c}_{p\sigma} + \mathrm{H.c.}\right). \tag{7.13}$$

Here, the first two terms describe the local Hamiltonian of the impurity site $1$, and they are directly adopted from the Hubbard model. Further, the last two terms give the on-site energies $\epsilon_p$ of the bath sites $p > 1$ and $V_p$ is the hybridization matrix element between the impurity site and the bath site $p$. Note that there is no interaction at the bath sites. The SIAM is illustrated in Fig. 7.4.

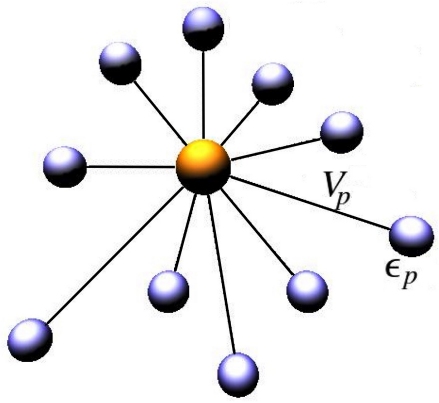


Figure 7.4: Single-impurity Anderson model. An impurity site is connected via the hopping energy $V_p$ to a set of non-interacting bath sites with on-site energies $\epsilon_p$.

The bath parameters give the SIAM hybridization function as [40, 69]

$$\Lambda^{\mathrm{SIAM}}(\mathrm{i}\omega_n) = \sum_p V_p g_p^M(\mathrm{i}\omega_n) V_p^* = \sum_p \frac{|V_p|^2}{\mathrm{i}\omega_n - \epsilon_p}, \tag{7.14}$$

where the Green function of an isolated bath site reads

$$g_p^M(\mathrm{i}\omega_n) = \frac{1}{\mathrm{i}\omega_n - \epsilon_p}. \tag{7.15}$$

In order for the SIAM to represent the DMFT action in Eq. (7.2), the initially unknown parameters $\epsilon_p$ and $V_p$ need to be chosen such that

$$\Lambda^{\mathrm{SIAM}}(\mathrm{i}\omega_n) = \Lambda(\mathrm{i}\omega_n), \tag{7.16}$$

where $\Lambda(\mathrm{i}\omega_n)$ is the hybridization function in Eq. (7.4). This condition can be strictly satisfied only if there is an infinite number of bath sites. However, in practical implementations only a finite number of bath sites are used, which results in a reduced accuracy of the method due to bath discretization. Equations (7.7)–(7.12) remain valid in the Hamiltonian representation with the hybridization function being $\Lambda^{\mathrm{SIAM}}(\mathrm{i}\omega_n)$.

### 7.2.3 Self-consistency loop

In the general case, the DMFT self-consistency loop is iterated for example in the following manner (see also Ref. [40]).

(i) Determine the hybridization function $\Lambda(\mathrm{i}\omega_n)$ which defines the impurity model. This is done as follows. Obtain $\Sigma_{\mathrm{latt}}(\mathrm{i}\omega_n)$ (in the first iteration one can set, e.g., $\Sigma_{\mathrm{latt}}(\mathrm{i}\omega_n) = 0$), compute the local part of the lattice Green function $G^M_{\mathrm{latt},jj}(\mathrm{i}\omega_n)$ from Eq. (7.11), and with Eqs. (7.10) and (7.12), solve for the hybridization function $\Lambda(\mathrm{i}\omega_n)$ in Eq. (7.9).

(ii) With $\Lambda(\mathrm{i}\omega_n)$, compute the impurity Green function in Eq. (7.8) using *an impurity solver*[4], and obtain the impurity self-energy $\Sigma_{\mathrm{imp}}(\mathrm{i}\omega_n)$ via the Dyson equation in Eq. (7.9).

(iii) Set $\Sigma^{\mathrm{new}}_{\mathrm{latt}}(\mathrm{i}\omega_n) = \Sigma_{\mathrm{imp}}(\mathrm{i}\omega_n)$.

(iv) Check if the self-energy has converged, i.e., if $\Sigma^{\mathrm{new}}_{\mathrm{latt}}(\mathrm{i}\omega_n) = \Sigma^{\mathrm{prev}}_{\mathrm{latt}}(\mathrm{i}\omega_n)$. If not, go to step (i) with the new self-energy and repeat.[5]

The self-consistency loop becomes particularly simple in the special case of the infinite-dimensional Hubbard model in a Bethe lattice (also called a Cayley tree) with a semi-circular density of states given by [67]

$$D(\epsilon) = \frac{\sqrt{4J_\infty^2 - \epsilon^2}}{2\pi J_\infty^2}, \tag{7.17}$$

where $J_\infty$ is hopping in the infinite-dimensional Hubbard model. See Fig. 7.5 for an illustration of the Bethe lattice with coordination number $z_d = 3$. One can show that the hybridization function of the impurity model is related to the local part of the Bethe lattice Green function by [40]

$$\Lambda(\mathrm{i}\omega_n) = J_\infty^2 G^M_{\mathrm{latt},jj}(\mathrm{i}\omega_n). \tag{7.18}$$

Thus, once an initial guess for $\Lambda(\mathrm{i}\omega_n)$ has been set, the impurity Green function can be computed. This then gives $G^M_{\mathrm{latt},jj}(\mathrm{i}\omega_n)$ via Eq. (7.10) and an updated $\Lambda(\mathrm{i}\omega_n)$ via

[4]The choice of the impurity solver depends on the representation of the impurity problem, which can be the DMFT action or the SIAM Hamiltonian, as well as on the interaction strength.

[5]We point out that there is no guarantee that the method converges in general or that the solution found via the procedure is unique. However, in practise the method is usually found to converge and the solution is often unique [301].

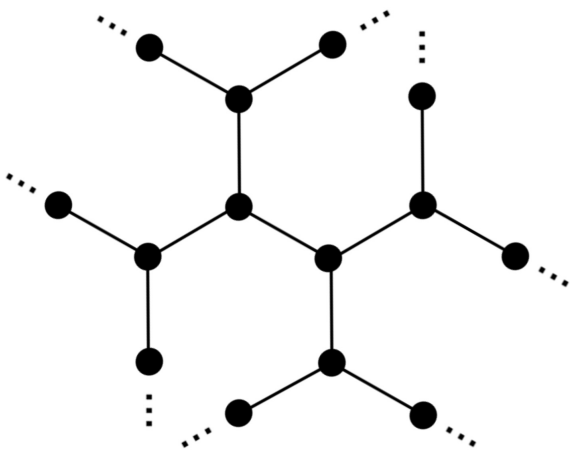

Figure 7.5: Bethe lattice. We illustrate a part of a Bethe lattice with coordination number $z_d = 3$.

Eq. (7.18). The procedure is repeated until convergence has been reached. Because of the simplicity of the self-consistency condition, the Bethe lattice is often chosen as the starting point for benchmarking DMFT simulations before advancing to more realistic lattice geometries. In Chapters 8 and 9, we consider the Hubbard model only in the Bethe lattice.

## 7.3 Non-equilibrium dynamical mean-field theory

DMFT has been successfully extended to describe non-equilibrium strongly correlated quantum dynamics [41]. The standard model studied in non-equilibrium DMFT is the time-dependent Hubbard model in Eq. (2.7). Here, we describe how the equilibrium DMFT formalism generalises to out-of-equilibrium problems.

### 7.3.1 Non-equilibrium DMFT equations

The DMFT action for non-equilibrium problems is given by [41]

$$\begin{aligned}\hat{S} = &-\mathrm{i}\int_{\mathcal{C}} d\bar{z}\,\left[U(\bar{z})\left(\hat{n}_{\uparrow}(\bar{z})-\frac{1}{2}\right)\left(\hat{n}_{\downarrow}(\bar{z})-\frac{1}{2}\right)-\mu\sum_{\sigma}\hat{n}_{\sigma}(\bar{z})\right]\\ &-\mathrm{i}\int_{\mathcal{C}} d\bar{z}\int_{\mathcal{C}} d\bar{z}'\sum_{\sigma}\hat{c}^{\dagger}_{\sigma}(\bar{z})\Lambda(\bar{z},\bar{z}')\hat{c}_{\sigma}(\bar{z}'),\end{aligned} \tag{7.19}$$

where $\mathcal{C}$ is the L-shaped time contour in Fig. 2.3, and $\Lambda(\bar{z}, \bar{z}')$ is the two-time non-equilibrium hybridization function. The time argument $\bar{z}$ is real time $t$ on the horizontal real time branch of $\mathcal{C}$ and imaginary time $\tau$ on the vertical imaginary time branch of $\mathcal{C}$. We point out that on the vertical branch, $\Lambda(\bar{z}, \bar{z}') = \Lambda(\tau - \tau')$, and Eq. (7.19) reduces to Eq. (7.2).

The equilibrium DMFT equations generalize to the non-equilibrium case in the following manner. The goal is to compute the impurity Green function

$$G_{\mathrm{imp}}(z, z') = -\mathrm{i}\langle \mathcal{T}_{\mathcal{C}} \hat{c}_{\sigma}(z) \hat{c}^{\dagger}_{\sigma'}(z') \rangle_S. \tag{7.20}$$

To determine $G_{\mathrm{imp}}(z, z')$, the auxiliary concepts from the equilibrium case need to be generalized to time-dependent problems. The non-equilibrium Weiss function is defined via the equation [41]

$$\mathcal{G}_0^{-1}(z, z') = \delta_{\mathcal{C}}(z, z')(\mathrm{i}\partial_z + \mu) - \Lambda(z, z'). \tag{7.21}$$

The impurity self-energy $\Sigma_{\mathrm{imp}}(z, z')$ is obtained from the Dyson equation

$$\left[(\mathcal{G}_0^{-1} - \Sigma_{\mathrm{imp}}) * G_{\mathrm{imp}}\right](z, z') = \delta_{\mathcal{C}}(z, z'), \tag{7.22}$$

where on the left hand side we have used the contour convolution in Eq. (2.85). The hybridization function $\Lambda(z, z')$ must be chosen such that the impurity Green function and impurity self-energy match the local part of the lattice Green function and local lattice self-energy, respectively, i.e.,

$$G_{\mathrm{imp}}(z, z') = G_{\mathrm{latt},jj}(z, z'), \tag{7.23}$$

$$\Sigma_{\mathrm{imp}}(z, z') = \Sigma_{\mathrm{latt},jj}(z, z') \equiv \Sigma_{\mathrm{latt}}(z, z'). \tag{7.24}$$

Here, $G_{\mathrm{latt},jj}$ and $\Sigma_{\mathrm{latt}}$ are related by the lattice Dyson equation which is given in momentum space by [41]

$$(\mathrm{i}\partial_z + \mu - \epsilon_{\mathbf{k}})\, G_{\mathrm{latt},\mathbf{k}}(z, z') - \left[\Sigma_{\mathrm{latt}} * G_{\mathrm{latt},\mathbf{k}}\right](z, z') = \delta_{\mathcal{C}}(z, z'), \tag{7.25}$$

where $\epsilon_{\mathbf{k}}$ is the lattice dispersion. The local part of the lattice Green function is obtained by summing $G_{\mathrm{latt},\mathbf{k}}$ over momentum, [41]

$$\begin{aligned} G_{\mathrm{latt},jj}(z,z') &= \sum_{\mathbf{k}} G_{\mathrm{latt},\mathbf{k}}(z,z') \\ &= \int d\epsilon\, D(\epsilon) G_{\mathrm{latt},\mathbf{k}}(z,z')|_{\epsilon=\epsilon_{\mathbf{k}}}. \end{aligned} \tag{7.26}$$

Similarly to the equilibrium case, Eqs. (7.20)–(7.26) need to be solved iteratively (for technical details, see Refs. [41, 78]). The self-consistency loop of equilibrium DMFT in Section 7.2.3 can be adapted to the non-equilibrium case by replacing the Matsubara frequency arguments by the two-time argument $z, z'$ in addition to the following changes in the equations

- Eq. (7.8) $\rightarrow$ Eq. (7.20),
- Eq. (7.9) $\rightarrow$ Eq. (7.22),
- Eq. (7.10) $\rightarrow$ Eq. (7.23),
- Eq. (7.11) $\rightarrow$ Eq. (7.26),
- Eq. (7.12) $\rightarrow$ Eq. (7.24).

In the special case of the time-dependent Hubbard model in Eq. (2.7) in a Bethe lattice, Eq. (7.18) generalises to [302]

$$\Lambda(z,z') = J_{\infty}(z) G_{\mathrm{latt},jj}(z,z') J_{\infty}(z'). \tag{7.27}$$

This again significantly simplifies self-consistency loop as explained after Eq. (7.18). We only use the simplified self-consistency loop with Eq. (7.27) in Chapter 9.

### 7.3.2 Hamiltonian approach to non-equilibrium DMFT

The non-equilibrium DMFT action in Eq. (7.19) can represented with a SIAM with time-dependent parameters given by [300]

$$\begin{aligned}
\hat{H}_{\mathrm{SIAM}}(t) &= \hat{H}_{\mathrm{loc}}(t) + \hat{H}_{\mathrm{bath}}(t) + \hat{H}_{\mathrm{hyb}}(t), && (7.28)\\
\hat{H}_{\mathrm{loc}}(t) &= U(t)\left(\hat{n}_{1\uparrow} - \frac{1}{2}\right)\left(\hat{n}_{1\downarrow} - \frac{1}{2}\right) - \mu\sum_{\sigma}\hat{n}_{1\sigma}, && (7.29)\\
\hat{H}_{\mathrm{hyb}}(t) &= \sum_{p>1}\left(V_p(t)\hat{c}^{\dagger}_{1\sigma}\hat{c}_{p\sigma} + \mathrm{H.c.}\right), && (7.30)\\
\hat{H}_{\mathrm{bath}}(t) &= \sum_{p>1,\sigma}\epsilon_p(t)\hat{c}^{\dagger}_{p\sigma}\hat{c}_{p\sigma}. && (7.31)
\end{aligned}$$

Again, the parameters $V_p(t)$ and $\epsilon_p(t)$ give the hybridization function as [compare with Eq. (7.14)]

$$\Lambda^{\mathrm{SIAM}}(z,z') = \sum_{p} V_p(z) g_p(z,z') V_p(z')^*. \tag{7.32}$$

Here, the Green function of an isolated bath site is given by [300]

$$g_p(z,z') = -\mathrm{i}\left\{\theta_{\mathcal{C}}(t,t') - n_F\left[\epsilon_p(0)\right]\right\}\mathcal{E}(z)\mathcal{E}(z')^{-1}, \tag{7.33}$$

where

$$\mathcal{E}(z) = \begin{cases} e^{-\mathrm{i}\int_0^t d\bar{t}\,\epsilon_p(\bar{t})}, & \text{for } z = t \\ e^{-\tau\epsilon_p(0)}, & \text{for } z = \tau \end{cases}. \tag{7.34}$$

The parameters must be chosen such that

$$\Lambda^{\mathrm{SIAM}}(z,z') = \Lambda(z,z') \tag{7.35}$$

holds on the entire time contour $\mathcal{C}$.

Contrary to the equilibrium case, *two* different SIAM hybridization functions are required to fulfil Eq. (7.35) out of equilibrium [78, 300]. The first function, $\Lambda^{\mathrm{SIAM}}_{-}(z,z')$, describes initial correlations in the system, i.e., bath sites that are coupled to the impurity site already at $t = 0$. The second function, $\Lambda^{\mathrm{SIAM}}_{+}(z,z')$, describes the dynamical build-up of correlations, i.e., bath sites that become coupled

to the impurity for $t > 0$. In Chapter 9, we consider for simplicity a system which is initially in the atomic limit, in which case $\Lambda^{\rm SIAM}_{-}(z, z') = 0$. Thus, here we consider only $\Lambda^{\rm SIAM}_{+}(t, t') \equiv \Lambda^{\rm SIAM}(t, t')$. We focus on real-time arguments, since all imaginary-time components of $\Lambda^{\rm SIAM}_{+}$ vanish. We can then write the hybridization function in terms of the lesser and greater components as

$$\Lambda^{\rm SIAM}(t, t') \;=\; \theta_{\mathcal{C}}(t, t')\Lambda^{>}(t, t') + \theta_{\mathcal{C}}(t', t)\Lambda^{<}(t, t'). \tag{7.36}$$

We can obtain a simple relation between $\Lambda^{\rm SIAM}(t, t')$ and the bath parameters, if we choose for simplicity that the bath energies have an initial value $\epsilon_p(0) \neq 0$ and for $t > 0$ they are set to zero [300]. Considering the case of zero temperature, we can have two sets of bath sites: initially occupied sites with energy $\epsilon_p(0) < 0$ and Green function $g_p(t, t') = \mathrm{i}\theta_{\mathcal{C}}(t', t)$, and initially unoccupied sites with energy $\epsilon_p(0) > 0$ and Green function $g_p(t, t') = -\mathrm{i}\theta_{\mathcal{C}}(t, t')$. Thus, we can write the hybridization function as

$$\Lambda^{\rm SIAM}(t, t') = \mathrm{i}\theta_{\mathcal{C}}(t', t) \sum_{p\,\text{occ.}} V_p(t)V_p(t')^* - \mathrm{i}\theta_{\mathcal{C}}(t, t') \sum_{p\,\text{unocc.}} V_p(t)V_p(t')^*. \tag{7.37}$$

Comparing this with Eq. (7.36), we can identify that

$$-\mathrm{i}\Lambda^{<}(t, t') \;=\; \sum_{p\,\text{occ.}} V_p(t)V_p(t')^*, \tag{7.38}$$

$$\mathrm{i}\Lambda^{>}(t, t') \;=\; \sum_{p\,\text{unocc.}} V_p(t)V_p(t')^*. \tag{7.39}$$

For a particle-hole symmetric system which we consider in Chapter 9, we have $\Lambda^{<}(t, t') = \Lambda^{>}(t, t')^*$, which is satisfied when the occupied and unoccupied bath sites come in pairs with complex conjugate hoppings [300]. It is then sufficient to solve either Eq. (7.38) or Eq. (7.39). We focus on Eq. (7.38) and take it that there is an equal number of occupied and unoccupied sites. We refer to the initially occupied sites as the lesser bath and to the initially unoccupied sites as the greater bath.

The form of Eq. (7.38) implies that the parameters $V_p(t)$ can be obtained from the matrix $-\mathrm{i}\Lambda^{<}(t_n, t_{n'}) \equiv (-\mathrm{i}\Lambda^{<})_{nn'}$ (with discretized time $t = n \times \delta t$, where $n$ is an

integer and $\delta t$ is the size of the time step) via a Cholesky decomposition [303] of the form $-\mathrm{i}\Lambda^< = QQ^\dagger$, where $Q$ is a lower triangular matrix whose elements give the parameters $V_p(t)$ [300]. The use of the Cholesky decomposition is efficient since the self-consistent update of the parameters $V_p(t)$ is done time step by time step, and earlier, already self-consistent parameter values do not need to be updated [300]. However, for a finite number $N_b = 2L_b$ of bath sites (with $L_b$ occupied and $L_b$ unoccupied sites), this Cholesky decomposition can be done exactly only for the first $L_b$ time-steps when we have enough free parameters $V_p(t_n)$.

After the first $L_b$ time-steps, the hybridization function gets updated by one row and column following an optimisation procedure [300]. This is done as follows. We denote by $Q^{(s)}$ the lower triangular matrix for time step $s$ such that

$$(-\mathrm{i}\Lambda^<)_s \approx Q^{(s)}(Q^{(s)})^\dagger, \tag{7.40}$$

where $(-\mathrm{i}\Lambda^<)_s$ is an $s \times s$ matrix with elements $(-\mathrm{i}\Lambda^<)_{nn'}$. For time steps $s \leq L_b$, Eq. (7.40) is exact and given by the Cholesky decomposition. We assume now that we have obtained a self-consistent $Q^{(s)}$ for some $s \geq L_b$. For time-step $s+1$, the matrix $(-\mathrm{i}\Lambda^<)_s$ gets updated by one row, denoted by the vector $\vec{a}_{s+1} = ((-\mathrm{i}\Lambda^<)_{s+1,1}, \ldots, (-\mathrm{i}\Lambda^<)_{s+1,s})$, and by one column given by $\vec{a}^\dagger_{s+1}$. We now need to find a $1 \times L_b$ row vector $\vec{q}_{s+1}$ such that

$$(-\mathrm{i}\Lambda^<)_{s+1} \approx Q^{(s+1)}(Q^{(s+1)})^\dagger, \tag{7.41}$$

where

$$(-\mathrm{i}\Lambda^<)_{s+1} = \begin{pmatrix} (-\mathrm{i}\Lambda^<)_s & \vec{a}^\dagger_{s+1} \\ \vec{a}_{s+1} & (-\mathrm{i}\Lambda^<)_{s+1,s+1} \end{pmatrix}, \tag{7.42}$$

and

$$Q^{(s+1)} = \begin{pmatrix} Q^{(s)} & (\vec{0}_s)^\dagger \\ \vec{q}_{s+1} & \vec{0}_{s+1-L_b} \end{pmatrix}. \tag{7.43}$$

Here, $\vec{0}_s$ is a row vector with $s$ zeros. Note that $Q^{(s+1)}$ only has $L_b$ columns with non-zero elements since we only have $L_b$ sites in the lesser bath. Since we know that $(-\mathrm{i}\Lambda^<)_s \approx Q^{(s)}(Q^{(s)})^\dagger$, we find $\vec{q}_{s+1}$ by solving the optimisation problem [300]

$$\min_{\vec{q}_{s+1}} \left\{ \left\| \vec{q}_{s+1}(Q^{(s)})^\dagger - \vec{a}_{s+1} \right\|^2 + \left| \vec{q}_{s+1}(\vec{q}_{s+1})^\dagger - (-\mathrm{i}\Lambda^<)_{s+1,s+1} \right|^2 \right\}, \tag{7.44}$$

where $\|\cdot\|$ is the Euclidean norm. The optimal $\vec{q}_{s+1}$ is used as an approximate update for the matrix $Q^{(s+1)}$. The procedure is repeated until a self-consistent $\vec{q}_{s+1}$ has been found. We emphasize that the update from time step $s$ to $s+1$ does not modify the previously calculated, self-consistent parameters $V_p(t_n)$ for $n \leq s$. Further technical details can be found in Ref. [300].

## 7.4 Classical impurity solvers and their limitations

Several numerical methods have been developed to calculate the impurity Green function in Eqs. (7.8) and (7.20). They can be broadly divided into diagrammatic methods, which compute the impurity Green function using diagrammatic expansions, and into Hamiltonian-based methods which do not entail diagrammatic techniques.

### 7.4.1 Diagrammatic methods

#### 7.4.1.1 Many-body perturbation theory

Diagrammatic many-body perturbation theory [69] was one of the earliest impurity solvers both in the equilibrium [40] and in the non-equilibrium [41] case. This method is usually divided into weak coupling and strong coupling solvers. Weak coupling perturbation theory relies on a small-order expansion of the self-energy in terms of Feynman diagrams. The resulting diagrams are then summed up analytically to obtain the self-energy in the DMFT self-consistency loop. This scheme can lead to a non-physical drifting of the total energy with time (even for a time-independent Hamiltonian) if the underlying approximations in the perturbation

expansion are not conserving [41, 69]. In this case the method remains accurate only for a short time. Strong coupling perturbation theory, on the other hand, computes the impurity Green function by expanding the DMFT action with respect to the hybridization term and then analytically summing the resulting small-order strong coupling diagrams [41]. We point out that perturbation theory methods cannot in general describe intermediate interactions accurately due to the lack of a small expansion parameter [41].

#### 7.4.1.2 Continuous-time quantum Monte Carlo

Continuous-time quantum Monte Carlo (CT-QMC) [304] is a diagrammatic method like perturbation theory but instead of exact summations of small-order diagrammatic expansions, it samples Feynman diagrams stochastically with appropriate (probability) weights. Similarly to perturbation theory, CT-QMC methods usually rely on either an interaction (weak coupling) or a hybridization (strong coupling) expansion.

When dealing with fermions, CT-QMC is often plagued with the sign problem [305] where the anticommutative fermionic statistics leads to rapidly varying sign changes that make the computation of expectation values of observables challenging. In addition, out of equilibrium CT-QMC suffers from a phase problem, also called 'dynamical sign problem', where the weights of the Feynman diagrams become complex due to the real-time branches of the contour $\mathcal{C}$. The phase problem becomes worse with increasing time, and as a result, CT-QMC is usually limited only to short times. For further details, see Ref. [41] and references therein.

Finally, CT-QMC is formulated for finite temperatures using the Matsubara formalism, and low temperatures are more challenging to describe with the method. The analytic continuation from Matsubara to real frequencies is not always numerically well-defined due to numerical noise resulting from the Monte Carlo sampling [75].

### 7.4.2 Hamiltonian-based methods

#### 7.4.2.1 Exact diagonalization

Exact diagonalization (ED) techniques [40,300] rely on the finite-dimensional SIAM Hamiltonian to compute the impurity Green function. The computational effort grows exponentially with the number of bath sites, which restricts these methods to relatively small sizes of the SIAM Hamiltonian. This limits the accuracy of the method. Furthermore, in the non-equilibrium case, more bath sites are required to describe longer times [300], and the accessible time is thus limited. On the other hand, since ED does not rely on a small expansion parameter, it can describe all interaction strengths accurately.

#### 7.4.2.2 Matrix product states

Matrix product state (MPS) impurity solvers [306–311], can usually access larger system sizes in the SIAM than ED, since the MPS representation of the state (see Appendix C) allows a quasi-exact description with a bond dimension that is much smaller than the dimension of the Hilbert space. In equilibrium DMFT, these methods are interesting for example since they can work directly on the real-frequency axis, thus avoiding the problem of the numerically ill-defined analytic continuation of CT-QMC [75], as well as being able to tackle multiband models. Out of equilibrium, MPSs can reach longer times than ED and are accurate for all interaction strengths [309]. However, large bond dimensions on the order of 1000 or larger are required [309], meaning that these methods are still computationally expensive.

# Chapter 8

## Few-qubit quantum-classical simulation of the infinite-dimensional Hubbard model

In this Chapter, we describe a proof-of-principle setup for a hybrid quantum-classical simulation of the infinite-dimensional Hubbard model. The results presented in this Chapter have been published in Ref. [3].

## 8.1 Introduction

In Chapter 7, we introduced the widely-adopted dynamical mean-field theory method. We also presented some classical solvers of the DMFT impurity problem and their limitations. The solution of the impurity problem is the bottleneck of classical DMFT schemes, and therefore it is worth considering alternative approaches to the classical numerical methods. Here, we propose a scenario where the impurity problem is solved with a *quantum simulator*, thus avoiding many issues that are inherent to the classical methods such as the fermionic sign problem in quantum Monte Carlo and the high computational cost of studying large impurity problems with Hamiltonian-based methods. So far, quantum simulation of fermionic models has been mostly restricted to the analogue paradigm, especially with ultracold atoms in optical lattices (see Chapter 3). Digital simulation approaches (see Chapter 6) have started to emerge in recent years, for example

based on superconducting circuits [11, 34, 244, 312]. The number of qubits in these digital simulators is, however, presently rather small. Thus, a direct implementation of the Hubbard model would suffer from severe finite size effects. It is nevertheless still possible for a digital quantum simulator with a restricted number of qubits to describe fermionic models directly in the thermodynamic limit when the DMFT approach is adopted. We therefore also provide a scientific application for small quantum devices with a limited number of qubits.

Here, we demonstrate this alternative method to solve the DMFT impurity problem with a proof-of-principle example. We focus on the minimal incarnation of DMFT, the so-called 'two-site' DMFT [313], where the impurity model consists of one impurity site and only one bath site. Both sites have local Hilbert space dimension four. The two-site system is subjected to two specially chosen self-consistency conditions that replace the self-consistency loop of full DMFT in Section 7.2.3. Since two-site DMFT considers only the smallest possible impurity model, the approach cannot match the accuracy of full DMFT, but it can still give a *qualitatively* correct description of the infinite-dimensional Hubbard model, and its simplicity makes it a good starting point before advancing to more accurate schemes. By a qualitatively correct description, we mean that two-site DMFT correctly predicts the existence of a Mott transition in the half-filled Hubbard model and that the spectral function has two Hubbard bands and a quasiparticle peak between them, but for example overestimates the quasiparticle weights in the metallic phase and the shape of the spectral function differs from that of full DMFT. For explicit details of two-site DMFT and its features compared to full DMFT, we refer to Ref. [313]. Note that two-site DMFT is only able to provide a qualitatively correct description of the Hubbard model even in infinite dimensions [313].

The two-site system corresponds to four qubits, two for the impurity site and two for the bath site, while a fifth, ancillary qubit is used for measurements. This

number of qubits is readily available in current digital quantum simulator platforms, with IBM having made a five-qubit quantum processor available to the public [314]. A nine-qubit processor has already been demonstrated in superconducting circuits [34,312,315]. Trapped-ion technologies also allow for digital quantum simulations with up to six qubits [21,33]. Being commensurate with current state-of-the-art technology is a further justification for studying this minimal model. As shown in Chapter 9, our scheme is readily generalisable to a larger number of qubits, allowing for more accurate simulations and potentially offering an exponential speed-up over classical Hamiltonian-based DMFT methods. For example, the number of multiqubit Mølmer–Sørensen gates given by Eq. (6.14) scales only linearly with the number of bath sites, enabling efficient simulations [227,260,280].

The self-consistency conditions are taken care of iteratively in a classical feedback loop, which thus completes the non-linear, hybrid quantum-classical device we introduce. Similar hybrid devices for DMFT calculations have been proposed in Ref. [221]. Quantum gates similar to the ones needed in the two-site scheme have been used in demonstrating digital quantum simulation of fermionic models with superconducting circuits [34,260] (see also Section 6.2.1). We thus focus on superconducting circuits as a candidate platform, although, e.g., trapped ions (see Section 6.2.2) or any other digital quantum simulation platform could in principle also be considered.

The rest of this Chapter is organised as follows. Section 8.2 introduces the two-site DMFT scheme. Section 8.3 discusses the implementation of this two-site scheme with special attention to superconducting circuits. In Section 8.4, we show the results of our analysis, and give a summary in Section 8.5. We present the derivation of one of the two-site DMFT self-consistency conditions in Appendix E and give an outline of the single-qubit interferometry measurement scheme in Appendix F.

## 8.2 Quantum simulator based on two-site DMFT

We consider the paramagnetic Hubbard model given by Eq. (2.5) in an infinite-dimensional Bethe lattice in the thermodynamic limit at zero temperature. This setup has very simple self-consistency relations, which makes it an ideal test-bed for a proof-of-principle demonstration of a hybrid quantum-classical scheme.

In terms of the single-impurity Anderson model (SIAM), the smallest impurity problem involves one fermionic site corresponding to the impurity and only one fermionic site corresponding to the entire dynamical mean-field. Since two qubits are needed to encode the local Hilbert space of a fermionic site, we only require four physical qubits to implement this representation in the lab. The SIAM Hamiltonian for only one bath site reads

$$\hat{H}_{\mathrm{SIAM},2} = U\hat{n}_{1\downarrow}\hat{n}_{1\uparrow} - \mu\sum_{\sigma}\hat{n}_{1\sigma} + \sum_{\sigma}\epsilon_c\hat{c}^{\dagger}_{2\sigma}\hat{c}_{2\sigma} + \sum_{\sigma}V\left(\hat{c}^{\dagger}_{1\sigma}\hat{c}_{2\sigma} + \mathrm{H.c.}\right). \tag{8.1}$$

Here, the subindex 2 of the SIAM Hamiltonian on the left hand side refers to the two-site system. The parameters $\epsilon_c$ and $V$ describe the on-site energy of the non-interacting bath site 2 and hopping between the impurity and the bath site, respectively, and give the hybridization function in Eq. (7.14) as

$$\Lambda(\omega) = \frac{V^2}{\omega - \epsilon_c}. \tag{8.2}$$

Here, we have denoted the SIAM hybridization function by $\Lambda$ instead of $\Lambda^{\mathrm{SIAM}}$ for simplicity. Note that Matsubara formalism is not required since we consider the zero temperature case. See Fig. 8.1 for illustration of the two-site SIAM.

For any finite number of bath sites, the self-consistency condition (7.10) can only be approximately satisfied. In the extreme case of two-site DMFT, it turns out to be more suitable to reformulate Eq. (7.10) in a manner specially focused on this minimal representation [313]. Thus, the initially unknown parameters $\epsilon_c$ and $V$ need to be determined such that two chosen self-consistency conditions are satisfied [313].


Figure 8.1: Two-site SIAM. The minimal Hamiltonian representation of the DMFT problem involves the impurity site, with on-site interaction $U$ and chemical potential $\mu$, coupled via the hopping energy $V$ to only one bath site. The bath site has on-site energy $\epsilon_c$.

The first condition is intuitive and requires that the electron filling $n_{\rm imp}$ of the impurity site and the filling $n_{\rm latt} = \langle n_{j\downarrow}\rangle + \langle n_{j\uparrow}\rangle$ of the translationally-invariant lattice model match, i.e.,

$$n_{\rm imp} \equiv n_{\rm latt}. \tag{8.3}$$

Formally this condition emerges from the comparison of the high-frequency (i.e., $1/\omega \to 0$) expansions of the impurity and lattice self-energies given by [313,316]

$$\Sigma_{\rm imp/latt}(\omega) = U\frac{n_{\rm imp/latt}}{2} + \frac{U\frac{n_{\rm imp/latt}}{2}(1-\frac{n_{\rm imp/latt}}{2})}{\omega} + \mathcal{O}(\omega^{-2}). \tag{8.4}$$

The second self-consistency condition is given by

$$V^2 = \mathcal{Z}M_2^{(0)} = \mathcal{Z}\int_{-\infty}^{\infty} d\epsilon\, \epsilon^2 D(\epsilon) = \mathcal{Z}J_\infty^2, \tag{8.5}$$

where quasiparticle weight reads

$$\mathcal{Z} = \left[1 - \frac{d{\rm Re}[\Sigma_{\rm imp}(\omega + {\rm i}0^+)]}{d\omega}\Big|_{\omega=0}\right]^{-1}. \tag{8.6}$$

In Eq. (8.5), $M_2^{(0)} = \int_{-\infty}^{\infty} d\epsilon\, \epsilon^2 D(\epsilon)$ is the second moment of the non-interacting density of states $D(\epsilon)$, and the final equality follows from the semicircular $D(\epsilon)$ of the Bethe lattice in Eq. (7.17). We derive Eq. (8.5) in Appendix E.

### 8.2.1 Two-site DMFT protocol

The hybrid quantum-classical device implementing two-site DMFT consists of a few-qubit digital quantum simulator in which the impurity Green function is measured and of a classical feedback loop in which the parameters of the two-site SIAM are updated. The two-site DMFT protocol is summarized in Fig. 8.2 and proceeds as follows (see also Ref. [313]).

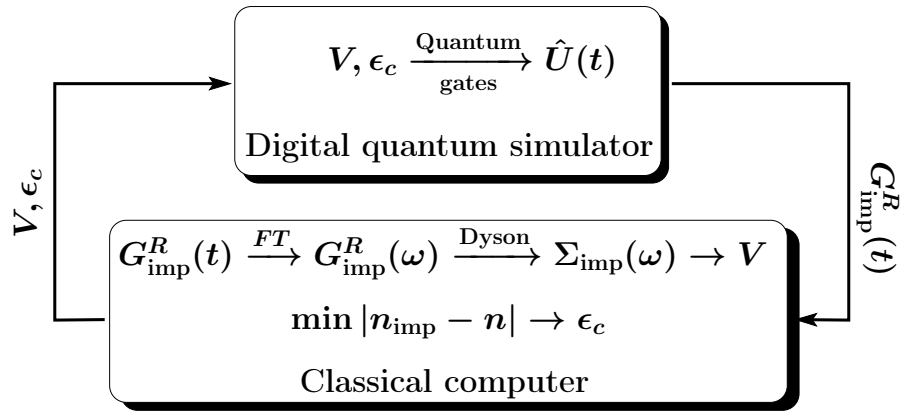


Figure 8.2: Non-linear hybrid quantum-classical scheme. A digital quantum simulator works in conjunction with a classical feedback loop to perform a proof-of-principle demonstration of a two-site DMFT calculation. Figure from Ref. [3].

1. First fix $U$ and $\mu$ to the desired values in the SIAM and set the unknown parameters $\epsilon_c$ and $V$ equal to an initial guess.

2. Measure the interacting retarded impurity Green function

$$\mathrm{i}G^R_{\text{imp}}(t) = \theta(t)\langle\{\hat{c}_{1\sigma,H}(t), \hat{c}^\dagger_{1\sigma,H}(0)\}\rangle_{GS}. \tag{8.7}$$

   This can be done using, e.g., single-qubit interferometry (see details in Appendix F). In short, an ancilla qubit interacts twice with the system via two-qubit gates, with the first time being before the system undergoes the dynamics governed by the SIAM Hamiltonian and the second time after the time-evolution. The $\hat{\sigma}^z$ and $\hat{\sigma}^y$ components of the ancilla are then measured at the end of the sequence which is repeated several times.

3. After Fourier-transforming the impurity Green function, the impurity self-energy is obtained classically from the Dyson equation

$$\Sigma_{\text{imp}}(\omega) = \mathcal{G}_0(\omega)^{-1} - G^R_{\text{imp}}(\omega)^{-1}. \tag{8.8}$$

   Here, the Weiss function is given by

$$\mathcal{G}_0^{-1}(\omega) = \omega + \mu - \Lambda(\omega). \tag{8.9}$$

From the derivative of the self-energy one obtains the quasiparticle weight $\mathcal{Z}$ which directly yields the updated hopping parameter $V$ via Eq. (8.5). The update for $\epsilon_c$ is found by minimizing the difference $|n_{\mathrm{imp}} - n|$ [313].

4. Steps 2 and 3 need to be repeated until $V$ and $\epsilon_c$ are self-consistent, and $n_{\mathrm{imp}} = n$.

The self-consistent Green function $G^R_{\mathrm{imp}}(\omega)$ and self-energy $\Sigma_{\mathrm{imp}}(\omega)$ thus obtained are used to calculate approximations to local single-particle properties of the Hubbard model. Note that for larger systems the two-site DMFT steps need to be replaced with the general DMFT self-consistency loop outlined in Section 7.2.3.

## 8.3 Quantum algorithm for the single-impurity Anderson model

Here, we consider the quantum gates of the digital quantum simulator part in Fig. 8.2, considering superconducting circuits as the platform for concreteness.

### 8.3.1 Jordan–Wigner transformation of the SIAM

To implement the two-site SIAM with qubits, the fermionic creation and annihilation operators need to be mapped onto tensor products of spin operators which then act on the qubits via quantum gates. In order to obtain as simple quantum gates as possible in Section 8.3.2 and in Appendix F, we consider an ordering of the qubits where the first two qubits encode the spin $\downarrow$ for both fermionic sites while the last two correspond to spin $\uparrow$. This is achieved via the Jordan–Wigner transformation given explicitly as

$$\hat{c}^\dagger_{1\downarrow} = \hat{\sigma}^-_1 = \frac{1}{2}\left(\hat{\sigma}^x_1 - \mathrm{i}\hat{\sigma}^y_1\right), \tag{8.10}$$

$$\hat{c}^\dagger_{2\downarrow} = \hat{\sigma}^z_1\hat{\sigma}^-_2 = \frac{1}{2}\hat{\sigma}^z_1\left(\hat{\sigma}^x_2 - \mathrm{i}\hat{\sigma}^y_2\right), \tag{8.11}$$

$$\hat{c}^\dagger_{1\uparrow} = \hat{\sigma}^z_1\hat{\sigma}^z_2\hat{\sigma}^-_3 = \frac{1}{2}\hat{\sigma}^z_1\hat{\sigma}^z_2\left(\hat{\sigma}^x_3 - \mathrm{i}\hat{\sigma}^y_3\right), \tag{8.12}$$

$$\hat{c}^\dagger_{2\uparrow} = \hat{\sigma}^z_1\hat{\sigma}^z_2\hat{\sigma}^z_3\hat{\sigma}^-_4 = \frac{1}{2}\hat{\sigma}^z_1\hat{\sigma}^z_2\hat{\sigma}^z_3\left(\hat{\sigma}^x_4 - \mathrm{i}\hat{\sigma}^y_4\right), \tag{8.13}$$

and $\hat{c}_{j\sigma} = \left(\hat{c}^\dagger_{j\sigma}\right)^\dagger$. Here, $\hat{\sigma}^x_l$, $\hat{\sigma}^y_l$, and $\hat{\sigma}^z_l$ are spin-$\frac{1}{2}$ Pauli operators for qubit $l$.

With the mappings in Eqs. (8.10)–(8.13), the hybridization terms in the SIAM described in Eq. (8.1) transform into

$$V\left(\hat{c}^\dagger_{1\downarrow}\hat{c}_{2\downarrow} + \text{H.c.}\right) = \frac{V}{2}\left(\hat{\sigma}^x_1\hat{\sigma}^x_2 + \hat{\sigma}^y_1\hat{\sigma}^y_2\right), \tag{8.14}$$

and

$$V\left(\hat{c}^\dagger_{1\uparrow}\hat{c}_{2\uparrow} + \text{H.c.}\right) = \frac{V}{2}\left(\hat{\sigma}^x_3\hat{\sigma}^x_4 + \hat{\sigma}^y_3\hat{\sigma}^y_4\right). \tag{8.15}$$

The number operators become

$$\hat{n}_{1\downarrow} = \frac{1}{2}\left(\hat{I} - \hat{\sigma}^z_1\right), \tag{8.16}$$

$$\hat{n}_{2\downarrow} = \frac{1}{2}\left(\hat{I} - \hat{\sigma}^z_2\right), \tag{8.17}$$

$$\hat{n}_{1\uparrow} = \frac{1}{2}\left(\hat{I} - \hat{\sigma}^z_3\right), \tag{8.18}$$

$$\hat{n}_{2\uparrow} = \frac{1}{2}\left(\hat{I} - \hat{\sigma}^z_4\right), \tag{8.19}$$

and thus the interaction term can be written as

$$U\hat{n}_{1\downarrow}\hat{n}_{1\uparrow} = \frac{U}{4}(\hat{\sigma}^z_1\hat{\sigma}^z_3 - \hat{\sigma}^z_1 - \hat{\sigma}^z_3), \tag{8.20}$$

up to a constant. The total Hamiltonian then reads

$$\begin{aligned}\hat{H}_{\text{SIAM,2}} =& \frac{U}{4}\left(\hat{\sigma}^z_1\hat{\sigma}^z_3 - \hat{\sigma}^z_1 - \hat{\sigma}^z_3\right) + \frac{\mu}{2}\left(\hat{\sigma}^z_1 + \hat{\sigma}^z_3\right) - \frac{\epsilon_c}{2}\left(\hat{\sigma}^z_2 + \hat{\sigma}^z_4\right) \\ &+ \frac{V}{2}\left(\hat{\sigma}^x_1\hat{\sigma}^x_2 + \hat{\sigma}^y_1\hat{\sigma}^y_2 + \hat{\sigma}^x_3\hat{\sigma}^x_4 + \hat{\sigma}^y_3\hat{\sigma}^y_4\right),\end{aligned} \tag{8.21}$$

where we have dropped constant terms.

### 8.3.2 Quantum gate decomposition of the time-evolution operator

We now consider how the Jordan–Wigner transformed SIAM in Eq. (8.21) can be implemented in an experimental arrangement based on superconducting circuits.

We present two alternative approaches. The first one couples the qubits with a transmission line resonator, which leads to the $XY$ gate in Eq. (6.8) between the qubits. The second approach is the $\mathrm{CZ}_\phi$ gate in Eq. (6.9), which can be obtained via a capacitive coupling of nearest-neighbour transmon qubits without using a resonator.

In order to use quantum gates for time-evolution, we utilize a Trotter decomposition[1] of the time-evolution operator corresponding to $\hat{H}_{\mathrm{SIAM},2}$ in Eq. (8.21). The first order Trotter expansion is given by

$$\hat{U}(t) = e^{-\mathrm{i}\hat{H}_{\mathrm{SIAM},2}t} \approx \Bigg( e^{-\mathrm{i}\frac{V}{2}(\hat{\sigma}_1^x\hat{\sigma}_2^x+\hat{\sigma}_1^y\hat{\sigma}_2^y)\frac{t}{N_T}} e^{-\mathrm{i}\frac{V}{2}(\hat{\sigma}_3^x\hat{\sigma}_4^x+\hat{\sigma}_3^y\hat{\sigma}_4^y)\frac{t}{N_T}} e^{-\mathrm{i}\frac{U}{4}\hat{\sigma}_1^z\hat{\sigma}_3^z\frac{t}{N_T}} \times e^{\mathrm{i}\left(\frac{U}{4}-\frac{\mu}{2}\right)\hat{\sigma}_1^z\frac{t}{N_T}} e^{\mathrm{i}\left(\frac{U}{4}-\frac{\mu}{2}\right)\hat{\sigma}_3^z\frac{t}{N_T}} e^{\mathrm{i}\frac{\epsilon_c}{2}\hat{\sigma}_2^z\frac{t}{N_T}} e^{\mathrm{i}\frac{\epsilon_c}{2}\hat{\sigma}_4^z\frac{t}{N_T}} \Bigg)^{N_T}. \tag{8.22}$$

Here, $N_T$ is the number of Trotter (i.e., time) steps and $\frac{t}{N_T}$ is the size of the time step.

The Trotterized time-evolution operator in Eq. (8.22) is in the form where the $XY$ gate in Eq. (6.8) can be readily utilized. The quantum circuit for a single Trotter step with these gates is shown in Fig. 8.3a.

To be able to utilize the $\mathrm{CZ}_\phi$ gates in Eq. (6.9), we write the time-evolution operator in Eq. (8.22) in terms of $\hat{\sigma}_l^z\hat{\sigma}_m^z$ (ZZ) interactions, taking into account that

$$\hat{\sigma}_l^x\hat{\sigma}_m^x = \mathcal{R}_y^{(l)}(\tfrac{\pi}{2})\hat{\sigma}_l^z\mathcal{R}_y^{(l)}(-\tfrac{\pi}{2})\mathcal{R}_y^{(m)}(\tfrac{\pi}{2})\hat{\sigma}_m^z\mathcal{R}_y^{(m)}(-\tfrac{\pi}{2}), \tag{8.23}$$

and

$$\hat{\sigma}_l^y\hat{\sigma}_m^y = \mathcal{R}_x^{(l)}(-\tfrac{\pi}{2})\hat{\sigma}_l^z\mathcal{R}_x^{(l)}(\tfrac{\pi}{2})\mathcal{R}_x^{(m)}(-\tfrac{\pi}{2})\hat{\sigma}_m^z\mathcal{R}_x^{(m)}(\tfrac{\pi}{2}), \tag{8.24}$$

where $\mathcal{R}_\alpha^{(l)}(\theta) = \exp(-\mathrm{i}\frac{\theta}{2}\hat{\sigma}_l^\alpha)$ is the rotation along the $\alpha$-axis of qubit $l$. Note that in the computational basis, one can write, e.g.,

$$\exp\left(-\mathrm{i}\,\frac{\phi}{2}\hat{\sigma}_1^z\hat{\sigma}_2^z\right) = \begin{pmatrix} 1 & 0 & 0 & 0 \\ 0 & e^{\mathrm{i}\phi} & 0 & 0 \\ 0 & 0 & e^{\mathrm{i}\phi} & 0 \\ 0 & 0 & 0 & 1 \end{pmatrix}, \tag{8.25}$$

[1] We mention that hybrid algorithms without Trotterization have been considered, e.g., in Ref. [317].

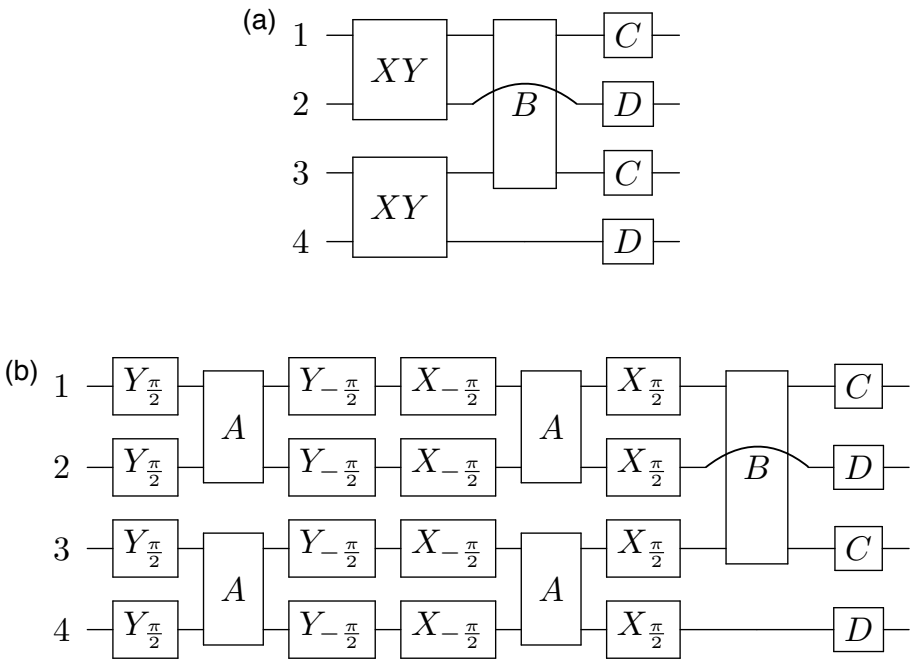


Figure 8.3: Quantum gates for one Trotter step. A single Trotter step is shown for (a) the $XY$ method and (b) the $\mathrm{CZ}_\phi$ method. Here, $B$ is the entangling gate $B = \exp\big(-\mathrm{i}\frac{U}{4}\hat{\sigma}_1^z\hat{\sigma}_3^z\frac{t}{N_T}\big)$, $A$ is a two-qubit gate given by $A = \exp\big(-\mathrm{i}\frac{V}{2}\hat{\sigma}_l^z\hat{\sigma}_m^z\frac{t}{N_T}\big)$, acting on qubits $l$ and $m$, and the quantum gates $C$ and $D$ are single qubit $\hat{\sigma}^z$-gates, given by $C = \exp\Big[\mathrm{i}\big(\frac{U}{4}-\frac{\mu}{2}\big)\hat{\sigma}_l^z\frac{t}{N_T}\Big]$ and $D = \exp\big(\mathrm{i}\frac{\epsilon_c}{2}\hat{\sigma}_l^z\frac{t}{N_T}\big)$, acting on qubit $l$. Finally, $X_\phi$ and $Y_\phi$ are $\phi$-rotations along the $x$ and $y$ axis, respectively. Figure from Ref. [3].

where we have neglected global phases. Thus, we have the decomposition

$$\exp\left(-\mathrm{i}\,\frac{\phi}{2}\hat{\sigma}_1^z\hat{\sigma}_2^z\right) = \mathcal{R}_x^{(1)}(\pi)\,\mathrm{CZ}_\phi\,\mathcal{R}_x^{(1)}(\pi)\mathcal{R}_x^{(2)}(\pi)\,\mathrm{CZ}_\phi\,\mathcal{R}_x^{(2)}(\pi). \tag{8.26}$$

The time-evolution operator in Eq. (8.22) in terms of ZZ interactions is given by

$$\begin{aligned}\hat{U}(t) = e^{-\mathrm{i}\hat{H}_{\mathrm{SIAM},2}t} \approx \Bigg(&\mathcal{R}_y^{(1234)}(\tfrac{\pi}{2})e^{-\mathrm{i}\frac{V}{2}\hat{\sigma}_1^z\hat{\sigma}_2^z\frac{t}{N_T}}e^{-\mathrm{i}\frac{V}{2}\hat{\sigma}_3^z\hat{\sigma}_4^z\frac{t}{N_T}}\mathcal{R}_y^{(1234)}(-\tfrac{\pi}{2})\\
&\times\mathcal{R}_x^{(1234)}(-\tfrac{\pi}{2})e^{-\mathrm{i}\frac{V}{2}\hat{\sigma}_1^z\hat{\sigma}_2^z\frac{t}{N_T}}e^{-\mathrm{i}\frac{V}{2}\hat{\sigma}_3^z\hat{\sigma}_4^z\frac{t}{N_T}}\mathcal{R}_x^{(1234)}(\tfrac{\pi}{2})\\
&\times\ e^{-\mathrm{i}\frac{U}{4}\hat{\sigma}_1^z\hat{\sigma}_3^z\frac{t}{N_T}}e^{\mathrm{i}\left(\frac{U}{4}-\frac{\mu}{2}\right)\hat{\sigma}_1^z\frac{t}{N_T}}e^{\mathrm{i}\left(\frac{U}{4}-\frac{\mu}{2}\right)\hat{\sigma}_3^z\frac{t}{N_T}}e^{\mathrm{i}\frac{\epsilon_c}{2}\hat{\sigma}_2^z\frac{t}{N_T}}e^{\mathrm{i}\frac{\epsilon_c}{2}\hat{\sigma}_4^z\frac{t}{N_T}}\Bigg)^{N_T},\end{aligned} \tag{8.27}$$

where $\mathcal{R}_\alpha^{(1234)}(\phi) = \mathcal{R}_\alpha^{(1)}(\phi)\mathcal{R}_\alpha^{(2)}(\phi)\mathcal{R}_\alpha^{(3)}(\phi)\mathcal{R}_\alpha^{(4)}(\phi)$. The sequence of gates for one Trotter step is depicted in Fig. 8.3b. A single Trotter step contains 5 ZZ two-qubit gates (corresponding to the $A$ and $B$ gates in Fig. 8.3b) between nearest-neighbour

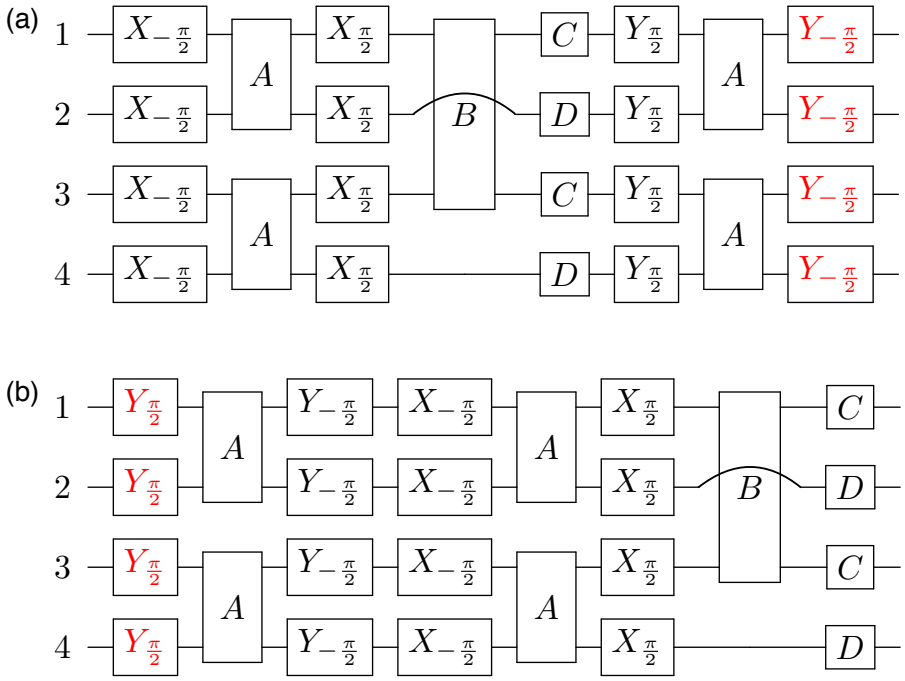


Figure 8.4: Reordering of quantum gates. The ordering of gates shown for (a) an odd Trotter step and (b) an even Trotter step in the $\mathrm{CZ}_\phi$ method. The gates depicted in red can be omitted as they cancel out during a sequence of time steps. Figure from Ref. [3].

qubits, 2 SWAP gates (for the $B$ gate which acts on qubits 1 and 3), and 20 single-qubit rotations. We note that a SWAP gate amounts to three $\mathrm{CZ}_\phi$ gates. One way to see this is to use the standard results that a SWAP gate equals three CNOT gates and that a CNOT gates equals one $\mathrm{CZ}_{\phi=\pi}$ gate and two Hadamard gates [318]. A ZZ gate amounts to two $\mathrm{CZ}_\phi$ gates [see Eq. (8.26)]. We can optimise the number of gates further if we consider different orderings for odd and even Trotter steps as in Fig. 8.4, such that subsequent gates may be suppressed. This reorganisation of interactions does not in principle affect the Trotter error. Hence, for a pair of Trotter steps, the number of gates is reduced, and we may only consider 10 ZZ two-qubit gates between nearest-neighbour qubits, 4 SWAP gates, and 32 single-qubit rotations.

## 8.4 Results

We focus on the half-filled case, i.e., $\mu = \frac{U}{2}$ and $\epsilon_c = 0$, which requires the smallest number of quantum gates, since the $C$ and $D$ gates in Section 8.3 vanish. Note that since the value of $\epsilon_c$ is fixed in this case, it need not be updated in the self-consistency loop. We use $J_\infty$, the Hubbard hopping in infinite dimensions, as our unit of energy, hence time $t$ is measured in units of $1/J_\infty$. Note that $t$ refers here to the time in the evolution operator $\hat{U}(t)$, not to the actual time to run the experiment.

In Fig. 8.5, we show for various Trotter steps $N_T$ up to time $t = 6/J_\infty$ the state fidelities $\mathcal{F} = |\langle\Psi(t)|\Psi_T(t)\rangle|^2$, where $|\Psi(t)\rangle$ denotes the state obtained with exact time-evolution using the full, non-Trotterized operator $\hat{U}(t) = \exp(-\mathrm{i}t\hat{H}_{\mathrm{SIAM},2})$ corresponding to the two-site SIAM in Eq. (8.1), and $|\Psi_T(t)\rangle$ is the state evolved using either the $XY$ or CZ$_\phi$ quantum gates. Note that the number of qubits corresponding to the two-site SIAM is fixed, leaving only $N_T$ as the parameter to be varied for increased accuracy. We use the initial state $|\Psi(t=0)\rangle = \hat{c}^\dagger_{1\downarrow}|\Psi_{\mathrm{GS}}\rangle / ||\hat{c}^\dagger_{1\downarrow}|\Psi_{\mathrm{GS}}\rangle||$, where $|\Psi_{\mathrm{GS}}\rangle$ is the ground-state of the two-site SIAM in Eq. (8.1), which is a relevant state for obtaining the impurity Green function at zero temperature [see Eq. (8.7)]. As expected, using $XY$ gates displays superior fidelities, since CZ$_\phi$ gates require an extra factorization of the hybridization term (see Section 8.3). For $N_T = 24$ steps, the state fidelity using $XY$ gates remains over 99% throughout the evolution. In what follows, we use only $XY$ gates for the time-evolution for concreteness.

As shown in Section 8.2, the main object of interest is the retarded impurity Green function. One possibility to measure $\mathrm{i}G^R_{\mathrm{imp}}(t)$ is single-qubit interferometry (see Appendix F for details), which raises the total number of qubits in the experimental arrangement to five. In Fig. 8.6 we plot the impurity Green function obtained from evolving the state with $XY$ gates compared to exact evolution of the two-site SIAM for different $N_T$. We see that the Green function from the $XY$

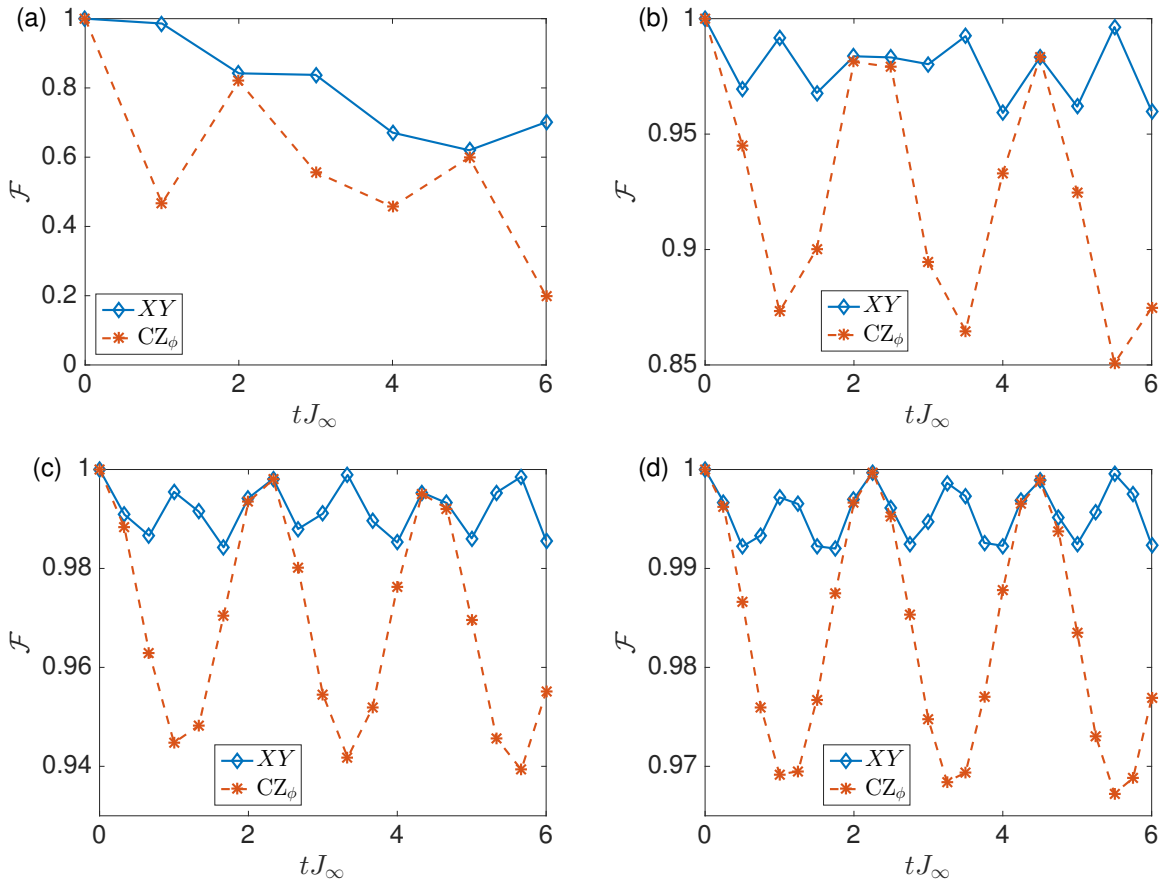


Figure 8.5: Time-evolution of the state fidelity. State fidelities $\mathcal{F} = |\langle\Psi(t)|\Psi_T(t)\rangle|^2$ using the $XY$ method (blue diamonds, line is to guide the eye) and $\mathrm{CZ}_\phi$ gates (red stars, dashed line is to guide the eye) obtained with (a) 6, (b) 12, (c) 18, and (d) 24 Trotter steps up to time $t = 6/J_\infty$. We set $U = 4J_\infty$ and $V = J_\infty$. Figure adapted from Ref. [3].

approach starts to follow the curve of the exact Green function better for increasing $N_T$. In our subsequent analysis, we use $N_T = 24$ up to $t = 6/J_\infty$ to study what two-site DMFT physics can be captured with the digital approach.

To obtain the impurity Green function in the frequency domain, we first consider some known and general analytic properties of the retarded Green function in Eq. (8.7). This Green function can be written as a sum of the particle and hole contributions as

$$\mathrm{i}G^R_{\mathrm{imp}}(t) = \theta(t)\sum_j \left(\left|\langle j|\hat{c}^\dagger_{1\sigma}|\Psi_{\mathrm{GS}}\rangle\right|^2 e^{-\mathrm{i}\omega_j t} + \left|\langle j|\hat{c}_{1\sigma}|\Psi_{\mathrm{GS}}\rangle\right|^2 e^{\mathrm{i}\omega_j t}\right), \tag{8.28}$$

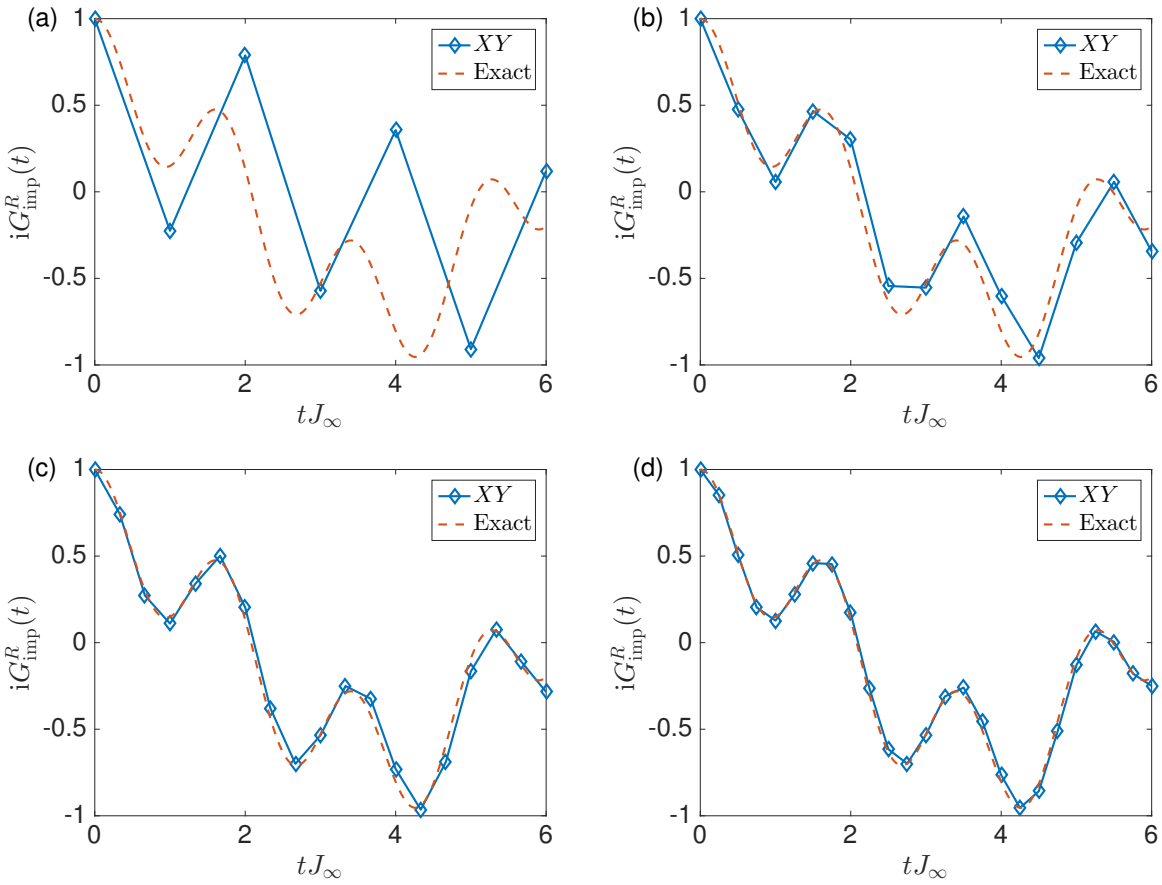


Figure 8.6: Impurity Green function in the time domain. The retarded impurity Green function $\mathrm{i}G^R_{\mathrm{imp}}(t)$ obtained with (a) 6, (b) 12, (c) 18, and (d) 24 Trotter steps up to time $t = 6/J_\infty$ using the $XY$ method (blue diamonds). Comparison is given to the exact Green function (red dashed line). We set $U = 4J_\infty$ and $V = J_\infty$. Figure adapted from Ref. [3].

where $|j\rangle$ is an eigenstate of $\hat{H}_{\mathrm{SIAM}}$ with eigenenergy $E_j$, and $\omega_j = E_j - E_{GS}$. In two-site DMFT, the interacting Green function is a four-pole function [313], which limits the number of terms in the above summation to four. Moreover, in the presence of particle-hole symmetry, we have $\left|\langle j|\hat{c}^\dagger_{1\sigma}|\Psi_{\mathrm{GS}}\rangle\right|^2 = \left|\langle j|\hat{c}_{1\sigma}|\Psi_{\mathrm{GS}}\rangle\right|^2$, and Eq. (8.28) can be written as

$$\mathrm{i}G^R_{\mathrm{imp}}(t) = 2\left[\alpha_1\cos(\omega_1 t) + \alpha_2\cos(\omega_2 t)\right]\theta(t), \tag{8.29}$$

where $\alpha_j = \left|\langle j|\hat{c}^\dagger_{1\sigma}|\Psi_{\mathrm{GS}}\rangle\right|^2$. Thus, to obtain the impurity Green function in the

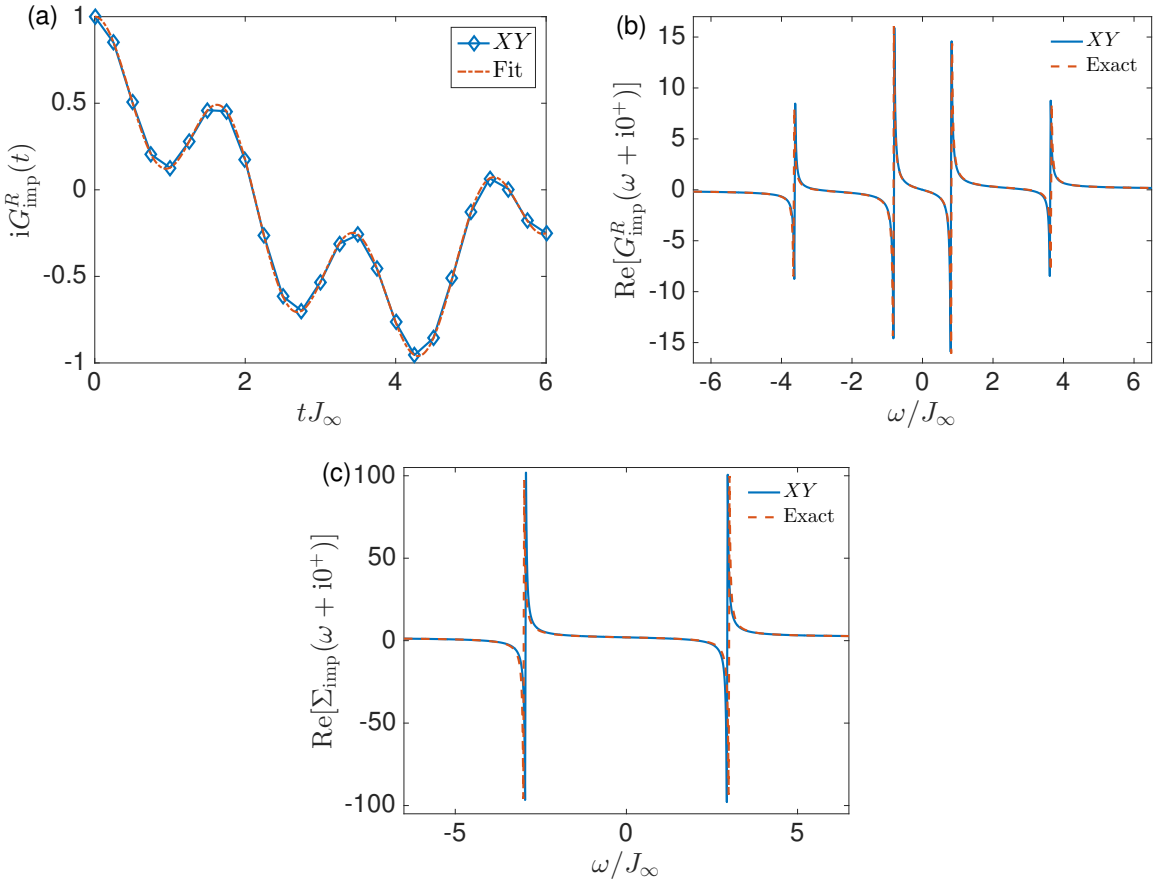


Figure 8.7: The retarded impurity Green function and self-energy in the frequency domain. (a) The residues and poles of the Green function can be obtained from a fit of the form in Eq. (8.29) (red dashed line) to the $G^R_{\mathrm{imp}}(t)$ data from the $XY$ method with 24 Trotter steps (blue diamonds). (b) The real part of the impurity Green function, $\mathrm{Re}\left[G^R_{\mathrm{imp}}(\omega+i0^+)\right]$ (blue line), with residues and poles obtained from the fit from (a), compared to the exact Green function (red dashed line). (c) Same as in (b), but for the self-energy $\mathrm{Re}\left[\Sigma_{\mathrm{imp}}(\omega+\mathrm{i}0^+)\right]$. We set $U=4J_\infty$ and $V=J_\infty$. In (b) and (c), we have broadened the peaks by setting the positive infinitesimal $0^+$ equal to $0.01$ for clarity. Figure adapted from Ref. [3].

frequency domain as

$$G^R_{\mathrm{imp}}(\omega+\mathrm{i}0^+) = \alpha_1\left(\frac{1}{\omega+\mathrm{i}0^+-\omega_1}+\frac{1}{\omega+\mathrm{i}0^++\omega_1}\right) + \alpha_2\left(\frac{1}{\omega+\mathrm{i}0^+-\omega_2}+\frac{1}{\omega+\mathrm{i}0^++\omega_2}\right), \tag{8.30}$$

we need to extract the unknown residues $\alpha_j$ and poles $\omega_j$ by fitting an expression of the form in Eq. (8.29) to the measurement data of $\mathrm{i}G^R_{\mathrm{imp}}(t)$, as shown in

Fig. 8.7a. This method to determine $\alpha_j$ and $\omega_j$ is far more reliable and requires fewer time steps than numerically Fourier-transforming the $\mathrm{i}G^R_{\mathrm{imp}}(t)$ data. It can also be readily generalised to larger systems by including more terms in the sum in Eq. (8.28). Figure 8.7b shows the real part of the impurity Green function in the frequency domain, $\mathrm{Re}\left[G^R_{\mathrm{imp}}(\omega + \mathrm{i}0^+)\right]$ (here, we explicitly include the infinitesimal imaginary part in the argument for clarity), with residues and poles obtained from the fit in Fig. 8.7a, while in Fig. 8.7c we plot the real part of the impurity self-energy, $\mathrm{Re}\left[\Sigma_{\mathrm{imp}}(\omega + \mathrm{i}0^+)\right]$, obtained utilizing the Dyson equation (8.8). We clearly see the four-pole structure of the Green function, while the self-energy has two poles. The results are in excellent agreement with the exact solution of the two-site SIAM, with the poles of the self-energy using fitted $\alpha_j$ and $\omega_j$ differing from the exact solution by 2%.

Once we have obtained the impurity Green function, and thus the impurity self-energy, we proceed according to the two-site DMFT protocol in Section 8.2 until self-consistency has been reached. In DMFT we are interested in the local lattice spectral function $A_{\mathrm{latt},jj}(\omega)$ which, at self-consistency, is given by the impurity spectral function $A_{\mathrm{imp}}(\omega)$. In the paramagnetic phase of the infinite-dimensional Hubbard model, the spectral function has a three peak structure with a lower and an upper Hubbard (sub)band and a quasiparticle peak with integrated spectral weight $\mathcal{Z}$ between the bands [40]. In two-site DMFT, since the self-energy has two poles, this three peak structure can be qualitatively reproduced with the spectral function [313]

$$A(\omega) = D\left[\omega + \mu - \Sigma_{\mathrm{imp}}(\omega)\right], \tag{8.31}$$

where $D(\epsilon)$ is the density of states of the Bethe lattice in Eq. (7.17). Figure 8.8 shows the spectral function in Eq. (8.31) where the impurity self-energy has been obtained both from the $XY$ method and from exact numerics of the two-site SIAM using the interactions $U = 5J_\infty$ and $U = 8J_\infty$. We notice that for $U = 5J_\infty$, the

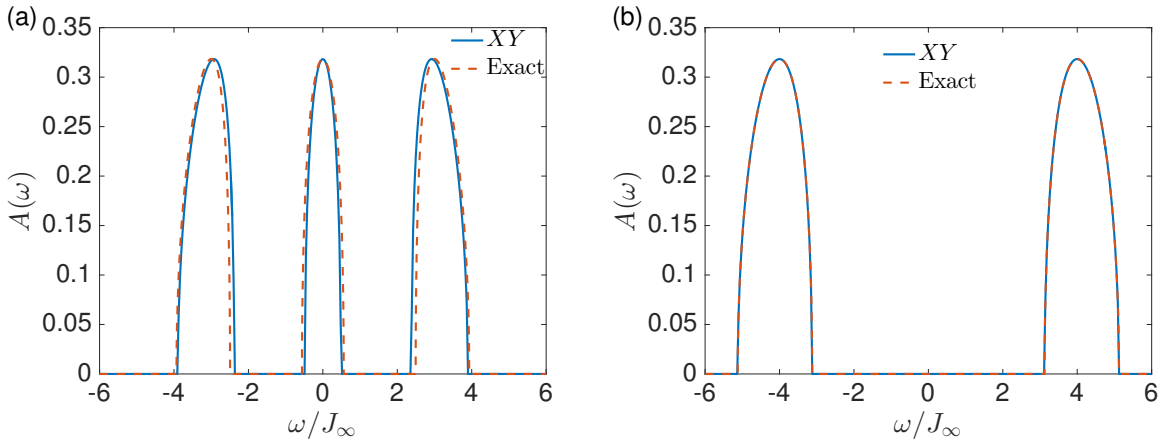


Figure 8.8: Spectral functions in the metallic and insulating phases. Spectral functions obtained with the $XY$ method with 24 Trotter steps (blue line) and exact solution of the two-site SIAM (red dashed line). The parameters of the two-site SIAM are iterated to self-consistency with (a) $U = 5J_\infty$ and (b) $U = 8J_\infty$. Figure adapted from Ref. [3].

Hubbard bands from the $XY$ method are slightly dislocated and the quasiparticle peak is slightly narrower compared with the exact solution of the two-site SIAM, but the agreement is still very good. The overall shape of the spectral function from the $XY$ method is unchanged compared to the exact case. This underestimation of the width of the quasiparticle peak stems from the fact that the fitting procedure in Fig. 8.7a causes the negative of the derivative of the self-energy in the $XY$ method to be a bit larger than the exact value from the two-site SIAM, i.e.,

$$-\frac{d\mathrm{Re}[\Sigma^{XY}_{\mathrm{imp}}(\omega+\mathrm{i}0^+)]}{d\omega}\Big|_{\omega=0} \gtrsim -\frac{d\mathrm{Re}[\Sigma^{\mathrm{exact}}_{\mathrm{imp}}(\omega+\mathrm{i}0^+)]}{d\omega}\Big|_{\omega=0}, \tag{8.32}$$

which leads to $\mathcal{Z}$ in Eq. (8.6) from the $XY$ method to be slightly smaller than in the exact solution of the two-site SIAM, i.e., $\mathcal{Z}^{XY} \lesssim \mathcal{Z}^{\mathrm{exact}}$. For $U = 8J_\infty$, the two spectral functions agree with maximum relative error of $10^{-8}$, since in this case $V = 0$ is found to be the self-consistent solution, whence the Trotterized evolution operator in Eq. (8.22) matches full evolution operator of the two-site SIAM, and thus there is no Trotter error. We observe that in Fig. 8.8 the central quasiparticle peak vanishes, which is characteristic of insulating behaviour. See Ref. [313] for a

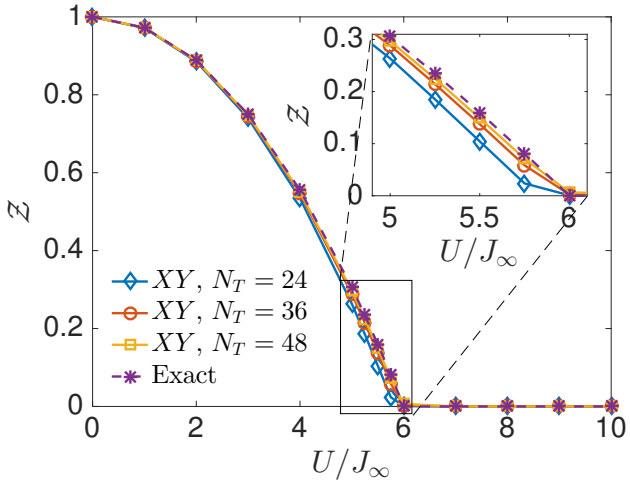


Figure 8.9: Quasiparticle weight as a function of interaction $U$. Self-consistent quasiparticle weight $\mathcal{Z}$ obtained from the $XY$ method with 24 (blue diamonds), 36 (red circles), and 48 Trotter steps (yellow squares), compared to the exact solution of the two-site SIAM (purple stars). Inset: Same plot zoomed into the region around the critical interaction, $U_c = 6J_\infty$. Figure adapted from Ref. [3].

discussion of the artifacts of the spectral functions in two-site DMFT compared to full DMFT.

To study the transition between the two types of spectral functions in Fig. 8.8, we plot in Fig. 8.9 the self-consistent quasiparticle weight $\mathcal{Z}$ obtained from the $XY$ method as a function of the interaction $U$ for different Trotter steps $N_T$. We also show $\mathcal{Z}$ from the exact solution of the two-site SIAM for comparison. We see that the digital approach captures the correct trend of the curve, but in the metallic side underestimates to a small degree the values of $\mathcal{Z}$ for interactions close to $U = U_c = 6J_\infty$, which is the critical interaction for Mott transition in two-site DMFT at half-filling [313]. These results are consistent with the spectral functions in Fig. 8.8. The underestimation of $\mathcal{Z}$ can be diminished by increasing $N_T$, as shown in Fig. 8.9. It is noteworthy to mention that two-site DMFT overestimates the quasiparticle weight compared to full DMFT for interactions $U < U_c$, as demonstrated in Ref. [313]. Above $U_c$, we find $\mathcal{Z} = 0$ to be the self-consistent solution, corresponding to the insulating phase.

## 8.5 Conclusion

We have proposed a quantum algorithm for two-site DMFT to be run on a small digital quantum simulator with a classical feedback loop, allowing the qualitative description of the infinite-dimensional Hubbard model in the thermodynamic limit. We have considered two alternative quantum gate decompositions consistent with state-of-the-art technology in superconducting circuits for the time-evolution operator. We found that an increasing number of Trotter steps improves the fidelity of our digital scheme to qualitatively describe the Mott transition. Our work therefore provides an interesting application for small-scale quantum devices. It also paves the way for more accurate quantum simulations of strongly correlated fermions in various lattice geometries, which are relevant to novel quantum materials, when the general self-consistency condition and larger number of qubits are used.

# Chapter 9

# HYBRID QUANTUM-CLASSICAL SIMULATION OF THE TIME-DEPENDENT INFINITE-DIMENSIONAL HUBBARD MODEL

In this Chapter, we generalise the hybrid quantum-classical approach in Chapter 8 to time-dependent problems and show that for a larger number of qubits the SIAM can be implemented efficiently in a digital quantum simulator using multiqubit Mølmer–Sørensen gates. The results presented in this Chapter have been published in Ref. [4].

## 9.1 Introduction

In Chapter 8, we introduced a proof-of-principle example of a hybrid quantum-classical simulation scheme that implements the DMFT method. However, this approach is only truly useful if it is scaled up to larger systems. In addition, the classical impurity solvers in non-equilibrium DMFT have severe limitations and are less established than in the equilibrium case, and thus it is relevant to ask whether the hybrid quantum-classical approach can be applied to out-of-equilibrium situations.

In this Chapter, we show that the scheme can be generalised to non-equilibrium problems *efficiently* if one uses, e.g., multiqubit Mølmer–Sørensen gates in the digital quantum simulator to approximate the unitary evolution described by the time-

dependent SIAM in Eq. (7.28). The parameters of the SIAM are again updated in a classical feedback loop according to Section 7.3.2.

This Chapter is organised as follows. In Section 9.2 we present the quantum algorithm for the time-dependent SIAM in terms of MS gates. In Section 9.3, we describe the setup which we use to test our approach. We show the results of our analysis in Section 9.4 and give a summary in Section 9.5. In Appendix G, we show how the single-qubit interferometry in Appendix F generalises to the non-equilibrium case. We describe the outline of our classical simulations in Appendix H and elucidate the super-fermion approach to open quantum systems in Appendix I.

## 9.2 Quantum algorithm for the time-dependent single-impurity Anderson model

### 9.2.1 Jordan–Wigner transformation of the time-dependent SIAM

We focus on the half-filled infinite-dimensional Hubbard model in Eq. (2.7). To solve the related DMFT impurity problem on a digital quantum simulator, we must represent the time-dependent SIAM Hamiltonian in Eq. (7.28) (with $\mu = 0$ and $\epsilon_p = 0$) in terms of spin operators that operate on the qubits of the simulator. This is achieved via the Jordan–Wigner transformation in Eqs. (6.1)–(6.3), in which we map $N$ fermions onto a string of $2N$ qubits. With the Jordan–Wigner transformation, the interaction term of the SIAM becomes

$$U(t)\left(\hat{n}_{1\uparrow}-\frac{1}{2}\right)\left(\hat{n}_{1\downarrow}-\frac{1}{2}\right)=\frac{U(t)}{4}\hat{\sigma}_1^z\hat{\sigma}_2^z, \tag{9.1}$$

while the hybridization, or hopping, terms read

$$\begin{aligned}V_p(t)\hat{c}_{1\downarrow}^\dagger\hat{c}_{p\downarrow}+\text{H.c.}=&\frac{1}{2}\text{Re}[V_p(t)]\left(\hat{\sigma}_1^x\hat{\sigma}_2^z\cdots\hat{\sigma}_{2p-2}^z\hat{\sigma}_{2p-1}^x+\hat{\sigma}_1^y\hat{\sigma}_2^z\cdots\hat{\sigma}_{2p-2}^z\hat{\sigma}_{2p-1}^y\right)\\&+\frac{1}{2}\text{Im}[V_p(t)]\left(\hat{\sigma}_1^y\hat{\sigma}_2^z\cdots\hat{\sigma}_{2p-2}^z\hat{\sigma}_{2p-1}^x-\hat{\sigma}_1^x\hat{\sigma}_2^z\cdots\hat{\sigma}_{2p-2}^z\hat{\sigma}_{2p-1}^y\right),\end{aligned} \tag{9.2}$$

$$V_p(t)\hat{c}^\dagger_{1\uparrow}\hat{c}_{p\uparrow} + \text{H.c.} = \frac{1}{2}\text{Re}[V_p(t)]\left(\hat{\sigma}^x_2\hat{\sigma}^z_3\cdots\hat{\sigma}^z_{2p-1}\hat{\sigma}^x_{2p} + \hat{\sigma}^y_2\hat{\sigma}^z_3\cdots\hat{\sigma}^z_{2p-1}\hat{\sigma}^y_{2p}\right) + \frac{1}{2}\text{Im}[V_p(t)]\left(\hat{\sigma}^y_2\hat{\sigma}^z_3\cdots\hat{\sigma}^z_{2p-1}\hat{\sigma}^x_{2p} - \hat{\sigma}^x_2\hat{\sigma}^z_3\cdots\hat{\sigma}^z_{2p-1}\hat{\sigma}^y_{2p}\right). \quad (9.3)$$

The total SIAM is given by the sum of the terms in Eqs. (9.1)–(9.3).

### 9.2.2 Quantum gate decomposition of the time-evolution operator

We now describe how to obtain the quantum gates corresponding to the unitary time-evolution operator $\hat{U}(t,t')$ of the SIAM given by Eqs. (9.1)–(9.3). We first discretise time as $t_n = n\times\delta t$, where $\delta t$ is a small time-step. We then breakup the time-evolution from $t=0$ to $t=t_n$ into a product of Trotter steps $\hat{U}(t_n,0)=\prod_{l=0}^{n-1}\hat{U}(l\to l+1)$. To obtain the necessary quantum gates to approximate the unitary evolution operator, we use a Trotter decomposition on the propagator $\hat{U}(l\to l+1)$ between each time $t_l$ and $t_{l+1}$ as $\hat{U}(l\to l+1)=e^{-\text{i}\delta t\hat{H}_{\text{SIAM}}(t_l)}\approx\prod_j e^{-\text{i}\delta t\hat{H}_j(t_l)}$, where $\hat{H}_{\text{SIAM}}(t_l)=\sum_j\hat{H}_j(t_l)$. Each term $e^{-\text{i}\delta t\hat{H}_j(t_n)}$ that consists of tensor products of $k$ Pauli operators can be implemented — up to local rotations — with an MS gate acting on the $k$ qubits, a single qubit rotation, and the inverse MS gate [278, 280]. For example, we have the decomposition

$$\exp\left(\text{i}\phi\sigma^z_1\sigma^x_2\sigma^x_3\cdots\sigma^x_k\right) = \hat{U}^{1,k}_{\text{MS}}\left(-\frac{\pi}{2},0\right)\hat{U}_{1,\text{loc}}(\phi)\hat{U}^{1,k}_{\text{MS}}\left(\frac{\pi}{2},0\right), \quad (9.4)$$

where the MS gate is given by Eq. (6.14). The local gate in Eq. (9.4) reads [280]

$$\hat{U}_{j,\text{loc}}(\phi) = \begin{cases}\exp(-\text{i}\phi\sigma^z_j), & \text{for } k=4n-1\\ \exp(\text{i}\phi\sigma^z_j), & \text{for } k=4n+1\\ \exp(-\text{i}\phi\sigma^y_j), & \text{for } k=4n-2\\ \exp(\text{i}\phi\sigma^y_j), & \text{for } k=4n\end{cases}, \quad n\in\mathbb{N}. \quad (9.5)$$

To implement a string of $\hat{\sigma}^y$ gates instead of $\hat{\sigma}^x$, we use a different MS gate with $\phi=\frac{\pi}{2}$ [see Eq. (6.14)], yielding the decomposition [280]

$$\exp\left(\text{i}\phi\sigma^z_1\sigma^y_2\sigma^y_3\cdots\sigma^y_k\right) = \hat{U}^{1,k}_{\text{MS}}\left(-\frac{\pi}{2},\frac{\pi}{2}\right)\hat{U}_{1,\text{loc}}(\phi)\hat{U}^{1,k}_{\text{MS}}\left(\frac{\pi}{2},\frac{\pi}{2}\right), \quad (9.6)$$

with the local gate

$$\hat{U}_{j,\mathrm{loc}}(\phi) = \begin{cases} \exp(-\mathrm{i}\phi\sigma_j^z), & \text{for } k = 4n-1 \\ \exp(\mathrm{i}\phi\sigma_j^z), & \text{for } k = 4n+1 \\ \exp(\mathrm{i}\phi\sigma_j^x), & \text{for } k = 4n-2 \\ \exp(-\mathrm{i}\phi\sigma_j^x), & \text{for } k = 4n \end{cases}, \quad n \in \mathbb{N}. \tag{9.7}$$

The terms emerging from the Trotter decomposition of the Jordan–Wigner transformed SIAM in Eqs. (9.1)–(9.3) can be constructed from Eqs. (9.4) and (9.6) by applying additional local rotations. For instance, we have

$$\begin{aligned} &\exp\left(\mathrm{i}\phi\hat{\sigma}_2^x\hat{\sigma}_3^z\cdots\hat{\sigma}_{2p-1}^z\hat{\sigma}_{2p}^x\right) \\ &= \exp\left(\mathrm{i}\frac{\pi}{4}\sum_{j=4}^{2p-1}\hat{\sigma}_j^y\right)\hat{U}_{\mathrm{MS}}^{2,2p}\left(-\frac{\pi}{2},0\right)\hat{U}_{3,\mathrm{loc}}(\phi)\hat{U}_{\mathrm{MS}}^{2,2p}\left(\frac{\pi}{2},0\right)\exp\left(-\mathrm{i}\frac{\pi}{4}\sum_{j=4}^{2p-1}\hat{\sigma}_j^y\right), \end{aligned} \tag{9.8}$$

where $\hat{U}_{3,\mathrm{loc}}(\phi) = \exp\left(-\mathrm{i}\phi\hat{\sigma}_3^z\right)$ for even $p$, and $\hat{U}_{3,\mathrm{loc}}(\phi) = \exp\left(\mathrm{i}\phi\hat{\sigma}_3^z\right)$ for odd $p$, with $\phi = -\frac{1}{2}\delta t\mathrm{Re}[V_p(t_l)]$. Similarly, e.g.,

$$\begin{aligned} &\exp\left(\mathrm{i}\phi\hat{\sigma}_1^x\hat{\sigma}_2^z\cdots\hat{\sigma}_{2p-2}^z\hat{\sigma}_{2p-1}^y\right) \\ &= \exp\left(\mathrm{i}\frac{\pi}{4}\hat{\sigma}_1^z\right)\exp\left(-\mathrm{i}\frac{\pi}{4}\sum_{j=3}^{2p-2}\hat{\sigma}_j^y\right)\hat{U}_{\mathrm{MS}}^{1,2p-1}\left(-\frac{\pi}{2},\frac{\pi}{2}\right)\hat{U}_{2,\mathrm{loc}}(\phi)\hat{U}_{\mathrm{MS}}^{1,2p-1}\left(\frac{\pi}{2},\frac{\pi}{2}\right) \\ &\quad\times\exp\left(\mathrm{i}\frac{\pi}{4}\sum_{j=3}^{2p-2}\hat{\sigma}_j^y\right)\exp\left(-\mathrm{i}\frac{\pi}{4}\hat{\sigma}_1^z\right), \end{aligned} \tag{9.9}$$

where $\hat{U}_{2,\mathrm{loc}}(\phi) = \exp\left(-\mathrm{i}\phi\hat{\sigma}_2^z\right)$ for even $p$, and $\hat{U}_{2,\mathrm{loc}}(\phi) = \exp\left(\mathrm{i}\phi\hat{\sigma}_2^z\right)$ for odd $p$, with $\phi = \frac{1}{2}\delta t\mathrm{Im}[V_p(t_l)]$.

We point out that the number of multiqubit MS gates scales only linearly with the number of bath sites. One way to see this is to note that Eqs. (9.2) and (9.3) have a total of 8 terms of the form considered on the left hand side of Eqs. (9.8) and (9.9). Each of these terms requires two MS gates as per Eqs. (9.8) and (9.9). Thus, a single bath site requires 16 MS gates, and $N_b$ bath sites requires $16N_b$ MS gates. This linear scaling allows for an efficient implementation of the unitary for the time-dependent SIAM with a digital quantum simulator[1] [227, 280]. To

[1]If one considers an ion trap implementation, we emphasize that each of the MS gates requires only one bichromatic field addressed globally on the set of qubits, even when the number of qubits is large.

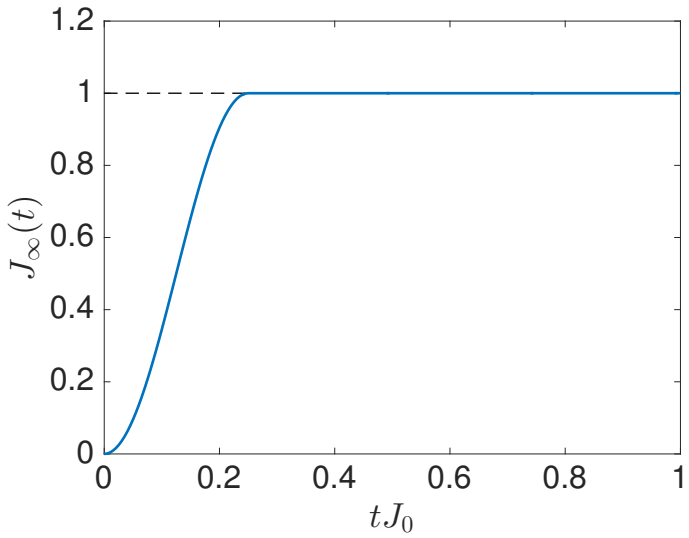


Figure 9.1: Hopping quench profile in Eq. (9.10).

compare, in a classical computer with exact diagonalization methods, the required computational resources scale *exponentially* with the number of bath sites. With classical MPS methods, very high bond dimensions are required for larger number of bath sites, which makes the simulations computationally demanding [309].

## 9.3 Setup

We study the hybrid quantum-classical scheme in the same example case considered in Ref. [300]. We are interested in the time evolution of the half-filled infinite-dimensional Hubbard model in the paramagnetic phase at zero temperature in a Bethe lattice with constant on-site interaction $U$ and time-dependent hopping $J_\infty(t)$. The hopping is turned on from the initial value $J_\infty = 0$ (i.e., we start from the atomic limit) to the final value $J_\infty = J_0 = 1$ with the profile [300]

$$J_\infty(t) = \begin{cases} \frac{1}{2}\left[1 - \cos(\omega_0 t)\right] & \text{for } t < t_q \\ 1 & \text{for } t \geq t_q \end{cases}, \tag{9.10}$$

where $\omega_0 = \pi/t_q$ and $t_q > 0$ is a suitable quench time. We use $J_0$ as the unit of energy and set $t_q = 0.25/J_0$. We plot the hopping quench profile in Fig. 9.1. This

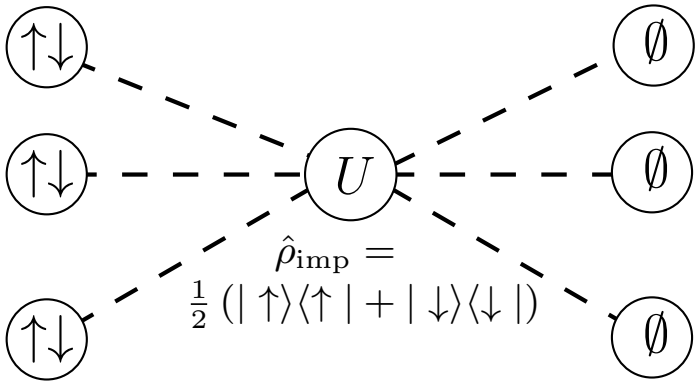


Figure 9.2: The ground-state of the atomic limit SIAM at half-filling. The central, interacting impurity site is initially decoupled (as indicated by the dashed lines) from the non-interacting bath sites, one half of which are doubly occupied and the other half empty. The impurity site is in the mixed state $\hat{\rho}_{\mathrm{imp}} = \frac{1}{2}(|\uparrow\rangle\langle\uparrow| + |\downarrow\rangle\langle\downarrow|)$.

kind of quench is representative of experimental ultracold atom dynamics [29, 57] and also of ultrafast dynamics probed in condensed matter systems [52].

We solve the dynamics of the system with non-equilibrium DMFT by mapping the DMFT action onto the time-dependent SIAM. Since we start from the atomic limit, the hybridization function $\Lambda_-$ in Section 7.3.2 vanishes. We denote the SIAM hybridization function by $\Lambda$ instead of $\Lambda^{\mathrm{SIAM}}$ for simplicity. In the paramagnetic phase and in the presence of particle-hole symmetry, the initial ground-state of the SIAM has a singly occupied impurity site in the completely mixed state of spin $\uparrow$ and spin $\downarrow$ with density operator $\hat{\rho}_{\mathrm{imp}} = \frac{1}{2}(|\uparrow\rangle\langle\uparrow| + |\downarrow\rangle\langle\downarrow|)$, and one half of the bath sites are doubly occupied and the other half empty, as explained after Eq. (7.39) and illustrated in Fig 9.2. For further details, see Ref. [300].

In practice, the system is prepared in two pure fermion occupational number states, $|\psi_0^a\rangle$ and $|\psi_0^b\rangle$, where $|\psi_0^a\rangle$ has the impurity in state $|\uparrow\rangle$ and $|\psi_0^b\rangle$ in state $|\downarrow\rangle$, along with the doubly occupied and empty bath states [300]. We then solve for two impurity Green functions $G^a_{\mathrm{imp},\sigma}$ and $G^b_{\mathrm{imp},\sigma}$, one for each subsystem $a$ and $b$, the average of which yields the total particle-hole symmetric impurity Green

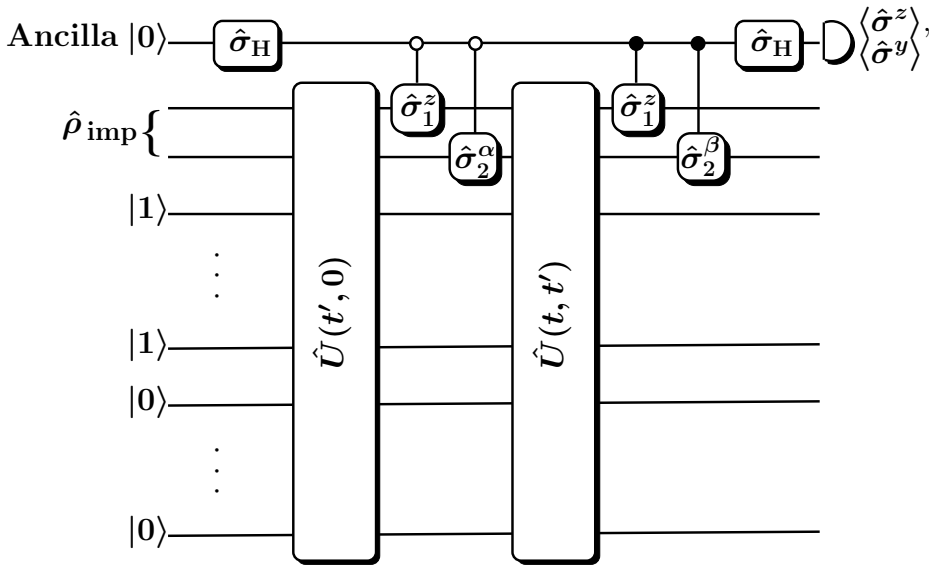


Figure 9.3: Quantum network to measure the $\langle\psi_0^s|\hat{U}(0,t)\hat{\sigma}_1^z\hat{\sigma}_2^\alpha\hat{U}(t,t')\hat{\sigma}_1^z\hat{\sigma}_2^\beta\hat{U}(t',0)|\psi_0^s\rangle$ contribution to the Green function $G_{\mathrm{imp},\uparrow}(t,t')$. Here, $\alpha,\beta\in\{x,y\}$. The impurity density operator is $\hat{\rho}_{\mathrm{imp}}=\frac{1}{2}\left(|0,1\rangle\langle 0,1|+|1,0\rangle\langle 1,0|\right)$. The time-evolution operators $\hat{U}$ are composed of a set of quantum gates according to Section 9.2.2. Figure adapted from Ref. [4].

function [300]

$$G_{\mathrm{imp},\sigma}(t,t')=\frac{1}{2}\left[G^a_{\mathrm{imp},\sigma}(t,t')+G^b_{\mathrm{imp},\sigma}(t,t')\right]. \tag{9.11}$$

Since we consider the case $T=0$, the time contour $\gamma$ in Fig. 2.2 suffices and we can restrict the Green function in Eq. (9.11) to real-time arguments. As the Hubbard model is in the Bethe lattice, the DMFT self-consistency condition is given by Eq. (7.27).

For implementation in a digital quantum simulator, the initial number states $|\psi_0^a\rangle$ and $|\psi_0^b\rangle$ are mapped onto product states of qubits via the Jordan–Wigner transformation in Eqs (6.1)–(6.3). The initial qubit configuration is that shown in Fig. 9.3, which depicts an example quantum network for measuring a contribution to the impurity Green function with single-qubit interferometry (see Appendix G). The non-equilibrium DMFT steps to obtain the self-consistent impurity

Green function up to a maximum simulation time $t_{\max} = N_T \times \delta t$ are then the following:

0. Guess an initial Green function $g_0$. For iteration $n = 1$, initialize the hybridization function as $\Lambda_1(t,t') = J_\infty(t) g_0(t,t') J_\infty(t')$.

1. For the $n$th iteration, obtain the hopping parameters $V_p^{(n)}(t)$ from the hybridization function $\Lambda_n(t,t')$ according to Section 7.3.2. With these parameters, the impurity model and the corresponding quantum gates are defined.

2. Measure, e.g., with single-qubit interferometry (see Appendix G) the impurity Green functions

$$G^s_{\mathrm{imp},\sigma} = \theta_\gamma(t,t') G^{s,>}_{\mathrm{imp},\sigma}(t,t') + \theta_\gamma(t',t) G^{s,<}_{\mathrm{imp},\sigma}(t,t'), \tag{9.12}$$

   where $\theta_\gamma(t,t')$ is the Heaviside function on the contour $\gamma$ in Fig. 2.2, and

$$\begin{aligned} G^{s,>}_{\mathrm{imp},\sigma}(t,t') &= -\mathrm{i}\langle\psi_0^s|\hat{U}(0,t)\hat{c}_{1\sigma}\hat{U}(t,t')\hat{c}^\dagger_{1\sigma}\hat{U}(t',0)|\psi_0^s\rangle, \\ G^{s,<}_{\mathrm{imp},\sigma}(t,t') &= \mathrm{i}\langle\psi_0^s|\hat{U}(0,t')\hat{c}^\dagger_{1\sigma}\hat{U}(t',t)\hat{c}_{1\sigma}\hat{U}(t,0)|\psi_0^s\rangle, \\ \hat{U}(t,t') &= \mathcal{T} e^{-\mathrm{i}\int_{t'}^{t} d\bar{t}\, \hat{H}_{\mathrm{SIAM}}(\bar{t})}. \end{aligned} \tag{9.13}$$

   Here, $s = a, b$. Use Eq. (9.11) to obtain the particle-hole symmetric impurity Green function $G_{\mathrm{imp},n}(t,t')$.

3. Use the DMFT self-consistency condition for the Bethe lattice $\Lambda_{n+1}(t,t') = v(t) G_{\mathrm{imp},n}(t,t') v(t')$ to obtain the hybridization function for iteration $n+1$.

4. Go to step 1 and iterate the steps until convergence is reached. The convergence variable can be, e.g., $\max|V_p^{(n)}(t) - V_p^{(n-1)}(t)|$, where the superscript refers to the iteration number.

From the self-consistent impurity Green function we obtain local single-particle observables. In addition to the Green function, in the time-evolution we determine the time-dependent double occupation $\langle d\rangle(t) = \langle \hat{n}_{1\uparrow}\hat{n}_{1\downarrow}\rangle(t)$, which is also averaged over the systems $s = a$ and $s = b$ [300].

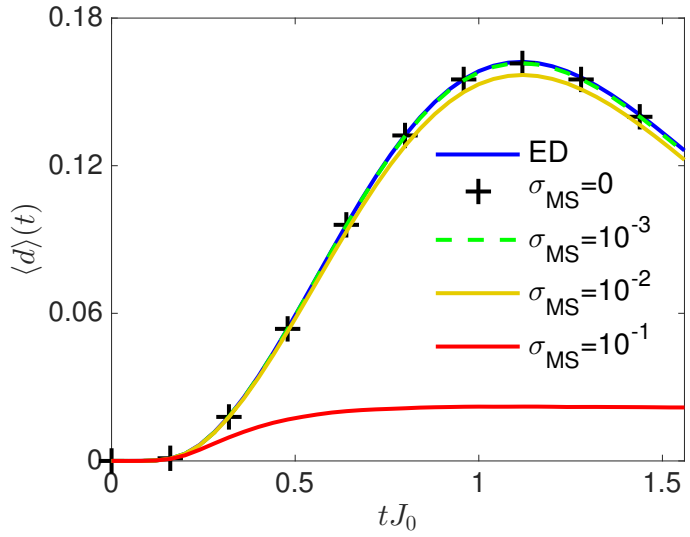


Figure 9.4: Impurity double occupation $\langle \hat{d} \rangle(t)$ as a function of time $t$. We show the numerically exact solution (blue solid curve), solution with Trotter errors $(+)$, solutions including gate errors of $\sigma_{\mathrm{MS}} = 0.1\%$ (green dashed curve), $\sigma_{\mathrm{MS}} = 1\%$ (yellow solid curve), and $\sigma_{\mathrm{MS}} = 10\%$ (red solid curve). Figure adapted from Ref. [4].

## 9.4 Results

### 9.4.1 Time-evolution with noisy gates

We emulate the operation of the hybrid quantum-classical device by classically evaluating the quantum networks in Fig. 9.3 (see Appendix H for further details), and the classical exponential scaling limits our simulations to small systems. In our simulations, we are able to accommodate $N_b = 2$ bath sites, which also limits the accessible time. This number of bath sites corresponds to a quantum device with 7 qubits, i.e., one ancilla qubit for measurements and six qubits implementing the SIAM. The largest MS gates then involve 5 qubits [between qubits 1 to 5, and 2 to 6, see Eqs. (9.2) and (9.3) for $p = 3$].

We choose a small time step of $\delta t = 0.04/J_0$ in the time discretisation and focus on the interaction strength $U = 2J_0$. As an example, we compare the impurity site double occupancy $\langle \hat{d} \rangle(t) = \langle \hat{n}_{1\downarrow} \hat{n}_{1\uparrow} \rangle(t)$ obtained from the self-consistent digitized simulation to the exact result in Fig. 9.4. We see that Trotter errors do not noticeably

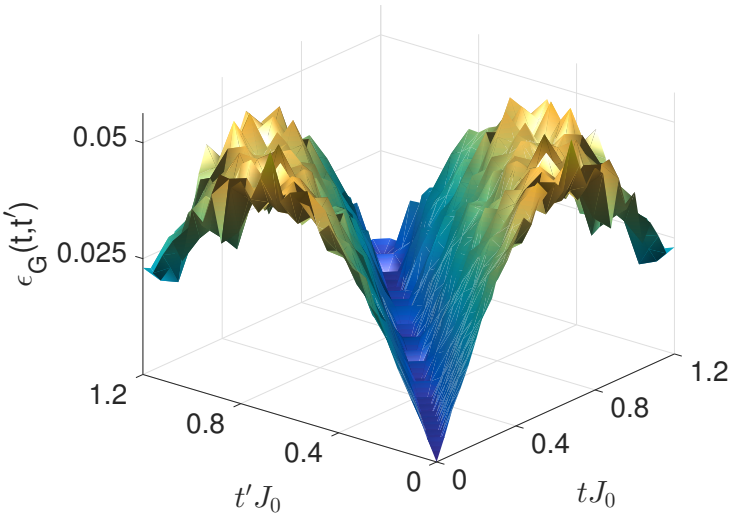


Figure 9.5: Absolute value of the difference $\epsilon_G(t,t')$ between the imaginary parts of the lesser Green function without gate errors and with gate errors of $\sigma_{\rm MS} = 1\%$. Results of calculations with gate errors were obtained by averaging over 128 realizations of the setup. Figure adapted from Ref. [4].

affect our results in this time scale due to the small value of the time step.

We are interested in knowing whether the hybrid scheme is robust against small gate errors[2]. To do this, we assume imperfect gates which are characterized by errors in the angles defining the gates [325, 326]. The imperfect MS gate is described by the unitary operator [compare with Eq. (6.14)]

$$\hat{U}_{\rm MS}^{l,m}\left(\theta+\epsilon_{\rm MS1},\phi+\epsilon_{\rm MS2}\right)=\exp\left\{-{\rm i}\frac{\theta+\epsilon_{\rm MS1}}{4}\left[\cos(\phi+\epsilon_{\rm MS2})\,\hat{S}_x+\sin(\phi+\epsilon_{\rm MS2})\hat{S}_y\right]^2\right\}, \tag{9.14}$$

where $\epsilon_{\rm MS1}$ and $\epsilon_{\rm MS2}$ are normally distributed random variables with zero mean [325, 326] (see also Appendix H). Similarly, imperfect single-qubit gates are given by unitary operators of the form $\hat{U}_{\rm loc}(\varphi+\epsilon)$ [see Eqs. (9.4)–(9.9)], where $\epsilon$ is also a normally distributed random variable with zero mean. We set the standard deviation of the single qubit error to $\sigma = 10^{-6}$ [326] and allow the standard deviation of MS gate errors $\sigma_{\rm MS}$ to vary between $0.1\%$ and $10\%$. As shown in Fig. 9.4, we

[2]See also, e.g., Refs. [317, 319–324] for theoretical studies of quantum processors in the presence of errors.

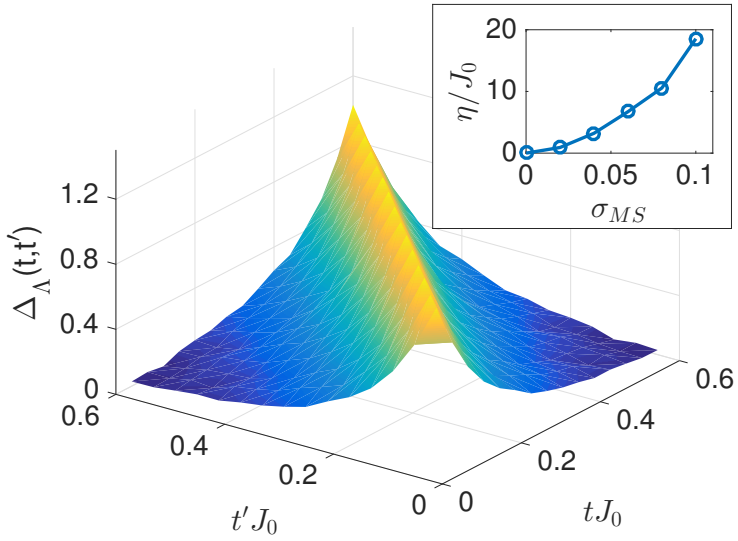


Figure 9.6: Deviation of the hybridization function $\Delta_\Lambda(t,t') = \mathrm{Im}\Lambda^<_\eta(t,t')/\mathrm{Im}\Lambda^<_0(t,t') \approx \exp(-\eta|t-t'|)$, where $\Lambda^<_{0(\eta)}(t,t')$ is the lesser component of the mean field, in the absence (presence) of gate errors (here, $\sigma_{\mathrm{MS}} = 6\%$) for constant $V_p$ and $U = 2J_0$, $N_b = 2$, and averaged over 128 realizations. Inset: the exponential decay rate $\eta$ versus $\sigma_{\mathrm{MS}}$. Figure adapted from Ref. [4].

obtain reasonably accurate results for the dynamics of the double occupancy even in the presence of gate errors: the double occupation differs from the exact result by only approximately $3\%$ for $\sigma_{\mathrm{MS}} = 1\%$. For a smaller gate error of $\sigma_{\mathrm{MS}} = 0.1\%$ the difference is insignificant up to $t = 1.5/J_0$.

In Fig. 9.5, we plot the error in the imaginary part of the lesser impurity Green function $G^<_{\mathrm{imp}}(t,t')$ induced by imperfect gates. We see that the diagonal values $G^<_{\mathrm{imp}}(t,t)$, which determine time-local single-particle observables [69], are almost unaffected by the gate errors. However, the gate errors make the impurity Green function decay faster with $t-t'$ than in the ideal case. They will thus affect especially the unequal-time single-particle correlation functions.

We further investigate the effect of imperfect gates by considering the impurity site coupled to two bath sites via constant $V_p$ and without self-consistency. We find that the imaginary part of the hybridization function with gate errors differs from the exact one by a factor of approximately $\exp(-\eta|t'-t|)$, as shown in Fig. 9.6. The

decay rate $\eta$ increases with $\sigma_{\rm MS}$ as displayed in the inset of Fig. 9.6. This numerical evidence suggests that gate errors have the same effect as 'smearing out' the bath energies $\epsilon_p$ to a width given by $\eta$. The impurity model including errors would then be equivalent to the bath sites possessing an effective finite coherence time $1/\eta$.

### 9.4.2 Noise reduction in the classical feedback loop

The presence of the classical feedback loop offers the possibility for reducing the effect of the noisy quantum gates. We study this in an auxiliary, non-interacting impurity system which comprises of the SIAM Hamiltonian in Eq. (7.28) with $U = 0$. We model a bath site $p$ with an effective coherence time $1/\eta$ by allowing an ideal bath site to incoherently exchange fermions with a particle reservoir at a rate $\Gamma_p = \eta$ (see, e.g., Refs. [327–329]). This system is described within the quantum master equation approach, where the density operator $\hat{\rho}(t)$ of the full system obeys the equation

$$\begin{aligned}\frac{\mathrm{d}}{\mathrm{d}t}\hat{\rho}(t) = &-\mathrm{i}[\hat{H}_{\rm SIAM}(t), \hat{\rho}(t)] \\ &+ \sum_{p>1,\sigma} \Gamma_p^- [2\hat{c}_{p\sigma}\hat{\rho}(t)\hat{c}_{p\sigma}^\dagger - \hat{\rho}(t)\hat{c}_{p\sigma}^\dagger\hat{c}_{p\sigma} - \hat{c}_{p\sigma}^\dagger\hat{c}_{p\sigma}\hat{\rho}(t)] \\ &+ \sum_{p>1,\sigma} \Gamma_p^+ [2\hat{c}_{p\sigma}^\dagger\hat{\rho}(t)\hat{c}_{p\sigma} - \hat{\rho}(t)\hat{c}_{p\sigma}\hat{c}_{p\sigma}^\dagger - \hat{c}_{p\sigma}\hat{c}_{p\sigma}^\dagger\hat{\rho}(t)],\end{aligned}$$

where $\Gamma_p^\pm$ are the rates of electron ejection ($-$) and injection ($+$) to bath site $p$. Here, we set the dissipation in the bath to have $\Gamma_p^\pm = \Gamma$.

Since the model is non-interacting and has Lindblad-type noise terms, we can use the so-called super-fermion formalism [330] (see also Appendix I) to compute the greater and lesser impurity Green functions given by

$$G_{{\rm imp},\sigma}^{>}(t,t') = \mathrm{i}\mathrm{Tr}[\hat{\rho}_0\hat{c}_{1\sigma}^\dagger(t')\hat{c}_{1\sigma}(t)], \tag{9.15}$$

$$G_{{\rm imp},\sigma}^{<}(t,t') = -\mathrm{i}\mathrm{Tr}[\hat{\rho}_0\hat{c}_{1\sigma}(t)\hat{c}_{1\sigma}^\dagger(t')]. \tag{9.16}$$

Here, the initial density operator is denoted by $\hat{\rho}_0$. We focus on a quench of the Hubbard hopping parameter $J_\infty(t)$ given by Eq. (9.10). The initial density operator

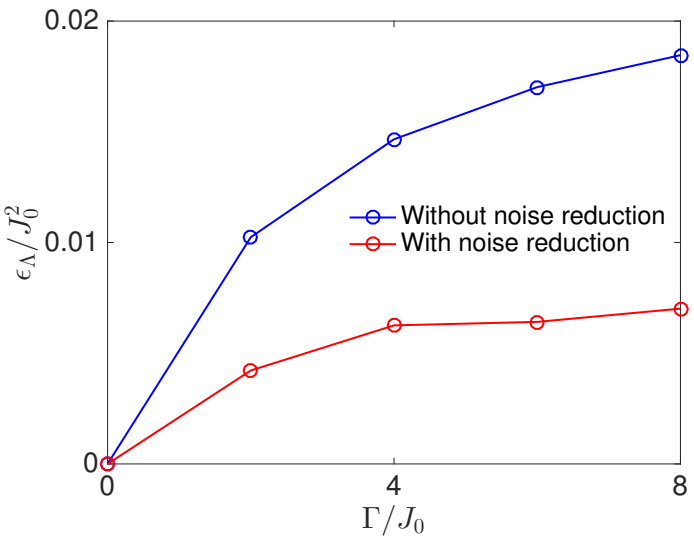


Figure 9.7: Average error in the self-consistent hybridization function $\epsilon_\Lambda = \overline{|\Lambda^<_{\text{noisy}}(t,t') - \Lambda^<_{\text{exact}}(t,t')|}$ (here, the overbar denotes average) for the non-interacting system with $N_b = 10$ noisy bath sites. Figure adapted from Ref. [4].

$\hat{\rho}_0$ is again chosen to model a $T = 0$ half-filled paramagnetic phase [300], with the impurity being in a singly occupied spin-mixed state $\hat{\rho}_{\text{imp}} = \frac{1}{2}(|\uparrow\rangle\langle\uparrow| + |\downarrow\rangle\langle\downarrow|)$, along with half the bath sites being doubly occupied and the other half empty.

Using the calculated lesser and greater impurity Green functions in Eqs. (9.15) and (9.16), we solve the non-equilibrium DMFT self-consistency loop using

(i) the standard time-slicing approach explained in Section 7.3.2,

(ii) a fitting procedure which attempts to correct for the effects of the bath noise. We solve numerically for the bath Green functions $g_p(t,t')$ again using the super-fermion approach [330]. To implement a noise-reduction scheme, we minimize $\left\|\sum_p V_p(t) g_p(t,t') V_p(t') - \Lambda(t,t')\right\|_F^2$ (where $\|\cdot\|_F$ is the Frobenius norm) over $V_p(t)$ to obtain the hybridizations corresponding to a noisy system.

The modification of the *classical* feedback loop in case (ii) significantly reduces the effect of gate errors compared to the standard case (i), as demonstrated in

Fig. 9.7, showing the reduction in average absolute error in the mean field $\Lambda(t, t')$. In the hybrid simulation scheme, the quantum network shown in Fig. 9.3 can be modified so that the ancilla qubit measures the bath Green functions, thus providing the information required for this noise-reduction scheme to be implemented.

## 9.5 Conclusion

We have proposed a hybrid quantum-classical approach to non-equilibrium DMFT. The DMFT impurity problem is solved on a digital quantum simulator, and the quantum gates are updated iteratively with the help of a classical feedback loop which takes care of the DMFT self-consistency. We emphasize that our scheme works directly in the thermodynamic limit and, since it does not require a small expansion term, gives accurate results for all values of the interaction $U$, in particular for the challenging situation of intermediate interactions like the example $U = 2J_0$ considered here. The implementation of the digitized time-evolution operator that approximates the unitary of the time-dependent SIAM can be done efficiently using multiqubit MS gates, the number of which scales only linearly with the number of bath sites in the SIAM. The number of available qubits in the simulator only limits the number of bath sites that can be included in the simulation and hence the maximally reachable simulation time $t_{\max}$.

Purely classical DMFT simulations are currently limited to approximately $25$ bath sites [309] and, because of fast growing SIAM entanglement [300, 309], scale exponentially with $t_{\max}$ despite efficiently implementing the feedback loop. Therefore, a quantum system with only about $50$ qubits coupled to a classical feedback loop would be able to improve upon current purely classical DMFT algorithms[3]. This number of qubits is commensurate with the plans of building larger quantum devices in the near future, such as in the Networked Quantum Information

[3]We point out that the largest classical simulations of quantum circuits outside the context of DMFT have simulated up to 45 qubits [322, 323, 331, 332]. The limit for quantum supremacy with state-of-the-art classical supercomputers has been estimated to be 48 qubits [323].

Technologies Hub [333], which is part of the United Kingdom National Quantum Technologies Programme [334]. Our hybrid simulation scheme thus provides an interesting scientific application of next generation, possibly imperfect, quantum devices.

# Part IV Conclusion

# Chapter 10

## SUMMARY AND OUTLOOK

In this thesis, we have studied different topics in the quantum simulation of fermionic models. We have utilised both the analogue and the digital paradigms of quantum simulation. We now summarise the main results of the thesis in Section 10.1 before exploring some possible future directions in Section 10.2.

## 10.1 Summary of results

We begin with the results of Part II. In Chapter 4, we studied the spin-asymmetric Josephson effect in the context of ultracold atoms that act as analogue quantum simulators of condensed matter systems. We investigated two different setups where the phenomenon could manifest.

First, we proposed a 3D ultracold atomic Fermi gas Josephson junction where the necessary spin-dependent potential could be created with spin-dependent interactions induced by the mean-field Hartree shift in the presence of a third spin component. This kind of setup would be an extension of the arrangement in Ref. [38], where the observation of Josephson plasma oscillations was reported. Motivated by the results of Ref. [38], we studied the plasma oscillation regime in our setup and showed that the spin-asymmetric Josephson effect manifests as a spin-dependent plasma oscillation amplitude. The Josephson plasma frequency is still the same for both components. The asymmetry in the amplitudes is given

by the ratio of the spin-dependent critical Josephson currents which are characteristic of the spin-asymmetric Josephson effect. We used BCS theory to estimate the asymmetry as a function of interaction strength and temperature, and showed that asymmetries on the order of a couple of per cent could be feasible. We also showed that the asymmetry grows with decreasing interaction strength and increasing temperature, which we explained by the behaviour of the Riedel peak at the potential $2\Delta$.

Second, we showed numerically using the TEBD method that similar spin-asymmetric Josephson-type currents take place in a 1D spin-dependent optical superlattice setup. We demonstrated that significant amplitude asymmetries up to 39% are achievable in this setup. Furthermore, we showed that the presence of the lattice and the competing hopping and interaction energy scales cause the Josephson signal to split into spin-asymmetric subpeaks. We elucidated the origin of this effect by studying smaller lattices using perturbation theory and showed that a possible explanation for the emergence of the Josephson sub-signals is the fact that the states participating in the Josephson-type processes have different kinetic energy contributions.

In Chapter 5, we studied the DC limit of the spin-asymmetric Josephson effect. We showed that the tunable DC critical Josephson current in ferromagnetic SFIFS Josephson junctions proposed in Ref. [39] can be explained at zero temperature by the DC spin-asymmetric Josephson effect. To this end, we also generalised in Appendix B the four-state model of the spin-asymmetric Josephson effect in Ref. [37] to a non-momentum conserving Josephson coupling. The SFIFS junction needs to be thin such that the SF bilayer can be considered a uniform magnetic superconductor. To show the equivalence of the phenomena, we derived the expression for the critical Josephson current in the ferromagnetic junction and in the junction with a spin-dependent potential using the same linear response formalism. We

obtained that the difference in the exchange fields of the SF bilayers has a one-to-one correspondence to the spin-dependent potential. As a result, the origin of the tunable critical Josephson current can be explained in terms of Fig. 4.4 of the spin-asymmetric Josephson effect.

We proceed to the results in Part III. In Chapter 8, we switched the focus from analogue to digital quantum simulators. We proposed a hybrid quantum-classical approach to simulating the infinite-dimensional Hubbard model directly in the thermodynamic limit. This approach implements the DMFT method: a small digital quantum simulator solves the dynamics of the DMFT impurity model, and the parameters of the impurity Hamiltonian, which directly yield the quantum gates of the simulator, are updated iteratively in a classically computed feedback loop. The smallest possible impurity model that is ideal for a proof-of-principle demonstration of the scheme consists of one fermionic impurity site which is connected to only one fermionic bath site. This system corresponds to a setup of five qubits, where four qubits implement the impurity model and a fifth, ancillary qubit is used for measurements of the impurity Green function. In this minimal incarnation of the DMFT problem, it is advisable to replace the self-consistency condition of full DMFT by two specially chosen conditions that determine the two free parameters of the impurity model. The resulting scheme is called two-site DMFT, which was first described in Ref. [313]. Using the two-site DMFT scheme, we showed that the minimal hybrid quantum-classical simulator can be used to qualitatively describe the Mott transition in the half-filled infinite-dimensional Hubbard model.

In Chapter 9, we showed how the proof-of-principle setup in Chapter 8 can be generalised to a larger number of qubits and to non-equilibrium problems using the Hamiltonian-based approach to non-equilibrium DMFT. We showed that the dynamics of the impurity model can be implemented efficiently using multi-qubit Mølmer–Sørensen gates, the number of which scales only linearly with the number of bath sites in the impurity Hamiltonian. In our simulations, we tried

to emulate the workings of an experiment and assumed imperfect quantum gates with random phase noise to see whether the scheme is robust against small gate errors. We showed that the scheme can give accurate results in the presence of $1\%$ phase noise variances in the Mølmer–Sørensen gates. For completeness we also mentioned an auxiliary non-interacting open quantum system where the effect of the noise of the quantum gates is modelled by letting the bath sites incoherently exchange fermions with a particle reservoir. In this setup the effect of the bath noise on the impurity hybridization function can be reduced significantly as shown in Fig. 9.7 by modifying the classical feedback loop where the updated parameters of the impurity Hamiltonian are obtained.

## 10.2 Outlook

We conclude by outlining some possible future directions of the presented work.

The spin-asymmetric Josephson effect in Part II is intriguing for instance because it shows that there is something fundamental left to be understood and discovered in the Josephson effect despite an extensive literature spanning five decades and a range of applications utilising the well-established phenomenon. On the theory side, one could try and come up with further experimental arrangements that would allow the observation of the spin-asymmetric currents with as large amplitude asymmetries as possible with current technology. In addition, including trapping effects (e.g., via the local density approximation) which we neglected in Chapter 4 and applying theory tools beyond BCS mean-field theory would allow more accurate calculations and make comparisons with experiments more realistic. On the experimental side, while the creation of the ultracold atom double well setup, realization of the spin-dependent potential using a third spin component, and observation of Josephson plasma oscillations are all in principle achievable with present-day tools and techniques, the experimental details and

the atom cloud preparation need to fleshed out even further. Moreover, the asymmetry in the plasma oscillation amplitudes is small, on the order of a couple of per cent, and it is on top of an already small plasma mode signal. This makes the observation of the asymmetry challenging, although one could possibly increase the signal-to-noise ratio with time-of-flight measurements of the centre-of-mass displacements [38]. The observation of full AC Josephson oscillations beyond the plasma oscillation regime in ultracold Fermi gases could provide the remedy, since in the full AC region the critical current asymmetry can be significant, over 10% [37]. Similarly, the amplitude asymmetries that could be achieved in the spin-dependent optical superlattice setup are high. Thus, the experimental realization of this kind of an arrangement would also provide a landmark step towards the observation of the spin-asymmetric Josephson effect. However, further study on how exactly this kind of a spin-dependent superlattice would be implemented in an experiment is still required. Finally, one could also investigate the magnitude of the effect in a thin Zeeman-split solid-state SIS Josephson junction.

The hybrid quantum-classical approach to quantum simulation and the study of strongly correlated fermion models in Part III is interesting for example since it could avoid many issues of classical impurity solvers and it would provide a scientific application for small scale (from five to $\sim$100 qubits) quantum devices. There are many ways in which the work presented in this thesis could be extended. For example, one could look into going beyond single-site DMFT and consider cluster extensions where one can include short-range spatial correlations. In the non-equilibrium case, the inclusion of initial impurity-bath correlations and thus having a non-zero $\Lambda_-$ would allow us to describe systems that are not initially in the atomic limit. In addition, considering different kinds of quantum gates (e.g., high-fidelity two-qubit gates) and error models besides Mølmer–Sørensen gates and phase noise would help identify the challenges facing the possible experimental realizations in different platforms. Importantly, the classical simulations of the

hybrid device should include more bath sites than in Chapter 9. However, the non-equilibrium setup is unlikely to be the first hybrid scheme implemented in the lab since it is more complicated than for example the two-site DMFT scenario in Chapter 8. The proof-of-principle setup with five qubits is commensurate with state-of-the-art techniques in superconducting circuits and trapped ions and could thus in principle be implemented with near-future technology although likely with a limited number of Trotter steps and reduced accuracy. Modelling (realistic) gate imperfections in the five-qubit setup would allow the identification of possible technical limitations and the testing of the robustness of the scheme against errors. It would also make the proposal more realistic regarding a possible near-future implementation in the lab.

# APPENDICES

# Appendix A

## DERIVATION OF THE HUBBARD MODEL

Here we present a simple derivation of the Hubbard model from the many-body Hamiltonian of a deep optical lattice. We first introduce the concept of Wannier functions which are used in the derivation.

## A.1 Bloch and Wannier functions

The Hamiltonian of a non-interacting particle in an optical lattice potential [see, e.g., Eq. (3.23)] is invariant under a translation by the lattice constant $a = \frac{\pi}{k_L}$, where $k_L$ is the laser wave number. This means that the translation operator and the Hamiltonian commute, i.e., they have a common eigenbasis. The states in this basis are referred to as Bloch functions or Bloch waves which have the form

$$\phi_q^{(n)}(x) = e^{iqx} u_q^{(n)}(x), \tag{A.1}$$

where $n$ denotes the energy band index and $q$ is the quasi-momentum, the values of which in the first Brillouin zone are $-\pi/a < q \leq \pi/a$ (or $-k_L < q \leq k_L$). Equation (A.1) is often referred to as the Bloch theorem [335]. The function $u_q^{(n)}$ satisfies the periodicity condition $u_q^{(n)}(x + a) = u_q^{(n)}(x)$.

Since Bloch functions are spatially delocalized, one usually uses the set of Wannier functions [336] to better describe the physics of deep lattices and localized

particles. They are obtained as a Fourier transform of the Bloch functions given by

$$w_n(x - x_j) = \mathcal{N}^{-1/2} \sum_q e^{-\mathrm{i}qx_j} \phi_q^{(n)}(x), \tag{A.2}$$

where $\mathcal{N}$ is a normalization constant and $x_j$ is a lattice site. Note, however, that the Wannier functions in Eq. (A.2) are not unique since the Bloch functions are defined up to an arbitrary phase. Different choices for the phases preserve the location of the centres $x_j$ of the Wannier functions (modulo a lattice vector) but lead to different spatial spreads [337]. However, in 1D for an isolated energy band there exists a unique maximally localized Wannier function for which the spatial spread is minimized [338]. In the general case, we point out that many numerical methods have been developed for finding a set of maximally localized Wannier functions for example for first-principles electronic structure calculations. For further details, see Ref. [339]. Related work for finding optimally localized Wannier functions has also been done in the context of optical lattices [340].

## A.2 Many-body Hamiltonian and the Hubbard model

We now show a simple derivation of the Hubbard model in Eq. (2.1) from the many-body Hamiltonian of a system of spin $\uparrow$ and spin $\downarrow$ fermions in an orthogonal optical lattice. The derivation is conceptually general and as such applicable also to systems beyond optical lattices. For details of *ab initio* derivations of Hubbard models in various optical lattice potentials and related numerical methods, see, e.g., Ref. [340].

The many-body Hamiltonian of the system is given by

$$\begin{aligned}\hat{H} = &\sum_{\sigma=\uparrow,\downarrow} \int d\mathbf{r}\, \hat{\Psi}_\sigma^\dagger(\mathbf{r}) \left[ -\frac{\nabla^2}{2m} + V(\mathbf{r}) \right] \hat{\Psi}_\sigma(\mathbf{r}) \\ &+ \int d\mathbf{r} \int d\mathbf{r}'\, U(\mathbf{r}, \mathbf{r}') \hat{\Psi}_\uparrow^\dagger(\mathbf{r}) \hat{\Psi}_\downarrow^\dagger(\mathbf{r}') \hat{\Psi}_\downarrow(\mathbf{r}') \hat{\Psi}_\uparrow(\mathbf{r}),\end{aligned} \tag{A.3}$$

where $\hat{\Psi}_\sigma^\dagger(\mathbf{r})$ and $\hat{\Psi}_\sigma(\mathbf{r})$ are the fermionic field operators that create and annihilate a spin $\sigma$ particle at $\mathbf{r}$, respectively. The optical lattice potential is given by

$$V(\mathbf{r}) = \sum_{\alpha=x,y,z} \tilde{s} E_R \sin^2(k_L \boldsymbol{\epsilon}_\alpha \cdot \mathbf{r}), \tag{A.4}$$

where $\boldsymbol{\epsilon}_\alpha$ is the unit vector along the $\alpha$-axis. The second term in Eq. (A.3) describes two-particle interactions via the scattering potential $U(\mathbf{r}, \mathbf{r}')$. In low temperatures, i.e., with low scattering energies, and in low densities we can use an effective potential, or pseudo-potential, defined in 3D as [137]

$$U(\mathbf{r}, \mathbf{r}') = g\delta(\mathbf{r} - \mathbf{r}'), \tag{A.5}$$

where $g = 4\pi a_s/m$, where $a_s$ is the 3D $s$-wave scattering length which is tunable via Feshbach resonances [48]. Equation (A.5) is a good approximation in ultracold gases due to the diluteness and low temperature of the atomic clouds [27]. Note that for the same reason, three-body processes are very unlikely to occur [27] and therefore they are not taken into account in the Hamiltonian in Eq. (A.3). The Hamiltonian thus becomes

$$\hat{H} = \sum_{\sigma=\uparrow,\downarrow} \int d\mathbf{r}\, \hat{\Psi}_\sigma^\dagger(\mathbf{r}) \left[ -\frac{\nabla^2}{2m} + V(\mathbf{r}) \right] \hat{\Psi}_\sigma(\mathbf{r}) + g \int d\mathbf{r}\, \hat{\Psi}_\uparrow^\dagger(\mathbf{r}) \hat{\Psi}_\downarrow^\dagger(\mathbf{r}) \hat{\Psi}_\downarrow(\mathbf{r}) \hat{\Psi}_\uparrow(\mathbf{r}). \tag{A.6}$$

For deep enough lattices (usually $\tilde{s} \gtrsim 5$ suffices [147]) the band gap between the two lowest-lying bands becomes large in comparison to the other relevant energy scales in the system [119]. We can thus assume that all atoms occupy the lowest energy band and write the field operators as

$$\hat{\Psi}_\sigma(\mathbf{r}) = \sum_j w_0(\mathbf{r} - \mathbf{r}_j) \hat{c}_{j\sigma}, \tag{A.7}$$

where we take the Wannier functions to be optimally localized [340]. Substituting this into Eq. (A.6) yields

$$\begin{aligned} \hat{H} = &\sum_{\sigma=\uparrow,\downarrow} \sum_{i,j} \int d\mathbf{r}\, w_0^*(\mathbf{r} - \mathbf{r}_i) \left[ -\frac{\nabla^2}{2m} + V(\mathbf{r}) \right] w_0(\mathbf{r} - \mathbf{r}_j) \hat{c}_{i\sigma}^\dagger \hat{c}_{j\sigma} \\ &+ g \sum_{ijkl} \int d\mathbf{r}\, w_0^*(\mathbf{r} - \mathbf{r}_i) w_0^*(\mathbf{r} - \mathbf{r}_j) w_0(\mathbf{r} - \mathbf{r}_k) w_0(\mathbf{r} - \mathbf{r}_l) \hat{c}_{i\uparrow}^\dagger \hat{c}_{j\downarrow}^\dagger \hat{c}_{k\downarrow} \hat{c}_{l\uparrow}. \end{aligned} \tag{A.8}$$

In deep lattices, we can restrict ourselves only to nearest-neighbour hopping since it is the dominating contribution. Furthermore, the use of optimally localized Wannier functions implies that we can take into account only the interaction of two particles with opposite pseudo-spin projections that occupy the same lattice site [340]. Thus, assuming a translation-invariant system, Eq. (A.8) becomes the Hubbard Hamiltonian

$$\hat{H} = -J \sum_{\sigma\langle ij\rangle} (\hat{c}^{\dagger}_{i,\sigma} \hat{c}_{j\sigma} + \text{H.c.}) + U \sum_{j} \hat{n}_{j\uparrow} \hat{n}_{j\downarrow}. \tag{A.9}$$

Here, the hopping $J$ is given by

$$J = -\int d\mathbf{r}\, w_0^*(\mathbf{r} - \mathbf{r}_i) \left[ -\frac{\nabla^2}{2m} + V(\mathbf{r}) \right] w_0(\mathbf{r} - \mathbf{r}_j) \tag{A.10}$$

and the on-site interaction strength reads

$$U = g \int d\mathbf{r}\, |w_0(\mathbf{r} - \mathbf{r}_j)|^4. \tag{A.11}$$

Note that the single-particle on-site energies of the form

$$\epsilon_i = \int d\mathbf{r}\, w_0^*(\mathbf{r} - \mathbf{r}_i) \left[ -\frac{\nabla^2}{2m} + V(\mathbf{r}) \right] w_0(\mathbf{r} - \mathbf{r}_i)$$

have been dropped in this simple case by redefining the zero energy level, which can be done since the Hubbard Hamiltonian conserves the total particle number and the system is translation invariant.

It is possible to obtain approximate analytical expressions for the parameters $J$ and $U$. In the limit $s \gg 1$, the hopping can be obtained from the width $W$ of the lowest Bloch band in the 1D Mathieu equation as $J = W/4$, yielding the expression [147]

$$J = \frac{4}{\sqrt{\pi}} E_R s^{3/4} e^{-2\sqrt{s}}. \tag{A.12}$$

A closed form for $U$ is obtained in the harmonic approximation by assuming a Gaussian form for the Wannier functions. The result is [147]

$$U = \sqrt{\frac{8}{\pi}} k_L a_s E_R s^{3/4}. \tag{A.13}$$

# Appendix B

## FOUR-STATE MODEL OF THE SPIN-ASYMMETRIC JOSEPHSON EFFECT WITH GENERAL TUNNELLING COUPLINGS

In Ref. [37] and in Section 4.2.3, the origin of the spin-asymmetric Josephson effect was elucidated with the dynamics of a Cooper pair in an effective four-state system. This was done for a momentum conserving tunnelling matrix element $\Omega_\sigma$, However, in general the tunnelling matrix is not diagonal in momentum space. This is case for example in the setup in Section 5.2. We now demonstrate that the Josephson dynamics can be reduced to the four-state description for a general form of the tunnelling coupling. More specifically, we show that in the second order of perturbation theory, the four-state description is valid, i.e., the total current can be given as a sum over all possible four state systems. This result has been published in Ref. [2].

We replace for notational convenience the $\uparrow$ / $\downarrow, L/R$ indices with one generic spin-label $\sigma = 1, 2, 3, 4$, with the correspondences

$$1 = \uparrow, L \tag{B.1}$$

$$2 = \downarrow, L \tag{B.2}$$

$$3 = \uparrow, R \tag{B.3}$$

$$4 = \downarrow, R. \tag{B.4}$$

We also absorb all single-particle potentials, including the spin-dependent ones, into to the variable $\xi_{\mathbf{k},\sigma}$ for simplicity, since they are not explicitly required here as we want to focus on the effect of the non-momentum conserving coupling. We assume that in the initial ground state $|\Psi(t=0)\rangle$ there is BCS-type pairing between the states 1 and 2, and between 3 and 4. Tunnelling is assumed between the states 1 and 3, and between 2 and 4. The Hamiltonian of the system is thus given by

$$\hat{H} = \hat{H}_0 + \hat{H}_\Omega, \tag{B.5}$$

where

$$\hat{H}_0 = \sum_{\mathbf{k},\sigma} \xi_{\mathbf{k},\sigma} \hat{n}_{\mathbf{k},\sigma} + \frac{g}{V_s} \sum_{\mathbf{k},\mathbf{k}'} \hat{c}^\dagger_{\mathbf{k},1} \hat{c}^\dagger_{-\mathbf{k},2} \hat{c}_{-\mathbf{k}',2} \hat{c}_{\mathbf{k}',1} + \frac{g}{V_s} \sum_{\mathbf{k},\mathbf{k}'} \hat{c}^\dagger_{\mathbf{k},3} \hat{c}^\dagger_{-\mathbf{k},4} \hat{c}_{-\mathbf{k}',4} \hat{c}_{\mathbf{k}',3}, \tag{B.6}$$

and

$$\begin{aligned} \hat{H}_\Omega &= \sum_{\mathbf{k},\mathbf{k}'} \Omega_{\mathbf{k}1,\mathbf{k}'3} \hat{c}^\dagger_{\mathbf{k}1} \hat{c}_{\mathbf{k}'3} + \text{H.c.} + \sum_{\mathbf{k},\mathbf{k}'} \Omega_{\mathbf{k}2,\mathbf{k}'4} \hat{c}^\dagger_{\mathbf{k}2} \hat{c}_{\mathbf{k}'4} + \text{H.c.} \\ &= \sum_{\mathbf{k}\sigma,\mathbf{k}'\sigma'} \Omega_{\mathbf{k}\sigma,\mathbf{k}'\sigma'} \hat{c}^\dagger_{\mathbf{k}\sigma} \hat{c}_{\mathbf{k}'\sigma'}, \end{aligned} \tag{B.7}$$

where $\Omega^*_{\mathbf{k}\sigma,\mathbf{k}'\sigma'} = \Omega_{\mathbf{k}'\sigma',\mathbf{k}\sigma}$.

The Josephson effect is derived in the interaction picture using second order perturbation theory with respect to $\hat{H}_\Omega(t) = e^{\mathrm{i}\hat{H}_0 t} \hat{H}_\Omega e^{-\mathrm{i}\hat{H}_0 t}$. The time-evolved state $|\Psi(t)\rangle$ to second order in the tunnelling is given by

$$|\Psi(t)\rangle \approx |\Psi(0)\rangle - \mathrm{i} \int_0^t dt_1 \, \hat{H}_\Omega(t_1) \, |\Psi(0)\rangle - \int_0^t \int_0^{t_1} dt_1 \, dt_2 \, \hat{H}_\Omega(t_1) \hat{H}_\Omega(t_2) \, |\Psi(0)\rangle \, . \tag{B.8}$$

We consider the time-evolution of the total particle number in the state $\sigma$, given by

$$N_\sigma(t) = \langle \Psi(t) | \hat{N}_\sigma | \Psi(t) \rangle. \tag{B.9}$$

The current is then given by the time derivative of $N_\sigma(t)$. However, our conclusion will be unaffected whether we consider $N_\sigma(t)$ or the current. Since the particle number is a slightly more convenient quantity to calculate here, we consider

$N_\sigma(t)$. The zeroth and first order contributions of $\hat{H}_\Omega$ to $N_\sigma(t)$ are the initial particle number and zero, respectively. The second order contribution reads

$$\begin{aligned}
\left\langle \hat{N}_\sigma \right\rangle_2 (t) = &\langle \Psi(0)| \int_0^t dt_2\, \hat{H}_\Omega(t_2) \hat{N}_\sigma \int_0^t dt_1\, \hat{H}_\Omega(t_1) \,|\Psi(0)\rangle \\
&- \langle \Psi(0)| \int_0^t \int_0^{t_1} dt_1\, dt_2\, \hat{N}_\sigma \hat{H}_\Omega(t_2) \hat{H}_\Omega(t_1) \,|\Psi(0)\rangle + \text{H.c.} \\
= &\int_0^t \int_0^t dt_1\, dt_2 \sum_{\mathbf{k}\sigma_1, \mathbf{k}'\sigma_1'} \sum_{\mathbf{p}\sigma_2, \mathbf{p}'\sigma_2'} \Omega_{\mathbf{k}\sigma_1, \mathbf{k}'\sigma_1'} \Omega_{\mathbf{p}\sigma_2, \mathbf{p}'\sigma_2'} \\
&\times \langle \Psi(0)| e^{\mathrm{i}\hat{H}_0 t_2} \hat{c}^\dagger_{\mathbf{k}\sigma_1} \hat{c}_{\mathbf{k}'\sigma_1'} e^{-\mathrm{i}\hat{H}_0 t_2} \hat{N}_\sigma e^{\mathrm{i}\hat{H}_0 t_1} \hat{c}^\dagger_{\mathbf{p}\sigma_2} \hat{c}_{\mathbf{p}'\sigma_2'} e^{-\mathrm{i}\hat{H}_0 t_1} \,|\Psi(0)\rangle \\
&- \int_0^t \int_0^{t_1} dt_1\, dt_2 \sum_{\mathbf{k}\sigma_1, \mathbf{k}'\sigma_1'} \sum_{\mathbf{p}\sigma_2, \mathbf{p}'\sigma_2'} \Omega_{\mathbf{k}\sigma_1, \mathbf{k}'\sigma_1'} \Omega_{\mathbf{p}\sigma_2, \mathbf{p}'\sigma_2'} \\
&\times \langle \Psi(0)| \hat{N}_\sigma e^{\mathrm{i}\hat{H}_0 t_2} \hat{c}^\dagger_{\mathbf{k}\sigma_1} \hat{c}_{\mathbf{k}'\sigma_1'} e^{-\mathrm{i}\hat{H}_0 t_2} e^{\mathrm{i}\hat{H}_0 t_1} \hat{c}^\dagger_{\mathbf{p}\sigma_2} \hat{c}_{\mathbf{p}'\sigma_2'} e^{-\mathrm{i}\hat{H}_0 t_1} \,|\Psi(0)\rangle + \text{H.c.}
\end{aligned} \tag{B.10}$$

In the first term after the second equality, we have relabelled $\mathbf{k}\sigma_1$ as $\mathbf{k}'\sigma_1'$ and vice versa.

We can simplify Eq. (B.10) by taking the BCS pairing correlations of the initial state $|\Psi(0)\rangle$ into account. They determine which matrix elements survive the summation over momenta and spin. We consider the case $\sigma_2 = 1$ as an example. Other spin indices are dealt similarly.

For $\sigma_2 = 1$, the tunnelling matrix element $\Omega_{\mathbf{p}\sigma_2, \mathbf{p}'\sigma_2'}$ directly sets $\sigma_2' = 3$ [see Eq. (B.7)]. For the other spin indices $\sigma_1$ and $\sigma_1'$ in Eq. (B.10), we similarly find the possible combinations

$$(\sigma_1, \sigma_1') = (1,3), (3,1), (2,4), (4,2). \tag{B.11}$$

The operators $\hat{N}_\sigma$ and $\hat{H}_0$ in Eq. (B.10) do not change the number of unpaired particles. We thus leave them out of the notation in the following for clarity, and denote the matrix elements in Eq. (B.10) simply by $\langle \Psi(0)| \hat{c}^\dagger_{\mathbf{k}\sigma_1} \hat{c}_{\mathbf{k}'\sigma_1'} \hat{c}^\dagger_{\mathbf{p}1} \hat{c}_{\mathbf{p}'3} \,|\Psi(0)\rangle$. We include the operators $\hat{N}_\sigma$ and $\hat{H}_0$ in the notation again later. The remaining operators

$\hat{c}^\dagger_{\mathbf{k}\sigma_1}\hat{c}_{\mathbf{k}'\sigma_1'}$ and $\hat{c}^\dagger_{\mathbf{p}1}\hat{c}_{\mathbf{p}'3}$ change the number of unpaired particles. To show this, consider the operator $\hat{c}^\dagger_{\mathbf{p}1}\hat{c}_{\mathbf{p}'3}$ acting on a state with no unpaired particles. As a result, two unpaired fermions are created, one in the state $|\mathbf{p}1\rangle$ and the other in the state $|-\mathbf{p}'4\rangle$ since the paired fermion in the state $|\mathbf{p}'3\rangle$ has been annihilated. For the matrix element $\langle\Psi(0)|\,\hat{c}^\dagger_{\mathbf{k}\sigma_1}\hat{c}_{\mathbf{k}'\sigma_1'}\hat{c}^\dagger_{\mathbf{p}1}\hat{c}_{\mathbf{p}'3}\,|\Psi(0)\rangle$ to be non-zero, the operator $\hat{c}^\dagger_{\mathbf{k}\sigma_1}\hat{c}_{\mathbf{k}'\sigma_1'}$ has to act so that both of these unpaired states are removed, either by annihilating the unpaired fermion or by creating the missing fermion to form a pair. Thus, for the spin indices $(\sigma_1,\sigma_1')=(1,3),(4,2)$ we find

$$\langle\psi(0)|\,\hat{c}^\dagger_{\mathbf{k}1}\hat{c}_{\mathbf{k}'3}\hat{c}^\dagger_{\mathbf{p}1}\hat{c}_{\mathbf{p}'3}\,|\psi(0)\rangle\equiv 0, \tag{B.12}$$

and

$$\langle\psi(0)|\,\hat{c}^\dagger_{\mathbf{k}4}\hat{c}_{\mathbf{k}'2}\hat{c}^\dagger_{\mathbf{p}1}\hat{c}_{\mathbf{p}'3}\,|\psi(0)\rangle\equiv 0. \tag{B.13}$$

In other words, these combinations of spin indices only break Cooper pairs. For the spin indices $(\sigma_1,\sigma_1')=(3,1),(2,4)$ we find non-zero matrix-elements for particular momenta $(\mathbf{k},\mathbf{k}')$, namely

$$\langle\Psi(0)|\,\hat{c}^\dagger_{\mathbf{k}3}\hat{c}_{\mathbf{k}'1}\hat{c}^\dagger_{\mathbf{p}1}\hat{c}_{\mathbf{p}'3}\,|\Psi(0)\rangle=\delta_{\mathbf{k},\mathbf{p}'}\delta_{\mathbf{k}',\mathbf{p}}\,\langle\Psi(0)|\,\hat{c}^\dagger_{\mathbf{k}3}\hat{c}_{\mathbf{k}'1}\hat{c}^\dagger_{\mathbf{k}'1}\hat{c}_{\mathbf{k}3}\,|\Psi(0)\rangle\,, \tag{B.14}$$

and

$$\langle\Psi(0)|\,\hat{c}^\dagger_{\mathbf{k}2}\hat{c}_{\mathbf{k}'4}\hat{c}^\dagger_{\mathbf{p}1}\hat{c}_{\mathbf{p}'3}\,|\Psi(0)\rangle=\delta_{\mathbf{k},-\mathbf{p}}\delta_{\mathbf{k}',-\mathbf{p}'}\,\langle\Psi(0)|\,\hat{c}^\dagger_{\mathbf{k}2}\hat{c}_{\mathbf{k}'4}\hat{c}^\dagger_{-\mathbf{k}1}\hat{c}_{-\mathbf{k}'3}\,|\Psi(0)\rangle\,. \tag{B.15}$$

We now know the form of the surviving matrix elements and we can return to the full notation. Using the matrix elements in Eqs. (B.12)–(B.15) and their equivalents for other spin indices (recall that Eqs. (B.12)–(B.15) were derived for $\sigma_2=1$),

Eq. (B.10) becomes

$$\begin{aligned}\left\langle \hat{N}_\sigma \right\rangle_2 (t) = &\int_0^t \int_0^t dt_1\, dt_2 \sum_{\mathbf{k}\sigma_1,\mathbf{k}'\sigma_1'} \Omega_{\mathbf{k}\sigma_1,\mathbf{k}'\sigma_1'} \Omega_{\mathbf{k}'\sigma_1',\mathbf{k}\sigma_1} \\ &\times \langle \Psi(0)| e^{\mathrm{i}\hat{H}_0 t_2} \hat{c}^\dagger_{\mathbf{k}\sigma_1} \hat{c}_{\mathbf{k}'\sigma_1'} e^{-\mathrm{i}\hat{H}_0 t_2} \hat{N}_\sigma e^{\mathrm{i}\hat{H}_0 t_1} \hat{c}^\dagger_{\mathbf{k}'\sigma_1'} \hat{c}_{\mathbf{k}\sigma_1} e^{-\mathrm{i}\hat{H}_0 t_1} |\Psi(0)\rangle \\ &- \int_0^t \int_0^{t_1} dt_1\, dt_2 \sum_{\mathbf{k}\sigma_1,\mathbf{k}'\sigma_1'} \Omega_{\mathbf{k}\sigma_1,\mathbf{k}'\sigma_1'} \Omega_{-\mathbf{k}\bar{\sigma}_1,-\mathbf{k}'\bar{\sigma}_1'} \\ &\times \langle \Psi(0)| e^{\mathrm{i}\hat{H}_0 t_2} \hat{c}^\dagger_{\mathbf{k}\sigma_1} \hat{c}_{\mathbf{k}'\sigma_1'} e^{-\mathrm{i}\hat{H}_0 t_2} \hat{N}_\sigma e^{\mathrm{i}\hat{H}_0 t_1} \hat{c}^\dagger_{-\mathbf{k}'\bar{\sigma}_1} \hat{c}_{-\mathbf{k}\bar{\sigma}_1} e^{-\mathrm{i}\hat{H}_0 t_1} |\Psi(0)\rangle + \text{H.c.} \\ &+ \int_0^t \int_0^t dt_1\, dt_2 \sum_{\mathbf{k}\sigma_1,\mathbf{k}'\sigma_1'} \Omega_{\mathbf{k}\sigma_1,\mathbf{k}'\sigma_1'} \Omega_{\mathbf{k}'\sigma_1',\mathbf{k}\sigma_1} \\ &\times \langle \Psi(0)| \hat{N}_\sigma e^{\mathrm{i}\hat{H}_0 t_2} \hat{c}^\dagger_{\mathbf{k}\sigma_1} \hat{c}_{\mathbf{k}'\sigma_1'} e^{-\mathrm{i}\hat{H}_0 t_2} e^{\mathrm{i}\hat{H}_0 t_1} \hat{c}^\dagger_{\mathbf{k}'\sigma_1'} \hat{c}_{\mathbf{k}\sigma_1} e^{-\mathrm{i}\hat{H}_0 t_1} |\Psi(0)\rangle \\ &- \int_0^t \int_0^{t_1} dt_1\, dt_2 \sum_{\mathbf{k}\sigma_1,\mathbf{k}'\sigma_1'} \Omega_{\mathbf{k}\sigma_1,\mathbf{k}'\sigma_1'} \Omega_{-\mathbf{k}\bar{\sigma}_1,-\mathbf{k}'\bar{\sigma}_1'} \\ &\times \langle \Psi(0)| \hat{N}_\sigma e^{\mathrm{i}\hat{H}_0 t_2} \hat{c}^\dagger_{\mathbf{k}\sigma_1} \hat{c}_{\mathbf{k}'\sigma_1'} e^{-\mathrm{i}\hat{H}_0 t_2} e^{\mathrm{i}\hat{H}_0 t_1} \hat{c}^\dagger_{-\mathbf{k}\bar{\sigma}_1} \hat{c}_{-\mathbf{k}'\bar{\sigma}_1'} e^{-\mathrm{i}\hat{H}_0 t_1} |\Psi(0)\rangle + \text{H.c.}\end{aligned} \tag{B.16}$$

We use the notation $\bar{\sigma}$ for opposite spin, with $\bar{1} = 2$, $\bar{2} = 1$, $\bar{3} = 4$, and $\bar{4} = 3$.

We can take the summation over the momenta and spin in front of the whole expression in Eq. (B.16). The result has the form

$$\begin{aligned}\left\langle \hat{N}_\sigma \right\rangle_2 (t) = \sum_{\mathbf{k}\sigma_1,\mathbf{k}'\sigma_1'} &[\text{Four-state system of transitions} \\ &|\mathbf{k}\sigma_1\rangle \leftrightarrow |\mathbf{k}'\sigma_1'\rangle \text{ and } |-\mathbf{k}\bar{\sigma}_1\rangle \leftrightarrow |-\mathbf{k}'\bar{\sigma}_1'\rangle],\end{aligned} \tag{B.17}$$

i.e., a summation over all allowed four-state systems. A single term of this sum is equivalent to the second order perturbation theory result in Section 4.2.3 but now with the momentum-dependent couplings $\Omega_{\mathbf{k}\sigma_1,\mathbf{k}'\sigma_1'}$ and $\Omega_{-\mathbf{k}\bar{\sigma}_1,-\mathbf{k}'\bar{\sigma}_1'}$ and the relevant initial state being the superposition of the Cooper pairs of states $|\mathbf{k}\sigma\rangle_1 |-\mathbf{k}\bar{\sigma}_1\rangle$ and $|\mathbf{k}'\sigma_1'\rangle |-\mathbf{k}'\bar{\sigma}_1'\rangle$. This superposition originates from the initial many-body state as follows. The initial state is given by two BCS states, with

$$|\Psi(0)\rangle = \prod_{\mathbf{p}} (u_{\mathbf{p}} + v_{\mathbf{p}} \hat{c}^\dagger_{\mathbf{p}1} \hat{c}^\dagger_{-\mathbf{p}2}) |\emptyset\rangle_L \prod_{\mathbf{p}'} (u_{\mathbf{p}'} + v_{\mathbf{p}'} \hat{c}^\dagger_{\mathbf{p}'3} \hat{c}^\dagger_{-\mathbf{p}'4}) |\emptyset\rangle_R . \tag{B.18}$$

Note that this is the same initial state as in Eq. (4.31). For each pair of the couplings $\Omega_{\mathbf{k}1,\mathbf{k}'3}$ and $\Omega_{-\mathbf{k}2,-\mathbf{k}'4}$, we express $|\Psi(0)\rangle$ as

$$\begin{aligned}|\Psi(0)\rangle &= (u_{\mathbf{k}} + v_{\mathbf{k}}\hat{c}^{\dagger}_{\mathbf{k}1}\hat{c}^{\dagger}_{-\mathbf{k}2})(u_{\mathbf{k}'} + v_{\mathbf{k}'}\hat{c}^{\dagger}_{\mathbf{k}'3}\hat{c}^{\dagger}_{-\mathbf{k}'4})\left|\tilde{\Psi}\right\rangle, \\ &= \left(u_{\mathbf{k}}u_{\mathbf{k}'} + v_{\mathbf{k}}u_{\mathbf{k}'}\hat{c}^{\dagger}_{\mathbf{k}1}\hat{c}^{\dagger}_{-\mathbf{k}2} + u_{\mathbf{k}}v_{\mathbf{k}'}\hat{c}^{\dagger}_{\mathbf{k}'3}\hat{c}^{\dagger}_{-\mathbf{k}'4} + v_{\mathbf{k}}v_{\mathbf{k}'}\hat{c}^{\dagger}_{\mathbf{k}1}\hat{c}^{\dagger}_{-\mathbf{k}2}\hat{c}^{\dagger}_{\mathbf{k}'3}\hat{c}^{\dagger}_{-\mathbf{k}'4}\right)\left|\tilde{\Psi}\right\rangle,\end{aligned} \tag{B.19}$$

where

$$\left|\tilde{\Psi}\right\rangle = \prod_{\mathbf{p}\neq\mathbf{k}}(u_{\mathbf{p}} + v_{\mathbf{p}}\hat{c}^{\dagger}_{\mathbf{p}1}\hat{c}^{\dagger}_{-\mathbf{p}2})\left|\emptyset\right\rangle_L \prod_{\mathbf{p}'\neq\mathbf{k}'}(u_{\mathbf{p}'} + v_{\mathbf{p}'}\hat{c}^{\dagger}_{\mathbf{p}'3}\hat{c}^{\dagger}_{-\mathbf{p}'4})\left|\emptyset\right\rangle_R, \tag{B.20}$$

The $u_{\mathbf{k}}u_{\mathbf{k}'}$-term corresponds to an empty state with respect to $\Omega_{\mathbf{k}1,\mathbf{k}'3}$ and $\Omega_{-\mathbf{k}2-\mathbf{k}'4}$, and does not contribute to the Josephson dynamics. The $v_{\mathbf{k}}v_{\mathbf{k}'}$-term also cannot contribute since it is Pauli blocked. Thus, similarly to the momentum-conserving case in Section 4.2.3, the Josephson physics results from the initial superposition of the two states $|\mathbf{k}1\rangle|-\mathbf{k}2\rangle$ and $|\mathbf{k}'3\rangle|-\mathbf{k}'4\rangle$ under the time-evolution induced by $\Omega_{\mathbf{k}1,\mathbf{k}'3}$ and $\Omega_{-\mathbf{k}2-\mathbf{k}'4}$. The 'intermediate' states $|\mathbf{k}1\rangle|-\mathbf{k}'4\rangle$ and $|-\mathbf{k}2\rangle|\mathbf{k}'3\rangle$ are required to describe the tunnelling processes, and thus the four-state system is complete.

To conclude, we have shown that the four-state description of the spin-asymmetric Josephson effect presented in Ref [37] and Section 4.2.3 can be applied also to the case of a general tunnelling coupling in the second order of perturbation theory.

# Appendix C

## TIME-EVOLVING BLOCK DECIMATION

Here we briefly describe the idea of the time-evolving block decimation (TEBD) algorithm [63,64] with which the numerical simulations of the spin-dependent superlattice setup in Chapter 4 were done. TEBD is a widely used numerical method to efficiently simulate both the real (according to $e^{-\mathrm{i}\hat{H}t}$) and imaginary (according to $e^{-\hat{H}\tau}$) time-evolution of one-dimensional quantum systems in a lattice, the Hamiltonian $\hat{H}$ of which comprises of at most nearest-neighbour interactions.

In TEBD, the (pure) quantum state of the system is stored as a matrix product state (MPS) (see, e.g., Ref. [341]) whose size is characterised by a 'bond dimension' $\chi$. The MPS representation of the state involves a product of matrices of size $\chi \times \chi$. Any pure quantum state can be expressed as an MPS if $\chi$ is large enough. In general, for an exact representation of the state, the dimension $\chi$ and thus the computational resources required for the simulation grow exponentially with the system size. However, the MPS description becomes practical and efficient if the state can be approximated quasi-exactly with a small $\chi$, often on the order of $\mathcal{O}(10^2)$. This is the case for example with the ground and low-lying excited states of one-dimensional quantum systems [342,343].

With the MPS form of the state, TEBD performs the time-evolution, either real or imaginary, by utilising a Suzuki-Trotter decomposition of the evolution operator $\hat{U}$ such that $\hat{U}$ is expressed as an approximate product of single-site and nearest-

neighbour operators of the form $e^{-\mathrm{i}\hat{H}_{i,i+1}\delta t}$ (or $e^{-\hat{H}_{i,i+1}\delta\tau}$). Each time a nearest-neighbour operator is acted on the state during the time-evolution, a singular value decomposition of the updated matrices of the MPS is applied and only the $\chi$ largest singular values are kept. This way the simulation stays efficient. A matrix product representation can be obtained for single-site and nearest-neighbour operators as well. This allows calculating the dynamical expectation values of these operators for an MPS. For further details of the TEBD algorithm, we refer to Refs. [63,64,197].

The 1D spin-dependent superlattice in Section 4.3 is well suited for the TEBD method. In the numerical simulations, we used a system size of $L = 50$ lattice sites, MPS bond dimension $\chi = 150$ and time-step $\delta t = 0.01J^{-1}$ in the real-time evolution. We found that increasing $L$ and $\chi$ resulted in no significant changes to the computed observables.

# Appendix D

## HIGHER-ORDER CORRECTIONS TO JOSEPHSON-LIKE OSCILLATIONS IN A SUPERLATTICE

In Fig. 4.11, we see that for experimentally observable particle oscillations the Josephson contribution consists of several sub-peaks instead of the single spin-asymmetric signal as predicted by the linear response result in Eqs. (4.26) and (4.29). Moreover, the central peak in Fig. 4.11 is slightly shifted from the typical Josephson frequency of $\delta_\uparrow + \delta_\downarrow$. Here, we elucidate the possible the origin of these effects by studying smaller lattice systems with second-order time-independent perturbation theory with respect to the tunnelling matrix elements in Eq. (4.46).

The shift of the Josephson frequency from $\delta_\uparrow + \delta_\downarrow$ can be obtained by considering a half-filled Hubbard dimer (a two-site system with two particles) governed by the superlattice Hubbard Hamiltonian in Eq. (4.46). Here, the unperturbed Hamiltonian is given by

$$\hat{H}_0 = U\left(\hat{n}_{1,\uparrow}\hat{n}_{1,\downarrow} + \hat{n}_{2,\uparrow}\hat{n}_{2,\downarrow}\right) + \sum_{\sigma=\uparrow,\downarrow} \frac{\delta_\sigma}{2}\left(\hat{n}_{1,\sigma} - \hat{n}_{2,\sigma}\right), \tag{D.1}$$

and the perturbation Hamiltonian reads

$$\hat{H}' = -\sum_{\sigma=\uparrow,\downarrow} J_\sigma \left(\hat{c}^\dagger_{2,\sigma}\hat{c}_{1,\sigma} + \text{H.c.}\right). \tag{D.2}$$

The Josephson-type oscillations (which are a second order effect in $J_\sigma$) occur between the paired states (compare with Section 4.2.3)

$$|1\rangle = |\uparrow\downarrow, \emptyset\rangle, \tag{D.3}$$

$$|2\rangle = |\emptyset, \uparrow\downarrow\rangle, \tag{D.4}$$

with the unperturbed eigenenergies

$$E_1^{(0)} = U + \frac{\delta_\uparrow}{2} + \frac{\delta_\downarrow}{2}, \tag{D.5}$$

$$E_2^{(0)} = U - \frac{\delta_\uparrow}{2} - \frac{\delta_\downarrow}{2}. \tag{D.6}$$

The first order corrections to the energies, $E_n^{(1)} = \langle n^{(0)}|\hat{H}'|n^{(0)}\rangle$ where $|n^{(0)}\rangle$ is an eigenstate of $\hat{H}_0$ with eigenenergy $E_n^{(0)}$, are zero, while the second order corrections can be calculated from

$$E_n^{(2)} = \sum_{m\neq n} \frac{\left|\langle m^{(0)}|\hat{H}'|n^{(0)}\rangle\right|^2}{E_n^{(0)} - E_m^{(0)}}, \tag{D.7}$$

yielding

$$E_1^{(2)} = \frac{J_\uparrow^2}{U + \delta_\uparrow} + \frac{J_\downarrow^2}{U + \delta_\downarrow}, \tag{D.8}$$

$$E_2^{(2)} = \frac{J_\uparrow^2}{U - \delta_\uparrow} + \frac{J_\downarrow^2}{U - \delta_\downarrow}. \tag{D.9}$$

Thus, we obtain the perturbed Josephson frequency as

$$\begin{aligned}\omega_J^{(2)} &= \left|E_1^{(0)} + E_1^{(2)} - \left(E_2^{(0)} + E_2^{(2)}\right)\right| \\ &= \delta_\uparrow + \delta_\downarrow + \frac{2J_\uparrow^2\delta_\uparrow}{\delta_\uparrow^2 - U^2} + \frac{2J_\downarrow^2\delta_\downarrow}{\delta_\downarrow^2 - U^2},\end{aligned} \tag{D.10}$$

where the last two terms give a rough estimate of the shift in the frequency in Fig. 4.11.

To elucidate the emergence of several Josephson signals, we investigate a four-site system described by the Hamiltonian in Eq. (4.46). We again take the unperturbed Hamiltonian to be

$$\hat{H}_0 = U\sum_{i=1}^{4} \hat{n}_{i,\uparrow}\hat{n}_{i,\downarrow} + \sum_{\sigma=\uparrow,\downarrow} \frac{\delta_\sigma}{2}\left(\hat{n}_{1,\sigma} - \hat{n}_{2,\sigma} + \hat{n}_{3,\sigma} - \hat{n}_{4,\sigma}\right), \tag{D.11}$$

while the perturbation reads

$$\hat{H}' = -\sum_{i=1}^{3}\sum_{\sigma=\uparrow,\downarrow} J_\sigma \left(\hat{c}^\dagger_{i+1,\sigma}\hat{c}_{i,\sigma} + \text{H.c.}\right). \tag{D.12}$$

As an example, we consider the following two paired states (other states are treated similarly)

$$|1\rangle = |\emptyset, \uparrow\downarrow, \emptyset, \uparrow\downarrow\rangle, \tag{D.13}$$

$$|2\rangle = |\uparrow\downarrow, \emptyset, \uparrow\downarrow, \emptyset\rangle, \tag{D.14}$$

which have Josephson-like oscillations with the state

$$|3\rangle = \frac{1}{\sqrt{2}}\left(|\uparrow\downarrow, \emptyset, \emptyset, \uparrow\downarrow\rangle + |\emptyset, \uparrow\downarrow, \uparrow\downarrow, \emptyset\rangle\right). \tag{D.15}$$

The unperturbed energies of the above states are given by $E_1^{(0)} = 2U - \delta_\uparrow - \delta_\downarrow$, $E_2^{(0)} = 2U + \delta_\uparrow + \delta_\downarrow$, and $E_3^{(0)} = 2U$, respectively. We can then calculate the frequency of the unperturbed Josephson oscillations as $\omega_J^{(0)} = \left|E_1^{(0)} - E_3^{(0)}\right| = \left|E_2^{(0)} - E_3^{(0)}\right| = \delta_\uparrow + \delta_\downarrow$ which is precisely the typical Josephson frequency.

The second order corrections can be obtained from Eq. (D.7) ($E_n^{(1)} = 0$ as above). We obtain

$$E_1^{(2)} = \frac{3J_\uparrow^2}{U - \delta_\uparrow} + \frac{3J_\downarrow^2}{U - \delta_\downarrow}, \tag{D.16}$$

$$E_2^{(2)} = \frac{3J_\uparrow^2}{U + \delta_\uparrow} + \frac{3J_\downarrow^2}{U + \delta_\downarrow}, \tag{D.17}$$

$$E_3^{(2)} = 2U\left(\frac{J_\uparrow^2}{U^2 - \delta_\uparrow^2} + \frac{J_\downarrow^2}{U^2 - \delta_\downarrow^2}\right). \tag{D.18}$$

The perturbed Josephson frequencies are then given by

$$\begin{aligned}\omega_{J,13}^{(2)} &= \left|E_1^{(0)} + E_1^{(2)} - \left(E_3^{(0)} + E_3^{(2)}\right)\right| \\ &= \delta_\uparrow + \delta_\downarrow + \frac{2J_\downarrow^2}{\delta_\downarrow - U} + \frac{2J_\uparrow^2}{\delta_\uparrow - U} + \frac{J_\downarrow^2}{\delta_\downarrow + U} + \frac{J_\uparrow^2}{\delta_\uparrow + U},\end{aligned} \tag{D.19}$$

and

$$\begin{aligned}\omega^{(2)}_{J,23} &= \left| E^{(0)}_2 + E^{(2)}_2 - \left( E^{(0)}_3 + E^{(2)}_3 \right) \right| \\ &= \delta_\uparrow + \delta_\downarrow + \frac{2J^2_\downarrow}{\delta_\downarrow + U} + \frac{2J^2_\uparrow}{\delta_\uparrow + U} + \frac{J^2_\downarrow}{\delta_\downarrow - U} + \frac{J^2_\uparrow}{\delta_\uparrow - U}. \end{aligned} \tag{D.20}$$

We see that the Josephson frequencies of these processes are no longer equal and the difference reads

$$\begin{aligned}\Delta\omega^{(2)}_J &= \omega^{(2)}_{J,13} - \omega^{(2)}_{J,23} \\ &= 2|U| \left( \frac{J^2_\uparrow}{U^2 - \delta^2_\uparrow} + \frac{J^2_\downarrow}{U^2 - \delta^2_\downarrow} \right). \end{aligned} \tag{D.21}$$

This is gives an estimate in the correct order of magnitude of the frequency separation between adjacent sub-peaks in Fig. 4.11, since $\Delta\omega^{(2)}_J \approx 0.51J$ (with $J = J_\uparrow = J_\downarrow$) in Eq. (D.21), whereas the splitting is $0.50J$ in Fig. 4.11.

# Appendix E

## Derivation of Eq. (8.5)

Here we show the derivation of Eq. (8.5) as per Ref. [313]. We consider the low-frequency expansion of the self-energy given by

$$\Sigma_{\mathrm{imp/latt}}(\omega) = a + b\omega + \mathcal{O}(\omega^2), \tag{E.1}$$

where $a$ and $b$ are constants. Since $b = \frac{d\Sigma(\omega)}{d\omega}|_{\omega=0}$, the quasiparticle weight is given by

$$\mathcal{Z} = \frac{1}{1-b}. \tag{E.2}$$

We define the so-called coherent parts of the lattice and impurity Green functions by substituting Eqs. (E.1) and (E.2) into Eqs. (7.11) and (7.9), i.e., [313]

$$G^{(\mathrm{coh})}_{\mathrm{latt},jj}(\omega) = \mathcal{Z}\int d\epsilon\, \frac{D(\epsilon)}{\omega - \mathcal{Z}(\epsilon - \mu + a)} \tag{E.3}$$

$$G^{(\mathrm{coh})}_{\mathrm{imp}}(\omega) = \frac{\mathcal{Z}}{\omega - \mathcal{Z}[\Lambda(\omega) - \mu + a]}. \tag{E.4}$$

Comparing the high-frequency expansions of these functions,

$$\begin{aligned} G^{(\mathrm{coh})}_{\mathrm{latt},jj}(\omega) &= \frac{\mathcal{Z}}{\omega}\int d\epsilon\, \frac{D(\epsilon)}{1 - \frac{\mathcal{Z}(\epsilon-\mu+a)}{\omega}} \\ &= \frac{\mathcal{Z}}{\omega} + \frac{\mathcal{Z}^2(a-\mu)}{\omega^2} + \frac{\mathcal{Z}^3[M_2^{(0)} + (a-\mu)^2]}{\omega^3} + \mathcal{O}(\omega^{-4}), \end{aligned} \tag{E.5}$$

and

$$G_{\mathrm{imp}}^{(\mathrm{coh})}(\omega) = \frac{\mathcal{Z}}{\omega}\frac{1}{1-\frac{\mathcal{Z}}{\omega}(\frac{V^2}{\omega}-\mu+a)} = \frac{\mathcal{Z}}{\omega}+\frac{\mathcal{Z}^2(a-\mu)}{\omega^2}+\frac{\mathcal{Z}^2V^2+\mathcal{Z}^3(a-\mu)^2}{\omega^3}+\mathcal{O}(\omega^{-4}), \tag{E.6}$$

and demanding that they match directly yields Eq. (8.5).

# Appendix F

## SINGLE-QUBIT INTERFEROMETRY FOR THE RETARDED IMPURITY GREEN FUNCTION

Here, we present a measurement scheme for the retarded impurity Green function in the two-site DMFT protocol in Chapter 8. The scheme has been published in Ref. [3].

## F.1 Definitions

The retarded zero temperature impurity Green function in the time domain can be written as

$$G^R_{\rm imp}(t) = \theta(t)\left[G^>_{\rm imp}(t) - G^<_{\rm imp}(t)\right], \tag{F.1}$$

where the greater and lesser Green functions are given by

$$G^>_{\rm imp}(t) = -{\rm i}\langle \hat{c}_{1\sigma,H}(t)\hat{c}^\dagger_{1\sigma,H}(0)\rangle_{GS}, \tag{F.2}$$

$$G^<_{\rm imp}(t) = {\rm i}\langle \hat{c}^\dagger_{1\sigma,H}(0)\hat{c}_{1\sigma,H}(t)\rangle_{GS}, \tag{F.3}$$

respectively. The average is computed in the ground-state $|\Psi_{\rm GS}\rangle$ of the two-site SIAM in Eq. (8.1). Here, $\sigma$ can be either $\downarrow$ or $\uparrow$ since we are considering a spin-symmetric case (i.e., $G^R_\downarrow = G^R_\uparrow$), and the $\hat{c}$-operators are given in the Heisenberg picture with respect to $\hat{H}_{\rm SIAM,2}$, i.e.,

$$\hat{c}_{1\sigma,H}(t) = \hat{U}^\dagger(t)\hat{c}_{1\sigma}\hat{U}(t) = e^{{\rm i}t\hat{H}_{\rm SIAM,2}}\hat{c}_{1\sigma,H}e^{-{\rm i}t\hat{H}_{\rm SIAM,2}}. \tag{F.4}$$

One possibility to measure the impurity Green function $G^R_{\mathrm{imp}}(t)$ is to use a single-qubit Ramsey interferometer [344] (see also, e.g., Ref. [345]). To this end, we introduce an ancilla qubit in addition to the 'system' qubits, raising the total number of qubits needed to implement the two-site DMFT scheme to five.

## F.2 Jordan–Wigner transformation

The greater and lesser components, $G^{>}_{\mathrm{imp}}(t)$ and $G^{<}_{\mathrm{imp}}(t)$, must be written in terms of spin operators by again mapping the $\hat{c}_{1\sigma}$ and $\hat{c}^\dagger_{1\sigma}$ operators onto Pauli operators via the Jordan–Wigner transformation in Eqs. (8.10)–(8.13). For concreteness, we focus on the case $\sigma =\downarrow$. We obtain

$$G^{>}_{\mathrm{imp}}(t) = -\frac{\mathrm{i}}{4}\Big(\langle\hat{U}^\dagger(t)\hat{\sigma}^x_1\hat{U}(t)\hat{\sigma}^x_1\rangle_{GS} + \mathrm{i}\langle\hat{U}^\dagger(t)\hat{\sigma}^x_1\hat{U}(t)\hat{\sigma}^y_1\rangle_{GS} - \mathrm{i}\langle\hat{U}^\dagger(t)\hat{\sigma}^y_1\hat{U}(t)\hat{\sigma}^x_1\rangle_{GS} + \langle\hat{U}^\dagger(t)\hat{\sigma}^y_1\hat{U}(t)\hat{\sigma}^y_1\rangle_{GS}\Big), \tag{F.5}$$

and

$$G^{<}_{\mathrm{imp}}(t) = \frac{\mathrm{i}}{4}\Big(\langle\hat{\sigma}^x_1\hat{U}^\dagger(t)\hat{\sigma}^x_1\hat{U}(t)\rangle_{GS} - \mathrm{i}\langle\hat{\sigma}^x_1\hat{U}^\dagger(t)\hat{\sigma}^y_1\hat{U}(t)\rangle_{GS} + \mathrm{i}\langle\hat{\sigma}^y_1\hat{U}^\dagger(t)\hat{\sigma}^x_1\hat{U}(t)\rangle_{GS} + \langle\hat{\sigma}^y_1\hat{U}^\dagger(t)\hat{\sigma}^y_1\hat{U}(t)\rangle_{GS}\Big). \tag{F.6}$$

## F.3 Measurement protocol

Each of the terms of the form $\langle\hat{U}^\dagger(t)\hat{\sigma}^\alpha_1\hat{U}(t)\hat{\sigma}^\beta_1\rangle$, where $\alpha,\beta \in \{x,y\}$, can be measured in the interferometer. This can be seen as follows. We denote the state of the system qubits by $\hat{\rho}_{\mathrm{sys}} = |\Psi_{\mathrm{GS}}\rangle\langle\Psi_{\mathrm{GS}}|$. We initialize the ancilla qubit in the state $|0\rangle$, yielding the total density operator $\hat{\rho}_{\mathrm{tot}} = |0\rangle\langle 0| \otimes \hat{\rho}_{\mathrm{sys}}$. The total system then undergoes the following evolution:

1. At time $t = 0$, a Hadamard gate $\hat{\sigma}_H = \frac{1}{\sqrt{2}}(\hat{\sigma}^z + \hat{\sigma}^x)$ is applied on the ancilla qubit, creating the superposition $|0\rangle_{\mathrm{ancilla}} \to (|0\rangle_{\mathrm{ancilla}} + |1\rangle_{\mathrm{ancilla}})/\sqrt{2}$.

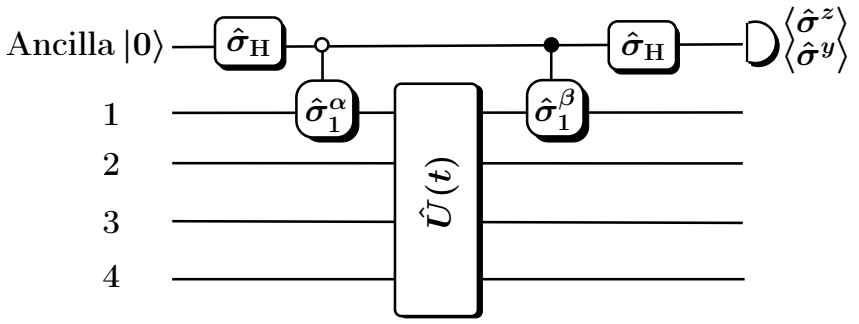


Figure F.1: Quantum network to measure the $\langle GS|\hat{U}^\dagger(t)\hat{\sigma}_1^\alpha\hat{U}(t)\hat{\sigma}_1^\beta|GS\rangle_{GS}$ contribution to the Green function $G^R_{\mathrm{imp}}(t)$. The time-evolution operator $\hat{U}(t)$ is composed of a set of quantum gates according to Section 8.3. Figure adapted from Ref. [3].

2. A Controlled-Pauli gate $\hat{\sigma}_1^\alpha$ is applied on the impurity qubit 1 if the ancilla qubit has state $|0\rangle$.

3. The system qubits undergo time evolution according to the unitary $\hat{U}(t)$ which is decomposed into quantum gates.

4. Another controlled Pauli gate $\hat{\sigma}_1^\beta$ is applied on the impurity qubit 1 if the ancilla qubit has state $|1\rangle$.

5. Another Hadamard gate is applied on the ancilla qubit.

Denoting the total unitary in steps 2-4 by $\hat{T}$, the state of the ancilla qubit after this evolution is given by

$$\begin{aligned}\hat{\rho}_{\mathrm{ancilla}} &= \mathrm{Tr}_{\mathrm{sys}}\left[\hat{\sigma}_H\hat{T}\hat{\sigma}_H\hat{\rho}_{\mathrm{tot}}\hat{\sigma}_H\hat{T}^\dagger\hat{\sigma}_H\right] \\ &= \frac{1+\mathrm{Re}[F(t)]}{2}|0\rangle\langle 0| - \mathrm{i}\frac{\mathrm{Im}[F(t)]}{2}|0\rangle\langle 1| + \mathrm{i}\frac{\mathrm{Im}[F(t)]}{2}|1\rangle\langle 0| \\ &+ \frac{1-\mathrm{Re}[F(t)]}{2}|1\rangle\langle 1|, \end{aligned} \tag{F.7}$$

where $F(t) = \mathrm{Tr}_{\mathrm{sys}}\left[\hat{T}_1^\dagger(t)\hat{T}_0(t)\hat{\rho}_{\mathrm{sys}}\right]$. We have denoted the controlled unitaries as $\hat{T}_1(t) = \hat{\sigma}_1^\alpha\hat{U}(t)$ and $\hat{T}_0(t) = \hat{U}(t)\hat{\sigma}_1^\beta$. Note that since the same $\hat{U}(t)$ appears in both

unitaries, only the Pauli gates $\hat{\sigma}_1^{\alpha/\beta}$ need to be controlled, as described above. Note also that $F(t) = \langle \hat{U}^\dagger(t)\hat{\sigma}_1^\alpha \hat{U}(t)\hat{\sigma}_1^\beta \rangle$.

We can rewrite the state of the ancilla qubit in Eq. (F.7) as

$$\hat{\rho}_{\text{ancilla}} = \frac{1}{2}\left(\hat{I} + \text{Re}[F(t)]\hat{\sigma}_z + \text{Im}[F(t)]\hat{\sigma}_y\right), \tag{F.8}$$

implying that $\text{Tr}_{\text{ancilla}}\left[\hat{\rho}_{\text{ancilla}}\hat{\sigma}^z\right] = \text{Re}[F(t)]$, and $\text{Tr}_{\text{ancilla}}\left[\hat{\rho}_{\text{ancilla}}\hat{\sigma}^y\right] = \text{Im}[F(t)]$. Thus, repeated measurements of the $\hat{\sigma}^z$ and $\hat{\sigma}^y$ components of the ancilla qubit yield the real and imaginary parts of the term $\langle \hat{U}^\dagger(t)\hat{\sigma}_1^\alpha \hat{U}(t)\hat{\sigma}_1^\beta \rangle_{GS}$. Note the relation $\hat{\sigma}^y = \exp(-\text{i}\pi\hat{\sigma}^x/4)\hat{\sigma}^z \exp(\text{i}\pi\hat{\sigma}^x/4)$, i.e., the measurements of $\hat{\sigma}^y$ can be done in the $\hat{\sigma}^z$ basis with an additional single-qubit operation. A classical summation of the terms and their complex conjugates for all $\alpha, \beta \in \{x, y\}$ according to Eqs. (F.5) and (F.6) yields the retarded impurity Green function in Eq. (F.1). See Fig. F.1 for the quantum network of the scheme.

# Appendix G

## SINGLE-QUBIT INTERFEROMETRY FOR THE NON-EQUILIBRIUM IMPURITY GREEN FUNCTION

The non-equilibrium impurity Green function in Chapter 9 can be measured for example with the single-qubit interferometry presented in Appendix F. The scheme generalises straightforwardly to the non-equilibrium case.

The impurity Green function is again given as sum of the greater and lesser Green functions [see Eq. (9.12)] which are given in terms of spin-operators via the Jordan–Wigner transformation. As a distinction to the equilibrium case, the different terms to be measured in the single-qubit interferometer are of the form $F(t,t') = \langle\psi_0^s|\hat{U}(0,t)\hat{\sigma}_1^\alpha\hat{U}(t,t')\hat{\sigma}_1^\beta\hat{U}(t',0)|\psi_0^s\rangle$ for spin projection $\sigma =\downarrow$, and $F(t,t') = \langle\psi_0^s|\hat{U}(0,t)\hat{\sigma}_1^z\hat{\sigma}_2^x\hat{U}(t,t')\hat{\sigma}_1^z\hat{\sigma}_2^x\hat{U}(t',0)|\psi_0^s\rangle$ for spin projection $\sigma =\uparrow$, with $\alpha,\beta \in \{x,y\}$. In addition, step 2 in the measurement protocol in Appendix F is preceded with a time-evolution according to the unitary $\hat{U}(t',0)$ which is decomposed into quantum gates, and in step 3 in Appendix F the time-evolution is given by $\hat{U}(t,t')$, also decomposed into quantum gates. Otherwise the Ramsey scheme for the non-equilibrium case is identical to the one in Appendix F. We show an example of the quantum networks in Fig. 9.3.

# Appendix H

## OUTLINE OF THE CLASSICAL SIMULATIONS OF THE HYBRID QUANTUM-CLASSICAL DEVICE

Here we describe how we perform the classical simulations of the single-qubit interferometer described in Appendix G. In the actual hybrid device, the single-qubit interferometry is done experimentally with a digital quantum simulator, and in our simulations we try to mimic the experimental procedure to some extent.

We consider the first $L_b$ time steps, where $L_b = N_b/2$ is the half the number of bath sites. We first obtain some initial guess hybridization parameters $V_p^{(0)}(t)$, where $t = 0, \delta t, \ldots, L_b \times \delta t$. Using $V_p^{(0)}(t)$ we construct *imperfect* quantum gates $\hat{U}_{\rm loc}(\varphi + \epsilon)$ and $\hat{U}_{\rm MS}^{l,m}(\theta + \epsilon_{\rm MS1}, \phi + \epsilon_{\rm MS2})$, where $\epsilon$, $\epsilon_{\rm MS1}$, and $\epsilon_{\rm MS2}$ are normally distributed random variables with zero mean and standard deviations $\sigma$, $\sigma_{\rm MS1}$, and $\sigma_{\rm MS2}$, respectively. These quantum gates yield the Trotterized unitary evolution operator $\hat{U}(t, t')$, where $t, t' = 0, \delta t, \ldots, L_b \times \delta t$. We use this evolution operator to compute the $(t = m \times \delta t, t' = n \times \delta t)$-point (with $m, n \leq L_b$) of $F(t, t')$ from the expectation values ${\rm Tr}_{\rm ancilla}\left[\hat{\rho}_{\rm ancilla}\hat{\sigma}_z\right]$ and ${\rm Tr}_{\rm ancilla}\left[\hat{\rho}_{\rm ancilla}\hat{\sigma}_y\right]$ as explained in Appendices F and G, and we average the results over several realizations to gather error statistics. After going through all the possible combinations of the controlled Pauli gates, we obtain $G_{\rm imp}(t = m \times \delta t, t' = n \times \delta t)$.

However, we interpret the computation of the point $(t = m \times \delta t, t' = n \times \delta t)$ as a perfect measurement which collapses the state of the system, and we cannot store

any information of the state at this time instant in memory, since we don't want to re-use any of the obtained wave functions later to avoid correlating the errors between different points in the Green function. We compute these points from independent realizations instead. This way we make our classical simulations to follow more closely what one would do in an experiment. This means that in order to compute another point $(t = (m+1)\times\delta t, t' = n\times\delta t)$ or $(t = m\times\delta t, t' = (n+1)\times\delta t)$, we have to propagate again from the origin $(t = 0, t' = 0)$ to the desired point and again average over several realizations. This procedure is repeated until we have obtained all the points of $G_{\rm imp}(t, t')$ until $(t = L_b \times \delta t, t' = L_b \times \delta t)$. This concludes the 'experimental', or quantum, part of the first $L_b$ time steps in the *first* iteration of the DMFT self-consistency loop.

The obtained $G_{\rm imp}(t, t')$ is then used in the classical computer to produce the hybridization function $\Lambda(t, t') = v(t)G_{\rm imp}(t, t')v(t')$. In the first $L_b$ time steps, we have enough parameters to do a Cholesky decomposition of $\Lambda(t, t')$ to obtain the new $V_p^{(1)}(t)$, which are used for updating $\hat{U}_{\rm loc}(\varphi + \epsilon)$ and $\hat{U}_{\rm MS}^{l,m}(\theta + \epsilon_{\rm MS1}, \phi + \epsilon_{\rm MS2})$. This begins the *second* iteration of the DMFT self-consistency loop where use the updated quantum gates to again measure $G_{\rm imp}(t, t')$ using the steps described above, always starting from the origin to compute one point in the time grid and averaging over several realizations. This non-linear process of 'measuring' $G_{\rm imp}(t, t')$ and using Cholesky decomposition of $\Lambda(t, t')$ to update $V_p(t)$ is repeated until we have $\max|V_p^{(n)}(t) - V_p^{(n-1)}(t)| < {\rm err}$, where ${\rm err}$ is a predetermined error threshold.

For the time steps $L_b+1, \ldots, N_T$ with $t_{\rm max} = N_T \times \delta t$, we adopt the 'time slicing' scheme of Ref. [300] (see Section 7.3.2), where we iterate one time step $s > L_b$ to self-consistency before moving to $s + 1$. In the classical part of the hybrid device, we update only $V_p(s \times \delta t)$ while keeping the previously obtained $V_p(l \times \delta t)$ with $l < s$ fixed. However, again when we want to reach the $s$th time step in the time grid, we have to start propagating from the origin.

Mimicking the experiment to this level makes our classical simulation computationally challenging. As a result, our simulations are limited to small system sizes and relatively short time scales.

# Appendix I

## SUPER-FERMION APPROACH TO OPEN QUANTUM SYSTEMS

Here, for the sake of completeness, we illustrate the idea of the super-fermion approach to open quantum systems by considering a single fermionic level with energy $\omega$ coupled to a thermal reservoir with decay rate $\Gamma^-$ and excitation rate $\Gamma^+$. The scheme can then be generalised to many sites. Further details on the super-fermion approach can be found in Ref. [330] and references therein.

The dynamics of the single level is described by the master equation

$$\begin{aligned}\frac{d}{dt}\hat{\rho}(t) = &-\mathrm{i}\omega\left[\hat{c}^\dagger\hat{c},\hat{\rho}(t)\right]\\ &+\frac{1}{2}\Gamma^-\left[2\hat{c}\hat{\rho}(t)\hat{c}^\dagger-\hat{c}^\dagger\hat{c}\hat{\rho}(t)-\hat{\rho}(t)\hat{c}^\dagger\hat{c}\right]\\ &+\frac{1}{2}\Gamma^+\left[2\hat{c}^\dagger\hat{\rho}(t)\hat{c}-\hat{c}\hat{c}^\dagger\hat{\rho}(t)-\hat{\rho}(t)\hat{c}\hat{c}^\dagger\right].\end{aligned} \tag{I.1}$$

We want to obtain the time-evolution of the operators $\hat{c}(t)$ and $\hat{c}^\dagger(t)$, with which we can calculate any single-particle correlation functions. To do this, we use the super-fermion formalism. The idea is to introduce an additional ancilla Fock space which is an identical copy of the original Fock space. We denote the annihilation and creation operators of the ancilla space by $\hat{d}$ and $\hat{d}^\dagger$, respectively. They anticommute with $\hat{c}$ and $\hat{c}^\dagger$.

We form a super-Fock space with the direct product of the original and the

ancilla Fock space. We define a number state in the super-Fock space as

$$|n|m\rangle = (\hat{c}^\dagger)^n(\hat{d}^\dagger)^m|\emptyset\rangle. \tag{I.2}$$

We then introduce a 'left vacuum' state[1] defined as

$$|I\rangle = \sum_{n=0}^{1}(-\mathrm{i})^n|n|n\rangle. \tag{I.3}$$

We have the following relations

$$\hat{c}|I\rangle = -\mathrm{i}\hat{d}^\dagger|I\rangle, \qquad \hat{c}^\dagger|I\rangle = -\mathrm{i}\hat{d}|I\rangle. \tag{I.4}$$

We act Eq. (I.1) on $|I\rangle$, and use Eq. (I.4) to obtain

$$\frac{d}{dt}|\rho(t)\rangle = -\mathrm{i}\hat{\mathcal{L}}|\rho(t)\rangle, \tag{I.5}$$

where $|\rho(t)\rangle = \hat{\rho}(t)|I\rangle$, and the Liouvillian reads

$$\begin{aligned}\hat{\mathcal{L}} = \omega(\hat{c}^\dagger\hat{c} - \hat{d}^\dagger\hat{d}) - \mathrm{i}\tilde{\Gamma}(\hat{c}^\dagger\hat{c} + \hat{d}^\dagger\hat{d}) \\ + \Gamma^-\hat{c}\hat{d} + \Gamma^+\hat{c}^\dagger\hat{d}^\dagger - \mathrm{i}\Gamma^+.\end{aligned} \tag{I.6}$$

Here, we have denoted $\tilde{\Gamma} = (\Gamma^- - \Gamma^+)/2$.

As stated above, we are interested in time-dependent correlation functions (i.e., Green functions) involving the creation and annihilation operators. To this end, we determine the commutator of $\hat{c}$, $\hat{c}^\dagger$, $\hat{d}$, and $\hat{d}^\dagger$ with $\hat{\mathcal{L}}$ to obtain an equation of motion for $\hat{c}(t)$ and $\hat{c}^\dagger(t)$ as

$$\frac{d}{dt}\hat{c}(t) = \mathrm{i}[\hat{\mathcal{L}}, \hat{c}(t)] \tag{I.7}$$

$$\frac{d}{dt}\hat{c}^\dagger(t) = \mathrm{i}[\hat{\mathcal{L}}, \hat{c}^\dagger(t)], \tag{I.8}$$

where $\hat{c}(t) = e^{\mathrm{i}\hat{\mathcal{L}}t}\hat{c}e^{-\mathrm{i}\hat{\mathcal{L}}t}$ and $\hat{c}^\dagger(t) = e^{\mathrm{i}\hat{\mathcal{L}}t}\hat{c}^\dagger e^{-\mathrm{i}\hat{\mathcal{L}}t}$. We find

$$[\hat{\mathcal{L}}, \hat{c}] = (-\omega + \mathrm{i}\tilde{\Gamma})\hat{c} - \Gamma^+\hat{d}^\dagger, \tag{I.9}$$

$$[\hat{\mathcal{L}}, \hat{d}^\dagger] = (-\omega - \mathrm{i}\tilde{\Gamma})\hat{d}^\dagger + \Gamma^-\hat{c}, \tag{I.10}$$

$$[\hat{\mathcal{L}}, \hat{c}^\dagger] = (\omega - \mathrm{i}\tilde{\Gamma})\hat{c}^\dagger - \Gamma^-\hat{d}, \tag{I.11}$$

$$[\hat{\mathcal{L}}, \hat{d}] = (-\omega + \mathrm{i}\tilde{\Gamma})\hat{d} + \Gamma^+\hat{c}^\dagger. \tag{I.12}$$

[1]The name 'left vacuum' comes from the fact that $\langle I|\hat{\mathcal{L}} = 0$, where $\hat{\mathcal{L}}$ is the Liouvillian [330].

The form of these equations implies the ansatz

$$\hat{c}(t) = \alpha(t)\hat{c} + \beta(t)\hat{d}^\dagger, \tag{I.13}$$

$$\hat{c}^\dagger(t) = \gamma(t)\hat{c}^\dagger + \delta(t)\hat{d}. \tag{I.14}$$

We thus obtain the following equations of motion

$$\begin{pmatrix} \dot{\alpha}(t) \\ \dot{\beta}(t) \end{pmatrix} = \begin{pmatrix} -\mathrm{i}\omega - \tilde{\Gamma} & \mathrm{i}\Gamma^- \\ -\mathrm{i}\Gamma^+ & -\mathrm{i}\omega + \tilde{\Gamma} \end{pmatrix} \begin{pmatrix} \alpha(t) \\ \beta(t) \end{pmatrix}, \tag{I.15}$$

$$\begin{pmatrix} \dot{\gamma}(t) \\ \dot{\delta}(t) \end{pmatrix} = \begin{pmatrix} \mathrm{i}\omega + \tilde{\Gamma} & \mathrm{i}\Gamma^+ \\ -\mathrm{i}\Gamma^- & \mathrm{i}\omega - \tilde{\Gamma} \end{pmatrix} \begin{pmatrix} \gamma(t) \\ \delta(t) \end{pmatrix}. \tag{I.16}$$

Solving these equations with the appropriate initial conditions yields $\hat{c}(t)$ and $\hat{c}^\dagger(t)$, which can then be used to calculate any single-particle correlation functions of the form $\langle I|\hat{c}^\dagger(t)\hat{c}(t')|\rho(0)\rangle$ [330].

# REFERENCES


[1] Kreula, J. M., Valtolina, G. & Törmä, P. Spin-asymmetric Josephson plasma oscillations. *Phys. Rev. A* **95**, 013634 (2017).

[2] Kreula, J. M., Heikkinen, M. O. J., Massel, F. & Törmä, P. Tunable critical supercurrent and spin-asymmetric Josephson effect in superlattices. *Phys. Rev. B* **89**, 064502 (2014).

[3] Kreula, J. M. *et al.* Few-qubit quantum-classical simulation of strongly correlated lattice fermions. *EPJ Quantum Technol.* **3**, 11 (2016).

[4] Kreula, J. M., Clark, S. R. & Jaksch, D. Non-linear quantum-classical scheme to simulate non-equilibrium strongly correlated fermionic many-body dynamics. *Sci. Rep.* **6**, 32940 (2016).

[5] Buluta, I. & Nori, F. Quantum simulators. *Science* **326**, 108–111 (2009).

[6] Johnson, T. H., Clark, S. R. & Jaksch, D. What is a quantum simulator? *EPJ Quantum Technol.* **1**, 1–12 (2014).

[7] Georgescu, I. M., Ashhab, S. & Nori, F. Quantum simulation. *Rev. Mod. Phys.* **86**, 153 (2014).

[8] Feynman, R. P. Simulating physics with computers. *Int. J. Theor. Phys.* **21**, 467–488 (1982).

[9] Bloch, I., Dalibard, J. & Nascimbène, S. Quantum simulations with ultracold quantum gases. *Nat. Phys.* **8**, 267–276 (2012).

[10] Blatt, R. & Roos, C. F. Quantum simulations with trapped ions. *Nat. Phys.* **8**, 277–284 (2012).

[11] Houck, A. A., Türeci, H. E. & Koch, J. On-chip quantum simulation with superconducting circuits. *Nat. Phys.* **8**, 292–299 (2012).

[12] Aspuru-Guzik, A. & Walther, P. Photonic quantum simulators. *Nat. Phys.* **8**, 285–291 (2012).

[13] Lanyon, B. P. *et al.* Towards quantum chemistry on a quantum computer. *Nat. Chem.* **2**, 106–111 (2010).

[14] Jaksch, D., Bruder, C., Cirac, J. I., Gardiner, C. W. & Zoller, P. Cold bosonic atoms in optical lattices. *Phys. Rev. Lett.* **81**, 3108–3111 (1998).

[15] Greiner, M., Mandel, O., Esslinger, T., Hänsch, T. W. & Bloch, I. Quantum phase transition from a superfluid to a Mott insulator in a gas of ultracold atoms. *Nature* **415**, 39–44 (2002).

[16] Jördens, R., Strohmaier, N., Günter, K., Moritz, H. & Esslinger, T. A Mott insulator of fermionic atoms in an optical lattice. *Nature* **455**, 204–207 (2008).

[17] Lamata, L., León, J., Schätz, T. & Solano, E. Dirac equation and quantum relativistic effects in a single trapped ion. *Phys. Rev. Lett.* **98**, 253005 (2007).

[18] Gerritsma, R. *et al.* Quantum simulation of the Dirac equation. *Nature* **463**, 68–71 (2010).

[19] Hauke, P., Marcos, D., Dalmonte, M. & Zoller, P. Quantum simulation of a lattice Schwinger model in a chain of trapped ions. *Phys. Rev. X* **3**, 041018 (2013).

[20] Kühn, S., Cirac, J. I. & Bañuls, M.-C. Quantum simulation of the Schwinger model: A study of feasibility. *Phys. Rev. A* **90**, 042305 (2014).

[21] Martinez, E. A. *et al.* Real-time dynamics of lattice gauge theories with a few-qubit quantum computer. *Nature* **534**, 516–519 (2016).

[22] Bermudez, A. *et al.* Wilson fermions and axion electrodynamics in optical lattices. *Phys. Rev. Lett.* **105**, 190404 (2010).

[23] Béri, B. & Cooper, N. R. $Z_2$ topological insulators in ultracold atomic gases. *Phys. Rev. Lett.* **107**, 145301 (2011).

[24] Mazza, L. *et al.* An optical-lattice-based quantum simulator for relativistic field theories and topological insulators. *New J. Phys.* **14**, 015007 (2012).

[25] Jaksch, D. & Zoller, P. The cold atom Hubbard toolbox. *Ann. Phys.* **315**, 52–79 (2005).

[26] Lewenstein, M. *et al.* Ultracold atomic gases in optical lattices: Mimicking condensed matter physics and beyond. *Adv. Phys.* **56**, 243–379 (2007).

[27] Bloch, I., Dalibard, J. & Zwerger, W. Many-body physics with ultracold gases. *Rev. Mod. Phys.* **80**, 885 (2008).

[28] Giorgini, S., Pitaevskii, L. P. & Stringari, S. Theory of ultracold atomic Fermi gases. *Rev. Mod. Phys.* **80**, 1215 (2008).

[29] Esslinger, T. Fermi–Hubbard physics with atoms in an optical lattice. *Annu. Rev. Condens. Matter Phys.* **1**, 129 (2010).

[30] Levin, K., Fetter, A. & Stamper-Kurn, D. (eds.) *Ultracold Bosonic and Fermionic Gases*, vol. 5 (Elsevier, 2012).

[31] Törmä, P. & Sengstock, K. (eds.) *Quantum Gas Experiments: Exploring Many-Body States*, vol. 3 (Imperial College Press, 2014).

[32] Lloyd, S. Universal quantum simulators. *Science* **273**, 1073–1078 (1996).

[33] Lanyon, B. P. *et al.* Universal digital quantum simulation with trapped ions. *Science* **334**, 57–61 (2011).

[34] Barends, R. *et al.* Digital quantum simulation of fermionic models with a superconducting circuit. *Nat. Commun.* **6**, 7654 (2015).

[35] Daintith, J. (ed.) *A Dictionary of Physics* (Oxford University Press, 2009), 6th edn.

[36] Paraoanu, G. S., Rodriguez, M. & Törmä, P. Josephson effect in superfluid atomic Fermi gases. *Phys. Rev. A* **66**, 041603 (2002).

[37] Heikkinen, M. O. J. *et al.* Spin-asymmetric Josephson effect. *Phys. Rev. Lett.* **105**, 225301 (2010).

[38] Valtolina, G. *et al.* Josephson effect in fermionic superfluids across the BEC-BCS crossover. *Science* **350**, 1505–1508 (2015).

[39] Bergeret, F. S., Volkov, A. F. & Efetov, K. B. Enhancement of the Josephson current by an exchange field in superconductor-ferromagnet structures. *Phys. Rev. Lett.* **86**, 3140 (2001).

[40] Georges, A., Kotliar, G., Krauth, W. & Rozenberg, M. J. Dynamical mean-field theory of strongly correlated fermion systems and the limit of infinite dimensions. *Rev. Mod. Phys.* **68**, 13 (1996).

[41] Aoki, H. *et al.* Nonequilibrium dynamical mean-field theory and its applications. *Rev. Mod. Phys.* **86**, 779–837 (2014).

[42] The rise of quantum materials. *Nat. Phys.* **12**, 105 (2016).

[43] Coleman, P. *Introduction to Many-Body Physics* (Cambridge University Press, 2015).

[44] Hubbard, J. Electron correlations in narrow energy bands. *Proc. Roy. Soc. London Ser. A* **276**, 238–257 (1963).

[45] Gutzwiller, M. C. Effect of correlation on the ferromagnetism of transition metals. *Phys. Rev. Lett.* **10**, 159 (1963).

[46] Kanamori, J. Electron correlation and ferromagnetism of transition metals. *Prog. Theor. Phys.* **30**, 275–289 (1963).

[47] Bloch, I. Ultracold quantum gases in optical lattices. *Nat. Phys.* **1**, 23–30 (2005).

[48] Chin, C., Grimm, R., Julienne, P. & Tiesinga, E. Feshbach resonances in ultracold gases. *Rev. Mod. Phys.* **82**, 1225 (2010).

[49] Cavalleri, A. *et al.* Tracking the motion of charges in a terahertz light field by femtosecond X-ray diffraction. *Nature* **442**, 664–666 (2006).

[50] Gedik, N., Yang, D.-S., Logvenov, G., Bozovic, I. & Zewail, A. H. Nonequilibrium phase transitions in cuprates observed by ultrafast electron crystallography. *Science* **316**, 425–429 (2007).

[51] Fausti, D. *et al.* Light-induced superconductivity in a stripe-ordered cuprate. *Science* **331**, 189–191 (2011).

[52] Wall, S. *et al.* Quantum interference between charge excitation paths in a solid-state Mott insulator. *Nat. Phys.* **7**, 114–118 (2011).

[53] Först, M. *et al.* Spatially resolved ultrafast magnetic dynamics launched at a complex-oxide hetero-interface. *Nat. Mater.* **14**, 883–888 (2015).

[54] Mitrano, M. *et al.* Possible light-induced superconductivity in $K_3C_{60}$ at high temperature. *Nature* **530**, 461–464 (2016).

[55] Dean, M. P. M. *et al.* Ultrafast energy-and momentum-resolved dynamics of magnetic correlations in the photo-doped Mott insulator $Sr_2IrO_4$. *Nat. Mater.* **15**, 601–605 (2016).

[56] Eisert, J., Friesdorf, M. & Gogolin, C. Quantum many-body systems out of equilibrium. *Nat. Phys.* **11**, 124–130 (2015).

[57] Langen, T., Geiger, R. & Schmiedmayer, J. Ultracold atoms out of equilibrium. *Annu. Rev. Condens. Matter Phys.* **6**, 201–217 (2015).

[58] Lee, P. A., Nagaosa, N. & Wen, X.-G. Doping a Mott insulator: Physics of high-temperature superconductivity. *Rev. Mod. Phys.* **78**, 17–85 (2006).

[59] Bethe, H. Zur Theorie der Metalle. *Z. Phys.* **71**, 205–226 (1931).

[60] White, S. R. Density matrix formulation for quantum renormalization groups. *Phys. Rev. Lett.* **69**, 2863 (1992).

[61] White, S. R. Density-matrix algorithms for quantum renormalization groups. *Phys. Rev. B* **48**, 10345 (1993).

[62] White, S. R. & Feiguin, A. E. Real-time evolution using the density matrix renormalization group. *Phys. Rev. Lett.* **93**, 76401 (2004).

[63] Vidal, G. Efficient classical simulation of slightly entangled quantum computations. *Phys. Rev. Lett.* **91**, 147902 (2003).

[64] Vidal, G. Efficient simulation of one-dimensional quantum many-body systems. *Phys. Rev. Lett.* **93**, 40502 (2004).

[65] Mott, N. F. Metal-insulator transition. *Rev. Mod. Phys.* **40**, 677 (1968).

[66] Rickayzen, G. *Green's Functions and Condensed Matter* (Dover Publications, Inc., 2013).

[67] Mahan, G. D. *Many-Particle Physics* (Kluwer Academic/Plenum Publishers, New York, 2000), 3rd edn.

[68] Fetter, A. L. & Walecka, J. D. *Quantum Theory of Many-Particle Systems* (Dover Publications Inc., 2003).

[69] Stefanucci, G. & van Leeuwen, R. *Nonequilibrium Many-Body Theory of Quantum Systems: A Modern Introduction* (Cambridge University Press, 2013).

[70] Jishi, R. A. *Feynman Diagram Techniques in Condensed Matter Physics* (Cambridge University Press, 2013).

[71] Martin, P. C. & Schwinger, J. Theory of many-particle systems. I. *Phys. Rev.* **115**, 1342–1373 (1959).

[72] Mattuck, R. D. *A Guide to Feynman Diagrams in the Many-body Problem* (Dover Publications Inc., 1992), 2nd edn.

[73] Mahan, G. D. *Applied Mathematics* (Springer Science & Business Media, 2012).

[74] Baym, G. & Mermin, N. D. Determination of thermodynamic Green's functions. *J. Math. Phys.* **2**, 232–234 (1961).

[75] Gubernatis, J., Kawashima, N. & Werner, P. *Quantum Monte Carlo Methods: Algorithms for Lattice Models* (Cambridge University Press, 2016).

[76] Kamenev, A. *Field Theory of Non-Equilibrium Systems* (Cambridge University Press, 2011).

[77] Schwabl, F. *Advanced Quantum Mechanics* (Springer Verlag, 2008), 3rd edn.

[78] Eckstein, M. *Nonequilibrium dynamical mean-field theory*. Ph.D. thesis, Universität Augsburg, Germany (2009).

[79] Strohmaier, N. *et al.* Interaction-controlled transport of an ultracold Fermi gas. *Phys. Rev. Lett.* **99**, 220601 (2007).

[80] Schneider, U. *et al.* Metallic and insulating phases of repulsively interacting fermions in a 3D optical lattice. *Science* **322**, 1520–1525 (2008).

[81] Cataliotti, F. S. *et al.* Josephson junction arrays with Bose-Einstein condensates. *Science* **293**, 843–846 (2001).

[82] Albiez, M. *et al.* Direct observation of tunneling and nonlinear self-trapping in a single bosonic Josephson junction. *Phys. Rev. Lett.* **95**, 010402 (2005).

[83] Levy, S., Lahoud, E., Shomroni, I. & Steinhauer, J. The ac and dc Josephson effects in a Bose–Einstein condensate. *Nature* **449**, 579–583 (2007).

[84] Pethick, C. J. & Smith, H. *Bose-Einstein Condensation in Dilute Gases* (Cambridge University Press, UK, 2001).

[85] Pitaevskii, L. & Stringari, S. *Bose-Einstein Condensation* (Oxford University Press, 2003).

[86] Jervis, D. & Thywissen, J. H. Making an Ultracold Gas. In Törmä, P. & Sengstock, K. (eds.) *Quantum Gas Experiments: Exploring Many-Body States*, chap. 2, 5–32 (Imperial College Press, 2014).

[87] Inguscio, M. & Fallani, L. *Atomic Physics: Precise Measurements and Ultracold Matter* (Oxford University Press, 2013).

[88] Truscott, A. G., Strecker, K. E., McAlexander, W. I., Partridge, G. B. & Hulet, R. G. Observation of Fermi pressure in a gas of trapped atoms. *Science* **291**, 2570–2572 (2001).

[89] Inguscio, M., Ketterle, W. & Salomon, C. (eds.) *Ultra-cold Fermi Gases, Proceedings of the International School of Physics Enrico Fermi, Course CLXIV, Varenna 2006* (IOS Press, 2007).

[90] Stamper-Kurn, D. M. & Thywissen, J. H. Experimental methods of ultracold atomic physics. In Levin, K., Fetter, A. & Stamper-Kurn, D. (eds.) *Ultracold Bosonic and Fermionic Gases*, chap. 1, 1–26 (Elsevier, 2012).

[91] Duarte, P. M. *et al.* All-optical production of a lithium quantum gas using narrow-line laser cooling. *Phys. Rev. A* **84**, 061406 (2011).

[92] Weiner, J., Bagnato, V. S., Zilio, S. & Julienne, P. S. Experiments and theory in cold and ultracold collisions. *Rev. Mod. Phys.* **71**, 1 (1999).

[93] DeMarco, B. & Jin, D. S. Onset of Fermi degeneracy in a trapped atomic gas. *Science* **285**, 1703–1706 (1999).

[94] Schreck, F. *et al.* Quasipure Bose-Einstein condensate immersed in a Fermi sea. *Phys. Rev. Lett.* **87**, 80403 (2001).

[95] Fukuhara, T., Takasu, Y., Kumakura, M. & Takahashi, Y. Degenerate Fermi gases of ytterbium. *Phys. Rev. Lett.* **98**, 030401 (2007).

[96] Taie, S. *et al.* Realization of a SU(2)×SU(6) system of fermions in a cold atomic gas. *Phys. Rev. Lett.* **105**, 190401 (2010).

[97] DeSalvo, B. J., Yan, M., Mickelson, P. G., Martinez de Escobar, Y. N. & Killian, T. C. Degenerate Fermi gas of $^{87}$Sr. *Phys. Rev. Lett.* **105**, 030402 (2010).

[98] Tey, M. K., Stellmer, S., Grimm, R. & Schreck, F. Double-degenerate Bose-Fermi mixture of strontium. *Phys. Rev. A* **82**, 011608 (2010).

[99] Lu, M., Burdick, N. Q. & Lev, B. L. Quantum degenerate dipolar Fermi gas. *Phys. Rev. Lett.* **108**, 215301 (2012).

[100] Greiner, M., Regal, C. A. & Jin, D. S. Emergence of a molecular Bose–Einstein condensate from a Fermi gas. *Nature* **426**, 537–540 (2003).

[101] Jochim, S. *et al.* Bose-Einstein condensation of molecules. *Science* **302**, 2101–2103 (2003).

[102] Zwierlein, M. W. *et al.* Observation of Bose-Einstein condensation of molecules. *Phys. Rev. Lett.* **91**, 250401 (2003).

[103] Regal, C. A., Greiner, M. & Jin, D. S. Observation of resonance condensation of fermionic atom pairs. *Phys. Rev. Lett.* **92**, 40403 (2004).

[104] Bartenstein, M. *et al.* Crossover from a molecular Bose-Einstein condensate to a degenerate Fermi gas. *Phys. Rev. Lett.* **92**, 120401 (2004).

[105] Zwierlein, M. W. *et al.* Condensation of pairs of fermionic atoms near a Feshbach resonance. *Phys. Rev. Lett.* **92**, 120403 (2004).

[106] Bourdel, T. *et al.* Experimental study of the BEC-BCS crossover region in lithium 6. *Phys. Rev. Lett.* **93**, 050401 (2004).

[107] Chin, C. *et al.* Observation of the pairing gap in a strongly interacting Fermi gas. *Science* **305**, 1128 (2004).

[108] Partridge, G. B., Strecker, K. E., Kamar, R. I., Jack, M. W. & Hulet, R. G. Molecular probe of pairing in the BEC-BCS crossover. *Phys. Rev. Lett.* **95**, 20404 (2005).

[109] Zwierlein, M. W., Abo-Shaeer, J. R., Schirotzek, A., Schunck, C. H. & Ketterle, W. Vortices and superfluidity in a strongly interacting Fermi gas. *Nature* **435**, 1047–1051 (2005).

[110] Köhler, T., Góral, K. & Julienne, P. S. Production of cold molecules via magnetically tunable Feshbach resonances. *Rev. Mod. Phys.* **78**, 1311–1361 (2006).

[111] Zürn, G. *et al.* Precise characterization of $^6$Li Feshbach resonances using trap-sideband-resolved RF spectroscopy of weakly bound molecules. *Phys. Rev. Lett.* **110**, 135301 (2013).

[112] Hazlett, E. L., Zhang, Y., Stites, R. W. & O'Hara, K. M. Realization of a resonant Fermi gas with a large effective range. *Phys. Rev. Lett.* **108**, 045304 (2012).

[113] Jochim, S. *Bose-Einstein condensation of molecules*. Ph.D. thesis, Leopold-Franzens-Universität Innsbruck, Austria (2004).

[114] Zwerger, W. (ed.) *The BCS-BEC Crossover and the Unitary Fermi Gas* (Springer-Verlag Berlin Heidelberg, 2012).

[115] Bardeen, J., Cooper, L. N. & Schrieffer, J. R. Microscopic theory of superconductivity. *Phys. Rev.* **106**, 162–164 (1957).

[116] Stoof, H. T. C., Houbiers, M., Sackett, C. A. & Hulet, R. G. Superfluidity of spin-polarized $^6$Li. *Phys. Rev. Lett.* **76**, 10–13 (1996).

[117] Houbiers, M. *et al.* Superfluid state of atomic $^6$Li in a magnetic trap. *Phys. Rev. A* **56**, 4864–4878 (1997).

[118] Bruun, G., Castin, Y., Dum, R. & Burnett, K. BCS theory for trapped ultracold fermions. *Euro. Phys. J. D* **7**, 433–439 (1999).

[119] Ueda, M. *Fundamentals and New Frontiers of Bose-Einstein Condensation* (World Scientific, Singapore, 2010).

[120] Cooper, L. N. Bound electron pairs in a degenerate Fermi gas. *Phys. Rev.* **104**, 1189 (1956).

[121] Tinkham, M. *Introduction to Superconductivity* (Dover Publications, 2004).

[122] Törmä, P. & Zoller, P. Laser probing of atomic Cooper pairs. *Phys. Rev. Lett.* **85**, 487–490 (2000).

[123] Kinnunen, J., Rodríguez, M. & Törmä, P. Pairing gap and in-gap excitations in trapped fermionic superfluids. *Science* **305**, 1131 (2004).

[124] Schirotzek, A., Shin, Y.-i., Schunck, C. H. & Ketterle, W. Determination of the superfluid gap in atomic Fermi gases by quasiparticle spectroscopy. *Phys. Rev. Lett.* **101**, 140403 (2008).

[125] Stoof, H. T. C., Gubbels, K. B. & Dickerscheid, D. B. M. *Ultracold Quantum Fields*, vol. 1 (Springer, 2009).

[126] Josephson, B. D. Possible new effects in superconductive tunnelling. *Phys. Lett.* **1**, 251–253 (1962).

[127] Barone, A. & Paterno, G. *Physics and Applications of the Josephson Effect* (John Wiley & Sons, 1982).

[128] Anderson, P. W. & Rowell, J. M. Probable observation of the Josephson superconducting tunneling effect. *Phys. Rev. Lett.* **10**, 230 (1963).

[129] Backhaus, S., Pereverzev, S. V., Loshak, A., Davis, J. C. & Packard, R. E. Direct measurement of the current-phase relation of a superfluid $^3$He-B weak link. *Science* **278**, 1435–1438 (1997).

[130] Sukhatme, K., Mukharsky, Y., Chui, T. & Pearson, D. Observation of the ideal Josephson effect in superfluid $^4$He. *Nature* **411**, 280–283 (2001).

[131] Abbarchi, M. *et al.* Macroscopic quantum self-trapping and Josephson oscillations of exciton polaritons. *Nat. Phys.* **9**, 275–279 (2013).

[132] Spuntarelli, A., Pieri, P. & Strinati, G. C. Josephson effect throughout the BCS-BEC crossover. *Phys. Rev. Lett.* **99**, 040401 (2007).

[133] Taylor, E. Josephson relation for the superfluid density in the BCS-BEC crossover. *Phys. Rev. B* **77**, 144521 (2008).

[134] Ancilotto, F., Salasnich, L. & Toigo, F. dc Josephson effect with Fermi gases in the Bose-Einstein regime. *Phys. Rev. A* **79**, 033627 (2009).

[135] Zou, P. & Dalfovo, F. Josephson oscillations and self-trapping of superfluid fermions in a double-well potential. *J. Low Temp. Phys.* **177**, 240–256 (2014).

[136] Marchenkov, A., Simmonds, R. W., Davis, J. C. & Packard, R. E. Observation of the Josephson plasma mode for a superfluid $^3\mathrm{He}$ weak link. *Phys. Rev. B* **61**, 4196–4199 (2000).

[137] Leggett, A. J. *Quantum Liquids* (Oxford University Press Oxford, 2006).

[138] Yurgens, A. A. Intrinsic Josephson junctions: Recent developments. *Supercond. Sci. Technol.* **13**, R85–R100 (2000).

[139] Trotzky, S. *et al.* Probing the relaxation towards equilibrium in an isolated strongly correlated one-dimensional bose gas. *Nat. Phys.* **8**, 325–330 (2012).

[140] Chin, J. K. *et al.* Evidence for superfluidity of ultracold fermions in an optical lattice. *Nature* **443**, 961–964 (2006).

[141] Greif, D. *et al.* Site-resolved imaging of a fermionic Mott insulator. *Science* **351**, 953–957 (2016).

[142] Cheuk, L. W. *et al.* Observation of 2D fermionic Mott insulators of $^{40}\mathrm{K}$ with single-site resolution. *Phys. Rev. Lett.* **116**, 235301 (2016).

[143] Grimm, R., Weidemüller, M. & Ovchinnikov, Y. B. Optical dipole traps for neutral atoms. *Adv. At. Mol. Opt. Phy.* **42**, 95–170 (2000).

[144] Becker, C. *et al.* Ultracold quantum gases in triangular optical lattices. *New J. Phys.* **12**, 065025 (2010).

[145] Tarruell, L., Greif, D., Uehlinger, T., Jotzu, G. & Esslinger, T. Creating, moving and merging Dirac points with a Fermi gas in a tunable honeycomb lattice. *Nature* **483**, 302–305 (2012).

[146] Jo, G.-B. *et al.* Ultracold atoms in a tunable optical kagome lattice. *Phys. Rev. Lett.* **108**, 045305 (2012).

[147] Bloch, I. & Zoller, P. Ultracold atoms and molecules in optical lattices. In Levin, K., Fetter, A. & Stamper-Kurn, D. (eds.) *Ultracold Bosonic and Fermionic Gases*, chap. 5, 121–156 (Elsevier, 2012).

[148] Mandel, O. *et al.* Coherent transport of neutral atoms in spin-dependent optical lattice potentials. *Phys. Rev. Lett.* **91**, 010407 (2003).

[149] Mandel, O. *et al.* Controlled collisions for multi-particle entanglement of optically trapped atoms. *Nature* **425**, 937–940 (2003).

[150] Brennen, G. K., Caves, C. M., Jessen, P. S. & Deutsch, I. H. Quantum logic gates in optical lattices. *Phys. Rev. Lett.* **82**, 1060–1063 (1999).

[151] Jaksch, D., Briegel, H.-J., Cirac, J. I., Gardiner, C. W. & Zoller, P. Entanglement of atoms via cold controlled collisions. *Phys. Rev. Lett.* **82**, 1975–1978 (1999).

[152] Liu, W. V., Wilczek, F. & Zoller, P. Spin-dependent Hubbard model and a quantum phase transition in cold atoms. *Phys. Rev. A* **70**, 033603 (2004).

[153] Cowan, R. D. *The Theory of Atomic Structure and Spectra* (University of California Press, 1981).

[154] Soltan-Panahi, P. *et al.* Multi-component quantum gases in spin-dependent hexagonal lattices. *Nat. Phys.* **7**, 434–440 (2011).

[155] Duan, L.-M., Demler, E. & Lukin, M. D. Controlling spin exchange interactions of ultracold atoms in optical lattices. *Phys. Rev. Lett.* **91**, 090402 (2003).

[156] Jotzu, G. *et al.* Creating state-dependent lattices for ultracold fermions by magnetic gradient modulation. *Phys. Rev. Lett.* **115**, 073002 (2015).

[157] Daley, A. J., Boyd, M. M., Ye, J. & Zoller, P. Quantum computing with alkaline-earth-metal atoms. *Phys. Rev. Lett.* **101**, 170504 (2008).

[158] Yi, W., Daley, A. J., Pupillo, G. & Zoller, P. State-dependent, addressable subwavelength lattices with cold atoms. *New J. Phys.* **10**, 073015 (2008).

[159] Daley, A. J., Ye, J. & Zoller, P. State-dependent lattices for quantum computing with alkaline-earth-metal atoms. *Euro. Phys. J. D* **65**, 207–217 (2011).

[160] Jotzu, G. *Probing topological Floquet-bands and quantum magnetism with ultracold fermions*. Ph.D. thesis, ETH Zürich, Switzerland (2015).

[161] Sebby-Strabley, J., Anderlini, M., Jessen, P. S. & Porto, J. V. Lattice of double wells for manipulating pairs of cold atoms. *Phys. Rev. A* **73**, 033605 (2006).

[162] Trotzky, S. *et al.* Time-resolved observation and control of superexchange interactions with ultracold atoms in optical lattices. *Science* **319**, 295–299 (2008).

[163] Anderlini, M. *et al.* Controlled exchange interaction between pairs of neutral atoms in an optical lattice. *Nature* **448**, 452–456 (2007).

[164] Greif, D., Uehlinger, T., Jotzu, G., Tarruell, L. & Esslinger, T. Short-range quantum magnetism of ultracold fermions in an optical lattice. *Science* **340**, 1307–1310 (2013).

[165] Pertot, D. *et al.* Relaxation dynamics of a Fermi gas in an optical superlattice. *Phys. Rev. Lett.* **113**, 170403 (2014).

[166] Dai, H.-N. *et al.* Generation and detection of atomic spin entanglement in optical lattices. *Nat. Phys.* (2016).

[167] Heikkinen, M. *Josephson effect in ultracold Fermi gases*. Master's thesis, Helsinki University of Technology (2009).

[168] Törmä, P. Spectroscopies — Theory. In Törmä, P. & Sengstock, K. (eds.) *Quantum Gas Experiments: Exploring Many-Body States*, chap. 10, 199–250 (Imperial College Press, 2014).

[169] Ambegaokar, V. & Baratoff, A. Tunneling between superconductors. *Phys. Rev. Lett.* **10**, 486–489 (1963).

[170] Baym, G. & Kadanoff, L. P. Conservation laws and correlation functions. *Phys. Rev.* **124**, 287 (1961).

[171] Baym, G. Self-consistent approximations in many-body systems. *Phys. Rev.* **127**, 1391–1401 (1962).

[172] Brantut, J.-P., Meineke, J., Stadler, D., Krinner, S. & Esslinger, T. Conduction of ultracold fermions through a mesoscopic channel. *Science* **337**, 1069–1071 (2012).

[173] Stadler, D., Krinner, S., Meineke, J., Brantut, J.-P. & Esslinger, T. Observing the drop of resistance in the flow of a superfluid Fermi gas. *Nature* **491**, 736–739 (2012).

[174] Brantut, J.-P. *et al.* A thermoelectric heat engine with ultracold atoms. *Science* **342**, 713–715 (2013).

[175] Krinner, S., Stadler, D., Husmann, D., Brantut, J.-P. & Esslinger, T. Observation of quantized conductance in neutral matter. *Nature* **517**, 64–67 (2015).

[176] Husmann, D. *et al.* Connecting strongly correlated superfluids by a quantum point contact. *Science* **350**, 1498–1501 (2015).

[177] Krinner, S. *et al.* Mapping out spin and particle conductances in a quantum point contact. *Proc. Natl. Acad. Sci. USA* **113**, 8144–8149 (2016).

[178] Regal, C. A. & Jin, D. S. Measurement of positive and negative scattering lengths in a Fermi gas of atoms. *Phys. Rev. Lett.* **90**, 230404 (2003).

[179] Gupta, S. *et al.* Radio-frequency spectroscopy of ultracold fermions. *Science* **300**, 1723–1726 (2003).

[180] Huckans, J. H., Williams, J. R., Hazlett, E. L., Stites, R. W. & O'Hara, K. M. Three-body recombination in a three-state Fermi gas with widely tunable interactions. *Phys. Rev. Lett.* **102**, 165302 (2009).

[181] Williams, J. R. *et al.* Evidence for an excited-state Efimov trimer in a three-component Fermi gas. *Phys. Rev. Lett.* **103**, 130404 (2009).

[182] Ottenstein, T. B., Lompe, T., Kohnen, M., Wenz, A. N. & Jochim, S. Collisional stability of a three-component degenerate Fermi gas. *Phys. Rev. Lett.* **101**, 203202 (2008).

[183] Ferrier Barbut, I. *et al.* A mixture of Bose and Fermi superfluids. *Science* **345**, 1035 (2014).

[184] Yao, X.-C. *et al.* Observation of coupled vortex lattices in a mass-imbalance Bose and Fermi superfluid mixture. *Phys. Rev. Lett.* **117**, 145301 (2016).

[185] Roy, R., Green, A., Bowler, R. & Gupta, S. Two-element mixture of Bose and Fermi superfluids. *Phys. Rev. Lett.* **118**, 055301 (2017).

[186] Deh, B., Marzok, C., Zimmermann, C. & Courteille, P. W. Feshbach resonances in mixtures of ultracold $^{6}$Li and $^{87}$Rb gases. *Phys. Rev. A* **77**, 010701 (2008).

[187] Repp, M. *et al.* Observation of interspecies $^{6}$Li-$^{133}$Cs Feshbach resonances. *Phys. Rev. A* **87**, 010701 (2013).

[188] Fulde, P. & Ferrell, R. A. Superconductivity in a strong spin-exchange field. *Phys. Rev.* **135**, A550–A563 (1964).

[189] Larkin, A. I. & Ovchinnikov, Y. N. Inhomogeneous state of superconductors. *Sov. Phys. JETP* **20**, 762 (1965).

[190] Casalbuoni, R. & Nardulli, G. Inhomogeneous superconductivity in condensed matter and QCD. *Rev. Mod. Phys.* **76**, 263–320 (2004).

[191] Zwierlein, M. W., Schirotzek, A., Schunck, C. H. & Ketterle, W. Fermionic superfluidity with imbalanced spin populations. *Science* **311**, 492–496 (2006).

[192] Partridge, G. B., Li, W., Kamar, R. I., Liao, Y.-a. & Hulet, R. G. Pairing and phase separation in a polarized Fermi gas. *Science* **311**, 503–505 (2006).

[193] Kinnunen, J., Jensen, L. M. & Törmä, P. Strongly interacting Fermi gases with density imbalance. *Phys. Rev. Lett.* **96**, 110403 (2006).

[194] Riedel, E. Zum Tunneleffekt bei Supraleitern im Mikrowellenfeld. *Z. Naturforsch.* **19a**, 1634 (1964).

[195] Werthamer, N. R. Nonlinear self-coupling of Josephson radiation in superconducting tunnel junctions. *Phys. Rev.* **147**, 255–263 (1966).

[196] Ku, M. J. H., Sommer, A. T., Cheuk, L. W. & Zwierlein, M. W. Revealing the superfluid lambda transition in the universal thermodynamics of a unitary Fermi gas. *Science* **335**, 563–567 (2012).

[197] Daley, A. J., Kollath, C., Schollwöck, U. & Vidal, G. Time-dependent density-matrix renormalization-group using adaptive effective Hilbert spaces. *J. Stat. Mech.: Theor. Exp.* **2004**, P04005 (2004).

[198] Taglieber, M., Voigt, A.-C., Aoki, T., Hänsch, T. W. & Dieckmann, K. Quantum degenerate two-species Fermi-Fermi mixture coexisting with a Bose-Einstein condensate. *Phys. Rev. Lett.* **100**, 010401 (2008).

[199] Wille, E. *et al.* Exploring an ultracold Fermi-Fermi mixture: Interspecies Feshbach resonances and scattering properties of $^{6}$Li and $^{40}$K. *Phys. Rev. Lett.* **100**, 053201 (2008).

[200] Tiecke, T. G. *et al.* Broad Feshbach resonance in the $^{6}$Li-$^{40}$K mixture. *Phys. Rev. Lett.* **104**, 053202 (2010).

[201] Hansen, A. H. *et al.* Production of quantum-degenerate mixtures of ytterbium and lithium with controllable interspecies overlap. *Phys. Rev. A* **87**, 013615 (2013).

[202] Edge, G. J. A. *et al.* Imaging and addressing of individual fermionic atoms in an optical lattice. *Phys. Rev. A* **92**, 063406 (2015).

[203] Omran, A. *et al.* Microscopic observation of Pauli blocking in degenerate fermionic lattice gases. *Phys. Rev. Lett.* **115**, 263001 (2015).

[204] Haller, E. *et al.* Single-atom imaging of fermions in a quantum-gas microscope. *Nat. Phys.* **11**, 738–742 (2015).

[205] Gerry, C. C. & Knight, P. L. *Introductory Quantum Optics* (Cambridge University Press, 2005).

[206] Ryazanov, V. V. *et al.* Coupling of two superconductors through a ferromagnet: Evidence for a $\pi$ junction. *Phys. Rev. Lett.* **86**, 2427–2430 (2001).

[207] Keizer, R. S. *et al.* A spin triplet supercurrent through the half-metallic ferromagnet $CrO_2$. *Nature* **439**, 825–827 (2006).

[208] Khaire, T. S., Khasawneh, M. A., Pratt, W. P. & Birge, N. O. Observation of spin-triplet superconductivity in Co-based Josephson junctions. *Phys. Rev. Lett.* **104**, 137002 (2010).

[209] Bergeret, F. S. & Tokatly, I. V. Singlet-triplet conversion and the long-range proximity effect in superconductor-ferromagnet structures with generic spin dependent fields. *Phys. Rev. Lett.* **110**, 117003 (2013).

[210] Bergeret, F. S., Volkov, A. F. & Efetov, K. B. Odd triplet superconductivity and related phenomena in superconductor-ferromagnet structures. *Rev. Mod. Phys.* **77**, 1321–1373 (2005).

[211] Golubov, A. A., Kupriyanov, M. Y. & Il'ichev, E. The current-phase relation in Josephson junctions. *Rev. Mod. Phys.* **76**, 411–469 (2004).

[212] Buzdin, A. I. Proximity effects in superconductor-ferromagnet heterostructures. *Rev. Mod. Phys.* **77**, 935–976 (2005).

[213] Meservey, R. & Tedrow, P. M. Spin-polarized electron tunneling. *Phys. Rep.* **238**, 173–243 (1994).

[214] Andreev, A. F. Thermal conductivity of the intermediate state of superconductors. *Sov. Phys. JETP* **19**, 1228–1231 (1964).

[215] Chtchelkatchev, N. M., Belzig, W. & Bruder, C. Josephson effect in $S_FXS_F$ junctions. *JETP Lett.* **75**, 646–650 (2002).

[216] Robinson, J. W. A., Halász, G. B., Buzdin, A. I. & Blamire, M. G. Enhanced supercurrents in Josephson junctions containing nonparallel ferromagnetic domains. *Phys. Rev. Lett.* **104**, 207001 (2010).

[217] Buzdin, A., Tollis, S. & Cayssol, J. Field-induced superconductivity with an enhanced and tunable paramagnetic limit. *Phys. Rev. Lett.* **95**, 167003 (2005).

[218] Clogston, A. M. Upper limit for the critical field in hard superconductors. *Phys. Rev. Lett.* **9**, 266–267 (1962).

[219] Chandrasekhar, B. S. A note on the maximum critical field of high-field superconductors. *Appl. Phys. Lett.* **1**, 7 (1962).

[220] Häffner, H., Roos, C. F. & Blatt, R. Quantum computing with trapped ions. *Phys. Rep.* **469**, 155–203 (2008).

[221] Bauer, B., Wecker, D., Millis, A. J., Hastings, M. B. & Troyer, M. Hybrid quantum-classical approach to correlated materials. *Phys. Rev. X* **6**, 031045 (2016).

[222] Wecker, D. *et al.* Solving strongly correlated electron models on a quantum computer. *Phys. Rev. A* **92**, 062318 (2015).

[223] Dallaire-Demers, P.-L. & Wilhelm, F. K. Method to efficiently simulate the thermodynamic properties of the Fermi-Hubbard model on a quantum computer. *Phys. Rev. A* **93**, 032303 (2016).

[224] Dallaire-Demers, P.-L. & Wilhelm, F. K. Quantum gates and architecture for the quantum simulation of the Fermi-Hubbard model. *Phys. Rev. A* **94**, 062304 (2016).

[225] Jordan, P. & Wigner, E. Über das Paulische Äquivalenzverbot. *Z. Phys.* **47**, 631–651 (1928).

[226] Sachdev, S. *Quantum Phase Transitions* (Cambridge University Press, 2011), 2nd edn.

[227] Lamata, L., Mezzacapo, A., Casanova, J. & Solano, E. Efficient quantum simulation of fermionic and bosonic models in trapped ions. *EPJ Quantum Technol.* **1**, 1 (2014).

[228] Clarke, J. & Wilhelm, F. K. Superconducting quantum bits. *Nature* **453**, 1031–1042 (2008).

[229] Devoret, M. H. & Schoelkopf, R. J. Superconducting circuits for quantum information: An outlook. *Science* **339**, 1169–1174 (2013).

[230] Schneider, C., Porras, D. & Schaetz, T. Experimental quantum simulations of many-body physics with trapped ions. *Rep. Prog. Phys.* **75**, 024401 (2012).

[231] You, J. Q. & Nori, F. Atomic physics and quantum optics using superconducting circuits. *Nature* **474**, 589–597 (2011).

[232] Bouchiat, V., Vion, D., Joyez, P., Esteve, D. & Devoret, M. Quantum coherence with a single Cooper pair. *Phys. Scr.* **T76**, 165 (1998).

[233] Nakamura, Y., Pashkin, Y. A. & Tsai, J. Coherent control of macroscopic quantum states in a single-Cooper-pair box. *Nature* **398**, 786–788 (1999).

[234] Mooij, J. E. *et al.* Josephson persistent-current qubit. *Science* **285**, 1036–1039 (1999).

[235] Martinis, J. M., Nam, S., Aumentado, J. & Urbina, C. Rabi oscillations in a large Josephson-junction qubit. *Phys. Rev. Lett.* **89**, 117901 (2002).

[236] Koch, J. *et al.* Charge-insensitive qubit design derived from the Cooper pair box. *Phys. Rev. A* **76**, 042319 (2007).

[237] Schreier, J. A. *et al.* Suppressing charge noise decoherence in superconducting charge qubits. *Phys. Rev. B* **77**, 180502 (2008).

[238] Barends, R. *et al.* Coherent Josephson qubit suitable for scalable quantum integrated circuits. *Phys. Rev. Lett.* **111**, 080502 (2013).

[239] Las Heras, U. *et al.* Digital quantum simulation of spin systems in superconducting circuits. *Phys. Rev. Lett.* **112**, 200501 (2014).

[240] Mezzacapo, A., Lamata, L., Filipp, S. & Solano, E. Many-body interactions with tunable-coupling transmon qubits. *Phys. Rev. Lett.* **113**, 050501 (2014).

[241] Salathé, Y. *et al.* Digital quantum simulation of spin models with circuit quantum electrodynamics. *Phys. Rev. X* **5**, 021027 (2015).

[242] Sillanpää, M. A., Park, J. I. & Simmonds, R. W. Coherent quantum state storage and transfer between two phase qubits via a resonant cavity. *Nature* **449**, 438–442 (2007).

[243] Majer, J. *et al.* Coupling superconducting qubits via a cavity bus. *Nature* **449**, 443–447 (2007).

[244] Blais, A., Huang, R.-S., Wallraff, A., Girvin, S. M. & Schoelkopf, R. J. Cavity quantum electrodynamics for superconducting electrical circuits: An architecture for quantum computation. *Phys. Rev. A* **69**, 062320 (2004).

[245] Wallraff, A. *et al.* Strong coupling of a single photon to a superconducting qubit using circuit quantum electrodynamics. *Nature* **431**, 162–167 (2004).

[246] Schoelkopf, R. J. & Girvin, S. M. Wiring up quantum systems. *Nature* **451**, 664–669 (2008).

[247] Filipp, S. *et al.* Multimode mediated qubit-qubit coupling and dark-state symmetries in circuit quantum electrodynamics. *Phys. Rev. A* **83**, 063827 (2011).

[248] DiCarlo, L. *et al.* Demonstration of two-qubit algorithms with a superconducting quantum processor. *Nature* **460**, 240–244 (2009).

[249] Song, C. *et al.* 10-qubit entanglement and parallel logic operations with a superconducting circuit. *arXiv:1703.10302* (2017).

[250] Las Heras, U. *Digital quantum simulations of spin models in superconducting circuits*. Master's thesis, University of the Basque Country (2013).

[251] Barends, R. *et al.* Superconducting quantum circuits at the surface code threshold for fault tolerance. *Nature* **508**, 500–503 (2014).

[252] Yamamoto, T. *et al.* Quantum process tomography of two-qubit controlled-Z and controlled-NOT gates using superconducting phase qubits. *Phys. Rev. B* **82**, 184515 (2010).

[253] Martinis, J. M. & Geller, M. R. Fast adiabatic qubit gates using only $\sigma_z$ control. *Phys. Rev. A* **90**, 022307 (2014).

[254] Jaynes, E. T. & Cummings, F. W. Comparison of quantum and semiclassical radiation theories with application to the beam maser. *Proc. IEEE* **51**, 89–109 (1963).

[255] García-Ripoll, J. J., Solano, E. & Martin-Delgado, M. A. Quantum simulation of Anderson and Kondo lattices with superconducting qubits. *Phys. Rev. B* **77**, 024522 (2008).

[256] Haeberlein, M. *et al.* Spin-boson model with an engineered reservoir in circuit quantum electrodynamics. *arXiv:1506.09114* (2015).

[257] Correa, B. V., Kurcz, A. & García-Ripoll, J. J. Bose–Hubbard models with photon pairing in circuit-QED. *J. Phys. B: At. Mol. Opt. Phys* **46**, 224024 (2013).

[258] Marcos, D., Rabl, P., Rico, E. & Zoller, P. Superconducting circuits for quantum simulation of dynamical gauge fields. *Phys. Rev. Lett.* **111**, 110504 (2013).

[259] Ballester, D., Romero, G., García-Ripoll, J. J., Deppe, F. & Solano, E. Quantum simulation of the ultrastrong-coupling dynamics in circuit quantum electrodynamics. *Phys. Rev. X* **2**, 021007 (2012).

[260] Las Heras, U., García-Álvarez, L., Mezzacapo, A., Solano, E. & Lamata, L. Fermionic models with superconducting circuits. *EPJ Quantum Technol.* **2**, 1–11 (2015).

[261] García-Álvarez, L. *et al.* Digital quantum simulation of minimal AdS/CFT. *arXiv:1607.08560* (2016).

[262] Paraoanu, G. S. Recent progress in quantum simulation using superconducting circuits. *J. Low Temp. Phys.* **175**, 633–654 (2014).

[263] Romero, G., Solano, E. & Lamata, L. Quantum simulations with circuit quantum electrodynamics. *arXiv:1606.01755* (2016).

[264] Cirac, J. I. & Zoller, P. Quantum computations with cold trapped ions. *Phys. Rev. Lett.* **74**, 4091–4094 (1995).

[265] Myerson, A. H. *et al.* High-fidelity readout of trapped-ion qubits. *Phys. Rev. Lett.* **100**, 200502 (2008).

[266] Blinov, B. B., Leibfried, D., Monroe, C. & Wineland, D. J. Quantum computing with trapped ion hyperfine qubits. *Quantum Inf. Process.* **3**, 45–59 (2004).

[267] Harty, T. P. *et al.* High-fidelity preparation, gates, memory, and readout of a trapped-ion quantum bit. *Phys. Rev. Lett.* **113**, 220501 (2014).

[268] Monz, T. *et al.* 14-qubit entanglement: Creation and coherence. *Phys. Rev. Lett.* **106**, 130506 (2011).

[269] Monroe, C., Meekhof, D. M., King, B. E., Itano, W. M. & Wineland, D. J. Demonstration of a fundamental quantum logic gate. *Phys. Rev. Lett.* **75**, 4714–4717 (1995).

[270] Schmidt-Kaler, F. *et al.* Realization of the Cirac–Zoller controlled-NOT quantum gate. *Nature* **422**, 408–411 (2003).

[271] Sørensen, A. & Mølmer, K. Quantum computation with ions in thermal motion. *Phys. Rev. Lett.* **82**, 1971–1974 (1999).

[272] Mølmer, K. & Sørensen, A. Multiparticle entanglement of hot trapped ions. *Phys. Rev. Lett.* **82**, 1835 (1999).

[273] Sørensen, A. & Mølmer, K. Entanglement and quantum computation with ions in thermal motion. *Phys. Rev. A* **62**, 022311 (2000).

[274] Solano, E., de Matos Filho, R. L. & Zagury, N. Deterministic Bell states and measurement of the motional state of two trapped ions. *Phys. Rev. A* **59**, R2539 (1999).

[275] Milburn, G. J., Schneider, S. & James, D. F. V. Ion trap quantum computing with warm ions. *Fortschr. Phys.* **48**, 801–810 (2000).

[276] Roos, C. F. Ion trap quantum gates with amplitude-modulated laser beams. *New J. Phys.* **10**, 013002 (2008).

[277] Benhelm, J., Kirchmair, G., Roos, C. F. & Blatt, R. Towards fault-tolerant quantum computing with trapped ions. *Nat. Phys.* **4**, 463–466 (2008).

[278] Müller, M., Hammerer, K., Zhou, Y. L., Roos, C. F. & Zoller, P. Simulating open quantum systems: from many-body interactions to stabilizer pumping. *New J. Phys.* **13**, 085007 (2011).

[279] Monz, T. *Quantum information processing beyond ten ion-qubits*. Ph.D. thesis, Leopold-Franzens-Universität Innsbruck, Austria (2011).

[280] Casanova, J., Mezzacapo, A., Lamata, L. & Solano, E. Quantum simulation of interacting fermion lattice models in trapped ions. *Phys. Rev. Lett.* **108**, 190502 (2012).

[281] Ballance, C. J., Harty, T. P., Linke, N. M., Sepiol, M. A. & Lucas, D. M. High-fidelity quantum logic gates using trapped-ion hyperfine qubits. *Phys. Rev. Lett.* **117**, 060504 (2016).

[282] Harty, T. P. *et al.* High-fidelity trapped-ion quantum logic using near-field microwaves. *Phys. Rev. Lett.* **117**, 140501 (2016).

[283] Porras, D. & Cirac, J. I. Effective quantum spin systems with trapped ions. *Phys. Rev. Lett.* **92**, 207901 (2004).

[284] Friedenauer, A., Schmitz, H., Glueckert, J. T., Porras, D. & Schätz, T. Simulating a quantum magnet with trapped ions. *Nat. Phys.* **4**, 757–761 (2008).

[285] Kim, K. *et al.* Quantum simulation of frustrated Ising spins with trapped ions. *Nature* **465**, 590–593 (2010).

[286] Casanova, J., García-Ripoll, J. J., Gerritsma, R., Roos, C. F. & Solano, E. Klein tunneling and Dirac potentials in trapped ions. *Phys. Rev. A* **82**, 020101 (2010).

[287] Gerritsma, R. *et al.* Quantum simulation of the Klein paradox with trapped ions. *Phys. Rev. Lett.* **106**, 060503 (2011).

[288] Zhang, X. *et al.* Time reversal and charge conjugation in an embedding quantum simulator. *Nat. Commun.* **6** (2015).

[289] Casanova, J. *et al.* Quantum simulation of quantum field theories in trapped ions. *Phys. Rev. Lett.* **107**, 260501 (2011).

[290] Zhang, X. *et al.* Fermion-antifermion scattering via boson exchange in a trapped ion. *arXiv:1611.00099* (2016).

[291] Shen, Y. *et al.* Quantum implementation of the unitary coupled cluster for simulating molecular electronic structure. *Phys. Rev. A* **95**, 020501 (2017).

[292] Maier, T., Jarrell, M., Pruschke, T. & Hettler, M. H. Quantum cluster theories. *Rev. Mod. Phys.* **77**, 1027–1080 (2005).

[293] Kotliar, G. *et al.* Electronic structure calculations with dynamical mean-field theory. *Rev. Mod. Phys.* **78**, 865–951 (2006).

[294] Metzner, W. & Vollhardt, D. Correlated lattice fermions in $d = \infty$ dimensions. *Phys. Rev. Lett.* **62**, 324 (1989).

[295] Müller-Hartmann, E. Correlated fermions on a lattice in high dimensions. *Z. Phys. B* **74**, 507–512 (1989).

[296] Müller-Hartmann, E. The Hubbard model at high dimensions: some exact results and weak coupling theory. *Z. Phys. B* **76**, 211–217 (1989).

[297] Held, K. Electronic structure calculations using dynamical mean field theory. *Adv. Phys.* **56**, 829 (2007).

[298] Georges, A. & Kotliar, G. Hubbard model in infinite dimensions. *Phys. Rev. B* **45**, 6479 (1992).

[299] Jarrell, M. Hubbard model in infinite dimensions: A quantum Monte Carlo study. *Phys. Rev. Lett.* **69**, 168 (1992).

[300] Gramsch, C., Balzer, K., Eckstein, M. & Kollar, M. Hamiltonian-based impurity solver for nonequilibrium dynamical mean-field theory. *Phys. Rev. B* **88**, 235106 (2013).

[301] Freericks, J. K. *Transport in multilayered nanostructures: The dynamical mean-field theory approach* (World Scientific, 2006).

[302] Eckstein, M. & Kollar, M. Near-adiabatic parameter changes in correlated systems: influence of the ramp protocol on the excitation energy. *New J. Phys.* **12**, 055012 (2010).

[303] Golub, G. H. & Van Loan, C. F. *Matrix Computations* (The Johns Hopkins University Press, 2013), 4 edn.

[304] Gull, E. *et al.* Continuous-time Monte Carlo methods for quantum impurity models. *Rev. Mod. Phys.* **83**, 349–404 (2011).

[305] Troyer, M. & Wiese, U.-J. Computational complexity and fundamental limitations to fermionic quantum Monte Carlo simulations. *Phys. Rev. Lett.* **94**, 170201 (2005).

[306] García, D. J., Hallberg, K. & Rozenberg, M. J. Dynamical mean field theory with the density matrix renormalization group. *Phys. Rev. Lett.* **93**, 246403 (2004).

[307] Ganahl, M., Thunström, P., Verstraete, F., Held, K. & Evertz, H. G. Chebyshev expansion for impurity models using matrix product states. *Phys. Rev. B* **90**, 045144 (2014).

[308] Wolf, F. A., McCulloch, I. P., Parcollet, O. & Schollwöck, U. Chebyshev matrix product state impurity solver for dynamical mean-field theory. *Phys. Rev. B* **90**, 115124 (2014).

[309] Wolf, F. A., McCulloch, I. P. & Schollwöck, U. Solving nonequilibrium dynamical mean-field theory using matrix product states. *Phys. Rev. B* **90**, 235131 (2014).

[310] Ganahl, M. *et al.* Efficient DMFT impurity solver using real-time dynamics with matrix product states. *Phys. Rev. B* **92**, 155132 (2015).

[311] Wolf, F. A., Go, A., McCulloch, I. P., Millis, A. J. & Schollwöck, U. Imaginary-time matrix product state impurity solver for dynamical mean-field theory. *Phys. Rev. X* **5**, 041032 (2015).

[312] Barends, R. *et al.* Digitized adiabatic quantum computing with a superconducting circuit. *Nature* **534**, 222 (2016).

[313] Potthoff, M. Two-site dynamical mean-field theory. *Phys. Rev. B* **64**, 165114 (2001).

[314] IBM Quantum Experience. `https://www.research.ibm.com/ibm-q/qx/`. (Retrieved 21 March, 2017).

[315] Kelly, J. *et al.* State preservation by repetitive error detection in a superconducting quantum circuit. *Nature* **519**, 66–69 (2015).

[316] Potthoff, M., Herrmann, T., Wegner, T. & Nolting, W. The moment sum rule and its consequences for ferromagnetism in the Hubbard model. *Phys. Status Solidi B* **210**, 199 (1998).

[317] Li, Y. & Benjamin, S. C. Efficient variational quantum simulator incorporating active error minimization. *Phys. Rev. X* **7**, 021050 (2017).

[318] Nielsen, M. A. & Chuang, I. L. *Quantum Computation and Quantum Information* (Cambridge University Press, 2000).

[319] Knill, E. Quantum computing with realistically noisy devices. *Nature* **434**, 39–44 (2005).

[320] Taylor, J. M. *et al.* Fault-tolerant architecture for quantum computation using electrically controlled semiconductor spins. *Nat. Phys.* **1**, 177–183 (2005).

[321] Nickerson, N. H., Li, Y. & Benjamin, S. C. Topological quantum computing with a very noisy network and local error rates approaching one percent. *Nat. Commun.* **4**, 1756 (2013).

[322] Sawaya, N. P. D., Smelyanskiy, M., McClean, J. R. & Aspuru-Guzik, A. Error sensitivity to environmental noise in quantum circuits for chemical state preparation. *J. Chem. Theory Comput.* **12**, 3097–3108 (2016).

[323] Boixo, S. *et al.* Characterizing quantum supremacy in near-term devices. *arXiv:1608.00263* (2016).

[324] Bermudez, A. *et al.* Assessing the progress of trapped-ion processors towards fault-tolerant quantum computation. *arXiv:1705.02771* (2017).

[325] Fowler, A. G., Hill, C. D. & Hollenberg, L. C. L. Quantum-error correction on linear-nearest-neighbor qubit arrays. *Phys. Rev. A* **69**, 042314 (2004).

[326] Viamontes, G. F., Markov, I. L. & Hayes, J. P. *Quantum Circuit Simulation* (Springer, 2009).

[327] Cuevas, J. C. & Scheer, E. *Molecular Electronics: An Introduction to Theory and Experiment*, vol. 1 (World Scientific, 2010).

[328] Arrigoni, E., Knap, M. & von der Linden, W. Nonequilibrium dynamical mean-field theory: An auxiliary quantum master equation approach. *Phys. Rev. Lett.* **110**, 086403 (2013).

[329] Dorda, A., Nuss, M., von der Linden, W. & Arrigoni, E. Auxiliary master equation approach to nonequilibrium correlated impurities. *Phys. Rev. B* **89**, 165105 (2014).

[330] Dzhioev, A. A. & Kosov, D. S. Super-fermion representation of quantum kinetic equations for the electron transport problem. *J. Chem. Phys.* **134**, 044121 (2011).

[331] Smelyanskiy, M., Sawaya, N. P. D. & Aspuru-Guzik, A. qHiPSTER: The quantum high performance software testing environment. *arXiv:1601.07195* (2016).

[332] Häner, T. & Steiger, D. S. 0.5 petabyte simulation of a 45-qubit quantum circuit. *arXiv:1704.01127* (2017).

[333] The Networked Quantum Information Technologies Hub. `https://nqit.ox.ac.uk`. (Retrieved 21 March, 2017).

[334] A bet on quantum. *Nat. Phys.* **11**, 89 (2015).

[335] Ashcroft, N. W. & Mermin, N. D. *Solid State Physics* (Brooks Cole, 1976).

[336] Wannier, G. H. The structure of electronic excitation levels in insulating crystals. *Phys. Rev.* **52**, 191–197 (1937).

[337] Marzari, N. & Vanderbilt, D. Maximally localized generalized Wannier functions for composite energy bands. *Phys. Rev. B* **56**, 12847–12865 (1997).

[338] Kohn, W. Analytic properties of Bloch waves and Wannier functions. *Phys. Rev.* **115**, 809 (1959).

[339] Marzari, N., Mostofi, A. A., Yates, J. R., Souza, I. & Vanderbilt, D. Maximally localized Wannier functions: Theory and applications. *Rev. Mod. Phys.* **84**, 1419–1475 (2012).

[340] Walters, R., Cotugno, G., Johnson, T. H., Clark, S. R. & Jaksch, D. *Ab initio* derivation of Hubbard models for cold atoms in optical lattices. *Phys. Rev. A* **87**, 043613 (2013).

[341] Verstraete, F., Murg, V. & Cirac, J. I. Matrix product states, projected entangled pair states, and variational renormalization group methods for quantum spin systems. *Adv. Phys.* **57**, 143–224 (2008).

[342] Verstraete, F. & Cirac, J. I. Matrix product states represent ground states faithfully. *Phys. Rev. B* **73**, 094423 (2006).

[343] Eisert, J., Cramer, M. & Plenio, M. B. Colloquium: Area laws for the entanglement entropy. *Rev. Mod. Phys.* **82**, 277 (2010).

[344] Dorner, R. *et al.* Extracting quantum work statistics and fluctuation theorems by single-qubit interferometry. *Phys. Rev. Lett.* **110**, 230601 (2013).

[345] Ekert, A. K. *et al.* Direct estimations of linear and nonlinear functionals of a quantum state. *Phys. Rev. Lett.* **88**, 217901 (2002).